

DANISH METEOROLOGICAL INSTITUTE

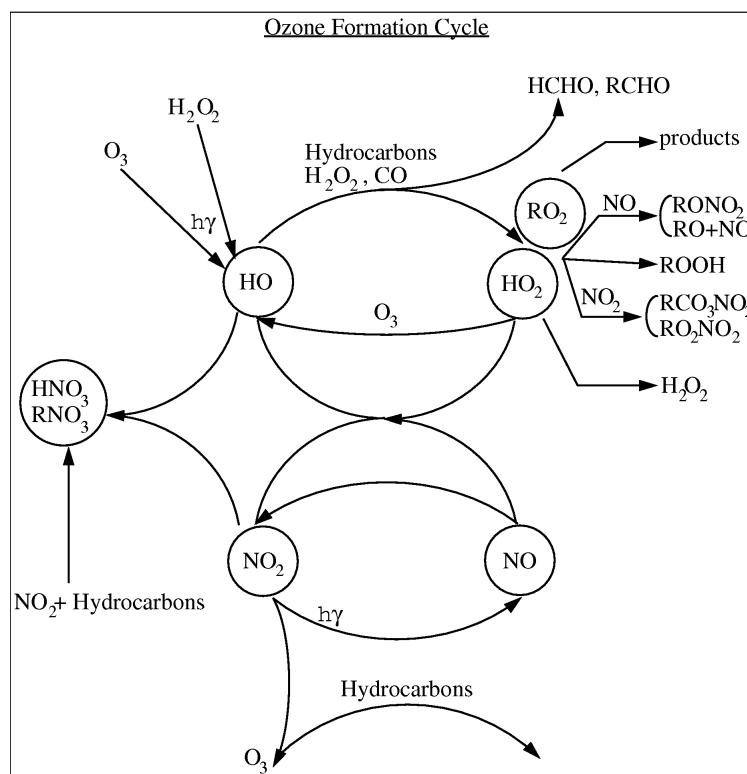
SCIENTIFIC REPORT

00-03

Surface Ozone and Tropospheric Chemistry with Applications to Regional Air Quality Modeling

PhD thesis

Allan Gross

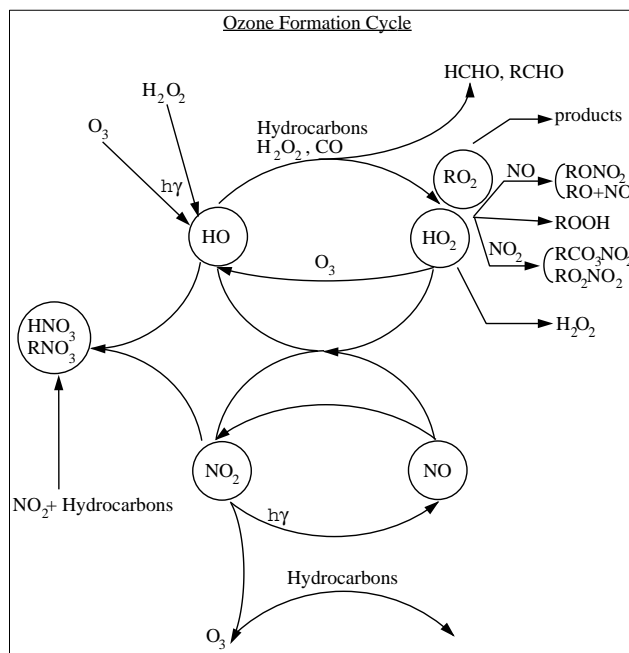


DMI

COPENHAGEN 2000

ISSN-Nr. 0905-3263 (printed)
ISSN Nr. 1399-1949 (online)
ISBN-Nr. 87-7478-406-4

Surface Ozone and Tropospheric Chemistry with Applications to Regional Air Quality Modeling



Allan Gross

Faculty of Science, University of Copenhagen
 Department of Geophysics
 Juliane Maries Vej 30, DK-2100 Copenhagen Ø, Denmark
 and
 Danish Meteorological Institute (DMI),
 Meteorological Research Department (FM),
 Lyngbyvej 100, DK-2100 Copenhagen Ø, Denmark

May 1999

Contents

Preface	v
List of Frequently Used Symbols	vii
Dansk Sammenfatning	xi
Abstract	xv
Introduction	1
1 Tropospheric Chemistry	13
1.1 Tropospheric Gas-Phase Chemistry	16
1.1.1 Background Troposphere	16
1.1.2 Polluted air	23
1.1.3 Formation of Water-Soluble Gases	30
1.2 Simulations	31
1.2.1 The Mechanisms	32
1.2.2 Comparison of the EMEP, RADM2 and RACM MCHs	35
1.3 Conclusion	63
2 Theoretical Treatment of Elementary Chemical Reactions	65
2.1 Outline of Dynamical and Statistical Methods to Calculate Bi-Molecular Rate Constants	68
2.2 Ab Initio Calculations	73
2.2.1 Theory	74
2.2.2 Results	77
2.3 Phase-Space Methods	81
2.3.1 Long-Range Potentials	81
2.3.2 Phase-Space Theory	86
2.4 Conclusion	113
3 Air Quality Modeling	117
3.1 MOON Model: Theory	121
3.1.1 Transport	122

3.1.2	Emissions and Transformation of Chemical Compounds During Transport	123
3.2	0-Dimensional Simulations	131
3.3	3-Dimensional Simulations	137
3.3.1	Comparison 1	139
3.3.2	Comparison 2	141
3.4	Conclusion	156
4	Conclusion and Prospects	159
4.1	The MOON Model	159
4.2	The New Quantum Statistical Model	162
4.3	Concluding Remarks	162
A	EMEP, RADM2 and RACM MCHs	165
B	Implementation of VOC Emissions	187
B.1	Methods	188
B.2	Comment	191
C	Numerical Solution of Complex Chemical MCHs	201
C.1	The QSSA Solver	202
C.2	The Chemical Solver in the MOON Model	204
D	How to run the MOON Model	211
D.1	Subroutines	215
D.2	Input (*.dat) Output (*.out) and Other Non-fortran Files	219
D.3	List of Non-Array Parameters	220
E	Isopleths and Scatter Plots	225
F	3-Dimensional Simulations	241
G	Titles and Abstracts of Articles	255
G.1	Tropospheric Chemistry	255
G.2	Theoretical Treatment of Elementary Chemical Reactions	256
G.3	Air Quality Modeling	259
	References	260

Preface

The present thesis is based on work done at the Danish Meteorological Institute (DMI) in collaboration with the Department of Geophysics, University of Copenhagen, during the period Marts 1996 to May 1999, toward obtaining a Ph.D. in Geophysics.

Atmospheric chemistry is of great interest in the understanding and modeling of the chemical composition of the atmosphere. The thesis deals both with modeling of complex atmospheric chemical mechanisms, atmospheric transport-chemical modeling (with special emphasis on surface ozone) and theoretical calculations of chemical rate constants with special application to atmospheric reactions. Most of the material in this thesis has already appeared or are in the process of being submitted for publication (*Appendix G*).

I would like to thank my advisor Associate Professor A.W. Hansen, Department of Geophysics, University of Copenhagen, for his guidance throughout the course of this work.

During the last three years, I have had the privilege to collaborate with Associate Research Professor W.R. Stockwell, Desert Research Institute. It has been a great pleasure for me to be a part of W.R. Stockwell tremendous flow of scientific ideas, and I am very grateful for his help, advice and inspiration during my Ph.D. studies. Furthermore, I would like to thank him and his wife J. Stockwell for their friendship and warm hospitality during a two month stay in Reno, Nevada.

It has been a great pleasure for me to work together with Associate Professor K.V. Mikkelsen, Department of Chemistry, University of Copenhagen, and Professor G.D. Billing, Department of Chemistry, University of Copenhagen, on some parts of the research presented in this thesis. I am also very much indebted to K.V. Mikkelsen, M. Kmit (FM, DMI) and B. Knudsen (FO, DMI) for their friendship and encouragement to me during the last three years.

Finally, I would like to acknowledge the hospitality of the Fraunhofer-Institut Für Atmosphärische Umweltforschung, Garmisch-Partenkirchen, Germany, and the Desert Research Institute, Nevada, USA, where I have worked 6 months and two months, respectively, during my Ph.D.-studies. Lastly, I want to thank my scientific colleagues at FM in particular the members in the air pollution group: A. Baklanov, J. Chenevez, S. Kiilsholm, A. Rasmussen and J.H. Sørensen, and head of FM L. Laursen.

Allan Gross. Copenhagen, May 1999.

List of Frequently Used Symbols

List of abbreviations, acronyms for transport models and chemical mechanisms and mathematical symbols used consistently throughout the thesis.

Abbreviations

- ABL: Atmospheric Boundary Layer.
- AOT: Accumulated Ozone exposure above Threshold.
- ACTM: Atmospheric Chemical Transport Model.
- CC: Coupled Cluster.
- CI: Configuration Interaction.
- CMWG: Chemical Mechanism Working Group.
- CRS: Chemical Reactions Scheme.
- DMI: Danish Meteorological Institute.
- DNMI: Norwegian Meteorological Institute.
- CoCo: Collision Complex.
- EBI: Eulerian Backward Iterative.
- ECMWF: European Centre for Medium-Range Weather Forecasts.
- EUMAC: EUropean Modelling of Atmospheric Constituents.
- EUROTRAC: EUROpean experiment on TRANsport and transformation of environmentally relevant trace Constituents in the troposphere over Europe.
- IEH: Implicit-Explicit Hybrid.
- GTO: Gaussian Type Orbitals.
- GETALFACTS: Gross ET AL.'s PHase space program packets to Treat larger chemical Systems.

- GSLCC: Geometric Short-Living CoCo.
- HF: Hartree-Fock.
- LSODE: Livermore Solver for Ordinary Differential Equations.
- MBPT: Many-Body Perturbation Theory.
- MCH: MeCHanism.
- MP: Møller Plesset perturbation theory.
- MP2: Møller Plesset second order perturbation theory.
- MO: Molecular Orbitals.
- NAPAP: National Acid Precipitation Assessment Program.
- ODE: Ordinary Differential Equation.
- PES: Potential Energy Surface.
- PST: Phase Space Theory.
- QSSA: Quasi-Steady-State Approximation.
- RAQM: Regional Air Quality Model.
- SCF: Self-Consistent Field.
- TOD: Total Ozone Dose.
- TST: Transition State Theory.
- VODE: Variable Coefficient Ordinary Differential Equation Solver.
- VTST: Variation Transition State Theory.
- WHO: World Health Organization.

Acronyms for transport models and chemical mechanisms

- ADOM-II: Acid Deposition and Oxidant Model II.
- CBM-IV: Carbon Bond Mechanism IV.
- DACFOS: Danish Atmospheric Chemistry FOrecasting System.
- DRAIS: Dreidimensionales Regionales Ausbreitungs- und Immissions-Simulationsmodell.

- EMEP = EMEP MSC-W:
EMEP = European Monitoring and Evaluations Program.
MSC-W = Meteorological Synthesizing Center-West.
- EURAD: EURopean Acid Deposition.
- HIRLAM: HIgh Resolution Limited Area Model.
- HPTM: Harwell Photochemical Trajectory Model.
- IVL: Swedish Environmental Research Institute.
- KAMM: Karlsruher Atmosphärische Mesoskaliges Modell.
- LOTOS: LOng Term Ozone Simulation.
- MACHO: Multi-layer Atmospheric CHEmistry Model.
- MCCM: Meteorology Chemistry Climate Model.
- MOON: Multi-trajectory Original Ordinary-differential-equation Numerical-box.
- RADM: Regional Acid Deposition Model.
- RADM2: second generation Regional Acid Deposition Model.
- RACM: Regional Atmospheric Chemistry Mechanism.
- REM3: Regional Eulerian Model with 3 chemical schemes.
- SAPRC-90: Statewide Air Pollution Research Center-90.
- SMVGEAR: "Eulerian" Sparse-Matrix Vectorized Gear.

Abbreviations of chemical compounds

- \dot{A} : atom A is a radical with one unpaired electron.
- $HO_x = HO + HO_2$.
- PAN: PeroxyAcetyl Nitrate.
- $NO_x = NO + NO_2$.
- $\dot{R}[-H]$: a H-atom is abstracted from the organic R-group.
- VOC: Volatile Organic Compounds.

Mathematical symbols

- \bar{a} : n -dimensional vector a .
- $a = \|\bar{a}\|$: norm of the vector \bar{a} .
- \underline{M} : $n \times m$ -matrix \underline{M} .
- $|\underline{M}|$: determinant of the matrix \underline{M} .
- $\{x\}$: emission of x .
- $[x]$: concentration of x .

Dansk Sammenfatning

Afhandlingen fokuserer på:

- Udviklingen og valideringen af en ny transport-kemimodel (Multi-trajectory Original Ordinary-differential-equation Numerical-box (MOON) model),
 1. det er, udfra min viden, den første Lagrangske transport-kemi model, der kan behandle et stort antal trajektorier på samme tid, samtidig med at en Gear algoritme og vektoriseringsteknik benyttes, og
 2. solveren indeholder en kemisk oversætter, der gør, at det er meget simpelt at addere kemiske reaktioner, emissioner, depositioner etc. til MOON modellen.
- en evaluering af nogle af de mest anvendte atmosfærekemiske gasfase mekanismer, der benyttes i luftkvalitetsmodeller, samt
- udviklingen af en ny kvantemekanisk statistisk model, der specielt kan anvendes til at beregne hastighedskonstanter for molekylære systemer med mange atomer, dvs. mange af de reaktioner, der forekommer i atmosfæren.

Atmosfærekemi er et nyt videnskabeligt felt på DMI initialiseret af forfatteren, endvidere er denne Ph.D. afhandling indleveret til forsvar på geofysisk institut ved Københavns Universitet. Formålet med afhandlingen er derfor at give folk fra tværfaglige geofysiske dicipliner en indfaldsvinkel til:

- Atmosfærekemi,
- simulering af komplekse atmosfærekemiske reaktionsskemaer, samt
- hvordan de kemiske reaktioner, der forekommer i atmosfæren kan beskrives v.h.j.a. teoretisk metoder.

Derfor indeholder hvert kapitel en introduktion til disse ovenstående områder. Afhandlingen omfatter eksklusive appendikser 158 sider med 53 tabeller og 60 figurer.

MOON Modellen

Transporten i MOON modellen bestemmes ud fra DMI-High Resolution Limited Area Model (DMI-HIRLAM) data, hvor DMI-HIRLAMs meteorologiske felter benyttes

ved beregningen af trajektorierne. Den numeriske integration af de kemiske reaktioner er foretaget v.hj.a. en Gear algoritme. Fordelene ved en Gear algoritme er følgende:

- Et komplekst kemiskema kan integreres uden speciel ad hoc justeringer af de kemiske reaktioner for at fjerne kemiskemaets stivhed,
- ordenen og tidsskridtet vælges v.hj.a. en adaptiv metode, der sikrer høj nøjagtighed for minimalt brug af computertid, samt
- der eksisterer metoder der med Gear tillader kemiske komponenters sensitivtets koefficienter at blive beregnet v.hj.a. en robust numerisk metode.

Ulempen ved en Gear algoritme er derimod, at den kan være en meget beregningstung integrator, hvis de kemiske komponenter, som indgår i reaktionerne, påvirkes af eksterne kilder f.eks. fra transport, emissioner eller depositioner. Derfor for at øge beregningshastigheden, er den anvendte Gear algoritme programmeret således at:

1. Computerkoden samler trajektorierne sammen i grupper, hvorom koden er gjort vektoriserbar,
2. sparse-matrix teknik benyttes til bestemmelse af korrektorvektoren i Gear algoritmen (se *Appendix C*),
3. trajektoriegrupperne er sorteret efter stivhed (se *Appendix C*),
4. de kemiske reaktioner er sorteret efter antal af reaktant og produkt termer,
5. transport-kemimodulet kan løse forskellige kemiske mekanismer i forskellige områder af atmosfæren: Stratosfæren, den frie troposfære og indenfor det atmosfæriske grænselag, og
6. sparse-matricer for nat og dag gasfase kemien, nat og dag heterogen kemien i de tre områder af atmosfæren nævnt under punkt 5, benyttes.

Formålet med at udvikle MOON modellen var at lave en model, der forbedrer simuleringen af de atmosfærekemiske komponenter sammenlignet med Danish Atmospheric Chemistry Forecasting System (DACFOS), samt at fremstille en model der forsimpler implementeringen af kemiske og fysiske parametre såsom hastighedskonstanter, emissioner og depositioner. DACFOSs kemimodul benytter European Monitoring and Evaluations Program Meteorological Synthesizing Center-West (EMEP) kemi-skemaet og Quasi-Steady-State Approximation (QSSA) metoden som integrator. Udover at MOON modellen benytter en bedre integrator end DACFOS, er den også udviklet således, at fire forskellige kemiskemaer kan benyttes (EMEP, second generation Regional Acid Deposition Model (RADM2), Regional Atmospheric Chemistry Mechanism (RACM) og Jacobsons kemiskema). En anden væsentlig

forskel mellem DACFOS og MOON modellen er, at DACFOS benytter parametriseret fotolyse hastigheder mens MOON modellen benytter modellerede.

De kemiske skemaer (RACM og EMEP), fotolyse beregningsmetoderne og solverne (QSSA og Gear), der benyttes i MOON modellen og DACFOS, er blevet sammenlignet v.hj.a. to forskellige typer 0-dim. boksmodel simuleringer, et landligt og et bymæssig scenarie. Derudover er MOON modellen blevet valideret mod europæiske målestationer og sammenlignet med DACFOS for perioden 11. august til 24. august 1995. Den forbrugte computer tid for MOON modellen er blevet bestemt for at undersøge om den kan benyttes som forudsigelsesmodel for overfladeozon.

Evalueringen af Atmosfære Kemi Mekanismerne

De kemiske mekanismer er en af de vigtigste byggestene i luftkvalitetsmodeller. Afhandlingen omhandler derfor også en evaluering af nogle af de mest anvendte atmosfærekemiske gasfase mekanismer i luftkvalitetsmodeller (EMEP, RADM2 og RACM). Sammenligningen af kemiskemaerne er foretaget på baggrund af scenarierne foreslået af Chemical Mechanism Working Group (CMWG) under EUROpean experiment on TRANsport and transformation of environmentally relevant trace Constituents in the thoposphere over Europe (EUROTRAC). Sammenligningen krævede mere end 3×230 0-dim. boksmodel simuleringer, der er blevet afviklet og analyseret.

Udviklingen af en Ny Kvantemekanisk Statistisk Model

Hastighedskonstanterne for atmosfæremekanismernes kemiske reaktioner er primært baseret på laboratorie eksperimenter. Teoretiske metoder har visse fordele i forhold til eksperimenter, f.eks. er det lettere at analysere hvilken kemisk reaktion, der forekommer mellem to molekyler. Men teoretiske metoder i denne sammenhæng har en meget begrænset udbredelse, fordi simuleringer af kemiske reaktioner for molekylære systemer af store molekyler er meget beregningskrævende. Afhandlingen vil derfor også give en kort beskrivelse af teoretiske metoder, der kan benyttes til at bestemme kemiske reaktioners hastighedskonstanter. Beskrivelsen vil indeholde en opsummering af disse metoders muligheder og begrænsninger. Derudover vil en ny kvantemekanisk statistisk model blive præsenteret. Formålet med at udvikle denne model var at introducere en approksimativ metode, der kan benyttes til at beregne hastighedskonstanter for reaktioner, der forekommer i atmosfæren. I denne afhandling er metoden testet på to atmosfærekemiske reaktioner.

I **Appendix G** er titler og resuméer af de artikler hvis indhold danner baggrunden for denne afhandling givet.

Abstract

The thesis focuses on:

- the development and validation of a new transport-chemical model (Multi-trajectory Original Ordinary-differential-equation Numerical-box (MOON) model),
 1. it is, to my knowledge, the first Lagrangian transport-chemical model that can handle a large number of trajectories simultaneously using a Gear algorithm and vectorization technic, and
 2. the solver contains a chemical compiler, therefore it is very simple to add chemical reactions, depositions, emissions etc. into the MOON model.
- an evaluation of some of the atmospheric gas-phase chemical mechanisms most often used in air quality models, and
- the development of a new quantum statistical model that enables the calculation of rate constants for large molecular systems, such as those appearing in many atmospheric reactions.

Atmospheric chemistry at DMI is a new research field, initiated by the writer. Moreover this dissertation is submitted for defense at the Department of Geophysics, University of Copenhagen. The objective with the dissertation is therefore to present to persons from interdisciplinary geophysical subjects approaches to:

- atmospheric chemistry,
- simulation of complex chemical reaction schemes, and
- how chemical reactions from the atmosphere can be described by theoretical methods.

For that reason each chapter contain an introduction to the topics mentioned above. Exclusive appendices the thesis consists of 158 pages including 53 tables and 60 figures.

The MOON Model

The MOON model's transport is estimated from the DMI-High Resolution Limited

Area Model (DMI-HIRLAM), where DMI-HIRLAM's meteorological fields are used to calculate the trajectories. The numerical integration of the chemical rate equations is performed with a Gear algorithm. The advantages of using a Gear algorithm are the following:

- a complex chemical scheme can be integrated without special ad hoc adjustments to the rate equations to remove stiffness,
- the order and the time steps are chosen by an adaptive method that ensures high accuracy for a minimum use of computer time, and
- there are methods available that for use with Gear allow chemical compounds' sensitivity coefficients to be calculated by a robust numerical method.

The disadvantage of using the Gear algorithm is that it can be very computationally expensive if the chemical compounds that appear in the chemical reactions are influenced by external sources, e.g. from transport, emissions or depositions. Therefore, certain improvements to the Gear algorithm have been made, in order to improve the computational speed:

1. the code gathers the trajectories into groups for vectorization,
2. a sparse-matrix technique is used to estimate the corrector vector for the Gear algorithm (see *Appendix C*),
3. the trajectory groups are sorted according to stiffness (see *Appendix C*),
4. the chemical reactions are sorted by the number of reactant and product terms,
5. the transport-chemical model can solve different chemical mechanisms in different areas of the atmosphere: the stratosphere, the free troposphere and inside the atmospheric boundary layer, and
6. sparse-matrices for night and day gas-phase chemistry and night and day heterogeneous chemistry, in all the three areas of the atmosphere mentioned under point 5, are used.

The purpose of the development of the MOON model was to make a model that improves the simulation of the atmospheric chemical compounds, compared to the Danish Atmospheric Chemistry Forecasting System (DACFOS), and to make a model that makes it easier to implement chemical and physical parameters such as rate constants, depositions and emissions. DACFOS's chemical module uses the European Monitoring and Evaluations Program Meteorological Synthesizing Center-West (EMEP) chemical scheme and the Quasi-Steady-State Approximation (QSSA) method as the integrator. The MOON model uses a better integrator than DACFOS, and it was also developed in such a way that four different chemical schemes can be used (EMEP, second generation Regional Acid Deposition Model (RADM2), Regional Atmospheric Chemistry Mechanism (RACM) and the Jacobson chemical

scheme). Another difference between DACFOS and the MOON model that is, DACFOS uses parameterized photolysis while the MOON model uses modeled photolysis.

The chemical schemes (RACM and EMEP), the different photolysis treatments and the solvers (QSSA and Gear) in DACFOS and the MOON model have been compared on the basis of two different 0-dim. box model runs, a rural and urban scenario. Furthermore, the MOON model has been validated against European measurement stations and DACFOS for the period of August 11 to August 24 1995. Its computer time is measured in order to determine if the MOON model can be used as surface ozone forecasting model.

The Evaluation of Atmospheric Chemical Mechanisms

Chemical mechanisms are some of the most important components in air quality models. Therefore, this thesis also involves an evaluation of some of the atmospheric gas-phase chemical mechanisms most often used in air quality models (EMEP, RADM2 and RACM). The comparison of the chemical schemes is based upon the scenarios suggested by the Chemical Mechanism Working Group (CMWG) under the EUROpean experiment on TRANsport and transformation of environmentally relevant trace Constituents in the troposphere over Europe (EUROTRAC). This comparison required that more than 3×230 0-dim. box model simulations be performed and analyzed.

The Development of a New Quantum Statistical Model

The rate constants for the chemical reactions that are part of the atmospheric chemical mechanisms are primarily based upon laboratory experiments. Theoretical methods have some advantages compared with experimental studies, e.g. it is easier to estimate which chemical reactions that occur between two molecules. However, theoretical methods have very limited use since simulations of chemical reactions between large molecules demand enormous amounts of computational resources. Therefore, the thesis will also give a brief presentation of theoretical methods that can be used to estimate chemical reaction rate constants. The discussion will include a description of the utility and limitations of these methods. Furthermore, a new quantum mechanical statistical model that has been developed will be presented. The purpose of developing this model was to introduce an approximate method that can be used to calculate rate constants for chemical reactions taking place in the atmosphere. In the thesis the new model has been tested on two atmospheric chemical reactions.

In **Appendix G** titles and abstracts of articles whose contents are the basis of this Ph.D. thesis are given.

Introduction

An important group of the secondary pollutants¹ are the photochemical oxidants. Among these ozone has been the most intensively studied compound. The chemical importance of the photochemical oxidants is due to the great oxidizing ability of the atmosphere. Therefore, the interest in photochemical oxidants is two fold, its impact on the atmospheric chemical composition and high concentrations of these (in particular ozone) damage human health, vegetation and materials.

The concentration of surface ozone has increased by a factor of 2.2 since the 1950s[1]. This increase is due to photochemical smog and direct transportation of ozone from urban centers among other things. Typical surface ozone concentrations in the summer are given in Table 0.1. The EU[3] has therefore introduced thresholds

Region	[O ₃] (ppbV)
Urban-suburban	100.-400.
Rural	50.-120.
Remote marine	20.-40.

Table 0.1: Typical summertime daily maximum surface ozone concentrations[2].

for surface ozone concentrations, see Table 0.2. Even though it was already clear in

	[O ₃]		Averaging Period (hours)
	($\mu\text{g}/\text{m}^3$)	(ppbV)	
Health projection threshold	110.	55.1	8
Vegetation projection threshold	200.	100.	1
	65.	33.	24
Population information threshold	180.	90.2	1
Population warning threshold	360.	180.	1

Table 0.2: EU directive of September 21, 1992[3], on thresholds for surface ozone concentrations in the air. The ppbV values are evaluated at temperature = 293 K and pressure = 101.3 kPa.

1915 that fossil fuel burning was a potential air pollutant, it was first around 1945 that urban pollution problems due to emissions from automobiles were recognized

¹Secondary pollutants are formed by chemical processes from primary pollutants and normal atmospheric constituents. Primary pollutants are emitted by anthropogenic sources.

in Los Angeles. Today this is a worldwide problem, for example in Tokyo, Athens, Rome and Paris. The surface ozone concentration in Los Angeles has been reduced in recent decades, see Table 0.3, due to very strict regulations of automobile emissions.

Year	SS	FS	HA	S1E	S2E	Basin Max.
	0.09 ppmV Year	0.12 ppmV Year	0.15 ppmV Year	0.20 ppmV Year	0.35 ppmV Year	Annual
1976	237 (168)	194 (136)	166 (119)	102 (74)	7 (7)	0.38
1977	242 (157)	208 (134)	184 (122)	121 (87)	11 (7)	0.39
1978	217 (155)	187 (136)	173 (126)	116 (86)	23 (17)	0.43
1979	226 (164)	191 (140)	169 (124)	120 (88)	17 (7)	0.45
1980	210 (143)	167 (113)	152 (102)	101 (66)	15 (6)	0.41
1981	222 (160)	180 (138)	159 (128)	99 (87)	5 (5)	0.37
1982	191 (143)	149 (117)	121 (97)	63 (48)	2 (0)	0.40
1983	190 (136)	152 (111)	138 (103)	84 (63)	3 (2)	0.39
1984	207 (164)	173 (138)	146 (115)	97 (75)	0 (0)	0.34
1985	206 (156)	158 (125)	136 (112)	83 (73)	7 (7)	0.39
1986	217 (166)	164 (131)	140 (117)	79 (70)	1 (1)	0.35
1987	196 (143)	160 (118)	130 (93)	66 (43)	0 (0)	0.33
1988	216 (156)	178 (124)	144 (101)	77 (56)	1 (0)	0.35
1989	211 (162)	157 (124)	120 (95)	54 (41)	0 (0)	0.34
1990	184 (133)	130 (98)	107 (80)	41 (31)	0 (0)	0.33
1991	183 (126)	130 (84)	100 (62)	47 (29)	0 (0)	0.32
1992	191 (140)	143 (106)	109 (79)	41 (35)	0 (0)	0.30
1993	185 (141)	124 (97)	92 (71)	24 (17)	0 (0)	0.28
1994	165 (130)	118 (99)	96 (82)	23 (23)	0 (0)	0.30
1995	154 (99)	98 (72)	59 (44)	14 (13)	0 (0)	0.26
1996	151 (117)	90 (79)	53 (49)	7 (7)	0 (0)	0.24
1997	141 (115)	68 (62)	28 (26)	1 (1)	0 (0)	0.21
1998**	114 (91)	62 (55)	43 (41)	12 (12)	0 (0)	0.24

Table 0.3: Historic surface ozone air quality trends, number of basin-days exceeding health standard levels. Basin-days represent the number of days a standard was exceeded anywhere in the South Coast Air Basin. The numbers in the parentheses are for the period from January to August. SS: State Standard, FS: Federal Standard, HA: Health Advisory, S1E: Stage 1 Episode and S2E: Stage 2 Episode. ** Data in the parenthesis for 1998 are preliminary and unvalidated, and subject to revision. Ref. [4].

Surface concentration of ozone is primarily influenced by NO_x ($\text{NO} + \text{NO}_2$), CO and Volatile Organic Compounds (VOC). The compounds: NO_x , CO and VOC are primarily emitted from fossil fuel burning and automobile sources. It is difficult, if not impossible, to predict ozone episodes from field observations alone and/or experimental studies, since surface ozone both has a long range transport² and chemical impact[6]. Therefore, scientists have developed Atmospheric Chemical Transport Models (ACTMs) in order to gain a better understanding of the chemistry, transport, emission and removal processes taking place in the atmosphere. Two kinds

²The lifetime of ozone in the troposphere is so long that it can be transported over large areas[5].

of transport (or physical) models including atmospheric chemistry have been developed – Lagrangian receptor point models and Eulerian grid models. The concept of the Lagrangian model is a moving air parcel that follows the wind field, whereas the Eulerian model uses a fixed coordinate system relative to the surface of the Earth. Thus, the Eulerian framework enables a more accurate physical model and the concentration of the compounds can be predicted in the entire grid domain. However, the Lagrangian framework is in general computationally less demanding. For air pollution problems governed by long range transport, as it mainly is in Denmark, the Lagrangian model concept is expected to be a reasonable approach. Furthermore, in ACTMs the computationally demanding part is the integration of the chemical reactions. In this respect a Lagrangian framework is best if detailed atmospheric chemistry is the scientific focus (for further discussion see introduction to *Chapter 3*).

The Impact of Ozone on the Environment

The impact of high concentration levels of ozone on the environment is many fold, therefore special attention has been devoted to ozone in the environment. Connections between ozone and human health have been reported by the World Health Organization (WHO) and the U.S. Environmental Protection Agency. The main results were that ozone can result in mucus membrane irritation, headache, reduced physical performance, change the lung function, reduce resistance to infections and increase the possibility of asthma. Experimental studies have shown that these effects on humans are observed at ozone concentrations above 100 ppbV[7].

The effect of ozone on natural vegetation varies a lot. Research indicates that plants which grow fast are most sensitive to ozone, and ozone can affect the growth of the biomass[8]. New results show that forests in the Nordic countries are more susceptible to ozone damage than forests in central Europe even though surface ozone levels are highest in central Europe[9]. This has to do with the long summer days and the relatively high humidity in the Nordic countries compared with central Europe[9]. Finally, elevated surface ozone concentrations result in a reduction of the yield of harvested corn. For corn the effect of ozone is especially important during flowering and the formation of grain. Ozone promotes leaf senescence. The chlorophyll content of the leaves as well as the chloroplast size of the leaves decline faster with increased ozone exposure[10].

Since ozone has a great oxidation ability, it can oxidize materials and in that way reduce the lifetime of materials. In the U.S. it has been estimated that ozone damage on materials amounts to \$2.5 billion every year[11].

Finally, an increase of ozone in the troposphere has two additional effects. Firstly, ozone is a greenhouse gas, that means it contributes to an increase in global warming. Secondly, it can reduce the UV penetration. This will to some extent compensate for the increased UV penetration from the stratosphere due to stratospheric ozone depletion.

Danish Atmospheric Chemistry FOrecasting System

At the Danish Meteorological Institute a 3-dimensional photochemical trajectory model, Danish Atmospheric Chemistry FOrecasting System (DACFOS), has been developed[12, 13]. A flow diagram of the elements in DACFOS is shown at Figure 0.1. The primary purpose of DACFOS is to forecast concentrations of photochem-

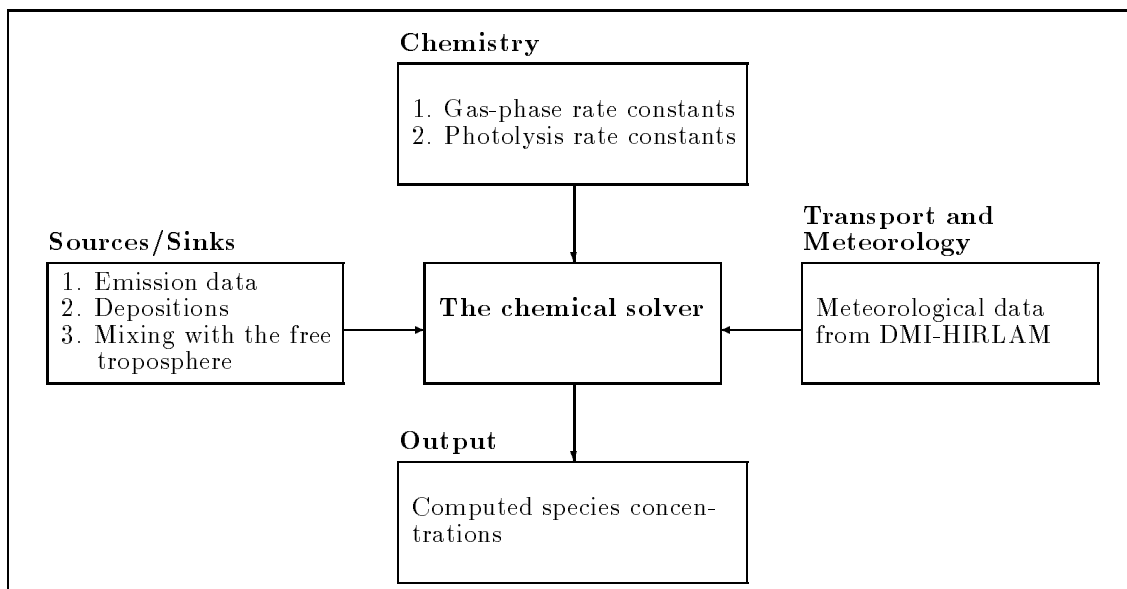


Figure 0.1: Flow diagram of the elements in DACFOS.

ical oxidants, especially surface ozone. At the moment this is done at 36 locations in Europe[14]. Presently, the European Monitoring and Evaluations Program Meteorological Synthesizing Center-West (EMEP) MeCHanism (MCH) is used in DACFOS, and as chemical integrator, the Quasi-Steady-State Approximation (QSSA) method. The chemical solver is driven by DMI's 3-dimensional Lagrangian puff model utilizing forecasting data from DMI-High Resolution Limited Area Model (DMI-HIRLAM)[15].

Traditional Lagrangian trajectory models calculate backward trajectories derived from a 2-dimensional wind field at a given pressure level, see e.g. the EMEP model[16, 17, 18], the Stedman and Williams model[19], the Harwell Photochemical Trajectory Model (HPTM)[20, 21] and the Atmospheric Chemistry and DEPosition (ACDEP) model[22, 23]. While the Stedman and Williams model and the EMEP model are single-layer trajectory models, the HPTM is a two layer model where the two layers are used to describe the diurnal variation of the boundary depth. The lower layer is the Atmospheric Boundary Layer (ABL) while the upper layer is the nighttime reservoir. Finally, in the ACDEP model, a full vertical resolution has been introduced.

In contrast to these models the backward trajectories in DACFOS are calculated on the basis of the 3-dimensional wind field from DMI-HIRLAM. The column followed by this 3-dimensional wind field is a single-layer because full vertical mixing

in the ABL is assumed. However, the ABL along the trajectories varies (diurnally and geographically) and therefore mixing between the free troposphere and the ABL occurs. This effect has been parameterized in DACFOS. Also, if the trajectory penetrates the top of the ABL into the free troposphere, mixing with the ABL is no longer assumed and emissions from the ground surface and depositions are turned off.

The emission inventory in DACFOS is the EMEP-grid from 1994, which is a 50×50 km grid covering the European continent and the Atlantic Ocean. The emission inventory contains emission data for SO_2 , NO_x and VOC and from the forest areas.

A more detailed description of DACFOS is given in *Chapter 3*.

Chemical Mechanisms

Regional Air Quality Models (RAQMs) are used to understand the effects on air quality of emissions from anthropogenic and biogenic sources. There are several examples which show that one of the central parts in RAQMs is the chemical mechanism[6, 24]. It is therefore important that the gas-phase mechanism includes all the important atmospheric chemical reactions and that the utilized rate constants and product yields for the gas-phase reactions, and the quantum yields and absorption cross sections for the photolysis reactions³ are of high accuracy, if RAQMs are to be able to predict realistic concentrations of surface ozone and other air pollutants. This is a rather problematic task because the chemical reactivity of the organic compounds in the polluted troposphere is extremely complicated. The master chemical mechanism developed by Jenkin et al.[25, 26] is based on the 120 most important emitted organic compounds for conditions typical of northwest Europe. Therefore, this master chemical mechanism includes over 2400 chemical species and over 7100 chemical reactions. Unfortunately, it is not possible to incorporate such a complex chemical mechanism in RAQMs today since the computational time will be too long for practical purposes.

A large variety of lumped gas-phase chemical mechanisms⁴ based on the knowledge of the atmospheric chemical composition, reactions and corresponding rate constants[27, 28, 29] have therefore been developed during the last couple of decades in order to describe the complex chemical composition of the troposphere. Examples of such mechanisms are the EMEP MCH[30], the second generation Regional Acid Deposition Model (RADM2) MCH[31], the Regional Atmospheric Chemistry Mechanism (RACM)[32], the Acid Deposition and Oxidant Model II (ADOM-II)

³Photolysis reactions are reactions by which a dissociation of a molecule occurs after it has absorbed a quantum of light, $h\nu$.

⁴Chemical reactions can be lumped together using different chemical constraints, e.g. chemical reactivity and/or similar organic functional groups, to surrogate chemical reactions. That means these lumped surrogate chemical reactions represent more than one real chemical reaction. When a chemical mechanism consists of lumped surrogate chemical reactions, it is called a lumped chemical mechanism.

Mechanism Abbreviation	Number of		Transport Model
	Species	Reactions	
EMEP MCH[30]	79	141	EMEP model[16, 17, 18] (Lag) DACFOS[12, 13] (Lag)
IVL MCH[37]	715	1640	HPTM[37, 20, 21] (Lag)
ADOM-II MCH[33]	47	114	ADOM-II[38]
RADM2 MCH[31]	63	158	RADM[35] (Eul) MCCM[36] (Eul) EURAD model[39] (Eul) KAMM/DRAIS[40] (Eul)
RACM MCH[32]	77	237	MCCM[36] (Eul)
CBM-IV[34]	27	63	LOTOS model[38] (Eul) REM3[41]
SAPRC-90 MCH[42]	60	155	REM3[41]
<p><u>Acronyms:</u> ADOM-II: Acid Deposition and Oxidant Model II. CBM-IV: Carbon Bond Mechanism IV. DACFOS: Danish Atmospheric Chemistry FOrecasting System. DRAIS: Dreidimensionales Regionales Ausbreitungs- und Immisions-Simulationsmodell. EMEP: European Monitoring and Evaluations Program Meteorological Synthesizing Centre-West. EURAD: EUROpean Acid Deposition. HPTM: Harwell Photochemical Trajectory Model. IVL: Swedish Environmental Research Institute. KAMM: Karlsruher Atmosphärische Mesoskaliges Modell. LOTOS: Long Term Ozone Simulation. MCCM: Meteorology Chemistry Climate Model. RACM: Regional Atmospheric Chemistry Mechanism. RADM: Regional Acid Deposition Model. RADM2: second generation Regional Acid Deposition Model. REM3: Regional Eulerian Model with 3 chemical schemes. SAPRC-90: Statewide Air Pollution Research Center-90</p>			

Table 0.4: Overview of the most frequently used atmospheric gas-phase chemical mechanisms in RAQMs. Lag and Eul refer to Lagrangian and Eulerian models, respectively.

MCH[33]⁵ and the Carbon Bond Mechanism IV (CBM-IV). Many of these mechanisms are used in RAQMs among others in the Lagrangian EMEP model, DACFOS, the Regional Acid Deposition Model (RADM)[35] and the Meteorology Chemistry Climate Model (MCCM)[36], see Table 0.4.

Solvers (QSSA and Gear)

The importance of the chemical mechanism in RAQMs requires that the numerical integration of the chemical mechanism is done properly. The system of Ordinary Differential Equations (ODEs) that describes the chemical species' concentration as a function of time is for the atmospheric chemical mechanisms extremely stiff (i.e. has drastically different rate constants). Therefore, it is not an easy task to solve these ODEs special efforts are required. For example Li and Rabitz[43] have developed a very nice theoretical lumping methodology that reduces the ODE to a large extent. However, the method cannot handle ODEs when the systems are too stiff as is the case for atmospheric chemical mechanisms.

In DACFOS the chemical solver used is the Quasi-Steady-State Approximation (QSSA) method[47]. Chapman and Underhill[44] and Bodenstein[45] were the first who applied the QSSA to chemical schemes. QSSA was applied to substantially nonstationary processes by Semenov[46]. Semenov used QSSA not on all of the intermediates but only some of them.

Before computers were available, the QSSA method was used to obtain approximate solutions of different types of chemical differential schemes. For the first generation of computers it was a large numerical problem to solve a stiff differential equation system like atmospheric mechanisms. In that period the QSSA method was used to convert stiff differential equation systems into non-stiff systems. The development of computer technology has made it possible to solve stiff differential equations directly. Even though the QSSA solver is the least accurate among the fast solvers⁶ it has been one of the most utilized methods to solve Chemical Reaction Schemes (CRSs) because of its simplicity.

Problems caused by the QSSA method are that several tests have shown[50]⁷:

1. that incorrect results can be obtained when the steady state approximation is used even though it appears to give a reasonable result,
2. when steady state approximations are used, the chemical balance in the CRS can be lost, and
3. even though the overall error may be small, the error can be significant for specific species, and such errors can propagate throughout the whole CRS (i.e.

⁵Currently used by the governments of Canada and the province of Ontario for regional pollution modeling.

⁶Other examples of fast solvers are the Eulerian Backward Iterative (EBI) solver[48] and Implicit-Explicit Hybrid (IEH) solver[49].

⁷In the paper by Turányi et al.[50] other references are given describing the problems using a QSSA method.

species) as time propagation is performed.

The commonly applied numerical algorithm for directly solving stiff ODEs is the Gear algorithm[51]. Besides it being possible to use it directly without any special ad hoc adjustments to the rate equations to remove stiffness, the strength of using the Gear algorithm is that it is considered to be a benchmark solver[47, 48, 49]. Therefore, a Gear algorithm is the preferred solver to use for solving ODE in RAQMs.

Objectives

This thesis seeks to provide insight into theoretical simulations of atmospheric chemistry and theoretical methods for calculating the most essential parameters for atmospheric chemistry mechanisms: chemical rate constants. In particular, this work focuses on the gas-phase chemistry of the continental troposphere. In Figure 0.2 we have illustrated how the different elements of the thesis interact with each other.

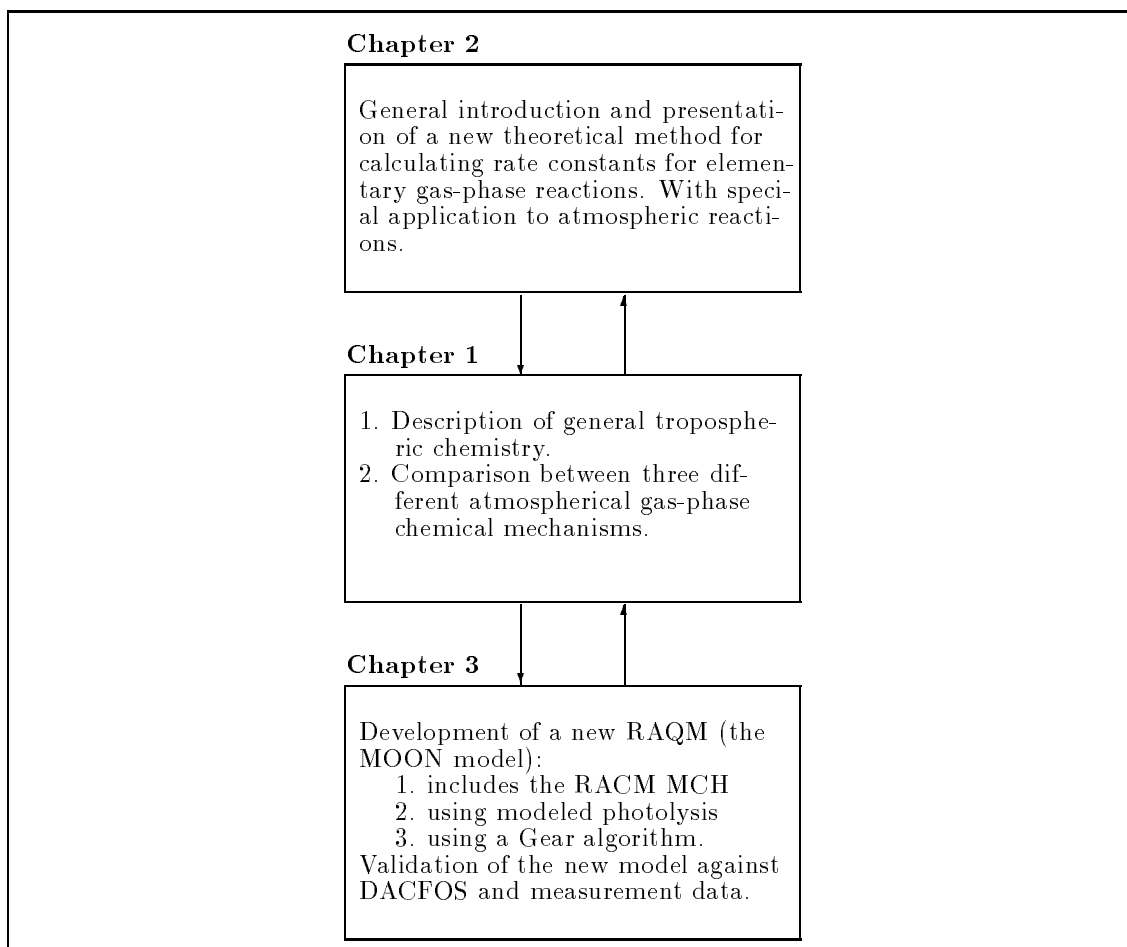


Figure 0.2: Flow diagram of the elements in the thesis.

Three different atmospheric gas-phase chemical mechanisms will be used in this thesis: the EMEP, RADM2 and RACM MCHs, and they are therefore presented

in *Appendix A*. These mechanisms will be used under relatively clean and polluted continental tropospheric conditions. Implementation of VOC emissions into atmospheric chemical mechanisms is easy yet poorly described in the literature. In order to do it properly one has to know how the mechanism is lumped together. Therefore, we give in *Appendix B* a description of how the VOC emissions are implemented in the three mechanisms. On the basis of 0-dimensional box model simulations[52], these three mechanisms are compared. We have simulated the mechanisms under “clean” and polluted tropospheric air conditions, and

- examined how carbon conservative they are, and
- investigated which concentration levels they predict, with special focus on surface ozone.

These results are presented in *Chapter 1*[53], together with

- a brief general description of tropospheric chemistry with special emphasis on surface ozone precursors.

The purpose of *Chapter 1* is twofold. Firstly, to give an overview of basic tropospheric gas-phase chemistry because atmospheric chemistry at DMI is a new research field. Secondly, to investigate which of the three mechanisms represents the chemistry of the ABL most accurately.

On the basis of the discussion in section *Solvers (QSSA and Gear)*, there grounds for replacing the QSSA chemical solver in DACFOS with the more reliable Gear algorithm. However, DACFOS is used for 48 hour surface ozone forecasts at 36 locations in Europe, and at each location, five arrival heights. This requires a run of $36 \times (48 + 6 + 1) \times 5$ chemical boxes along the Lagrangian trajectories. For that purpose the Gear algorithm developed by Hindmarsh[54], and Brown et al.[55] will be too slow. However, if a vector-parallel computer is available, a Gear algorithm’s computer speed can be improved tremendously if programmed properly. Using a Gear algorithm to integrate a CRS can either be vectorized over the species or trajectories. The Hindmarsh, and Brown et al. solvers can easily be reversed so they vectorize over species, but vectorization around boxes will speed up the program to a much larger extent[56]. We have therefore

- developed a new transport-chemical model (Multi-trajectory Original Ordinary-differential-equation Numerical-box (MOON) model) that
 1. can handle a large number of trajectories at the same time using a Gear algorithm and vectorization technique,
 2. uses modeled photolysis, and
 3. contains a chemical compiler (therefore it is very simple to add for example chemical reactions, depositions and emissions into the model).⁸

⁸It is, to my knowledge, the first Lagrangian transport-chemical model with these properties.

This model vectorizes around trajectories.

The MOON model is based upon the Sparse-Matrix Vectorized Gear code (SMVGEAR) developed by Jacobson[56]. We have changed this “Eulerian” SMVGEAR solver to a Lagrangian SMVGEAR model (called the MOON model[57]). *Chapter 3* provides a full description of the MOON model and all the differences between the MOON model and DACFOS.

In *Appendix C* the mathematical concepts of the QSSA (in DACFOS) and the Gear algorithm (in the MOON model) are described. In order to utilize the MOON model in a proper manner several input parameters and files have to be set up and made. *Appendix D* gives a detailed description of how to set up these files and parameters for the MOON model. Furthermore, the MOON model can also be used as a 0-dimensional box model and can be run for specific areas of the atmosphere. How this is done is also explained in *Appendix D*.

In *Chapter 3* we have validated the MOON model[57]. This involves

- a comparison of the MOON model against DACFOS on the basis of two different 0-dim. box model runs, a rural and urban scenario,
- a validation of the utility of the QSSA solver against the Gear algorithm in RAQMs,
- a test of the utility of parameterized photolysis rates versus “exact” photolysis rates,
- a validation of the MOON model against DACFOS for 25 locations in Europe for the period of August 11 to August 24 1995 on the basis of 3-dim. model runs, and
- an investigation of the computational speed of the MOON model.

The employment of basic theoretical chemistry for application in atmospheric chemistry is a topic of increasing importance. In *Chapter 2* we have

- described different theoretical methods – dynamical, statistical as well as molecular electronic methods – that are available and computationally possible to use on supercomputers of today, and
- described in detail the importance of having access to high quality potential energy values for the theoretical methods[58, 59, 60, 61].

Chapter 2 will primarily focus on a description of dynamical, statistical-dynamical and statistical methods utility to calculate gas-phase rate constants. Due to the requirement of ab initio calculations when these methods are used on molecular systems, *Chapter 2* also provides

- a description of the current status of ab initio electronic structure methods.

Finally, *Chapter 2* presents

- a new quantum-statistical model based on Phase-Space Theory (PST)[62] that can be used to calculate rate constants for arbitrary gas-phase reactions.

For that purpose a phase-space program package to calculate rate constants for chemical systems, GETALFACTS, has been developed, and the method has been tested on two atmospheric chemical hydroxylradical reactions[63]. The phase-space model developed needs spectroscopic data for the species involved in the reactions. For that purpose we have used the molecular electronic structure program Gaussian 94[64].

As indicated by this *Introduction*, many model tools have been used in the work presented in this thesis. Many of these tools can be retrieved for free. An overview of the tools and where they can be obtained is described in Table 0.5.

Tool	Developer	The Tool can be Obtained From
<i>Atmospheric Chemical Mechanisms:</i>		
EMEP MCH	Simpson	Ref. [30]
RADM2 MCH	Stockwell	Ref. [31]
RACM MCH	Stockwell	Ref. [32]
<i>Chemical Solvers/Transport Models:</i>		
QSSA solver	DNMI	
Gear algorithm	Brown et al.	www.nea.tr/abs/html/ests0426.html
SBOX	Stockwell & Seefeld	email: wstock@dri.edu
SMVGEAR solver	Jacobson	email: jacobson@ce.stanford.edu
MOON model	Gross	email: agr@dmi.dk
DACFOS	Jensen et al.	
<i>Molecular Electronic Structure Program:</i>		
Gaussian 94	Frisch et al.	payment
<i>Phase-space program package:</i>		
GETALFACTS 98	Gross et al.	email: agr@dmi.dk

Table 0.5: Model tools used in the thesis.

Chapter 1

Tropospheric Chemistry

For regional scale problems, tropospheric chemistry can be divided into two main groups: the chemistry of the background and polluted troposphere [2, 65]. The constituents of the background troposphere can be grouped as follows:

1. the primary compounds are nitrogen (N_2), oxygen (O_2) and several noble gases,
2. in addition e.g. SO_2 , CO , CO_2 , NO , NO_2 , N_2O , O_3 , HNO_3 , NH_3 , $HCHO$, HNO_2 , H_2O , CH_4 , H_2 , H_2O_2 , reduced sulfur and biogenically emitted organic compounds occur, and
3. small amounts of urban air pollutants.

Due to the low concentrations of urban air pollutants, the chemistry of background air is quite simple, if biogenically emitted organic compounds are not considered. On the other hand, the polluted air cases, especially with highly varying VOC, give rise to very complicated CRSs.

A large variation of anthropogenic emissions into the atmosphere has been recognized as crucial for the Earth's climate and the chemical composition of the atmosphere[66]. Below some of the most important sources are outlined:

1. *Combustion of biomass.* Species emitted are CO , CO_2 , NO , NO_2 , CH_4 , CH_3Cl and variations of other hydrocarbons.
2. *Coal production and use.* CH_4 is emitted during mining and manufacturing of coal. During the combustion of coal major amounts of CO_2 , CO , hydrocarbons, NO , NO_2 , SO_2 and soot are released, as well as small amounts of HCl , NH_3 and trace metals.
3. *Petroleum production and use.* Combustion of petroleum produces primarily CO_2 , CO , a large number of hydrocarbon compounds and carbon soot. At high temperature, combustion of petroleum also produces different types of nitrogen oxides. Petroleum does also contain sulfur, a component that varies a lot in the different petroleum products. This lead to emissions of SO_2 .

4. *Natural gas production and use.* Only emission of CO₂ and perhaps CH₄ are of importance.
5. *Industrial processes.* Aside from the combustion of fossil fuels to produce energy under industrial processing, three classes of emitants have received special attention: CFC's, CO₂ and atmospheric particles.

Therefore, emissions of compounds from anthropogenic activities can roughly be classified as

1. sulfur-containing compounds,
2. halogen-containing compounds,
3. nitrogen-containing compounds,
4. carbon-containing compounds, and
5. atmospheric particles.

Aside from the anthropogenic impact there is also a natural atmospheric source of sulfur-containing compounds from biological decay, combustion of organic matter and sea spray. Sulfur compounds decay quickly in the atmosphere (except SO₂ which has an approximate residence time of 40 days[2]) and there is a strong dominance of anthropogenic sulfur relative to natural sulfur[67]. Therefore, only anthropogenic sulfur emissions are considered in RAQMs and atmospheric gas-phase mechanisms only contain very simple inorganic gas-phase sulfur chemistry of SO₂. Furthermore, sulfur-containing gases are major participants in gas to particle conversion, and SO₂ and SO₄ are important chemical compounds in aerosol and cloud chemistry[68]

Most of the halocarbons are inactive in the troposphere, the only active ones being those containing labile H-atoms or C-C double bonds since these molecules can be oxidized by atmospheric HO radicals. The non-reactive halocarbons are therefore transported to the stratosphere where they are photodissociated by the shorter wavelengths of the solar radiation spectrum. This halocarbon sink releases free Cl-atoms that lead to the observed stratospheric ozone depletion which is especially observed over Antarctica. Hence, CFC gases have received much international attention since Farman et al.[69] reported that the total amount of ozone in the atmosphere over the observational site in Antarctica decreased rapidly during the southern hemisphere's spring.

The most important anthropogenic emitants in relation to tropospheric gas-phase chemistry are the nitrogen- and carbon-containing compounds. Among the nitrogen compounds, NO and NO₂ are the most important from a chemical point of view, because these are highly active catalysts in most atmospheric chemical chains and therefore have a great impact on the formation processes of ozone, see *Section 1.1*. NO₃ is very important for nighttime atmospheric chemistry.

The major atmospheric gas-phase carbon-containing compounds are CO, CO₂, CH₄ and VOC. From a chemical point of view, the chemical reactions of CO, CO₂

and CH_4 are rather simple. CO_2 is inactive, CO and CH_4 react with HO resulting in the formation of HO_2 and CO_2 , and CH_3O_2 and H_2O , respectively, see *Section 1.1.1*. The opposite is true for the atmospheric chemistry of VOC. The atmospheric composition of VOC is rather complex. It consists of a broad spectra of compounds containing almost all the different organic functional groups. Therefore, VOC has a major impact on almost all the concentration levels of the important species in the atmosphere. This will be discussed further later in this chapter.

Particulate matter can either be solid or liquid. Particulate matter in the atmosphere may affect the atmospheric chemical production, reduce visibility, fog formation and precipitation, and reduce the solar radiation. For example,

1. high concentrations of SO_2 can form sulfuric acid droplets by oxidation. This can serve as condensation nuclei for formation of small fog droplets, and
2. a large range of heterogeneous processes can take place on particle surfaces, e.g. soot's interaction with a number of gas-phase species including NO_2 , O_3 and SO_2 can affect the production of air pollutants.

This outline of the different chemical compounds and their effects on the atmosphere is not complete. For example, we have not described the importance of the emissions from biogenic compounds such as isoprene, α -pinene, β -pinene and d-limonene on the tropospheric chemical composition, even though this has a major impact on tropospheric ozone chemistry. The reason is that we are only looking at the chemistry of the urban plume versus the rural areas in this chapter.

The purpose of this chapter is to describe the effect of anthropogenic emissions on the tropospheric chemical composition and to investigate how the gas-phase mechanisms – EMEP, RADM2 and RACM, represent the chemistry of the troposphere. This description will especially focus on the chemistry of ozone. These tasks are accomplished as follows:

- first a general view over tropospheric chemistry will be given in *Section 1.1*.

This overview encompasses both the background tropospheric air (rural areas) and polluted air chemistry (urban plumes). We describe the most important chemical compounds and reactions in these areas of the atmosphere.

- The second step is a description of the usefulness of three chemical mechanisms to describe the tropospheric chemical composition, *Section 1.2*.

This is handled by a two-step procedure

1. a description of how the chemical mechanisms are constructed, *Section 1.2.1*, and
2. a comparison of the three mechanisms is performed based on the scenarios suggested by the Chemical Mechanism Working Group (CMWG) under EUROTRAC[38] using 0-dimensional box model simulations, *Section 1.2.2*.

1.1 Tropospheric Gas-Phase Chemistry

Until the early 1970s it was believed that tropospheric ozone was chemically inert, and that the only source of tropospheric ozone was an intrusion of stratospheric ozone and the only sink was its destruction at the Earth's surface[65]. Today it is accepted that much of the production of tropospheric ozone stems from nitrogen oxides and VOC. Müller and Brasseur[6] have shown that about 50% of tropospheric ozone comes from chemical interaction with nitrogen oxides and VOC and 50% from above their model domain. Figures 1.1 and 1.2 simplified illustrations of ozone formation in the tropospheric background and polluted air are presented. The main task in atmospheric chemistry is to identify key chemical reactions that are important for the atmospheric chemical composition. In the following a more detailed description of tropospheric chemistry, especially ozone, is given based upon Refs. [2, 32, 65, 70, 71, 72, 73, 74].

1.1.1 Background Troposphere

In order to describe the chemical composition of the background troposphere we must describe

- the chemistry of nitrogen oxides and its connection with that of ozone.

Then proceed with that of

- carbon monoxide since its atmospheric chemistry is the simplest.

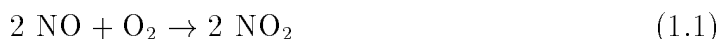
Finally, we consider

- the chemistry of the simplest alkane.

Due to our definition of the background troposphere, a description of urban air pollutants' impact on tropospheric chemistry will first be performed in the next section.

The Basic Photochemical Cycle of NO_2 , NO and O_3

The basic photochemical cycle of NO_2 , NO and O_3 are the reactions 1.2, 1.3 and 1.4 in Figure 1.1. These reactions show the conversion between NO_2 and NO with an interplay of O_3 , and it illustrates the most important tropospheric source of ozone. As described in the introduction of this chapter, the main atmospheric source of nitrogen oxides comes from combustion processes. NO is the dominant emitant from these processes i.e., approximately 90% of anthropogenic emitted NO_x is NO . To some extent NO_2 is formed by:



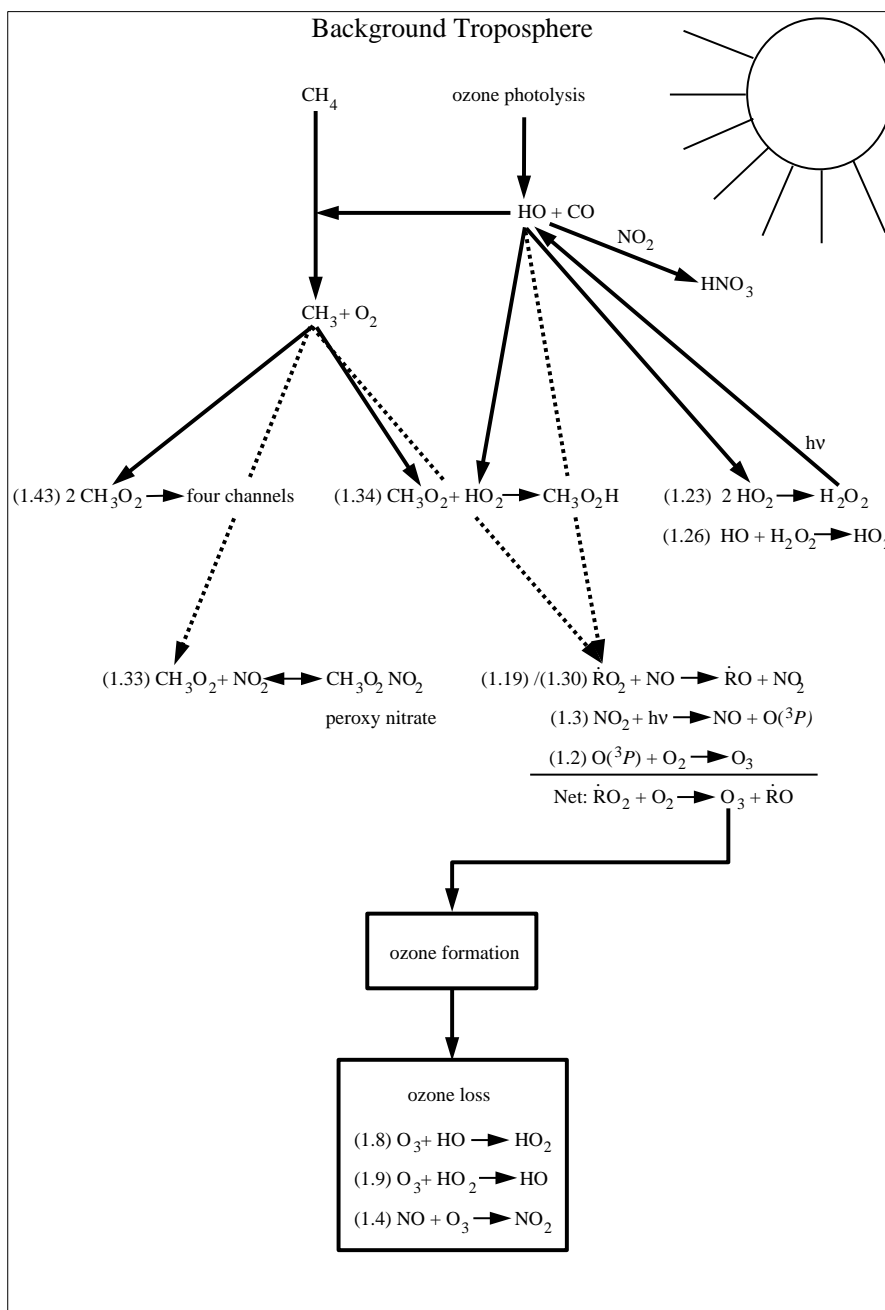


Figure 1.1: Simplified illustration of ozone formation in the tropospheric background, and sinks of radicals that are important for ozone's chemistry: HO₂, CH₃O₂, NO₂ and HO. R can either be CH₃ or H.

Even very low concentrations of atmospheric NO₂ initiate complex series of chemical reactions that produce photochemical smog. The major contributor to tropospheric ozone is the two step termolecular recombination reaction¹:



¹In Section 2.1 we have simulated the termolecular recombination reaction for ozone formation utilizing quasi-classical trajectories.

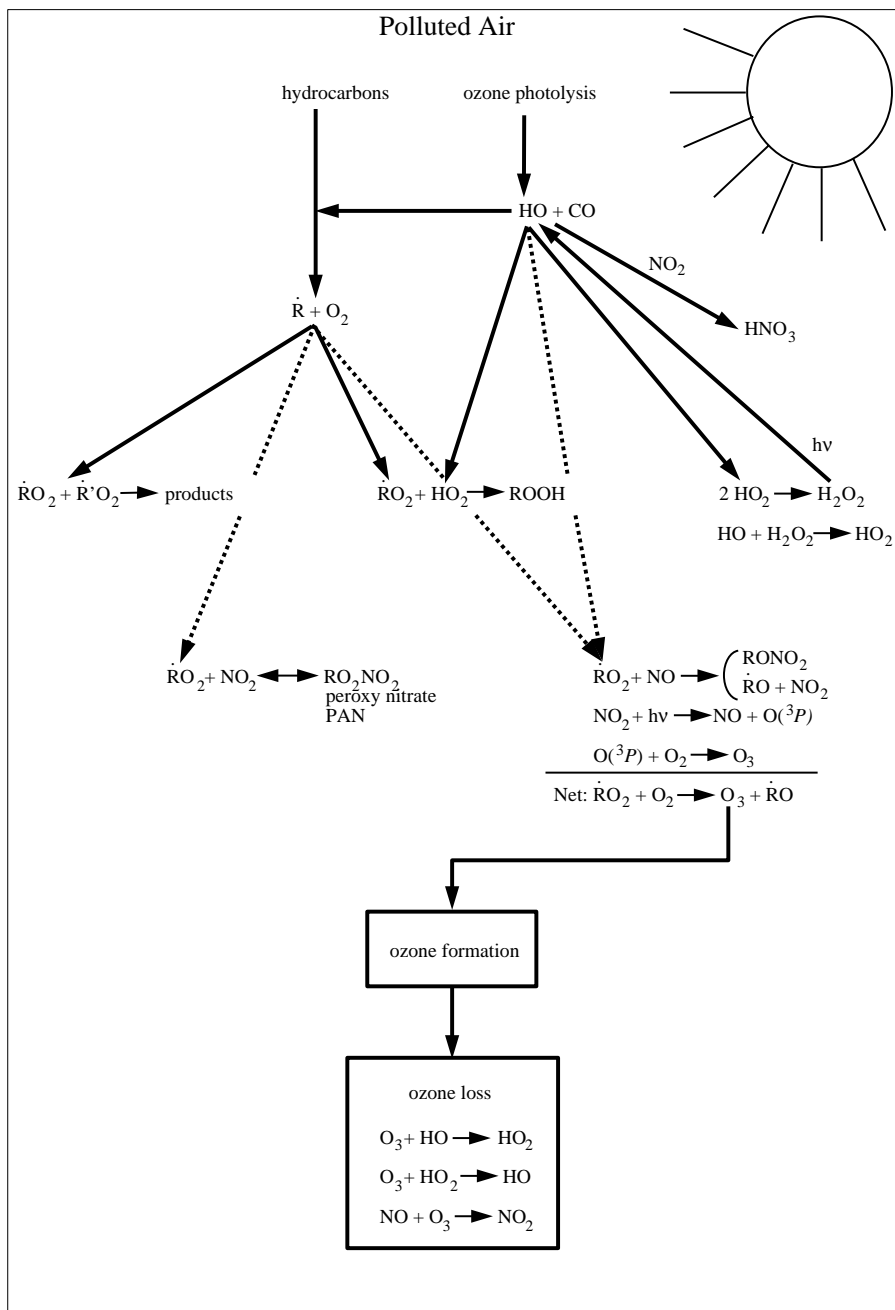


Figure 1.2: Simplified illustration of ozone formation in polluted air, and sinks of radicals that are important for ozone's chemistry: HO_2 , RO_2 , NO_2 and HO .

where M is an inert atom or molecule, in the atmosphere primarily O_2 or N_2 . In order to form ozone from this reaction we need $\text{O}({}^3P)$ which is obtained from the photolysis of NO_2 :



therefore reaction 1.2 will not be active during nighttime. Some of the formed ozone is destroyed by reacting with NO , but this reaction then forms NO_2 :



We see that reactions 1.2-1.4 is a closed cycle and therefore ozone is not produced by these three reactions alone.

Ozone's Impact

Ozone has an important chemical impact in the troposphere even though only about 10% of all atmospheric ozone is located there. The reason is that ozone determines the oxidation capacity by being the major source of hydroxyl radicals. Hydroxyl radicals are produced by ozone by a two step mechanism, a fraction of ozone is photolysed to O_2 and the first excited state of oxygen:



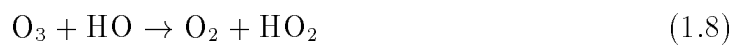
then $O(^1D)$ can either be de-excited to $O(^3P)$ by a collision with an inert atom/molecule:



or it can react with gaseous water:



The formation of hydroxyl radicals starts two possible ozone destruction reactions:



and in total we have



and the formation of HNO_3

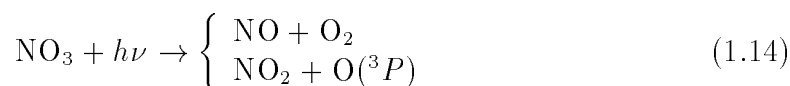


Hydroxyl radicals are important species in the troposphere since they initiate the oxidation of many gaseous hydrocarbons, halogenocarbons, organosulphur compounds, CO, NO_2 , H_2S , SO_2 , etc. (see *Section 1.1.2*).

The formed NO_2 in reaction 1.4 will in the daytime be removed according to the photolysis process 1.3. But during the nighttime it is possible that NO_2 reacts with ozone forming NO_3 that together with NO_2 form an equilibrium with N_2O_5 , i.e.



This does not occur during the daytime because NO_3 is rapidly removed by photolysis:

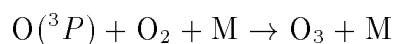
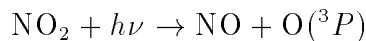


Other reactions, existing in the nitrogen-oxygen chemical system, should be included for a more complete description, e.g.:



CO/HO Impact

As was the case for ozone, the concentration levels of hydroxyl radicals are also strongly influenced by the presence of NO/NO₂-species. The background tropospheric concentration level of CO is around 100-120 ppbV[2, 38], therefore the reaction of HO with CO can initiate one of the atmospheric NO/NO₂ catalytic reaction chains

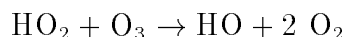
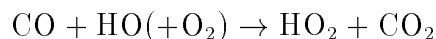


and in total we have



This reaction chain occurs in the presence of sufficiently large concentrations of nitric oxide. Note that HO and HO₂ also serve as catalysts.

For low nitric oxide conditions, it is more likely that the much less reactive reaction between HO₂ and ozone will be more dominant than reaction 1.19. This creates another reaction chain that destroys ozone instead of creating it:



and in total we have



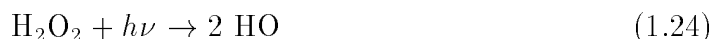
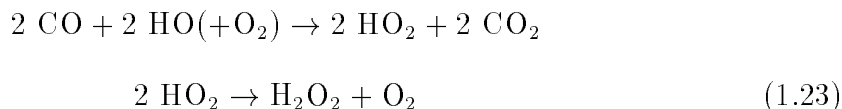
The ratio between reaction 1.9 and 1.19, at 298 K, that leads to formation of HO is

$$\frac{[\text{O}_3] k_{1.9}}{[\text{NO}] k_{1.19}} = 2.5 \times 10^{-4} \frac{[\text{O}_3]}{[\text{NO}]} \quad (1.22)$$

where $k_{1.9}$ and $k_{1.19}$ are the rate constants for reaction 1.9 and 1.19, respectively. The rates for these two reactions are taken from Ref. [29]. This shows that the second reaction chain will dominate when the concentration of ozone is 4050 times higher than that of NO. The primary chemical source of NO in the background troposphere comes from the photolysis of NO₂, reaction 1.3, while the dominant removing reactions of NO are 1.4 and 1.19. Within the rural and urban limit, the

dominant reaction chain will almost always be the NO rich chain. For the simulations presented in this chapter, *Section 1.2*, the NO poor situation occurs only in special cases during nighttime.

Another important chain mechanism initiated by reaction 1.18 also occurs



and in total we have



The concentration of ozone is not affected by this chain but two atmospherically important species H_2O_2 and HO_2 act as catalysts in the chain mechanism. HO_2 is a highly reactive species, therefore reaction 1.23 is competitive with the two other HO_2 reactions (1.9 and 1.19). Both HO_2 and H_2O_2 are water-soluble and are therefore important agents in cloud-chemistry and water containing aerosols. Furthermore, the hydrogen peroxide radical is a highly active chemical agent, whose self-reaction undergoes



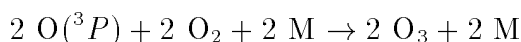
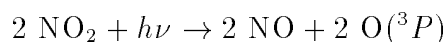
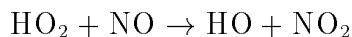
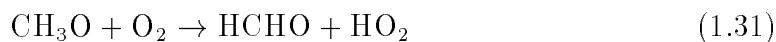
and in total we have



Hydrogen peroxide radicals react also with organic peroxy radicals, see *Section 1.1.2*.

CH₄/HO Impact

Methane also influences the background tropospheric chemistry. As was the case for carbon monoxide, methane chemistry is initiated by hydroxyl radicals forming another radical, CH_3 . The methyl radical starts chain reactions similar to the CO/HO case. Again we have two cases depending on the NO concentration. In the NO rich regime a rapid formation of ozone and formaldehyde occurs:



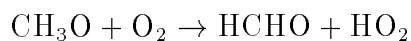
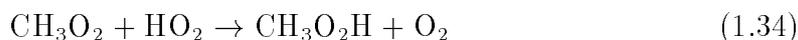
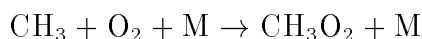
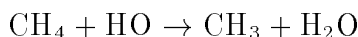
and in total we have



Equilibrium is possible between NO_2 , CH_3O_2 and CH_3OONO_2 :



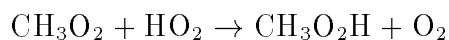
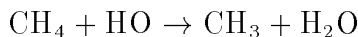
In the NO poor regime, two competing chain reactions can occur



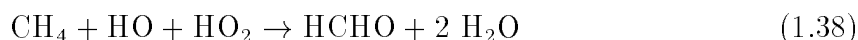
and in total we have



or



and in total we have



The reactions in the two reaction chains (chain 1.32 and chain 1.36/1.38) that determine the switch between the high and low NO regimes are reactions 1.30 and 1.34. The ratio between these two reactions is

$$\frac{k_{1.30}[\text{NO}]}{k_{1.34}[\text{HO}_2]} = 1.4 \frac{[\text{NO}]}{[\text{HO}_2]} \quad (1.39)$$

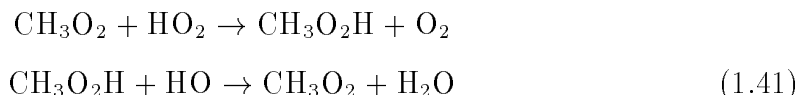
where $k_{1.30}$ and $k_{1.34}$ are the rate constants of reactions 1.30 and 1.34, respectively. These rate constants are taken from Ref. [29] at 298 K. This shows that both chains dominate under “clean” and polluted conditions. For the two low regime cases, reactions 1.35 and 1.37 are the chain determining reactions. From these we get

$$\frac{J_{1.35}}{k_{1.37}[\text{HO}]} \quad (1.40)$$

²The reaction of $\text{CH}_3\text{O}_2\text{H}$ with HO has been discussed in *Section 2.3.2.4* and the rate constant of the reaction has been calculated utilizing phase-space technique.

where $J_{1.35}$ is photolysis rate of reaction 1.35 and $k_{1.37}$ is the rate constant of reaction 1.37. We see that the time of day determines which of the two chains is the important one.

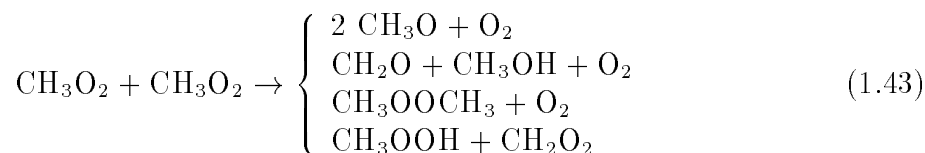
Both the low and high NO concentration regimes form the simplest peroxy radical, CH_3O_2 . Due to this peroxy radicals' similarity with HO_2 it triggers similar chain reactions, such as:



and in total we have

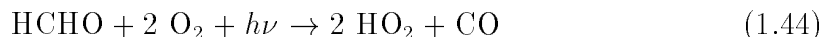


The methyl peroxy radical self-reaction is much more complicated. Experimental investigation shows that four reaction channels are observed[29]:

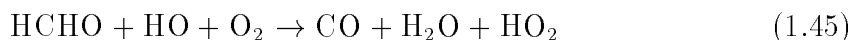


but due to the complexity of this self-reaction, many open questions remain[75].

In all three reaction chains described above, formaldehyde is formed. Formaldehyde is also a primary pollutant and therefore the chemistry of that compound is important. In this context three possible reactions of formaldehyde exist



and



and



Finally, NO_3 formed during nighttime can react with aldehydes forming HNO_3 (see *Section 1.1.3*):



1.1.2 Polluted air

In the previous subsection, we described the chemistry of the background tropospheric gas-phase chemistry. That section illustrated the fundamental importance of HO because it triggers the chemistry of CO and CH_4 . From these reactions many important radicals are formed: $\text{O}({}^3P)$, $\text{O}({}^1D)$, HO_2 , CH_3 , CH_3O and CH_3O_2 . In polluted air a large variety of VOC from anthropogenic sources must be incorporated in the description of the tropospheric chemistry. The starting point in deriving the impact of VOC on the tropospheric chemistry is the possible photolysis to other reactive compounds and the reactions with hydroxy radicals. In Table B.1 a list of VOC emissions for European boundary layer simulations is presented[21].

Alkane Chemistry

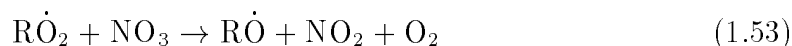
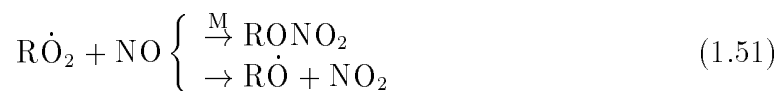
Alkanes can be transported over long distances due to their chemical stability, therefore they play an important role in tropospheric chemistry, e.g. the approximate residence time of methane is 7 years[2]. HO can either attack alkanes on a terminal or internal carbon atom and thereby form alkyl peroxy radicals



and in total we have



These alkyl peroxy radicals are highly reactive and can react with a large variety of atmospheric chemical compounds[70]:

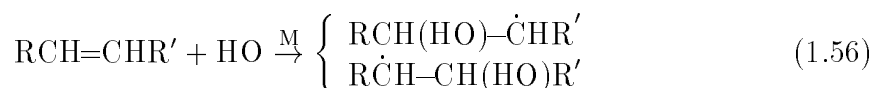


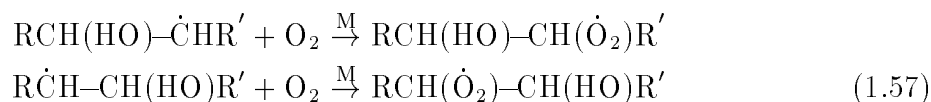
The alkoxy radicals ($\text{R}\dot{\text{O}}$) either react with O_2 , decompose or change to another isomer of $\text{R}\dot{\text{O}}$. The $\text{R}\dot{\text{O}} + \text{O}_2$ reaction leads to the formation of a carbonyl compound and HO_2 . It can also decompose to a carbonyl compound and an organic peroxy radical after addition of O_2 . Finally, it can undergo an isomerization that, after reaction with O_2 and NO , leads to the formation of a carbonyl and HO_2 .

The chemical reaction of peroxy radical + peroxy radical is rather complex and will therefore not be described in detail in this thesis. Its complexity involves a large number of different kinds of RO_2 that can be formed from the emitted VOC. Furthermore, many different kinds of reaction products can be formed from these different interactions between the peroxy radical + peroxy radical. For a more detailed description see Ref. [32, 76].

Alkene Chemistry

In contrast to alkanes, alkenes have a double bond, therefore these compounds are very reactive. Many different atmospheric chemical species can be added to the double bond of the alkenes: e.g. HO, O_3 and NO_3 [2, 74]. For monoalkenes, dienes and trienes with non-conjugated double bonds, hydroxyl radicals can be added to the double bond and followed by a rapid reaction with O_2 [70]:



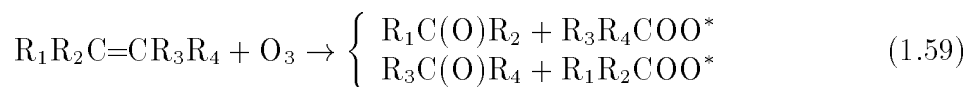


and in total we have



We see that alkyl peroxy radicals are formed in both channels, and these radicals can then react as described under alkane chemistry.

Alkenes can react with ozone and form a highly energy-rich ozonide as an intermediate. This intermediate decomposes automatically to a carbonyl compound and a highly energy-rich Criegee intermediate[74]:

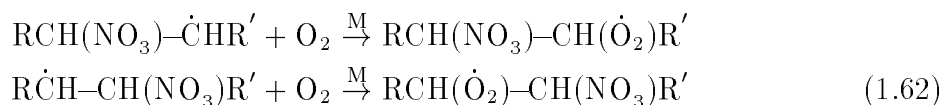
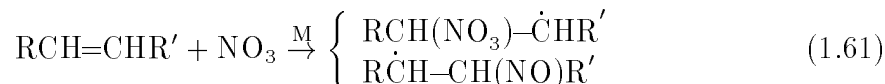


The highly energy-rich Criegee intermediate can either be de-excited to a stable molecule or further decomposed:

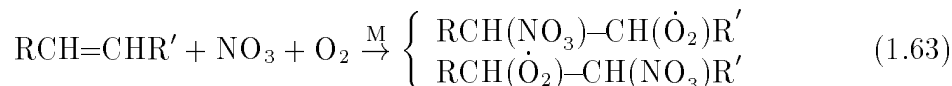


Ref. [70] gives examples of products formed from different highly energy-rich Criegee intermediates. These stable Criegee intermediates react primarily with H_2O producing either hydroxyl radicals or hydrogen peroxide[32] plus products of the Criegee intermediate's aldehyde, carboxylic acid, ester and ether[32].

NO_3 is added to the double bond in alkenes in the same manner as HO [70] followed by a reaction with O_2 which result in formation of peroxy radicals:



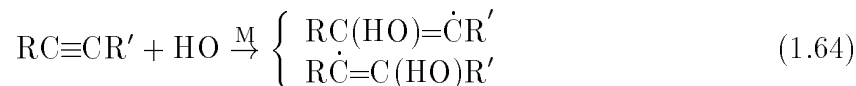
totally we have



The reactive part in the β -nitroalkyl peroxy radicals formed by reaction 1.63 are the peroxy radical. This can react with NO , HO_2 , and $\text{R}\dot{\text{O}}_2$ in a manner similar to that described in reactions 1.51, 1.54 and 1.55. The alkoxy radicals formed from β -nitroalkyl peroxy radicals interaction with NO and peroxy radicals can either react with O_2 , decompose or isomerize as described in section *Alkane Chemistry*. Contrary to alkane chemistry, β -nitroalkyl peroxy radicals interact reversibly with NO_2 forming a thermally unstable nitro peroxy nitrate.

Alkyne Chemistry

Knowledge of alkynes' impact on atmospheric chemistry is rather limited. Alkynes have a triple bond, therefore it is reasonable to believe that alkynes' atmospheric chemistry is similar to that of the alkenes', but only the alkynes' interaction with HO is considered to be important presently:



The alkene radicals formed can either decompose to a carbonyl containing compound that reacts with O₂ or reacts directly with O₂ forming an alkoxy peroxy radical. Again, peroxy radicals are formed as was the case for alkane and alkene, and the chemistry of these is described under alkane chemistry.

Carbonyl Chemistry

A large variety of carbonyl containing compounds exist in the troposphere since these compounds are both emitted from anthropogenic sources and formed chemically. Carbonyls either photolyze or react with HO, NO₃ or HO₂. Its interaction with NO₃ is of negligible importance under atmospheric conditions[70]. In this section aldehydes, ketones and dicarbonyls will be discussed.

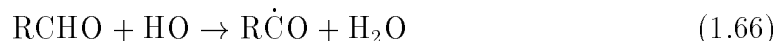
Aldehydes

The three simplest aldehydes are the most important in the troposphere. Formaldehyde and acetaldehyde are photolyzed as follows:



while only the upper channel is important for propanal.

Aldehydes react with the hydroxyl radical and form alkoxy radicals³



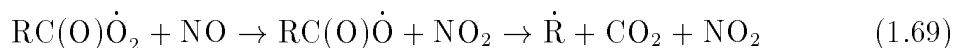
and these radicals react further with O₂. For H $\dot{\text{C}}\text{O}$ we have that



while for higher aldehydes we obtain peroxy radicals,



These peroxy radicals can react with NO, making

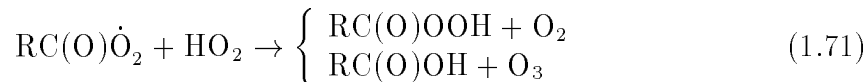


³The reaction of CH₃CHO with HO has been discussed in *Section 2.3.2.4* and the rate constant of the reaction has been calculated utilizing phase-space technique.

with NO_2 , forming



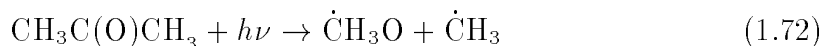
and with HO_2 , forming



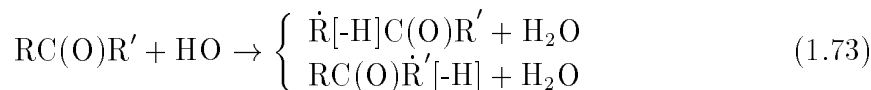
Further reactions with alkyl peroxy radicals occur, as described in section *Alkane Chemistry*. If $\text{R} = \text{CH}_3$ in reaction 1.70, PAN is formed.

Ketones

Photolysis data of acetone are the only ones available for ketones. Acetone photolyzes to an acetyl peroxy radical and methyl radical



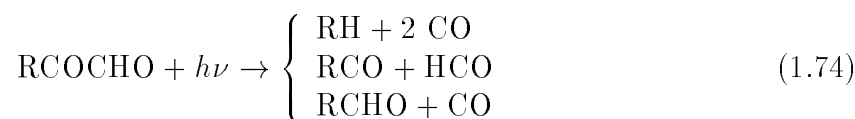
The reactions between ketones and hydroxyl radicals form



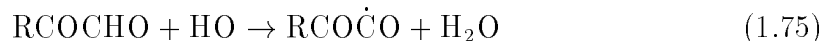
These products depend highly on which H-atom is extracted from the ketones, see for instance Ref. [70]. We see that reaction 1.73 forms carbonyl radicals where the carbonyl group remains intact. This reaction controls the isomer product formation. Therefore, the chemistry of these carbonyl radicals follows the chemistry described in the section *Alkane Chemistry*.

Saturated Dicarboxyls

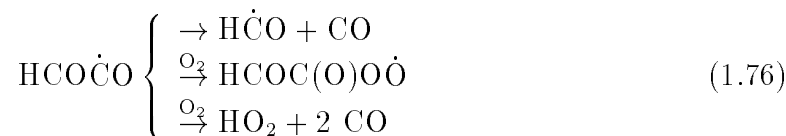
Within the class of saturated dicarboxyls, glyoxal and methylglyoxal are of central importance in the chemical reaction schemes of the troposphere. These two compounds have three photolysis channels[28]:



The important atmospheric reactions of glyoxal and methylglyoxal are their interactions with HO and O_2 . Glyoxal and methylglyoxal react with HO forming oxy radicals:



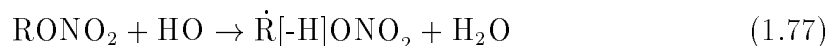
For glyoxal, the oxy radical formed can either decompose to $\text{H}\dot{\text{C}}\text{O}$ or react with O_2 :



Under atmospheric conditions, methylglyoxal does not react with O_2 , it only decomposes to $\text{CH}_3\dot{\text{C}}\text{O}$ and CO.

Organic Nitrate and Nitrite Chemistry

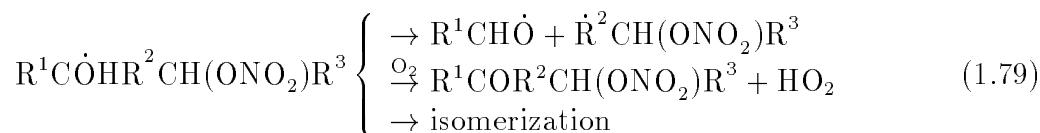
Due to anthropogenic emissions of NO_x , a large variety of nitrogen containing organic compounds can be formed in the troposphere. Alkyl nitrates are primarily formed by photooxidation of alkanes by NO_x . The reactions of alkyl nitrates with NO_3 and O_3 are expected to be so slow that they have no importance in the atmosphere, even though no experimental measurements are available for these reactions. Thus, the loss of alkyl nitrates takes place via a H-abstraction reaction between hydroxyl radicals and alkyl nitrates. The H-atom can in principle be removed from all the C-atoms in the alkyl nitrate:



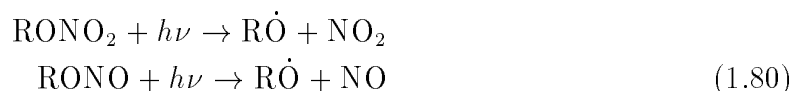
These alkyl nitrate radicals undergo reactions with NO and O_2 forming alkyl nitrate oxy radicals which either decompose, isomerize or react with O_2 :



and



Alkyl nitrates and nitrites can be photolysed to alkoxy radicals:



The chemistry of alkoxy radicals is described in section *Alkane Chemistry*. The photolysis of alkyl nitrites occurs very rapidly and therefore its reaction with hydroxyl radicals is negligible under atmospheric conditions.

Presently, the only studied peroxyacyl nitrate is PAN. PAN's interaction with hydroxyl radicals is slow in the lower troposphere. It is not expected to photodissociate in the troposphere and it is not highly water soluble. This enables PAN to be transported over long distances. Instead, the dominant loss of PAN is the unimolecular thermal decomposition reaction:



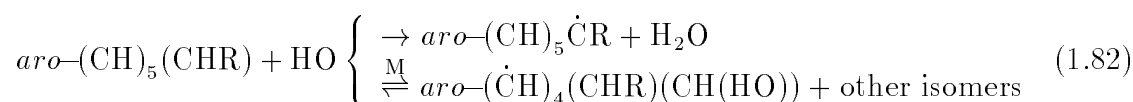
which is the reverse reaction of 1.70. The peroxy radical formed can decompose further according to reaction 1.69. Therefore, PAN acts as a reservoir for NO_x [2].

Aromatic Chemistry

Two groups of aromatic compounds are important to consider in tropospheric chemistry: the mono- and polycyclic aromatic compounds. This section only deals with

the chemistry of the monocyclic aromatic compounds and the reader is referred to Refs. [71, 77] for further information and references concerning the chemistry of polycyclic aromatic compounds.

The chemistry of aromatic compounds either involves the substituent groups or the aromatic ring. Anthropogenic aromatic compounds react primarily with hydroxyl radicals[70], and in this case the addition of hydroxyl radicals is the dominant reaction[70]. In the RACM MCH[32] $\approx 90\%$ is considered to be addition of hydroxyl radicals to the aromatic ring and $\approx 10\%$ a reaction with the substituent groups on the aromatic ring. The reaction of hydroxyl radicals with aromatic compounds (*aro*-(CH)₆ symbolize benzene) can be illustrated as



The chemistry of the substituent groups on the aromatic compound is identical to that described in one of the sections concerning the chemistry of alkane, alkene, alkyne, carbonyl, organic nitrates or organic nitrites chemistry, depending on which functional group CHR belongs to[70].

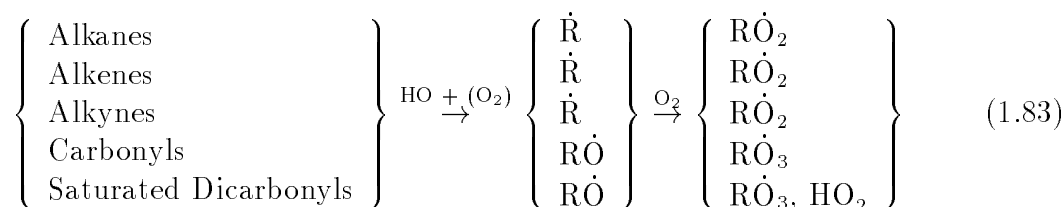
Even though the hydroxyl radical addition to the aromatic ring is the most important channel, the product radical has a limited lifetime of ≈ 0.3 s at 298 K and atmospheric pressure[71] before it breaks into the reactants again. A comparison of the rate constants between the aromatic radicals formed in reaction 1.82 and possible atmospheric compounds shows that, at room temperature and atmospheric pressure, the important reactions are the reactions with O₂ and NO₂[71]. Presently, there are still many uncertainties related to the chemistry of the aromatic radicals and the product yields[2, 32, 71], but the following possible reaction pathways are assumed. The reaction with NO₂ can add NO₂ to the aromatic ring (with H₂O as a residue product) and/or from cresol (with HONO as a residue product). The reaction with O₂ forms peroxy radicals, where -(OO \dot{O}) is directly attached to the aromatic ring. We will in this context not go into further detail since this chemistry is highly uncertain. For further information consult Refs. [2, 32, 71].

Overview

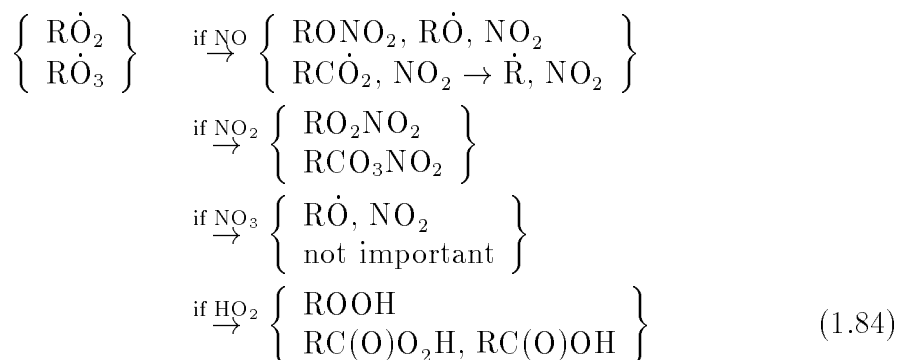
The description given above is only a short summary over the most important atmospheric compounds emitted or formed in photochemical smog. A description of alcohols, ethers, carboxylic acids, hydroperoxides, unsaturated carbonyls and unsaturated dicarbonyls has been omitted here since it would be too comprehensive to include in this context.

Aside from the special alkene reactions, reactions 1.56-1.62, general trends of

the chemistry are seen for all the functionally groups. It is observed that



and $\text{R}\dot{\text{O}}_2$ and $\text{R}\dot{\text{O}}_3$ react with either NO , NO_2 , NO_3 or HO_2 giving



See also the illustration in Figure 1.2.

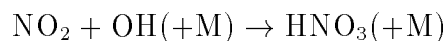
1.1.3 Formation of Water-Soluble Gases

Some of the primary and secondary gas-phase compounds in the troposphere are water-soluble. In that respect a well-known compound is carbon dioxide:

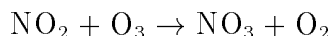


and this weak acid can further dissociate to carbonate and bicarbonate.

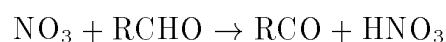
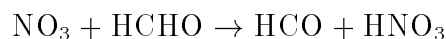
During the daytime, the concentration of NO_3 is very low due to photolytic destruction of NO_3 , see reaction 1.14. In the daytime HNO_3 is formed by nitrogen dioxide and hydroxyl radicals:



During the nighttime NO_3 is accumulated through the reaction



and NO_3 can react with a large variety of species, especially aldehydes, to form HNO_3 [78]:



Moreover, in the presence of NO_3 and NO_2 a chemical equilibrium with N_2O_5 is formed:

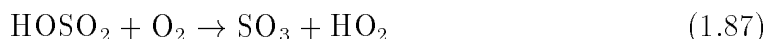
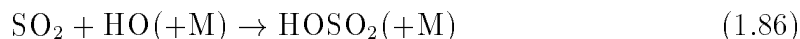


In the presence of water, e.g. on cloud droplets and water containing aerosols, N_2O_5 reacts with water and forms HNO_3



The formation of HNO_3 in the lower troposphere is a major sink of nitrogen. The reason is that HNO_3 is chemically very inactive in this atmospheric region nevertheless it is quickly removed by dry and wet deposition.

In the background troposphere the concentration of SO_2 is around 1-10 ppbV[2] (of course much higher in areas of anthropogenic combustion). Atmospheric sulphur dioxide reacts with HO starting a three step chain mechanism[79]:



and totally we have



Reaction 1.86 is the key reaction of this chain mechanism. The other compounds in the mechanism are either formed or exist in high concentrations in the atmosphere.

Other gaseous compounds from the troposphere are also water-soluble, e.g. H_2O_2 (highly water-soluble and therefore clouds are a major sink for hydrogen peroxide) and HO_2 (rainout is an important sink).

1.2 Simulations

In order to understand atmospheric chemistry and the utility of different gas-phase chemical mechanisms in RAQMs, we have simulated different scenarios that represent remote, moderately to rather polluted European environments for the background troposphere. This investigation using a 0-dimensional chemical box model as described in Figure 1.3 utilizing some of the most utilized atmospheric gas-phase chemical mechanisms:

- the EMEP MCH,
- the RADM2 MCH, and
- the RACM MCH.

The version of these three mechanisms used are those given in *Appendix A*. The integrator in the 0-dimensional box model is the benchmark solver:

- the Gear algorithm.

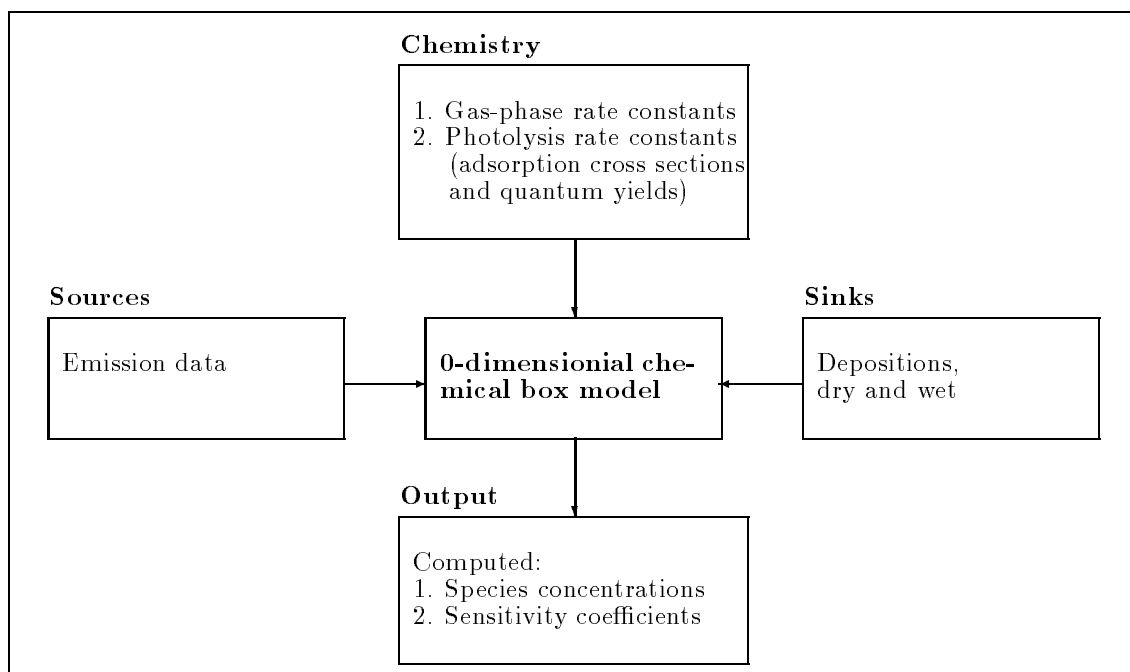


Figure 1.3: Flow diagram of the elements in a standard 0-dimensional gas-phase chemical box model.

1.2.1 The Mechanisms

The inorganic chemistry of the troposphere is “well-known”[32], and it can be represented with relatively few chemical reactions. It is the chemistry of the organic compounds that complicates tropospheric chemistry, especially those arising from the hundreds of anthropogenic VOC that are emitted into the atmosphere (see *Section 1.1.2* and Ref. [32]). Hence, this area of atmospheric chemistry is extremely complicated and the number of chemical reactions that involve organic compounds is enormous. Therefore, lumped chemical mechanisms that describe the atmospheric chemistry have been developed, and these are the ones that are used in RAQMs. The EMEP, RADM2 and RACM MCHs are representations of these kinds of mechanisms.

EMEP MCH

The EMEP MCH was developed to be used in a single layer trajectory model. This model was developed with the purpose of studying the transport and chemical formation of surface ozone over Europe. The first generation of the EMEP MCH was an updated version of the chemical mechanisms presented by Eliassen et al.[80] and Hov et al.[81]. For the subsequent version[82], the rate constants and reaction pathways were updated mainly according to Atkinson[72] and IUPAC[83]. Furthermore, in order to improve the influence of the most important biogenic emissions, the isoprene chemistry was extended. The isoprene chemistry in the EMEP MCH was a lumped version of the isoprene chemistry presented by Paulson and Seinfeld[84].

Finally, the peroxy radical chemistry was improved in this second generation.

In the third EMEP MCH version[85], the HO and HO₂ reactions R132–R141 (Table A.4) were added to the mechanism. The addition of the HO and HO₂ reactions was done in order to treat isoprene and other VOC similarly in the mechanism.

The EMEP MCH used in this thesis is the version given in EMEP MSC-W Report 3/97[30], see *Appendix A*. This version of the EMEP MCH contains 79 species, 24 photolysis, 28 inorganic and 89 organic reactions. In this version the parameterization of the photolysis rates[30, 86] (J) had been changed from

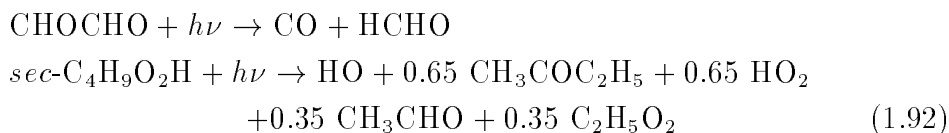
$$J = A \exp(-B \sec\theta) \quad (1.90)$$

to

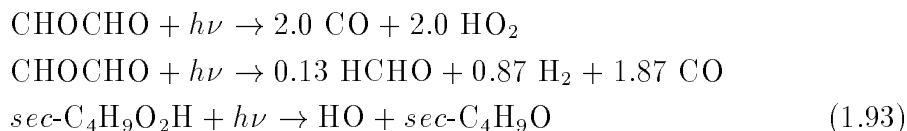
$$J = A (\cos\theta)^B \exp(-C \sec\theta) \quad (1.91)$$

A and B are given in Ref. [82], A , B and C are given in Table A.3 and θ is the solar zenith angle. This resulted in a few changes of some of the photolysis reactions.

In the old version, the following reactions were presented:



and in the new version we have



The change of the photolysis parameterization is done because the parameterization previously used could under some conditions give very incorrect photolysis rates[30].

The recent EMEP MCH has been evaluated against the IVL MCH[37]. Due to the much greater complexity of the IVL MCH compared to the EMEP MCH, this mechanism was considered as a benchmark mechanism by the EMEP MCH developer (D. Simpson), especially since the same reference data are used to update the mechanisms. The main results of this comparison were that the mechanisms agree reasonably well considering the different complexity of the models.

Presently, the EMEP MCH can be considered as a subset of the chemical scheme of the IVL MCH.

RADM2 and RACM MCHs

The RADM2[31] and RACM[32] MCHs are treated together since the RADM2 MCH is built on the earlier developed RADM MCH[24]. The RACM MCH is a revised version of RADM2 MCH. Hence, the basic organic lumping concept in the two mechanisms is the same. The lumping of the atmospheric organic compounds in the RADM, RADM2 and RACM MCHs is based on three concepts:

- the emission inventory from National Acid Precipitation Assessment Program (NAPAP) of U.S.,
- the similarity of chemical reactivity within the organic functional groups, and
- the reactivity of the organic compounds with HO.

Contrary to the EMEP MCH where the lumping groups are represented by organic molecules, surrogate species are introduced in the RADM, RADM2 and RACM MCHs.

The RADM MCH was the gas-phase chemical mechanism in the first version of the regional acid deposition model[35]. The RADM2 MCH is based on the RADM MCH, the Lurmann et al. mechanism[33], the carbon bond mechanism by Whitten et al.[34], the explicit mechanism by Leone and Seinfeld[87], and the master mechanism by Keer and Calvert[88]. Thus, the number of surrogate species has been increased in RADM2 MCH to

1. three classes of higher alkanes in RADM2 MCH and one in RADM MCH,
2. improve and include more details of aromatic chemistry,
3. represent internal and terminal alkenes, two higher alkene classes have been introduced,
4. introduce isoprene as an explicit compound,
5. encompass a more detailed description of the peroxy radical – peroxy radical reactions, and finally
6. include ketones and dicarbonyls, which have been removed from the aldehyde class to a class of their own.

The RADM2 MCH has 21 inorganic and 42 organic compounds, 9 inorganic and 12 organic photolytic reactions, and 29 inorganic and 108 organic reactions.

The RADM2 MCH was published in 1990, and since then both NASA[89], IUPAC[83] and others have presented new experimental results of atmospherically related reactions. Therefore, the RACM MCH is both an updated version of the RADM2 MCH based on these new experimental works and some improvements of the scheme due to new atmospheric chemistry knowledge. Examples of improvement in the inorganic chemistry are e.g.

1. O(³P) reaction with nitrogen oxides and ozone,
2. HO's reaction with H₂ and nitrous acid, and
3. some NO₃ reactions have been added,

and for the organic chemistry,

1. a more explicit treatment of NO_3 reactions with alkenes,
2. an improved treatment of the aromatic chemistry,
3. the reactions of unsaturated dicarbonyl species and unsaturated peroxyxynitrate with HO and NO_2 (addition reactions and ozonolysis) have been added,
4. an improvement in the PAN chemistry,
5. an improvement in the organic peroxy radical–peroxy radical reactions,
6. organic peroxy + NO_3 reactions were added, and
7. a complete revision of the oxidation mechanism for isoprene.

This has led to a more detailed mechanism. Presently Stockwell’s mechanism includes 21 inorganic and 56 organic species, 9 inorganic and 14 organic photolysis, and 35 inorganic and 179 organic reactions.

Both the RADM2 and RACM MCHs have been evaluated against the University of California, Riverside Environmental Chamber Data Base for Evaluating Oxidant Mechanisms[90].

Comment

A major difference between the chemical mechanisms developed by Simpson and Stockwell are their atmospheric usability. The RADM2 and RACM MCHs is developed so it can simulate the chemistry from the Earth’s surface to the top of the troposphere, and both rural and polluted urban conditions. On the other hand, the EMEP MCH has exchanged the Troe expressions with the simpler Arrhenius expressions whenever possible in the temperature range 283 K - 303 K. Therefore, the EMEP MCH can only be used in the ABL in Europe.

1.2.2 Comparison of the EMEP, RADM2 and RACM MCHs

Different atmospheric chemical mechanisms use different treatments of photolysis, and different solvers are used to integrate chemical reactions in ACTMs. For example the EMEP MCH uses in its first versions the parameterization given in Eq. (1.90) while the newest version uses the parameterization given in Eq. (1.91). Contrary to these simple parameterizations the RADM2 and RACM MCHs use the photolysis program described in *Section 3.1.2* and *Appendix D*. The intention with this comparison is to compare the chemical schemes and not the different treatments of the photolysis in the mechanisms (i.e. the radiative transfer) or the different chemical solvers⁴. For consistency, we have used the prescribed photolysis frequencies from

⁴The comparison by CMWG under EUROTRAC[38] also involved a comparison of different solvers. In this thesis we have compared the EMEP MCH integrated using a QSSA solver towards the EMEP and RACM MCHs integrated using a Gear algorithm. The results from this comparison are presented in *Chapter 3*.

CMWG[38] and a Gear algorithm as numerical integrator of the mechanisms⁵.

The aim with this comparison is to investigate whether they predict similar or different concentration levels for the fundamental chemical compounds in the troposphere, in particular ozone. Therefore, we have performed $3 \times (81+150)$ 0-dim. box model simulations, see Table 1.1-1.3. The conditions given in Tables 1.1 and 1.2 give rise to 81 simulations for each mechanism. These environmental data are used for simulations without emissions. The conditions given in Tables 1.1 and 1.3 lead to 150 simulations for each mechanism. For these simulations VOC, CO, SO₂ and NO are added to the box simulations as emissions. Since we vary the concentrations and emissions of VOC, CO, SO₂ and NO we simulate both rural (“clean air”) and urban (polluted air) cases. All the simulations are started at noon local time (hour 12) and simulated for 72 hours (hour 84).

date	July 1, 1985, clear sky
ground albedo	0.10
solar declination	23 °
longitude	0.0 °
latitude	45 ° north
altitude (km)	0.0
temperature (K)	288.15
pressure (mbar)	1013.25
N (molecules/cm ³)	2.55×10^{19}
H ₂ O (%)	1.00
O ₃ (ppbV)	50.0
HNO ₃ (ppbV)	0.10
CO (ppbV)	200.
CH ₄ (ppbV)	1700
H ₂ (ppbV)	500.
H ₂ O ₂ (ppbV)	2.00
HCHO (ppbV)	1.00
O ₂ (%)	20.9
N ₂ (%)	78.1

Table 1.1: Scenarios simulated in the model comparison between the EMEP, RADM2 and RACM MCHs. The constant initial conditions in all the simulations.

Based on typical concentration levels of NO_xs and VOC in rural and urban areas, see Stockwell et al.[91] and Graedel[92], we have selected a rural (Rural) and urban (Urban) case for further investigations⁶. The Rural case is the cleanest case in the rural region (VOC, CO, SO₂, NO, NO₂) = (1.0 ppbC, 189. pptV, 17.3 pptV, 0.75 ppbV, 0.25 ppbV) and the Urban case is (VOC, CO, SO₂, NO, NO₂) = (0.5 ppmC, 94.5 ppbV, 8.66 ppbV, 37.5 ppbV, 12.5 ppbV). This Urban case is less polluted than the most polluted scenarios used to evaluate the QSSA[47], EBI[48]

⁵The Gear solver has over the years been considered a benchmark solver for testing new chemical solvers, see *Introduction, Solvers (QSSA and Gear) and Appendix C*.

⁶Throughout this thesis the capitalized version of rural, i.e. Rural, and urban, i.e. Urban, will refer to these two special cases.

(VOC, CO, SO ₂)	(NO, NO ₂)
(1.0 ppbC, 189. pptV, 17.3 pptV)	(75.0 pptV, 25.0 pptV)
(5.0 ppbC, 945. pptV, 86.6 pptV)	(375. pptV, 125. pptV)
(10. ppbC, 1.89 ppbV, 173. pptV)	(0.75 ppbV, 0.25 ppbV)
(50. ppbC, 9.45 ppbV, 866. pptV)	(3.75 ppbV, 1.25 ppbV)
(0.1 ppmC, 18.9 ppbV, 1.73 ppbV)	(7.50 ppbV, 2.50 ppbV)
(0.5 ppmC, 94.5 ppbV, 8.66 ppbV)	(37.5 ppbV, 12.5 ppbV)
(1.0 ppmC, 189. ppbV, 17.3 ppbV)	(75.0 ppbV, 25.0 ppbV)
(5.0 ppmC, 945. ppbV, 86.6 ppbV)	(375. ppbV, 125. ppbV)
(10. ppmC, 1.89 ppmV, 173. ppbV)	(750. ppbV, 250. ppbV)

Table 1.2: Scenarios simulated in the model comparison between the EMEP, RADM2 and RACM MCHs. The varied initial concentrations in the simulations. All simulations are without emissions. VOC represents anthropogenic non-methane VOC.

(VOC, CO, SO ₂)	(NO, NO, NO ₂)
(0.5 pptC/min, .0949 pptV/min, .00866 pptV/min)	(.037 pptV/min, 2.86 pptV, 7.14 pptV)
(1.0 pptC/min, .189 pptV/min, .0173 pptV/min)	(.185 pptV/min, 14.3 pptV, 35.7 pptV)
(5.0 pptC/min, .949 pptV/min, .0866 pptV/min)	(.370 pptV/min, 28.5 pptV, 71.4 pptV)
(10. pptC/min, 1.89 pptV/min, .173 pptV/min)	(1.85 pptV/min, 143. pptV, 357. pptV)
(50. pptC/min, 9.49 pptV/min, .866 pptV/min)	(3.70 pptV/min, 286. pptV, 714. pptV)
(0.1 ppbC/min, 18.9 pptV/min, 1.73 pptV/min)	(18.5 pptV/min, 1.43 ppbV, 3.57 ppbV)
(0.5 ppbC/min, 94.9 pptV/min, 8.66 pptV/min)	(37.0 pptV/min, 2.86 ppbV, 7.14 ppbV)
(1.0 ppbC/min, 189. pptV/min, 17.3 pptV/min)	(185. pptV/min, 14.3 ppbV, 35.7 ppbV)
(5.0 ppbC/min, 949. pptV/min, 86.6 pptV/min)	(370. pptV/min, 28.6 ppbV, 71.4 ppbV)
(10. ppbC/min, 1.89 ppbV/min, 173. pptV/min)	(1.85 ppbV/min, 143. ppbV, 357. ppbV)
(50. ppbC/min, 9.49 ppbV/min, 866. pptV/min)	
(0.1 ppmC/min, 18.9 ppbV/min, 1.73 ppbV/min)	
(0.5 ppmC/min, 94.9 ppbV/min, 8.66 ppbV/min)	
(1.0 ppmC/min, 189. ppbV/min, 17.3 ppbV/min)	
(5.0 ppmC/min, 945. ppbV/min, 86.6 ppbV/min)	

Table 1.3: Scenarios simulated in the model comparison between the EMEP, RADM2 and RACM MCHs. The varied initial concentrations and emissions in the simulations. VOC represents anthropogenic non-methane VOC.

and IEH[49] solvers.

1.2.2.1 Discussion of the Results

In this section the 0-dimensional modeling results from the comparison of the EMEP, RADM2 and RACM MCHs are presented[53]. This is done as follows:

1. a presentation of other comparison studies of atmospheric chemical mechanisms,
2. a description of the carbon conservatism of the mechanisms, and
3. a discussion of the concentration levels of

- ozone
- NO, NO₂, HO, HO₂ and RO₂

that the three mechanisms predict.

Other Comparison Studies of Atmospheric Chemical Mechanisms

The important impact of atmospheric chemical mechanisms in RAQMs has given rise to several comparison studies of atmospheric chemical mechanisms over the years. In Table 1.4 some of these studies are outlined⁷. Many of these studies have

Reference	Number of MCHs (e.g. MCHs)
Dunker et al.[93] 1984	4
Leone and Seinfeld[87] 1985	6
Shafer and Seinfeld[94] 1986	6
Stockwell[24] 1986	3
Hough[95] 1988	20 (CBM-IV)
Dodge[96] 1989	3 (CBM-IV, ADOM)
Derwent[97, 98] 1990/93	24 (CBM-IV, RADM2, EMEP1, EMEP2)
Jeffries and Tonnesen[99] 1994	2 (CBM-IV, SAPRC90)
CMWG comparison[38] 1996/98	12 (RADM2, CBM-IV, EMEP3, ADOM, IVL)
Andersson-Sköld and Simpson[37] 1997	2 (IVL, EMEP4)
Stockwell et al.[32] 1997	2 (RADM2, RACM)
Comparison in this chapter[53]	3 (RADM2, RACM, EMEP4)

Table 1.4: Overview of atmospheric chemical comparison studies.

a very sketchy description of the simulation setup e.g. the use of chemical solver and the model concept.

⁷Olson et al.[100] have also performed a comprehensive comparison of a large variety of tropospheric chemical mechanisms, but this study primarily involved chemical schemes related to global modeling. Therefore, these chemical schemes do not include the same detailed chemical description as in the work mentioned in Table 1.4.

These comparison studies have used different methodologies. For example the comparisons by Hough[95], Dodge[96] and Derwent[97, 98] have been performed using a trajectory model. The studies by Shafer and Seinfeld[94], Stockwell[24], Jeffries and Tonnesen[99], CMWG comparison[38] and Stockwell et al.[32] have been done using 0-dimensional box model simulations. Andersson-Sköld and Simpson[37] have compared the IVL and EMEP MCHs using both a trajectory model and 0-dimensional box model. In the work by Hough[95] and Derwent[97, 98], the mechanisms utilized have been adjusted such that the inorganic chemistry is identical and the rate constants have been updated with the most recently accepted chemical rate constants.

The previously comparison studies outlined in Table 1.4 show that substantially different results are observed among the early mechanisms[87, 93, 95]. Hough[95] found that mechanisms published after 1984 gave better results. In particular, the results for ozone and nitric acid agreed reasonably well but the simulated concentration levels of e.g. PANs, hydrogen peroxide, aromatic compounds and organic peroxides were rather different. These trends are seen even today because many of the atmospheric chemical mechanisms are made to predict tropospheric ozone concentrations[24, 38, 96].

Dunker et al.[93] stated that three of the chemical mechanisms used in their comparison study have been adapted to detailed grid and trajectory atmospheric simulations, and generally the ozone concentration levels in these type of simulations agree well with measurements. This could be seen as a paradox as Dunker et al. got substantially different results in their comparison of the tested mechanisms. It is important to note that transport-chemical models require input data of inflow boundary condition for each compound, the solar radiations influence by clouds and aerosols etc. This is data which is obtained by comparison between model results and measurements. This compensates to some degree for the differences between the mechanisms. Therefore, the best way of comparing atmospheric chemical mechanisms is simulations only including chemical reactions and photolysis under clear sky conditions however eventually in addition with constant chemical sources and sinks, as we have done in this thesis.

The Carbon Conservatism of the EMEP, RADM2 and RACM MCHs

Discussion of the Isopleths

An ideal chemical mechanism should be carbon conservative. On the basis of the runs described in Tables 1.1, 1.2 and 1.3, we have tested how much carbon is gained or lost during the runs. The total carbon (tot_{Carbon}) of a mechanism at a given time can be calculated by multiplying the concentration of the species by the number of carbon atoms in the molecule (see Tables A.1 and A.2) and then adding all these quantities together. That means

$$tot_{Carbon} = \sum_i Cn_i \times conc_i \quad (1.94)$$

where the sum is over all carbon containing compounds, Cn_i is the number of carbons

in the i th carbon compound and $conc_i$ is its concentration. On the basis of Eq. (1.94) we have calculated tot_{Carbon} after one day and three days of the simulations. Both cases are at noon where the photolysis is most active. The results are presented in Figures 1.4 - 1.9.

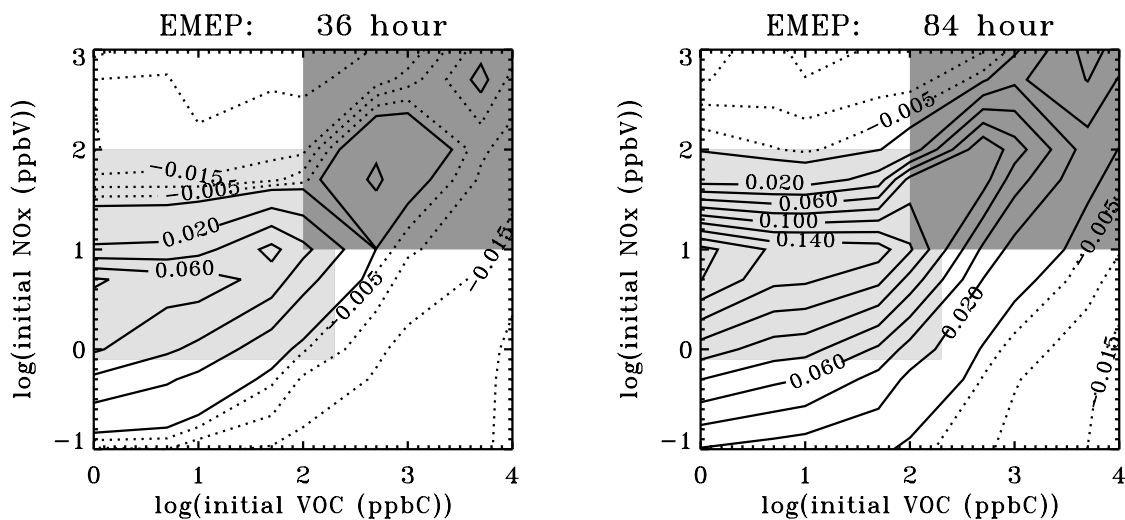


Figure 1.4: Deviation between total carbon put into the EMEP MCH and the amount of total carbon left in the mechanism at hour 36 and 84. The plots are based on 81 zero-dimensional box model calculations as described in Tables 1.1 and 1.2. Contour levels [(exact VOC into the EMEP MCH – VOC in the EMEP MCH at a given time)/exact VOC into the EMEP MCH] $-0.020, -0.015, -0.010, -0.005, 0.00, 0.02, 0.04, 0.06, 0.08, 0.10, 0.12, 0.14, 0.16$ and 0.18 . VOC represents anthropogenic non-methane VOC. The light gray indicates the range of NO_x and VOC concentrations observed in rural areas[91]. The dark gray indicates the range of NO_x and VOC concentrations observed in urban areas[92].

The figures shows that all three mechanisms are not carbon conservative, even though it is claimed in Ref. [38] that the EMEP MCH is. The non-carbon conservative EMEP reactions are R74, R75, R77, R97, R98, R102, R114, R116, R118, R121, R126, R127 and R129 (see Table A.4).

Figures 1.4 - 1.6 show how carbon preserving the mechanisms are during a three day run without emissions added to the mechanisms during the simulations. From these figures, we conclude that all the mechanisms lose carbon during the simulation. However, the EMEP MCH loss of carbon is very limited, maximum 18% in the rural area and 10% in the urban area, compared with the RADM2 and RACM MCHs which can lose carbon in the range 12.5% to 45% and 7.5% to 35% in the rural area and 7.5% to 25% and 2.5% to 25% in the urban area, respectively.

Figures 1.7 - 1.9 show that the mechanisms preserve carbon much better when VOC emissions are added to the mechanisms during the simulation. This can be explained from the fact that implementation of VOC in the RADM2 and RACM MCHs is almost carbon conservative (see Table B.4), and much more carbon conservative than the mechanisms itself.

The EMEP MCH is a more carbon conservative mechanism itself but a less carbon conservative mechanism due to VOC implementation than the RADM2 and

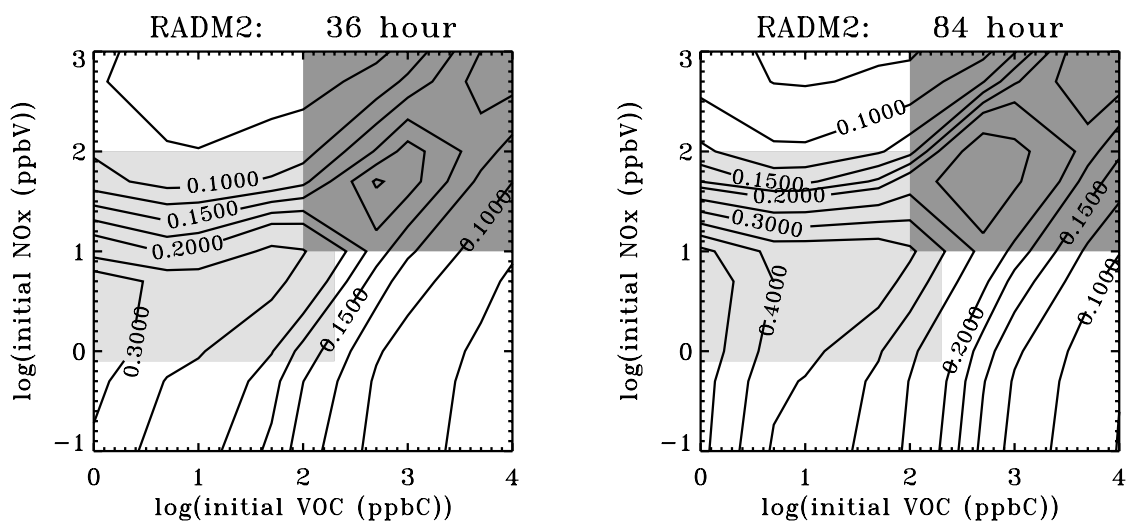


Figure 1.5: Deviation between total carbon put into the RADM2 MCH and the amount of total carbon left in the mechanism at hour 36 and 84. The plots are based on 81 zero-dimensional box model calculations as described in Tables 1.1 and 1.2. Contour levels $[(\text{exact VOC into the RADM2 MCH} - \text{VOC in the RADM2 MCH at a given time}) / \text{exact VOC into the RADM2 MCH}]$ 0.075, 0.100, 0.125, 0.150, 0.175, 0.20, 0.25, 0.30, 0.35, 0.40, 0.45 and 0.50. VOC represents anthropogenic non-methane VOC. The light gray indicates the range of NO_x and VOC concentrations observed in rural areas[91]. The dark gray indicates the range of NO_x and VOC concentrations observed in urban areas[92].

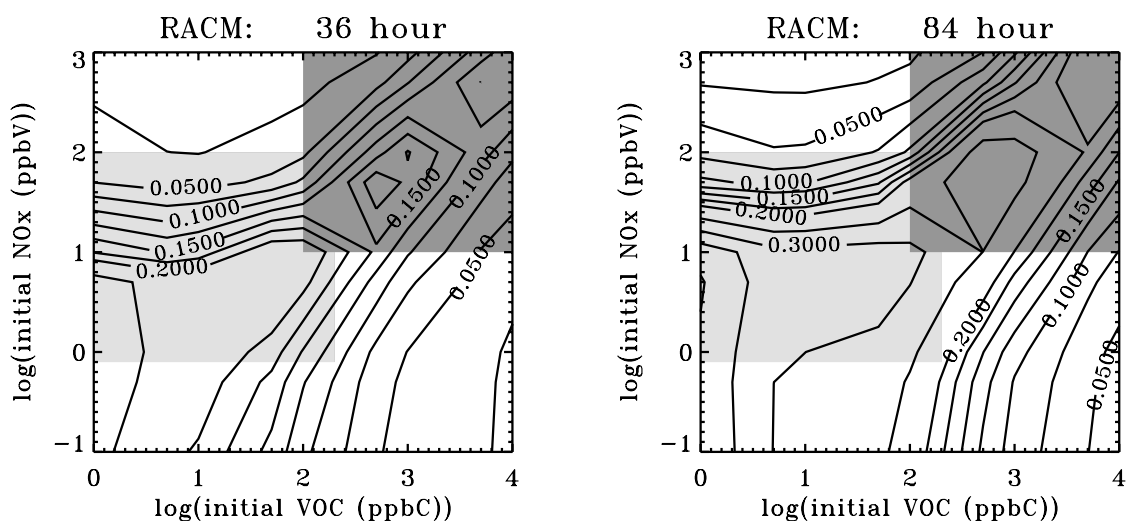


Figure 1.6: Deviation between total carbon put into the RACM MCH and the amount of total carbon left in the mechanism at hour 36 and 84. The plots are based on 81 zero-dimensional box model calculations as described in Tables 1.1 and 1.2. Contour levels $[(\text{exact VOC into the RACM MCH} - \text{VOC in the RACM MCH at a given time}) / \text{exact VOC into the RACM MCH}]$ 0.025, 0.050, 0.075, 0.100, 0.125, 0.150, 0.175, 0.20, 0.25, 0.30, 0.35 and 0.40. VOC represents anthropogenic non-methane VOC. The light gray indicates the range of NO_x and VOC concentrations observed in rural areas[91]. The dark gray indicates the range of NO_x and VOC concentrations observed in urban areas[92].

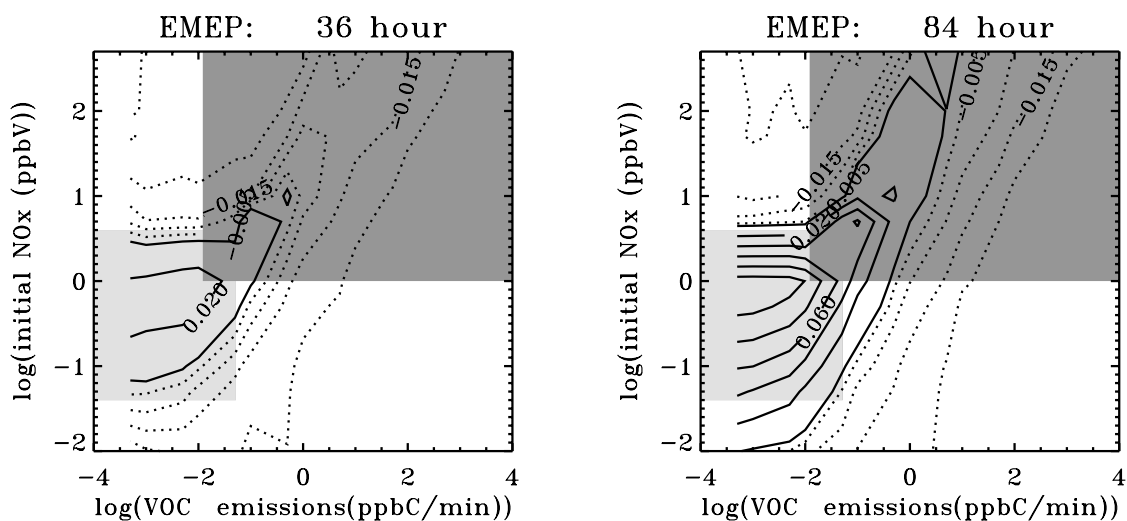


Figure 1.7: Deviation between total carbon put into the EMEP MCH and the amount of total carbon left in the mechanism at hour 36 and 84. The plots are based on 150 zero-dimensional box model calculations as described in Tables 1.1 and 1.3. Contour levels [(exact VOC into the EMEP MCH – VOC in the EMEP MCH at a given time)/exact VOC into the EMEP MCH] -0.020 , -0.015 , -0.010 , -0.005 , 0.000 , 0.020 , 0.040 , 0.060 , 0.080 and 0.100 . VOC represents anthropogenic non-methane VOC. The light gray indicates the range of NO_x and VOC emissions observed in rural areas[101]. The dark gray indicates the range of NO_x and VOC emissions observed in urban areas[101].

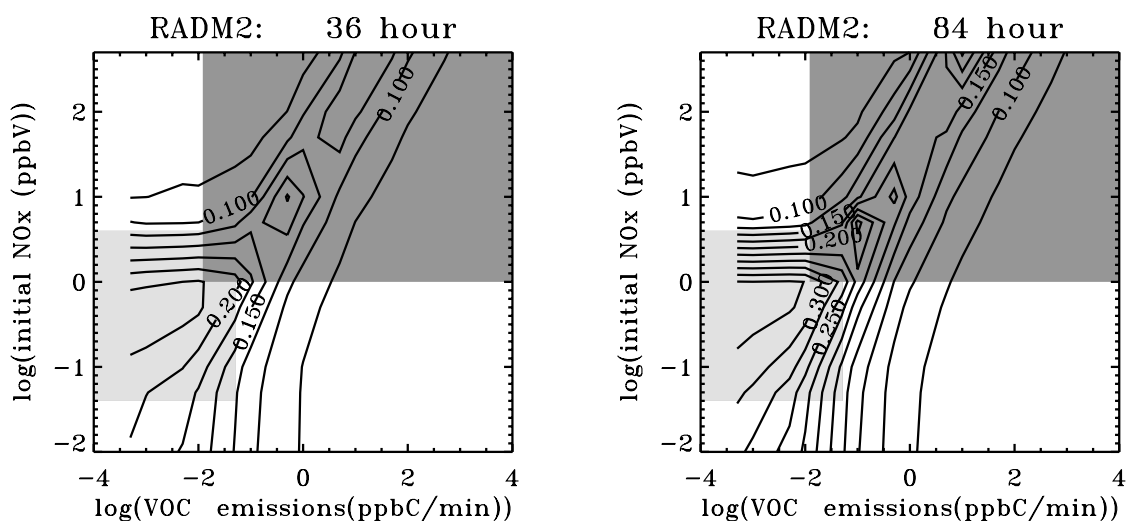


Figure 1.8: Deviation between total carbon put into the RADM2 MCH and the amount of total carbon left in the mechanism at hour 36 and 84. The plots are based on 150 zero-dimensional box model calculations as described in Tables 1.1 and 1.3. Contour levels [(exact VOC into the RADM2 MCH – VOC in the RADM2 MCH at a given time)/exact VOC into the RADM2 MCH] 0.025 , 0.050 , 0.075 , 0.100 , 0.125 , 0.150 , 0.175 , 0.200 , 0.225 , 0.250 , 0.275 , 0.300 and 0.325 . VOC represents anthropogenic non-methane VOC. The light gray indicates the range of NO_x and VOC emissions observed in rural areas[101]. The dark gray indicates the range of NO_x and VOC emissions observed in urban areas[101].

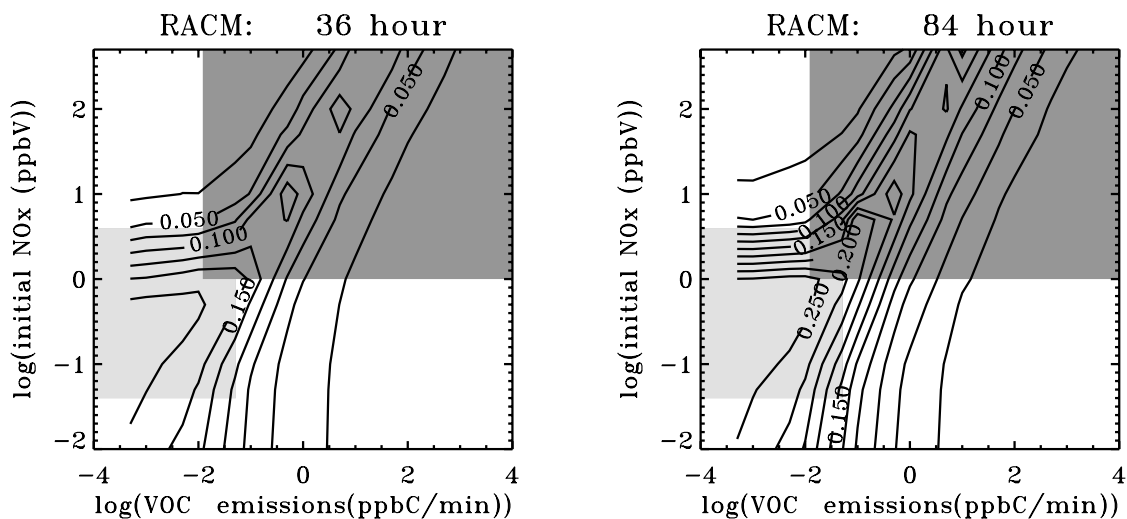


Figure 1.9: Deviation between total carbon put into the RACM MCH and the amount of total carbon left in the mechanism at hour 36 and 84. The plots are based on 150 zero-dimensional box model calculations as described in Tables 1.1 and 1.3. Contour levels $[(\text{exact VOC into the RACM MCH} - \text{VOC in the RACM MCH at a given time}) / \text{exact VOC into the RACM MCH}]$ 0.025, 0.050, 0.075, 0.100, 0.125, 0.150, 0.175, 0.200, 0.225 and 0.250. VOC represents anthropogenic non-methane VOC. The light gray indicates the range of NO_x and VOC emissions observed in rural areas[101]. The dark gray indicates the range of NO_x and VOC emissions observed in urban areas[101].

RACM MCHs. Hence, for the EMEP MCH carbon is gained during the VOC implementation and lost by running the mechanism. These two oppositely directed effects more or less neutralize each other.

The general trend for all the runs with respect to increasing order of carbon conservatism is therefore

- due to the mechanism: $\text{RADM2} < \text{RACM} < \text{EMEP}$,
- due to implementation of VOC emissions: $\text{EMEP} < \text{RADM2} < \text{RACM}$, and
- both points together: $\text{RADM2} < \text{RACM} < \text{EMEP}$.

Furthermore, both an increase of NO_x and VOC influences the carbon conservatism of the mechanisms, since we do not observe a linear trend in either the direction of the abscissa or the ordinate.

Discussion of the Carbon Loss from Specific Reactions

In Figures 1.10 - 1.15, plots of the Rural and Urban case simulations of the most important non-conservative reactions are shown. A general trend in Figures 1.4 - 1.9 is that in the rural areas the carbon conservatism is less pronounced than in the urban areas. However, in the rural areas, the amount of VOC is much less than in the urban areas, hence the Urban case loses much more carbon than the Rural case simulation (see Figure 1.10 together with Figure 1.11, Figure 1.12 together with 1.13

and Figure 1.14 together with 1.15). But the denominator has a much higher value in the urban areas than in the rural areas in Figures 1.4-1.9.

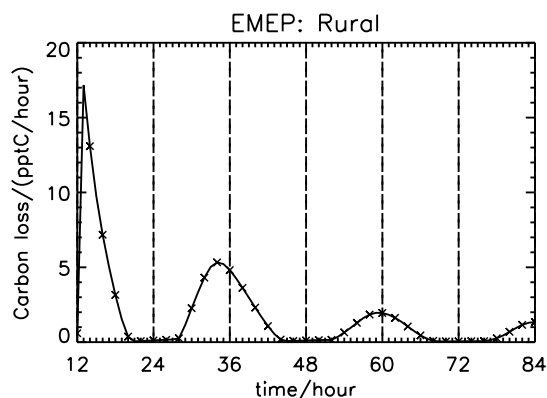


Figure 1.10: Loss of carbon for the Rural case simulation. The simulations are started at noon with output every 15 min.

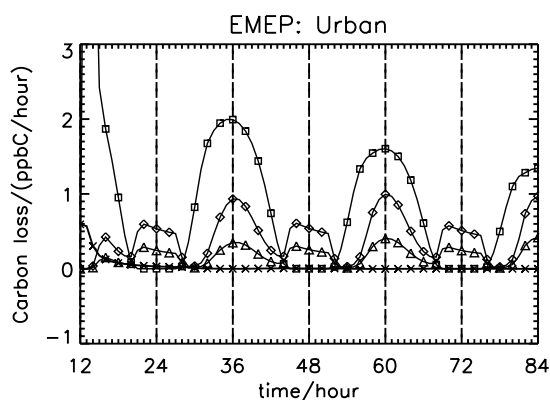


Figure 1.11: Loss of carbon for the Urban case simulation. The simulations are started at noon with output every 15 min. Total loss - (R74 + R75 + R77) (\times), loss due to R74 (\square), R75 (\triangle) and R77 (\diamond). See Table A.4 for a description of R???.

Due to the different ways in which the three mechanisms design their surrogate species the number of non-carbon conservative reactions is drastically higher for the RADM2 (82 reactions) and RACM MCHs (145 reactions) than the EMEP MCH (13 reactions). The dominant loss in the EMEP MCH stems from reaction R74: $\text{CH}_3\text{COO}_2 + \text{NO} \rightarrow \text{NO}_2 + \text{CH}_3$, see Figure 1.11. For a simulation with VOC emission, we see that this reaction initially adds a lot of carbon to the mechanism. The two other EMEP reactions which have a reasonable influence on the mechanism's total carbon are R75: $\text{CH}_3\text{O}_2 + \text{CH}_3\text{COO}_2 \rightarrow \text{CH}_3\text{O} + \text{CH}_3$ and R77: $2 \text{CH}_3\text{OO}_2 \rightarrow 2 \text{CH}_3$. Owing to the fact that all the organic reactants in these three reactions do not appear initially, while NO does, the carbon loss due to R74 is higher than the carbon loss due to the two other reactions. Additionally we observe that the carbon loss follows the diurnal cycle of NO.

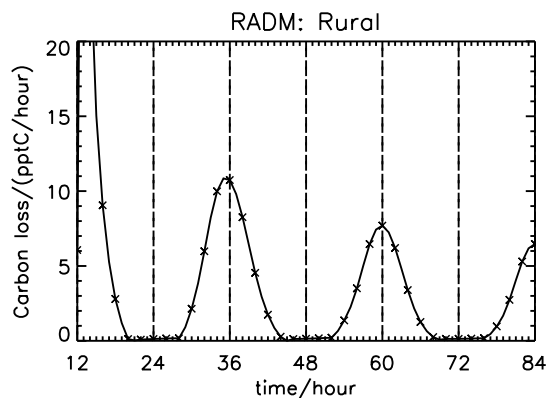


Figure 1.12: Loss of carbon for the Rural case simulation. The simulations are started at noon with output every 15 min.

In addition to a plot of the total carbon loss for the Urban case for the RADM2 and RACM MCHs (Figures 1.13A and 1.15A) we have also plotted the loss from their most significant reaction groups and reactions in these groups. Note that only reaction groups with a total loss over 1 ppbC/hour are plotted.

The overall picture for the RADM2 and RACM MCHs is that many of the same reactions in the two mechanisms appear to be the important carbon loss reactions. Comparing Figures 1.13B and 1.15B, the same trends/sizes of the curves are seen for the different loss reactions, but the gain reaction $\text{OP2} + \text{HO} \rightarrow$ adds more carbon in the RACM MCH than the RADM2 MCH. This reaction gives rise to more carbon in the RACM MCH by a factor 1.4 compared with the RADM2 MCH. Furthermore, the differences between the losses/gains shown in Figures 1.13 and 1.15 can be explained from the fact that the RACM MCH produces more HO_2 and HO than the RADM2 MCH and less NO_3 .

Concentration Levels Simulated by the EMEP, RADM2 and RACM MCHs

This comparison of the three mechanisms is primarily related to how they predict the concentration levels of ozone. Therefore, on the basis of the discussion in *Section 1.1* we will only focus on the O_3 , NO, NO_2 , HO, HO_2 and RO_2 species.

Ozone: Isopleths

Due to the interest in ozone in relation to air pollution problems (see *Introduction*) we have plotted a midnight and noon time isopleths of ozone for the EMEP, RADM2 and RACM MCHs based on the simulations described in *Section 1.2.2*, see Figures 1.16 and 1.17⁸. For all three mechanisms, when the concentrations of initial VOC < 10 ppbC (0.01 ppbC/min)₁₇⁹, the ozone concentration increases as initial NO_x

⁸Note, that even though we have used the definition from Graedel[92]/Berge[101] to define typical concentration/emission levels of NO_x s and VOC in urban areas, we find in the upper right corner of the isopleths, Figures 1.16 and 1.17, unrealistically high ozone concentrations are achieved due to the simplicity of the model in use.

⁹The (XXXX)₁₇ refers to the results plotted in Figure 1.17.

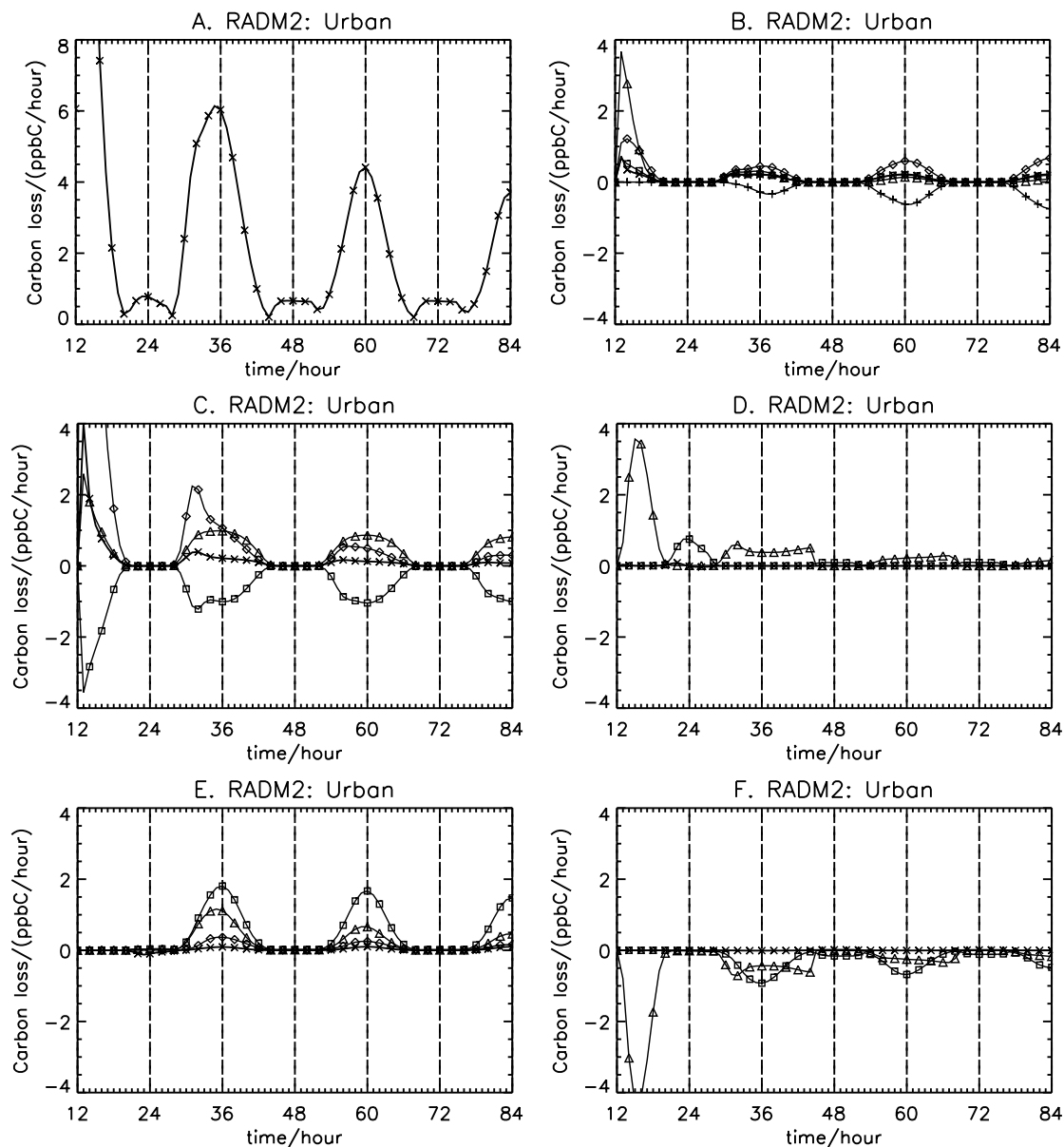


Figure 1.13: Loss of carbon for the Urban case simulation. The simulations are started at noon with output every 15 min. **A:** Total loss. **B:** Loss due to (HO + organic compound reactions) – (R53 + R60 + R61 + R64 + R70) (×), R53 (□), R60 + R61 (△), R64 (◇) and R70 (+). **C:** Loss due to (NO + organic peroxy radical reactions) – (R80 + R86 + R88 + R89) (×), R80 (□), R86 (△) and R88 + R89 (◇). **D:** Loss due to (NO₃ + organic compound reactions) – (R94 + R98) (×), R94 (□) and R98 (△). **E:** Loss due to (HO₂ + organic peroxy radical reactions) – (R109 + R110 + R111 + R117 + R118 + R119) (×), R109 + R110 + R111 (□), R117 + R118 (△) and R119 (◇). **F:** Loss due to (operator reactions) – R149 + R154 (×), R149 (□) and R154 (△). See Table A.6 for a description of R???.

increases until ≈ 4 ppbV (1.0 ppbV)₁₇ then the ozone concentration drops rapidly. In this region the ozone concentration is almost insensitive to the VOC chemistry. For low NO_x, i.e. < 2 ppbV (0.3 ppbV)₁₇, we observe that the concentration of ozone is almost constant as the concentration of initial VOC increases up to 100 ppbC (0.01 ppbC/min)₁₇ then the ozone concentration drops. For all the isopleths,

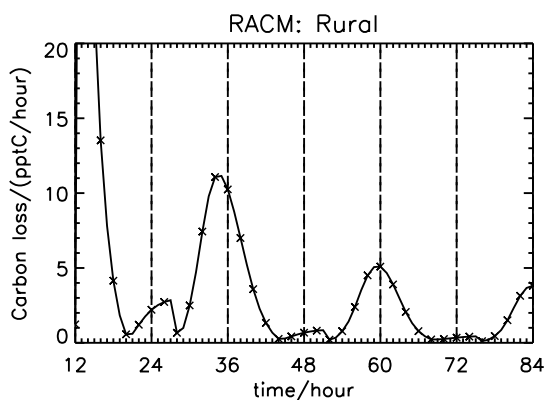


Figure 1.14: Loss of carbon for the Rural case simulation. The simulations are started at noon with output every 15 min.

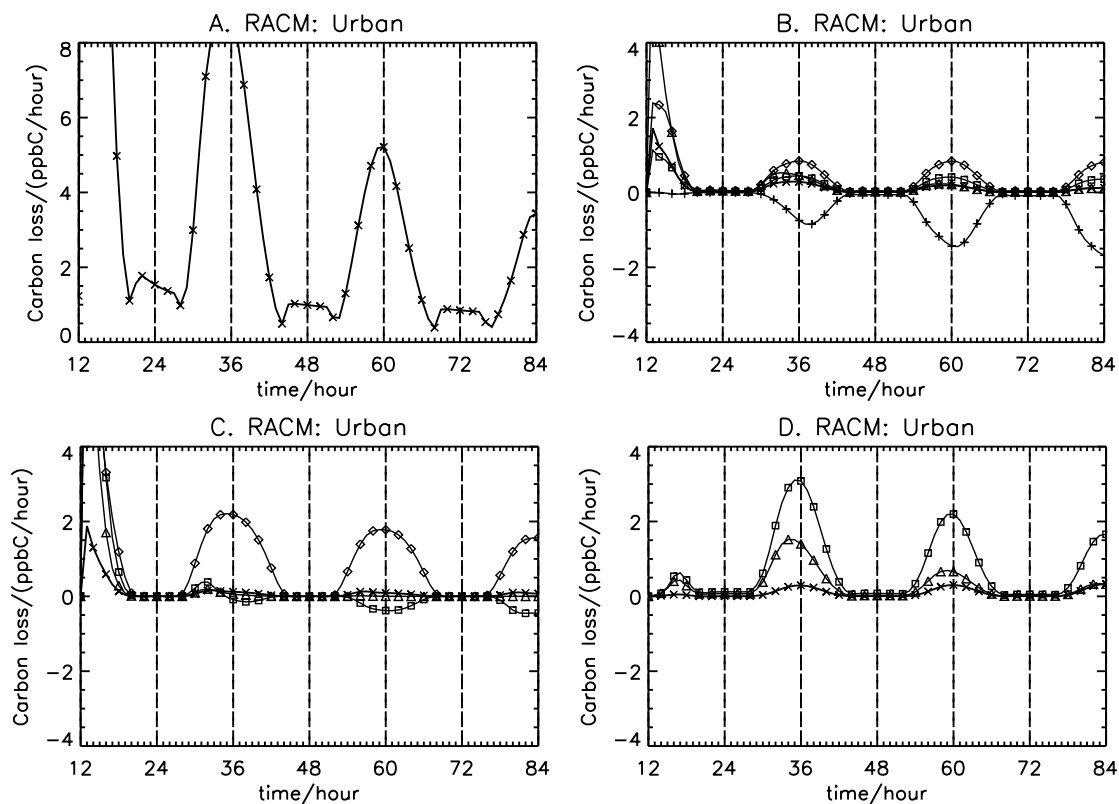


Figure 1.15: Loss of carbon for the Urban case simulation. The simulations are started at noon with output every 15 min. **A:** Total loss. **B:** Loss due to (HO + organic compounds) – (R63 + R73 + R74 + R77 + R86) (\times), R63 (\square), R73 + R74 (\triangle), R77 (\diamond) and R86 ($+$). **C:** Loss due to (NO + organic peroxy radicals) – (R132 + R133 + R134 + R135 + R143 + R145 + R146) (\times), R132 + R133 + R134 + R135 (\square), R143 (\triangle) and R145 + R146 (\diamond). **D:** Loss due to (HO₂ + organic peroxy radicals) – (R152 + R153 + R154 + R161 + R162) (\times), R152 + R153 + R154 (\square) and R161 + R162 (\triangle). See Table A.8 for a description of R???.

the “ridge line” lies almost in the middle of the rural and urban areas (indicated by the light and dark gray areas in the figures). Both Figures 1.16 and 1.17 show that

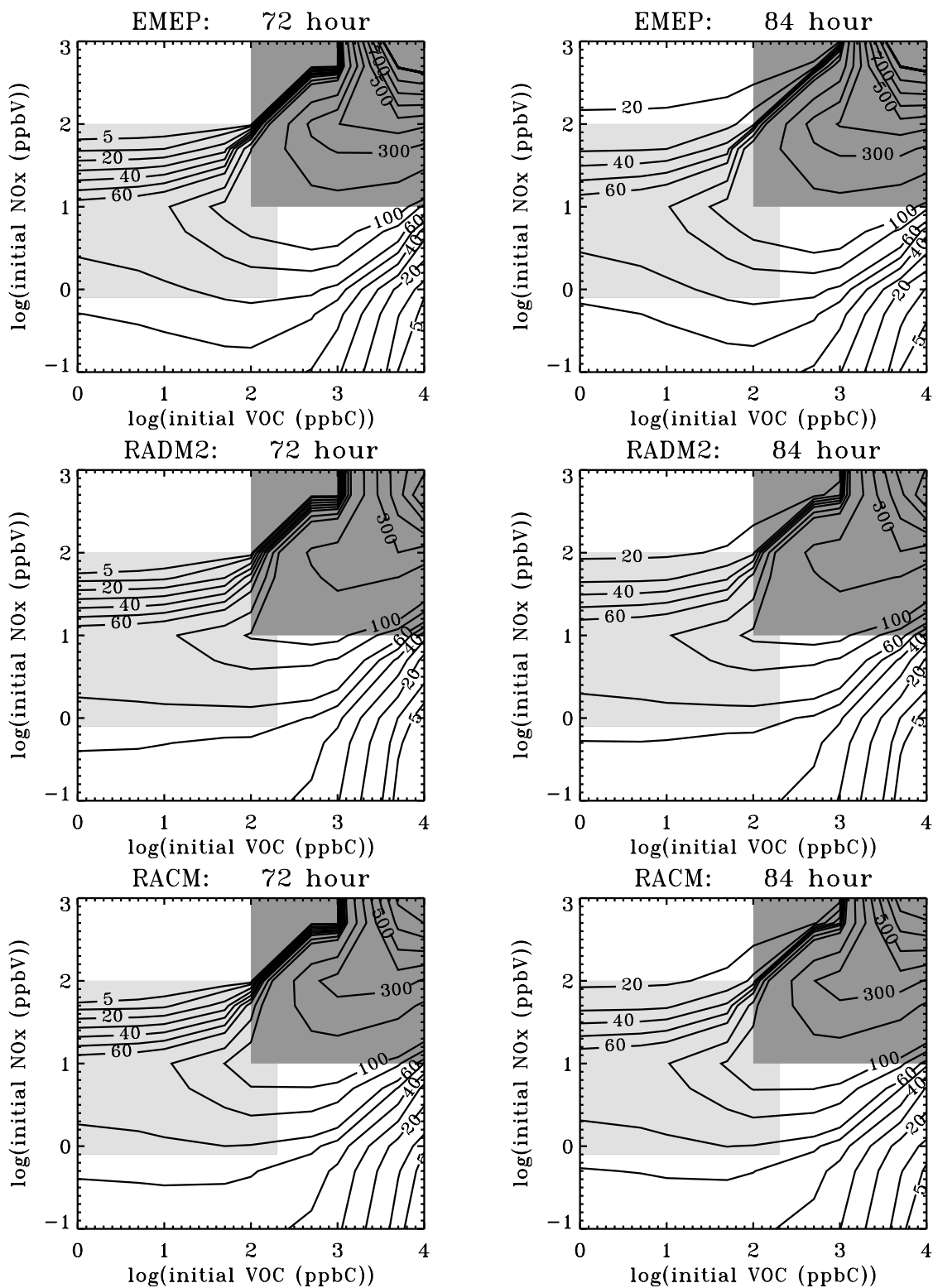


Figure 1.16: Isopleths of the O₃ concentration (in ppbV) obtained from the EMEP, RADM2 and RACM MCHs at hour 72 (nighttime) and 84 (daytime). The plots are based on 81 zero-dimensional box model calculations as described in Tables 1.1 and 1.2. Contour levels are 5, 10, 20, 30, 40, 50, 60, 80, 100, 200, 300, 400, 500, 600, 700 and 800. VOC represents anthropogenic non-methane VOC. For a definition of the light and dark gray areas, see the figure caption for Figure 1.4.

the formation of ozone in relation to NO_x and VOC is highly nonlinear.

As seen in *Section 1.1.1*, the basic photochemical cycle of NO_2 , NO and O_3 does not lead to any production of ozone. Production of ozone can only occur if reactions other than those in the photochemical cycle can convert NO into NO_2 . In this respect hydroperoxy radicals, reaction 1.19, and organic peroxy radicals, reaction 1.84a, convert NO into NO_2 . Formation of hydroperoxy radicals and peroxy radicals require hydroxy radicals, reactions 1.8 and 1.83, which means sinks of hydroperoxy, peroxy and hydroxy radicals, reactions 1.11, 1.23, 1.84b and 1.84d, prevent ozone formation. Therefore, the availability of HO_2 , RO_2 and especially HO and its reactions with CO and hydrocarbons are important. The formation of ozone is highly nonlinear, since NO_x s and VOC acts both as sinks and sources of these radicals. The nonlinearity of ozone is discussed by Lin et al.[102].

Isopleths of ozone can be split into NO_x -saturated, NO_x -sensitive and VOC-sensitive regimes. These regimes have been defined in different ways. Based on Ref. [103] we define them as follows:

1. the VOC-sensitive regime refers to situations where a percent change in anthropogenic VOC results in a significantly larger change in the ozone concentration compared with the same percent change in NO_x ,
2. the NO_x -sensitive regime where a percent change in NO_x results in a significantly larger change in the ozone concentration compared with the same percent change in anthropogenic VOC, and
3. the NO_x -saturated regime where an increase in the NO_x concentration will result in lower ozone concentration.

In Figures 1.16 and 1.17 the NO_x -saturated regime lies above the “ridge line” of the isopleths.

We observe not surprisingly that the rural area in Figures 1.16 and 1.17 lies within the NO_x -sensitive regime. The situation is a bit more complicated for the urban area. For the simulations without emissions the “ridge line” splits the isopleths in a VOC-sensitive regime which is equal to the NO_x -saturated regime, and a NO_x -sensitive regime which is below the “ridge line”. For the simulations with emissions we also have a VOC-sensitive regime below the “ridge line” when the emissions from VOC are high. In general, we obtain very similar behavior of the isopleths for the three mechanisms.

Ozone: Scatter Plots

To illustrate further the differences between the three mechanisms, scatter plots for the ozone concentration between the RACM and EMEP MCHs are presented in Figures 1.18 and 1.20 and between the RACM and RADM2 MCHs in Figures 1.19 and 1.21.

These figures show that the EMEP MCH gives more ozone than the RACM MCH and the RADM2 MCH gives less ozone than the RACM MCH. In particular

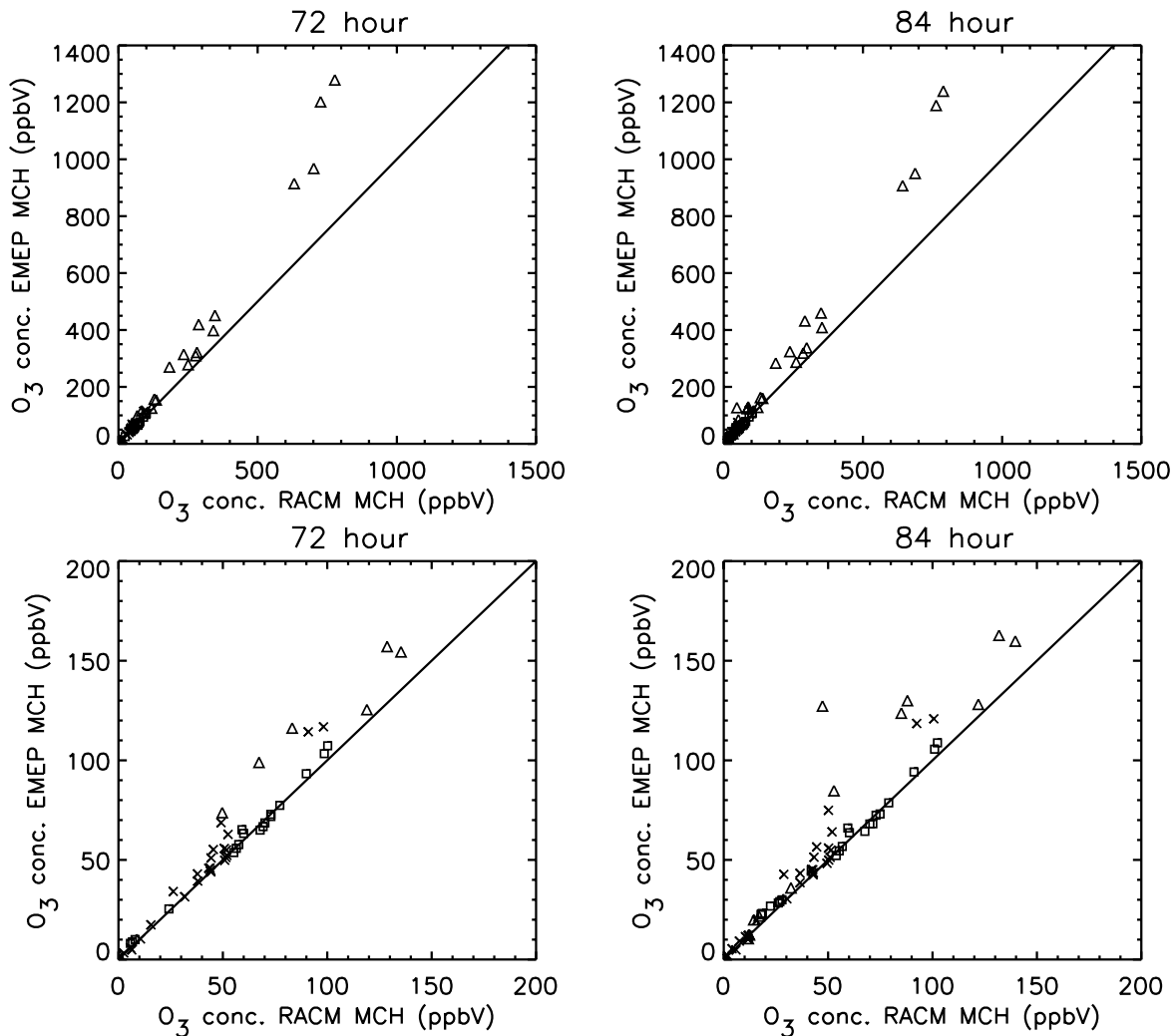


Figure 1.18: Scatter plots for the ozone concentration between the RACM and EMEP MCHs for the 81 zero-dimensional box model simulations as described in Table 1.1 and 1.2 at hour 72 (nighttime) and 84 (daytime). \square : rural, \triangle : urban and \times : neither rural nor urban. The definition of urban and rural is according to the light and dark gray areas described in the caption for Figure 1.4. Note that lower plots are zoom-ins of the upper plots.

the urban case simulations predict different ozone concentration for the mechanisms. This information is also presented in Table 1.5 where positive biases are obtained for the EMEP MCH relative to the RACM MCH and negative biases are obtained for the RADM2 MCH relative to the RACM MCH. This is also seen in Table 1.6 where the average values of the mechanisms in the urban, rural and neither urban nor rural areas are shown.

The scatter plots and tables also show that the differences between the mechanisms in the rural areas are very small. For the urban areas (see Figures 1.16-1.17) two points should be noted:

1. very large differences between the mechanisms are observed in the upper and right regions of the urban area, in the cleaner urban region (lower left corner

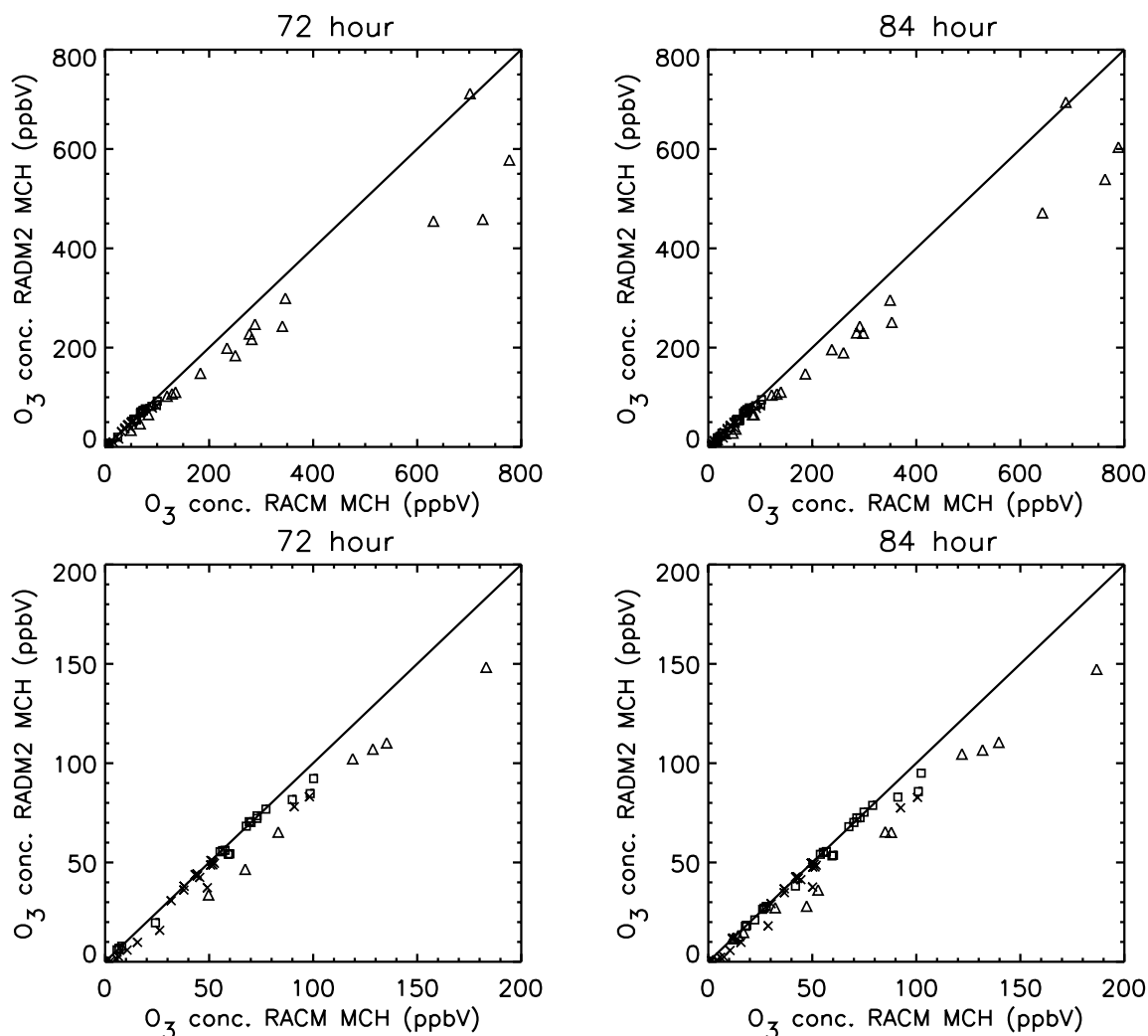


Figure 1.19: Scatter plots for the ozone concentration between the RACM and RADM2 MCHs for the 81 zero-dimensional box model simulations as described in Table 1.1 and 1.2 at hour 72 (nighttime) and 84 (daytime). \square : rural, \triangle : urban and \times : neither rural nor urban. The definition of urban and rural is according to the light and dark gray areas described in the caption for Figure 1.4. Note that lower plots are zoom-ins of the upper plots.

of the urban area) the differences are smaller, and

2. in the urban area the differences between the mechanisms are more pronounced due to the different descriptions of the organic chemistry.

Finally, we have calculated the root mean square error of the EMEP and RADM2 MCHs relative to the RACM MCH (Table 1.7), and the weighted root mean square error of the EMEP and RADM2 MCHs relative to that of the RACM MCH (Table 1.8). The RACM MCH has been used as a reference because results in Tables 1.5 and 1.6 indicate that the RACM MCH in general gives concentrations that are in between the results of the EMEP and RADM2 MCHs. These tables indicate that the ozone concentrations in the urban area obtained by the RADM2 MCH are closer to the results given by the RACM MCH than the results obtained by the EMEP MCH. The opposite holds for rural areas. These two tables indicate strongly that the similarity between the mechanisms is large in the rural area and limited in the

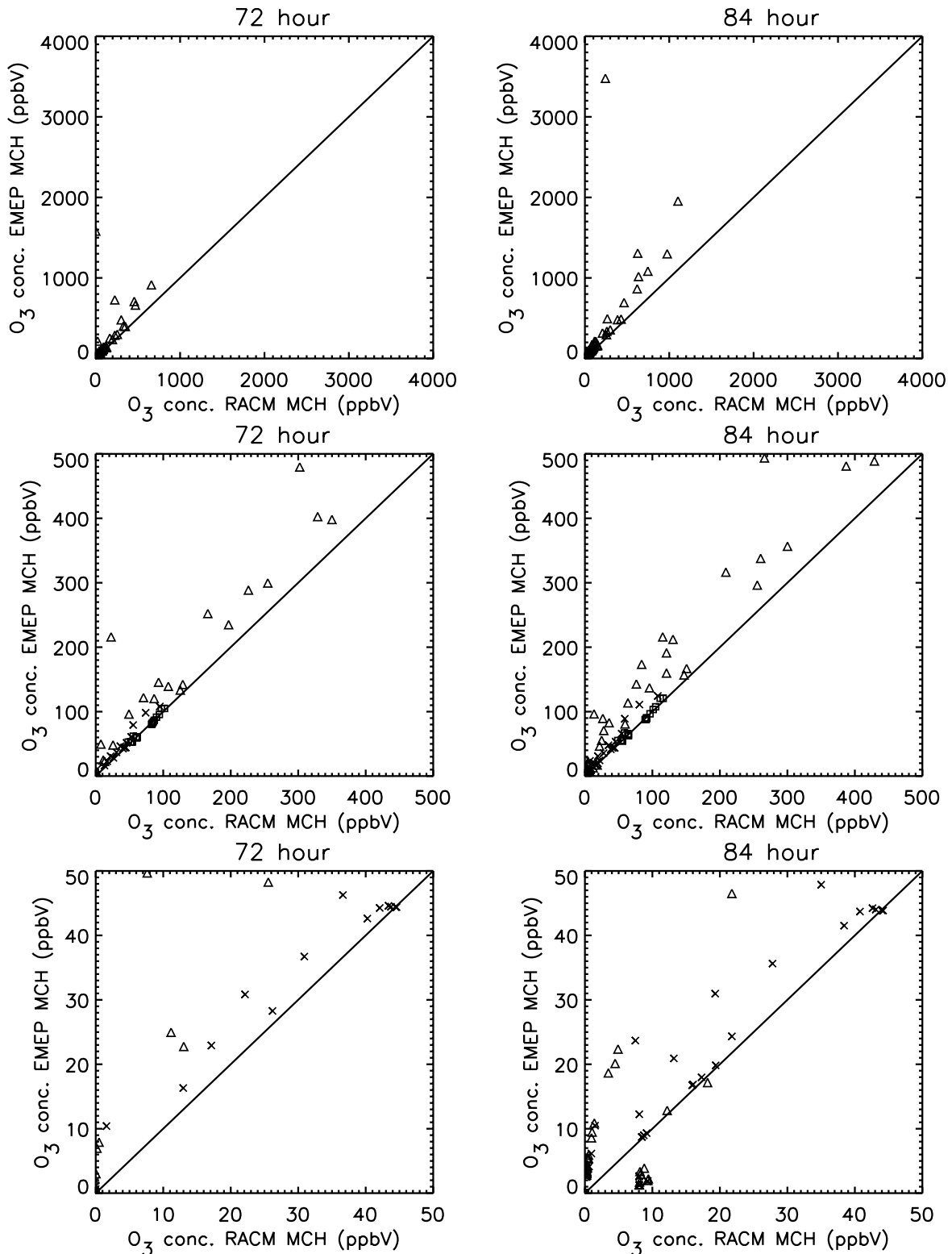


Figure 1.20: Scatter plots for the ozone concentration between the RACM and EMEP MCHs for the 150 zero-dimensional box model simulations as described in Table 1.1 and 1.3 at hour 72 (nighttime) and 84 (daytime). □: rural, △: urban and ×: neither rural nor urban. The definition of urban and rural is according to the light and dark gray areas described in the caption for Figure 1.7. Note that lower plots are zoom-ins of the upper plots.

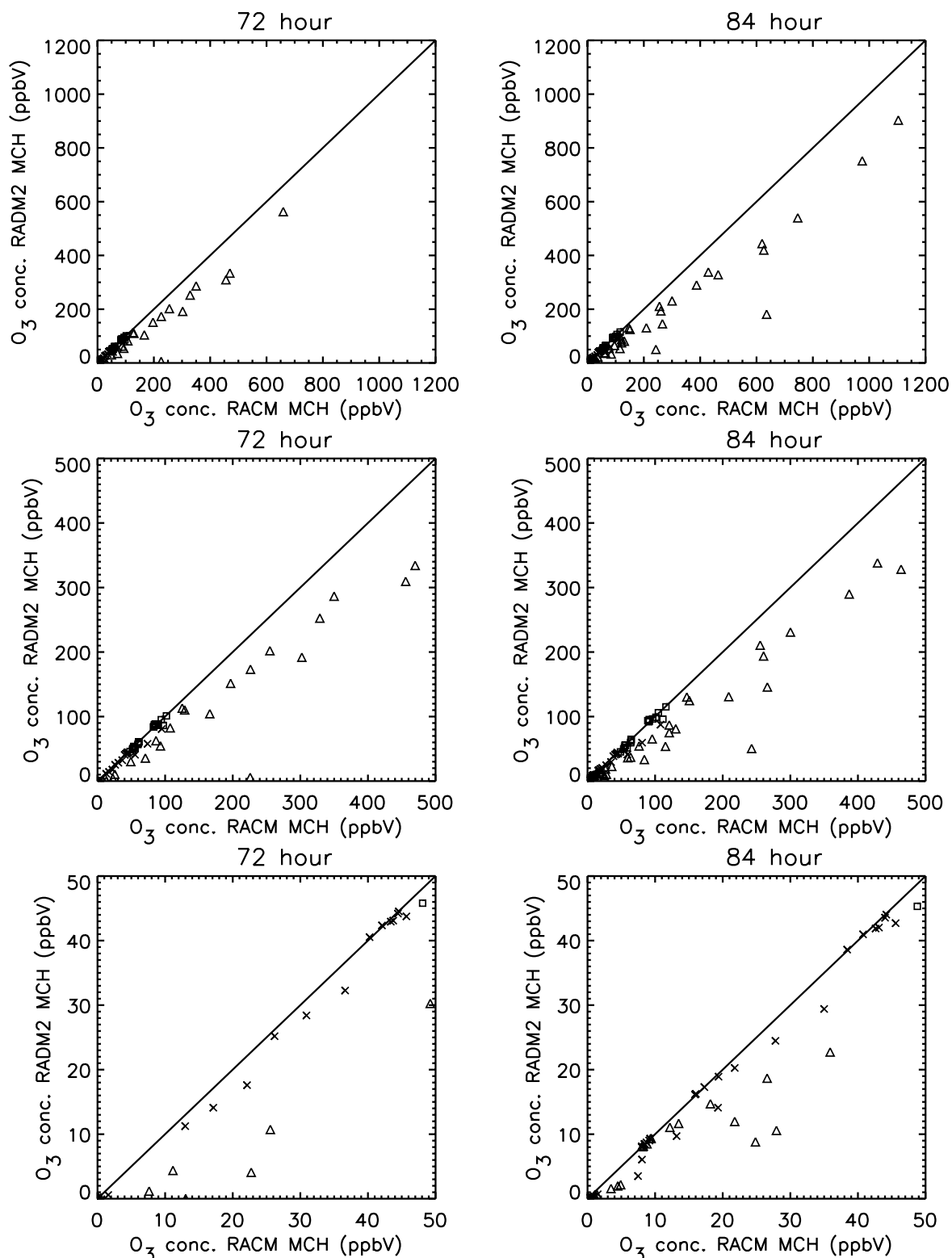


Figure 1.21: Scatter plots for the ozone concentration between the RACM and RADM2 MCHs for the 150 zero-dimensional box model simulations as described in Table 1.1 and 1.3 at hour 72 (nighttime) and 84 (daytime). \square : rural, \triangle : urban and \times : neither rural nor urban. The definition of urban and rural is according to the light and dark gray areas described in the caption for Figure 1.7. Note that lower plots are zoom-ins of the upper plots.

<i>Hour 72</i>						
	EMEP MCH			RADM2 MCH		
	urban	rural	rest	urban	rural	rest
O ₃ (ppbV)	89.72	1.032	3.487	-48.83	-2.100	-2.656
NO (ppbV)	-1.136	-1.547	4.691	7.811	0.1760	0.08300
NO ₂ (ppbV)	3.785	1.324	-4.567	-1.746	0.07406	-0.02643
HO (10 ⁻⁵ pptV)	-36.39	-4.907	-4.660	-257.7	-90.93	-14.74
HO ₂ (pptV)	2.252	0.3210	0.5359	-4.049	-0.3493	-0.5184
RO ₂ (pptV)	26.34	1.331	1.914	25.20	2.211	0.2451
<i>Hour 84</i>						
	EMEP MCH			RADM2 MCH		
	urban	rural	rest	urban	rural	rest
O ₃ (ppbV)	90.46	1.728	3.961	-47.49	-2.167	-2.837
NO (ppbV)	-1.399	-1.037	4.457	7.152	0.2048	0.08576
NO ₂ (ppbV)	5.885	0.9324	-4.342	-0.1739	0.0463	-0.002767
HO (10 ⁻³ pptV)	-3.700	-10.67	-2.932	-36.46	-15.66	-7.322
HO ₂ (pptV)	-1.155	0.2890	-3.009	-13.69	-1.261	-8.982
RO ₂ (pptV)	42.74	1.637	14.70	58.83	4.169	37.62

Table 1.5: Biases of the EMEP MCH relative to the RACM MCH and the RADM2 MCH relative to the RACM MCH for the 81 simulations without emissions in the urban, rural and neither rural nor urban areas. $bias = N^{-1} \sum_i^N (C_x^i - C_{RACM}^i)$, where N is the number of cases in the three areas, and C_x^i is the concentration of mechanism x of case i .

urban area (due to point 1 and 2 above). The differences between the mechanisms will be explained below.

Ozone: the Rural and Urban Cases

In order to explain in more detail the differences between the mechanisms we have in Figure 1.22 plotted the ozone concentration as a function of time for the selected Rural and Urban cases.

For the Rural case after an increase from 50 ppbV to 57-58 ppbV during the first day and night, the ozone concentration decreases to 52-54 ppbV at hour 84. In contrast to the general trend of the ozone isopleths we find that in the Rural case the EMEP MCH gives less ozone than the RADM2 and RACM MCHs. However these results are in agreement with the LAND case in Poppe et al. and Kuhn et al.[38]. For the Rural case the three mechanisms only differ by maximum 2 ppbV at hour 84.

In the Urban case the ozone concentration from hour 12 to 24 increase rapidly from 50 ppbV to 207.9 ppbV, 187.3 ppbV and 132.2 ppbV for the EMEP, RACM and RADM2 MCHs, respectively, followed by a much more moderate increase of up to 286.9 ppbV, 259.9 ppbV and 189.8 for the EMEP, RACM and RADM2 MCHs,

<i>Hour 72</i>									
	RACM MCH			EMEP MCH			RADM2 MCH		
	urban	rural	rest	urban	rural	rest	urban	rural	rest
O ₃ (ppbV)	226.9	47.98	25.77	316.6	49.01	26.58	178.1	45.88	24.40
NO (ppbV)	97.43	5.709	3.694	96.29	4.162	2.693	105.2	5.885	3.808
NO ₂ (ppbV)	69.32	17.17	11.18	73.10	18.50	11.97	67.57	17.25	11.16
HO (10 ⁻⁵ pptV)	291.4	104.3	62.37	255.0	99.43	56.88	33.75	13.41	7.765
HO ₂ (10 ⁻² pptV)	551.5	45.10	26.69	776.7	77.20	44.78	146.6	10.17	6.000
RO ₂ (pptV)	40.74	1.836	1.107	67.078	3.167	1.874	65.93	4.047	2.428

<i>Hour 84</i>									
	RACM MCH			EMEP MCH			RADM2 MCH		
	urban	rural	rest	urban	rural	rest	urban	rural	rest
O ₃ (ppbV)	234.48	55.24	35.80	324.9	56.97	36.94	187.0	53.08	34.39
NO (ppbV)	102.6	12.44	8.049	101.2	11.40	7.378	109.8	12.65	8.182
NO ₂ (ppbV)	61.81	10.75	6.957	67.70	11.68	7.561	61.64	10.80	6.987
HO (10 ⁻³ pptV)	76.98	161.2	85.50	73.28	150.5	79.78	40.52	145.5	75.80
HO ₂ (pptV)	41.41	15.72	8.070	40.26	16.01	8.275	27.72	14.46	7.305
RO ₂ (pptV)	105.5	9.032	5.033	148.3	10.67	6.107	164.4	13.20	7.713

Table 1.6: The average concentrations obtained in the EMEP, RADM2 and RACM MCHs for the 81 simulations without emissions in the urban, rural and neither rural nor urban areas.

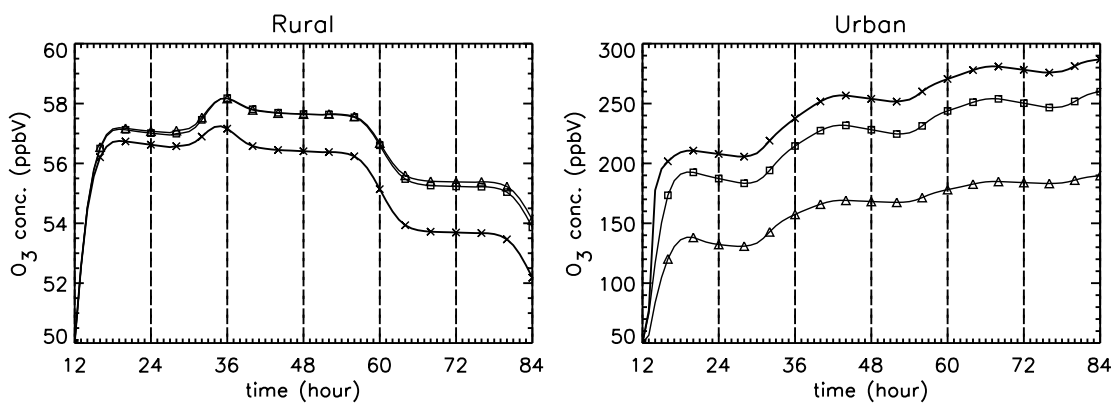


Figure 1.22: The ozone concentration from the Rural and Urban case simulations described in Section 1.2.2. The simulations are started at noon with output every 15 min. ×: EMEP MCH. □: RACM MCH. △: RADM2 MCH.

respectively. This Urban case corresponds to a SS, FS, HA and S1E ozone episode from Los Angeles, see Table 0.3.

Contrary to the Rural case where reasonable agreement between the three mechanisms concentrations for NO, NO₂, HO, HO₂ and RO₂ are observed, this is not observed for the Urban case, see Figures 1.23-1.27. We found that the increase

<i>Hour 72</i>						
	EMEP MCH			RADM2 MCH		
	urban	rural	rest	urban	rural	rest
O ₃ (ppbV)	166.0	2.790	7.046	85.21	4.334	4.817
NO (ppbV)	17.46	3.657	14.31	21.00	0.7104	0.2620
NO ₂ (ppbV)	19.05	3.616	14.14	5.295	0.8081	0.05994
HO (10 ⁻⁴ ppptV)	11.40	4.029	0.7293	42.79	14.12	2.146
HO ₂ (pptV)	3.305	0.4232	1.129	5.950	0.5176	0.7409
RO ₂ (pptV)	45.02	1.922	4.649	39.32	3.590	6.507
<i>Hour 84</i>						
	EMEP MCH			RADM2 MCH		
	urban	rural	rest	urban	rural	rest
O ₃ (ppbV)	155.8	3.432	8.145	76.36	4.515	5.217
NO (ppbV)	14.54	2.163	12.75	18.51	0.6358	0.2720
NO ₂ (ppbV)	23.34	2.016	12.55	1.883	0.2490	0.03484
HO (10 ⁻⁴ ppptV)	475.5	144.3	45.73	557.0	267.7	113.7
HO ₂ (pptV)	6.487	0.4213	6.003	58.43	2.423	12.67
RO ₂ (pptV)	64.12	3.222	22.16	85.38	8.758	50.59

Table 1.7: Root Mean Square Error (*RMSE*) of the EMEP MCH relative to the RACM MCH and the RADM2 MCH relative to the RACM MCH for the 81 simulations without emissions in the urban, rural and neither rural nor urban areas. $RMSE = \sqrt{N^{-1} \sum_i^N (C_x^i - C_{RACM}^i)^2}$, where N is the number of cases in the three areas, and C_x^i is the concentration of mechanism x of case i .

of the ozone concentration using the EMEP and RACM MCHs is almost identical from hour 24 to 84 while the RADM2 MCH forms approximately 18 ppbV less ozone in that period. Figures 1.26 and 1.27 show that in the start of the simulation the EMEP MCH predicts much higher levels of HO₂+RO₂ than the RACM MCH, and the RACM MCH predicts much higher levels of HO₂+RO₂ than the RADM2 MCH. From hour 24 to 84 the RADM2 MCH is the mechanism among the three that predicts the highest concentrations of RO₂. On the other hand, the concentrations of HO₂ are highest for the EMEP MCH during the entire simulation while the RADM2 MCH is the mechanism that predicts the smallest amount of HO₂. Moreover, if the concentration of HO₂ is added together with the concentration of RO₂, we find that the concentration levels of HO₂+RO₂ reflect reasonably well the trends of ozone formation for the three mechanisms. This is indicated by Tables 1.5-1.8 and Figures E.11, E.12, E.14 and E.15. These results illustrate the differences in photochemical activity and treatment of peroxy radical reactions in the three mechanisms.

In summary, we have in Figure 1.28 schematically illustrated the formation and losses of ozone for the three mechanisms in the Rural and Urban case. The figure shows the primarily ozone production coming from

<i>Hour 72</i>						
	EMEP MCH			RADM2 MCH		
	urban	rural	rest	urban	rural	rest
O ₃ (ppbV)	58.55	0.7383	2.014	28.96	1.250	1.308
NO (ppbV)	5.767	1.861	32.71	5.966	0.3059	0.4937
NO ₂ (ppbV)	7.845	1.431	13.35	1.885	0.2250	0.02614
HO (10 ⁻⁴ pptV)	4.026	1.315	0.1110	15.53	5.234	0.3357
HO ₂ (pptV)	1.077	0.08825	0.7267	1.936	0.1813	0.4537
RO ₂ (pptV)	15.42	0.7067	3.661	12.99	1.394	5.404

<i>Hour 84</i>						
	EMEP MCH			RADM2 MCH		
	urban	rural	rest	urban	rural	rest
O ₃ (ppbV)	53.31	0.7457	1.929	24.98	1.230	1.247
NO (ppbV)	5.421	0.9394	19.98	5.973	0.2205	0.3569
NO ₂ (ppbV)	9.492	0.8152	14.63	0.5360	0.07022	0.03564
HO (10 ⁻⁴ pptV)	153.4	40.80	8.089	187.0	65.62	20.37
HO ₂ (pptV)	1.227	0.1155	2.524	5.034	0.6167	5.243
RO ₂ (pptV)	18.82	1.221	20.67	25.33	3.322	43.73

Table 1.8: Weighted Root Mean Square Error (*WRMSE*) of the EMEP MCH relative to the RACM MCH and the RADM2 MCH relative to the RACM MCH for the 81 simulations without emissions in the urban, rural and neither rural nor urban areas. $WRMSE = \sqrt{N^{-1} \sum_i^N \frac{C_{RACM}^i}{\langle C_{RACM} \rangle} (C_x^i - C_{RACM}^i)^2}$, where N is the number of cases in the three areas, C_x^i is the concentration of mechanism x of case i , and $\langle C_{RACM} \rangle$ is the average value in the three areas obtained in the RACM MCH.

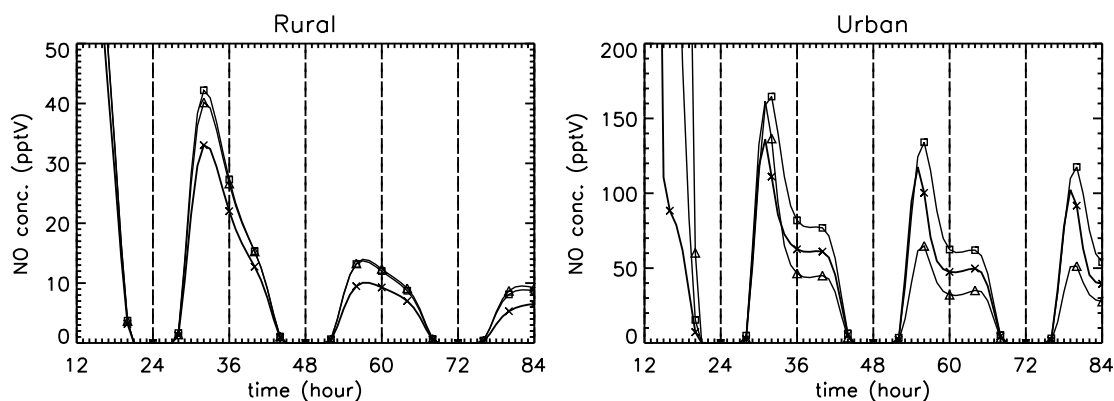


Figure 1.23: The NO concentration from the Rural and Urban case simulations described in Section 1.2.2. The simulations are started at noon with output every 15 min. ×: EMEP MCH. □: RACM MCH. △: RADM2 MCH.

- the NO₂ interconversion with NO,

and the different losses of ozone from

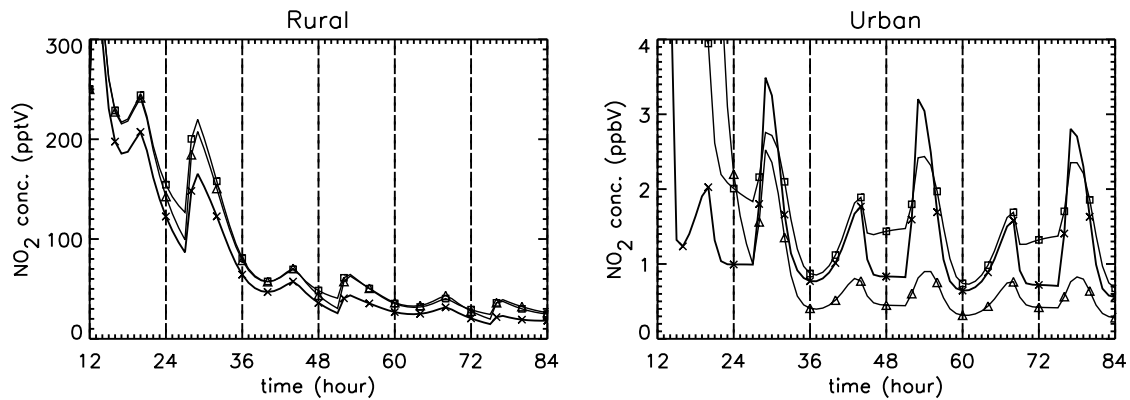


Figure 1.24: The NO₂ concentration from the Rural and Urban case simulations described in Section 1.2.2. The simulations are started at noon with output every 15 min. ×: EMEP MCH. □: RACM MCH. △: RADM2 MCH.

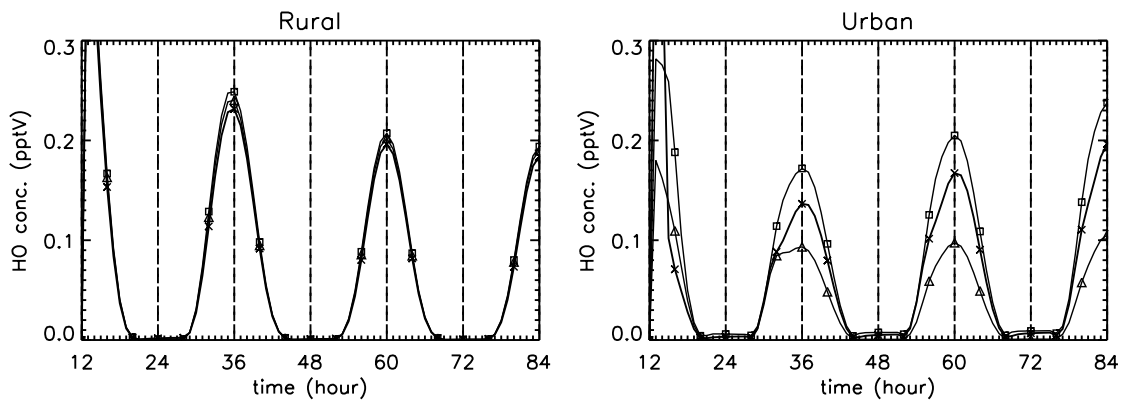


Figure 1.25: The HO concentration from the Rural and Urban case simulations described in Section 1.2.2. The simulations are started at noon with output every 15 min. ×: EMEP MCH. □: RACM MCH. △: RADM2 MCH.

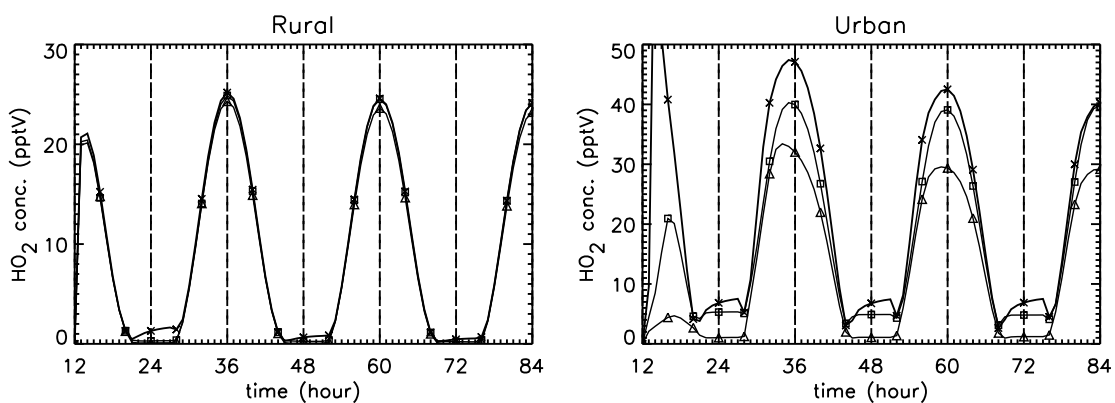


Figure 1.26: The HO₂ concentration from the Rural and Urban case simulations described in Section 1.2.2. The simulations are started at noon with output every 15 min. ×: EMEP MCH. □: RACM MCH. △: RADM2 MCH.

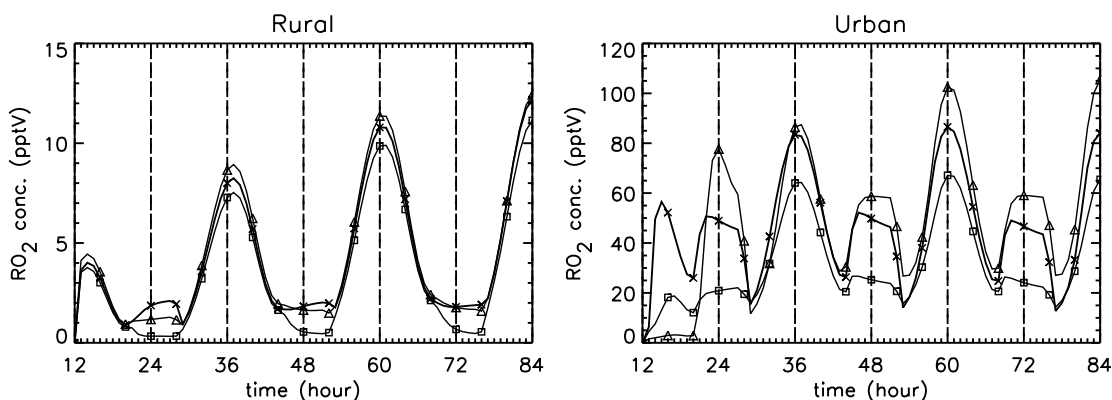


Figure 1.27: The RO_2 concentration from the Rural and Urban case simulations described in Section 1.2.2. The simulations are started at noon with output every 15 min. \times : EMEP MCH. \square : RACM MCH. \triangle : RADM2 MCH.

- its photolysis to $\text{O}(^1D)$ followed by a reaction with H_2O giving HO,
- its reaction with HO, HO_2 and peroxy radicals, and
- its reactions with hydrocarbons.

Therefore, the total production of ozone after hour 72, 81 and 84 can be calculated from this figure by taking the ozone production from the NO_2 interconversion with NO and subtracting the rest of the numbers in the figure from this number.

Figure 1.28 shows that all three mechanisms lose ozone in the Rural case both during the day- and nighttime. For the Urban case, ozone is only lost during the night. In general the dominant trends from the figure are in line with the discussion above.

NO, NO_2 , HO, HO_2 and RO_2

The resulting isopleths of ozone, Figures 1.16 and 1.17, show very similar behavior for the three mechanisms both for nighttime and daytime. The similar behavior is also observed for other atmospheric compounds such as NO, NO_2 , HO, HO_2 and RO_2 . Therefore, we have only plotted the isopleths and scatter plots for these compounds on the basis of the 81 simulations without emissions. These plots are presented in *Appendix E*. We will not outline in detail the specific NO_x and VOC sensitive regimes as it was done in the section describing the isopleths of ozone. Instead we will focus on some fundamental trends.

NO is produced primarily from photolysis of NO_2 , this is for example observed in Figure 1.23 where the concentration of NO follows a diurnal variation with the highest values in the morning when NO_2 starts to photolyse. During the nighttime this source of NO is removed and NO is rapidly lost due to its reactions with O_3 and NO_3 . In the NO_x saturated regime, see Figure E.1, high concentration levels of NO occur during the whole simulation because the change in NO is too small. In the non- NO_x saturated regime, the NO concentrations drop to very low concentrations

during the nighttime. The isopleths also show a sharp gradient corresponding to the “ridge line” in the isopleths of ozone. We find that the daytime NO concentration for the three mechanisms after the three day simulation in the urban area follows

- $\text{conc.}_{RACM} > \text{conc.}_{EMEP} > \text{conc.}_{RADM2}$

and in the rural area follows

- $\text{conc.}_{RADM2} \approx \text{conc.}_{RACM} > \text{conc.}_{EMEP}$.

Some similarities between the isopleths of NO and NO₂ are observed. In the NO_x saturated regime, Figures E.1 and E.4, the concentration is high during the whole simulation. In the non-NO_x saturated regime, a decrease of NO₂ appears going from (last) midnight to (last) noon. This is contrary to the time evolution of NO since the nighttime losses of NO produce NO₂. The general trend for the rural (night and day) and urban (night and day) is for NO₂

- $\text{conc.}_{RACM} > \text{conc.}_{EMEP} > \text{conc.}_{RADM2}$.

The last three atmospheric chemical compounds we have plotted are the odd hydrogen radicals[103]: HO, HO₂ and RO₂. The compound HO is needed in order to activate the chemistry of HO₂ and RO₂. Due to the photolysis of H₂O₂ and O₃ the concentration of HO shows very regular behavior. In the Rural case, the three mechanisms give almost identical concentrations of HO, see Figure 1.25. The reason could be that HO is formed from the same photolysis frequencies of H₂O₂ and O₃ and almost the same rate constants of inorganic HO-reactions in all three mechanisms. Approximately the same concentration levels are also observed for HO₂ and RO₂ in the Rural case. For the Urban case very different concentration levels are observed. We find that it is very difficult to pick out the reactions in the mechanisms that are responsible for these differences since this is a matter that is closely related to the lumped organic species. Furthermore, it is very surprising that RO₂ gives such similar results, because RO₂ in the three mechanisms consists of very different lumped species (Figure 1.27). Based on the model runs performed in this chapter and the description of the three mechanisms in the literature it is not possible to analyze in detail this matter further. We need to know in particular how the mechanisms are lumped together, i.e. the weighting factors.

For the isopleths of daytime HO, the “ridge line” is close to that of ozone’s isopleths due to the close relationship between ozone photolysis and HO formation. Such a pronounced relationship is not seen for HO₂ and RO₂. The general trend for HO and HO₂ rural (day) and urban (day) is

- $\text{conc.}_{RACM} > \text{conc.}_{EMEP} > \text{conc.}_{RADM2}$.

For HO₂ rural (night) and urban (night) and RO₂ rural (night and day) and urban (night and day)

- $\text{conc.}_{EMEP} > \text{conc.}_{RACM} > \text{conc.}_{RADM2}$.

1.3 Conclusion

We found that the atmospheric chemical mechanisms used in this thesis are not carbon conservative even though it is claimed in Ref. [38a] that the EMEP MCH should be. We find it strange, because if the EMEP MCH is carbon conservative, why are VOC emissions not implemented in a carbon preserving manner (see *B.2 Comment*). The carbon loss due to implementation of VOC emissions into the RACM MCH has almost been eliminated compared to the previous mechanism developed by Stockwell (RADM2 MCH), see *B.2 Comment*. The reverse is observed during the simulation of the mechanisms. A comparison of Figure 1.5, 1.12 and 1.13 with Figures 1.6, 1.14 and 1.15 shows that the carbon loss of the RADM2 and RACM MCHs is almost similar.

Even though the simulations indicate that the EMEP MCH is the most carbon conservative mechanism of the three, the results demonstrate that this is merely because carbon is gained when VOC is implemented into the EMEP MCH compared to the RACM MCH (compare Figure 1.4a to Figure 1.4b and Figure 1.6a to Figure 1.6b).

An investigation such as that performed above can be a topic of discussion. We have taken the mechanisms and used them on an “as is” basis. From that point of view, the developers of the three mechanisms could claim that the non-carbon conservative reactions in the mechanisms could be adjusted to carbon conservative reactions by chemical compounds of high atmospheric concentrations, such as H_2O , CO_2 and O_2 .

DACFOS (which uses the EMEP MCH) is used to forecast ozone over Europe, therefore we have a special interest in testing how the EMEP, RADM2 and RACM (the newest mechanisms among the three) MCHs simulate ozone. Due to the impact of NO , NO_2 , HO , HO_2 and RO_2 on ozone, this chapter has focussed on these five atmospheric compounds together with ozone. We found a close relationship between the predicted concentration levels of $\text{HO}_2 + \text{RO}_2$ and ozone for the three mechanisms. Even though the isopleths of ozone for the three mechanisms look similar, our statistical calculations and scatter plots show pronounced differences in the urban case. In general

- the EMEP MCH gives more ozone than the RACM MCH, and
- the RADM2 MCH gives less ozone than the RACM MCH.

We calculated biases (Table 1.5), average concentrations (Table 1.6), root mean square errors (Table 1.7) and weighted root mean square errors (Table 1.8) in order to understand the differences between the mechanisms. Figures E.1 and E.4 show a very sharp gradient in going from the non- NO_x saturated to the NO_x saturated regime. Therefore only the weighted root mean square error reflects the nature of the whole isopleths of NO and NO_2 .

Figure 1.22 (Urban case) shows that the ozone concentration predicted by the RACM MCH is closer to that of the EMEP MCH than that of the RADM2 MCH.

Tables 1.5-8 show that the ozone concentration from the RACM MCH runs lie closer to the results given by the RADM2 MCH than the EMEP MCH. This indicates that a single urban or rural scenario is not the best way to compare atmospheric chemical mechanisms. A proper way would be simulating an entire isopleth over a wide variety of NO_x s and VOC as done here.

A general problem in the modeling of environmental problems is to decide which chemical mechanism is the most reliable. Stockwell et al.[31, 32] compared the RADM2 and RACM MCH with indoor environmental chamber studies. Using these studies to evaluate atmospheric chemical mechanisms is also problematic since chamber walls can serve as sources and sinks for O_3 , NO_x , aldehydes, ketones and HO. Moreover, the effects of VOC on ozone depends on the environment where VOC react, and this influence on the tropospheric ozone concentration does not have to be the same as those measured in the laboratory. However, chamber experiments performed over several days using outdoor chambers, such as the European Photoreactor, are a better method for providing data, where the concentrations are determined by reactions with the same relative importance as in the real atmosphere. Unfortunately, the availability of experimental data of this type is very limited.

In conclusion, the RACM MCH is a revised version of the RADM2 MCH and the RACM MCH includes improved reaction schemes for the reactions involving organic peroxy radicals, oxygenated compounds, aromatic compounds and biogenically emitted compounds compared to that of the RADM2 MCH. Thus, the RACM MCH must be considered to be superior to the RADM2 MCH. On the other hand, based on the comparison performed in this chapter it is not possible to conclude if the RACM MCH describes the tropospheric chemistry better than the EMEP MCH. Nevertheless the RACM MCH has some advantages over the EMEP MCH:

- the RACM MCH is newer than the EMEP MCH, i.e. a more updated version of the reaction rates and chemical reaction scheme, and
- the EMEP MCH is constrained to be used only in the ABL[30] in a limited temperature interval,

even though the EMEP MCH is more carbon conservative than the RACM MCH. Hence, the trajectories calculated by DACFOS can enter the ABL from the free troposphere or come from cold geographic areas. On the other hand, our primary interest is to forecast surface ozone in the summer season. Therefore, in general the EMEP MCH can be applied to the cases we are interested in, but we have chosen the RACM MCH for the new MOON model due to its greater flexibility.

Chapter 2

Theoretical Treatment of Elementary Chemical Reactions

Atmospheric chemistry models are used to predict the effects of emissions on air quality[35] and these models require gas-phase chemical mechanisms to predict the concentrations of ozone and other photochemical air pollutants. The mechanism should include all important chemical reactions with their rate constants in order to make accurate predictions of air pollutants. Unfortunately this is not an easy task because the organic chemistry of the polluted atmosphere is extremely complicated. One recent mechanism[25, 26] requires 2400 chemical compounds and 7100 chemical reactions to describe the degradation of 120 emitted organic compounds (see also *Introduction, Chemical Mechanisms*). An important weakness of detailed gas-phase chemical mechanisms is that relatively few rate constants have been measured.

Many of the rate parameters or product yields for organic compounds that are emitted into the atmosphere are difficult to measure because many of these reactions have multiple channels with relatively low product yields[74]. Most of the rate parameters and product yields used in highly detailed atmospheric chemistry mechanisms are estimated from analogy with known reactions or through empirical structure - reactivity relationships. The uncertainty in rate parameters is usually greater for the more reactive organic compounds. Even for those reactions with measured rate parameters, the temperature dependence is not well characterized[28, 29]. This is important because the ambient temperature of the troposphere spans a range from near 300 K in the lower troposphere down to about 200 K near the tropopause[104]. Due to experimental obstacles rate parameters are most accurately known near 298 K[28, 29].

Some of the methods often used to calculate rate constant for unknown reactions are structural correlation methods[76, 105], rate constants versus the bond dissociation or the first vertical ionization potential[106], and correlation of the rate constants for NO_3 with those for the reactions of the HO radicals and $\text{O}(^3P)$ atoms[106]. The disadvantage of these methods is that they may have errors on the order of 10^2 to 10^4 .

For these reasons theoretical calculations that enable the estimation of rate

parameters have the possibility of improving atmospheric chemistry mechanisms. If a computational method at least could provide the relative magnitude of rate parameters for similar reactions, the method could be used to determine branching ratios and trends. Such information would be of interest for the further development of the chemical mechanisms.

The goal with this chapter is to describe the most commonly used methods to calculate bi-molecular elementary chemical rate constants when no exterior forces (e.g. electric or magnetic fields) are acting on the system. We emphasize the problems related to the use of these methods. We address the type of information about a given system that is needed in order for a theoretical model to estimate a rate constant. Above we stressed that it is difficult to measure rate constants at temperatures very different from 298 K. In contrast theoretical models do not have such problems if sufficient information about the system of interest is available.

The chapter is organized as follows:

- in *Section 2.1* a brief presentation of existing theoretical methods is given.

The application of the theoretical methods in this chapter is applied to how to calculate rate constants of atmospheric chemical reactions. One type of the method is in this context particularly useful: phase-space methods. Phase-space methods justify themselves through their applicability even to large molecular systems even though they are the least accurate of all the theoretical methods, see Table 2.1, because transition state informations is not needed.

In all of the methods described in *Section 2.1*, ab initio calculations of high quality are of fundamental importance. This is also described in

- *Section 2.1* where we present calculated rate constants for ozone formation and ozone's isotopic exchange reactions.

We have obtained the results using quasi-classical trajectories on different Potential Energy Surfaces (PESs). In phase-space methods potential energies for the reactants and products and the energy barrier or long-range potential (if the chemical reaction does not have an energy barrier) are required but yet not available for most of atmospheric organic compounds and chemical reactions. Therefore,

- in *Section 2.2* a general description of electronic structure theory, its usability and computational possibilities today will be presented,
 1. *Section 2.2.1* different ab initio calculations to calculate the above – mentioned potential energies are described, and
 2. in *Section 2.2.2* the results we have obtained for different molecules are presented.

In this chapter we introduce a new theoretical phase-space method[62] that can be used to calculate rate constants for chemical reactions. This new method is based on a method developed by Light and co-workers[107]. They have used the method on tri-atomic systems while we have expanded the method to arbitrary chemical reactions.

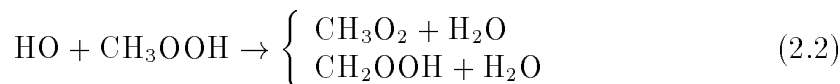
Dynamic Methods	Input Requirements	Output Information	Accuracy Greatest
Full dynamics: Quantum Quantum-Classical Classical	Full 3N-6 dimensional surface	State (rot-vib) resolved, angle resolved, cross sections, rates, differential cross sections	
Reaction path: Quantum-Classical Classical	Full 1 dimensional surface, $V_o(s)$ 3N-8 harmonics	State (rot-vib) resolved, cross sections, rates	
Statistical-Dynamical	Input Requirements	Output Information	Accuracy Smallest
Variation Transition- State Theory (VTST)	Full 1 dimensional surface, $V_o(s)$	Rates	
Statistical	Input Requirements	Output Information	Accuracy Smallest
Transition-State Theory (TST)	Saddlepoint and reac- tant information	Rates	
Phase-Space Theory (PST)	Reactant and pro- duct information	State (rot-vib) resolved, cross sections, rates	

Table 2.1: Different theoretical methods, their requirements and applicability.

- In *Section 2.3* a theoretical description of the phase-space method is given along with a test of the method on two different atmospheric chemical reactions[63]:



and



Since phase-space theory is based on a long-lived Collision Complex (CoCo), we also introduce a factor, which when multiplied by the rate constant, will be an estimate of the rate constant if it were to take place via a short-lived CoCo, as is the case for abstraction reactions. This means that the model can be used to calculate an interval in which the correct rate constant will be found.

We want to emphasize that this new method is an approximative method. Therefore, this method shall only be used in cases in which no alternative for obtaining a rate constant, other than structural correlation methods[76, 105], rate constants versus the bound dissociation or the first vertical ionization potential[106],

and correlation of the rate constants for NO_3 with those for the reactions of the OH radicals and $\text{O}(^3P)$ atoms, exists. If experimental results are available for the chemical system of interest, these are to be preferred over results obtained by phase-space techniques.

2.1 Outline of Dynamical and Statistical Methods to Calculate Bi-Molecular Rate Constants

Theoretical models can be grouped into three different classes:

- dynamic,
- statistical-dynamic, and
- statistical methods,

see Table 2.1. Furthermore, dynamic methods can be grouped into

- fully dynamic and
- reaction path methods,

see Table 2.1. The benchmark in dynamic methods is the Hamilton operator. When no exterior forces act on a chemical reaction, the quantum mechanical Hamilton operator is simply equal to the sum of the kinetic energy operator and the potential energy. Since the 1930s, the relationship between PESs and the dynamics of molecular/atomic collisions has been known – this is the numerical solution to the classical or quantum mechanical equations of motion. An analysis of the outcome of the molecular/atomic collisions can be used e.g. to calculate the reaction probability of the reaction. From these results the total rate constant is obtained by integrating over the impact parameter and averaging over the Boltzmann distribution.

If the motion of the system of nuclei¹ is treated quantum mechanically, the accuracy of the calculations is only limited by the accuracy of the PES and the number of basis function used to expand the wave function that describes the system. Unfortunately, fully quantum mechanical simulations demand enormous computational resources, even for triatomic systems. Since fully quantum mechanical treatment of most molecular systems is so computationally expensive or impossible, mixed quantum-classical² or purely classical treatments are very popular for solving various inelastic, elastic and reactive scattering problems.

Today, if a PES is available, classical trajectory methods can always be used since only the coordinates and momenta of the nuclei describe the dynamics. Such calculations are not very time consuming. The coordinates and momenta of the

¹The motion can be divided into three types – translational, vibrational and rotational.

²In quantum-classical simulations some of the molecular motion is handled quantum mechanically, some classically.

nuclei are functions of time, therefore in classical dynamics one follows the system as it goes from reactants to products during a collision. The outcome of a single trajectory in classical dynamics is not very meaningful. Instead one has to average over a large number of trajectories to obtain reliable results. Classical trajectories are valid when the momentum is great (i.e. the relative speed), the energy is high, the colliding nuclei are heavy and the temperature of the system is not too low. In general classical trajectory computations are often accurate for calculating total rate constants if a reliable PES of the chemical system is known.

In reaction path methods, the dynamics are performed along the reaction path (the minimum-energy part on the PES). As indicated by the name of the model, in contrast with the fully dynamic methods, only PES information along the reaction path is required. Therefore the Hamilton operator is only required in this region. Both classical and quantum-classical theories of these methods have been developed[108].

A general problem with dynamical methods is the necessity of potential energy information. It is still a formidable undertaking to obtain reliable PESs even for triatomic systems. Naturally, this limits the applicability of dynamic methods and justifies the use of more approximative methods such as Transition State Theory (TST), Variation Transition State Theory (VTST) and Phase-Space Theory (PST).

Applying TST to a chemical reaction gives the total rate constant for that reaction. The basic assumption of TST is that a chemical reaction takes place by forming an activated complex (transition state) which is in equilibrium with the reactants. In TST the activated complex is positioned at the top of the activation barrier, and it is assumed that once the system has crossed the transition state configuration, it does not return. In order to use TST one only needs detailed spectroscopic and potential energy information about the reactants and the transition state. Finding the transition state (the PES's first order saddle points) can be very difficult. There is not a general method that can be used to estimate the position of the transition state. Furthermore, there is no guarantee that a single transition state between the reactants and products exists. And as the number of nuclei in a chemical system increases, the number of possible transition states increases as well. In spite of TST needs much less PES information, it is only possible to obtain the necessary PES information for a very limited number of molecular systems.

In VTST the usual transition state expression is evaluated along the reaction path and the VTST rate constant is obtained where the transition state rate has its minimum. This corresponds to the situation where the flux from reactants to products is a minimum. This method needs PES information for the whole reaction path and is therefore less applicable than TST.

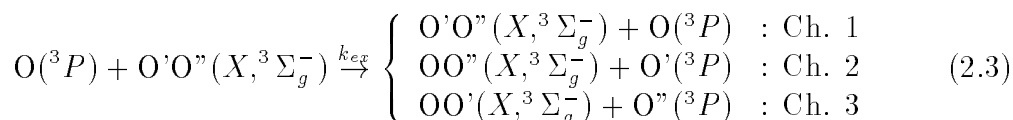
PST requires information about the reactant and product channels of the chemical reaction, vibrational frequencies, moments of inertia, potential energy in their ground state equilibrium configuration, and the energy barrier or the long-range potential (if the chemical reaction does not have an energy barrier). But this can be calculated with sufficient accuracy using electronic structure theory. Moreover, state (rot-vib) resolved and total cross sections and rates can be calculated

within this approach. PST can be used for all known chemical reactions as long as all the species in the reactant and product channels are known.

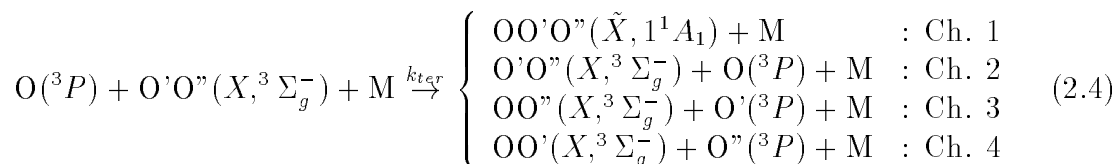
In Table 2.1 we have outlined the different methods described in this section. The rate of accuracy goes from top (most accurate) to the bottom (least accurate). This is closely related to the amount of PES information needed in order to apply the methods. Furthermore, PST and dynamic methods are the most informative.

PES's Importance

In all the methods described above, PES information about the chemical system is of fundamental importance, thus the result from the used methods is highly dependent on the quality of the PES. We have illustrated this problem using quasi-classical trajectories on the isotopic exchange reactions



and the isotopic termolecular recombination reactions for ozone formation



In these two reactions, O, O' and O'' are different oxygen isotopes, i.e. either ^{16}O or ^{18}O , and M is an Argon atom[59]. We have calculated the rate constants for these two reactions on three different PESs; one surface obtained by Sheppard and Walker (SW)[58, 60, 61, 109], another by Yamashita et al. (YMQl)[58, 60, 61, 110] and finally a modified version of YMQl (mYMQl)[59] (the work carried out in this section). In our first investigations of reaction 2.3[60, 61], we obtained significantly different results. The YMQl PES has a barrier, thus the rate increases with the temperature, while the SW surface does not have a barrier, thus the rate constant becomes almost temperature independent. Furthermore, we found that the calculations using the YMQl PES underestimated the rate constants compared with other theoretical[111, 112, 113, 114, 115] and experimental results[116, 117, 118, 119, 120, 121, 122, 123], whereas the calculations using the SW surface greatly overestimated the rate constants. In addition to these differences we could not form stable ozone on the YMQl PES. It was possible to form stable ozone on the SW PES, but again the SW PES overestimated the rate constant for ozone formation[61]. These facts emphasize the necessity of modifying the YMQl PES so it has no barrier in the exit-entrance channels, see Refs. [59] for more details.

In Tables 2.2 - 2.6 the results are outlined together with all existing simulations and experiments performed on the two systems. A comparison of our results with the experimental and theoretical results shows that the mYMQl significantly

O+O'O'' (O,O',O'')	O+O'O'' Ch. 1	O'+OO'' Ch. 2	O''+OO' Ch. 3	$k_{ex}/10^{-12}\text{cm}^3\text{s}^{-1}$
(¹⁶ O, ¹⁶ O, ¹⁶ O)	80.0 ± 0.3	1.25 ± 0.03	1.27 ± 0.03	
(¹⁶ O, ¹⁶ O, ¹⁸ O)	79.1 ± 0.3	1.28 ± 0.03	1.17 ± 0.03	1.17 ± 0.03
(¹⁶ O, ¹⁸ O, ¹⁸ O)	78.5 ± 0.3	1.16 ± 0.03	1.10 ± 0.02	2.28 ± 0.05
(¹⁸ O, ¹⁸ O, ¹⁸ O)	75.2 ± 0.3	1.17 ± 0.02	1.14 ± 0.03	
(¹⁸ O, ¹⁸ O, ¹⁶ O)	76.0 ± 0.3	1.16 ± 0.02	1.30 ± 0.03	1.30 ± 0.03
(¹⁸ O, ¹⁶ O, ¹⁶ O)	76.9 ± 0.3	1.28 ± 0.03	1.25 ± 0.03	2.53 ± 0.05

Table 2.2: The theoretical rate constants at 300 K for the isotopic exchange reaction using the mYMQl surface. The rate constants are in units of ($10^{-12}\text{cm}^3\text{s}^{-1}$)[59].

T/K	$k_{ex}/10^{-12}\text{cm}^3\text{s}^{-1}$	Ref.	Method
$^{16}\text{O}+^{16}\text{O}_2 \rightarrow ^{16}\text{O}_2+^{16}\text{O}$			
300	2.5	[121]	1
300	3.2	[121]	2
300	6.3	[121]	2
300	7.0	[120]	1
300	5.4	[120]	2
$^{16}\text{O}+^{16}\text{O}^{18}\text{O} \rightarrow ^{16}\text{O}_2+^{18}\text{O}$			
300	1.62 ± 0.09	[115]	3
400	1.82 ± 0.10	[115]	3
500	2.01 ± 0.11	[115]	3
300	1.78	[114]	4
400	1.88	[114]	4
500	1.93	[114]	4
$^{16}\text{O}+^{18}\text{O}_2 \rightarrow ^{16}\text{O}^{18}\text{O}+^{18}\text{O}$			
300	32. ± 2.3	[60]	3
350	30. ± 2.3	[60]	3
400	28. ± 2.2	[60]	3
450	27. ± 2.1	[60]	3
500	26. ± 2.1	[60]	3
300	0.027 ± 0.004	[60]	5
350	0.042 ± 0.006	[60]	5
400	0.061 ± 0.014	[60]	5
450	0.087 ± 0.017	[60]	5
500	0.12 ± 0.02	[60]	5
300	1.7 $^{+0.10}_{-0.06}$	[116]	6

Table 2.3: The experimental and theoretical rate constants for the isotopic exchange reaction. The different methods used to measure the rates can be described as follows – Method 1: theoretical calculation using an adiabatic channel method, Method 2: theoretical calculation using maximum free energy, Method 3: theoretical calculation using quasi-classical trajectories on the SW PES, Method 4: theoretical calculation using semi-classical state expansion method on the SW PES, Method 5: theoretical calculation using quasi-classical trajectories on the YMQl PES, Method 6: experimental measurement using discharge flow photolysis.

improves the results. The difference between the new results presented in this thesis compared with the results obtained for reaction 2.3 by Gross and Billing[60], Stace

T/K	$k_{ex}/10^{-12}\text{cm}^3\text{s}^{-1}$	Ref.	Method
$^{18}\text{O}+^{18}\text{O}^{16}\text{O} \rightarrow ^{18}\text{O}_2+^{16}\text{O}$			
300	0.018 ± 0.004	[60]	1
350	0.023 ± 0.004	[60]	1
400	0.038 ± 0.009	[60]	1
450	0.052 ± 0.011	[60]	1
500	0.068 ± 0.013	[60]	1
$^{18}\text{O}+^{16}\text{O}_2 \rightarrow ^{18}\text{O}^{16}\text{O}+^{16}\text{O}$			
300	3.82 ± 0.13	[115]	2
400	4.08 ± 0.14	[115]	2
500	4.09 ± 0.15	[115]	2
300	3.9	[113]	3
500	3.0	[113]	3
300	1.6	[112]	3
400	1.7	[112]	3
500	1.8	[112]	3
300	3.64 ± 0.44	[111]	3
500	3.10 ± 0.40	[111]	3
300	3.79	[115]	4
400	4.07	[115]	4
500	4.24	[115]	4
300	3.83	[114]	5
400	3.95	[114]	5
500	4.00	[114]	5
298	2.9 ± 0.5	[123]	6
298	2.8	[122]	7
298	2.8	[119]	7
298	1.0 ± 0.20	[118]	8
335	1.2 ± 0.45	[118]	8
352	1.5 ± 0.17	[118]	8
362	1.6	[118]	8
381	1.3 ± 0.18	[118]	8
402	1.7 ± 0.33	[118]	8
310	1.0	[117]	6

Table 2.4: The experimental and theoretical rate constants for the isotopic exchange reaction. The different methods used to measure the rates can be described as follows – Method 1: theoretical calculation using quasi-classical trajectories on the YMQL PES, Method 2: theoretical calculation using quasi-classical trajectories on the SW PES, Method 3: theoretical calculation using quasi-classical trajectories, Method 4: theoretical calculation using quasi-classical detailed method trajectories on the SW PES, Method 5: theoretical calculation using semi-classical state expansion method on the SW PES, Method 6: experimental measurement using discharge flow, Method 7: experimental measurement using high pressure recombination, Method 8: experimental measurement using discharge flow photolysis.

and Murrell[111], Varandas and Murrell[112], Varandas and Pais[113] and Chajia and Jacon[115] and for reaction 2.4 by Gross and Billing[61] has to do with the choice of the PES, because the same theoretical method has been used in all of these simulations. This is therefore a good illustration of how dependent theoretical simulations are on a reliable PES.

O+O'O''+Ar (O,O',O'',Ar)	OO'O''+Ar Ch. 1	O+O'O''+Ar Ch. 2	O'+OO''+Ar Ch. 3	O''+OO'+Ar Ch. 4
(¹⁶ O, ¹⁶ O, ¹⁶ O,Ar)	3.67 ± 0.22	103. ± 0.9	13.3 ± 0.5	12.1 ± 0.4
(¹⁶ O, ¹⁶ O, ¹⁸ O,Ar)	3.74 ± 0.21	106. ± 0.9	14.7 ± 0.5	15.9 ± 0.6
(¹⁶ O, ¹⁸ O, ¹⁸ O,Ar)	3.87 ± 0.21	108. ± 1.0	14.4 ± 0.5	14.7 ± 0.4
(¹⁸ O, ¹⁸ O, ¹⁸ O,Ar)	4.00 ± 0.25	101. ± 0.9	12.3 ± 0.4	11.9 ± 0.4
(¹⁸ O, ¹⁸ O, ¹⁶ O,Ar)	3.42 ± 0.23	91.9 ± 0.9	13.0 ± 0.4	13.9 ± 0.5
(¹⁸ O, ¹⁶ O, ¹⁶ O,Ar)	3.87 ± 0.24	92.9 ± 0.9	13.7 ± 0.5	15.0 ± 0.8

Table 2.5: The theoretical rate constants for ozone formation at 300 K using the mYMQML surface. The rate constants are in units of ($10^{-34} \text{ cm}^6 \text{ s}^{-1}$)[59].

T/K	$k_{ter}/10^{-34} \text{ cm}^6 \text{ s}^{-1}$	Ref.	Method
¹⁶ O+ ¹⁶ O ₂ +Ar → ¹⁶ O ₃ +Ar			
300	4.5	[124]	1
350	3.0	[124]	1
400	2.1	[124]	1
300	40.	[125]	2
350	27.	[125]	2
400	23.	[125]	2
300	40.	[125]	3
350	38.	[125]	3
400	37.	[125]	3
300	19.7 ± 4.2	[61]	4
350	14.2 ± 3.0	[61]	4
400	10.4 ± 2.2	[61]	4
300	0.0	[61]	5
350	0.0	[61]	5
400	0.0	[61]	5

Table 2.6: The experimental and theoretical rate constants for ozone formation – Method 1: experimental measurement using high pressure recombination, Method 2: theoretical calculation using quasi-classical trajectories for reaction Ar-O₂+O→O₃+Ar and statistical mechanics to determine the pseudo-equilibrium constant for reaction O₂+Ar→Ar-O₂ (where the Ar-O₂ intermolecular bending-stretching motion is separated from the intramolecular O₂ vibration), Method 3: theoretical calculation using quasi-classical trajectories for reaction Ar-O₂+O→O₃+Ar and statistical mechanics to determine the pseudo-equilibrium constant for reaction O₂+Ar→Ar-O₂ (where three local independent modes of Ar-O₂ are assumed and are treated using the harmonic oscillator approximation), Method 4: theoretical calculation using quasi-classical trajectories on the SW PES, Method 5: theoretical calculation using quasi-classical trajectories on the YMQML PES.

2.2 Ab Initio Calculations

Ab initio calculations play a central role in theoretical chemistry, because of their applicability to many molecular phenomena. The primary use of ab initio calculations is to calculate potential energies (among others, PESs). This involves very complicated mathematical treatments. This section does not include a detailed description of different kinds of ab initio methods, because this is a large subject on its own (for a more detailed description of the subject see e.g. Ref. [126]). Instead a general

picture of ab initio calculations utility will be given. Electronic structure studies on CH_3CHO , CH_3CO , CH_3OOH , CH_3O_2 , CH_2OOH , OH and H_2O have been made and will be discussed. These results are calculated on the basis of the molecular electronic structure program Gaussian 94[64].

2.2.1 Theory

The Schrödinger equation for a molecule, if the motion of the electrons and nuclei is treated according to the Born-Oppenheimer approximation, can be separated into two parts – an electronic and a nuclear part. This gives:

$$(T_{el}(R) + V_{ne}(R, r) + V_{nn}(R) + V_{ee}(r))\Phi(R, r) = E(R)\Phi(R, r) \quad (2.5)$$

$$(T_{nuc}(R) + E(R))\chi(R) = E_{tot}\chi(R) \quad (2.6)$$

where R and r are the position of the nuclei relative to the center of mass of the molecule and the position of the electrons relative to the center of mass, respectively. $T_{nuc}(R)$ and $T_{el}(r)$ represent the kinetic energy operators for the nuclei and the electrons, respectively. $V_{nn}(R)$, $V_{ne}(R, r)$ and $V_{ee}(r)$ determine the electrostatic potential energies due to the nucleus-nucleus, nucleus-electron and electron-electron interactions, respectively. E_{tot} and $E(R)$ are the total energy of the system and the electronic energy as a function of nuclear coordinate, respectively. Finally, the two wave functions – the electronic wave function $\Phi(R, r)$ for a given nuclear configuration R and the nuclear wave function $\chi(R)$ – arise from the approximation that the motion of the nuclei and the electrons are separable, i.e. the total wave function Ψ can be written as

$$\Psi(R, r) = \Phi(R, r)\chi(R) \quad (2.7)$$

This implies that the potential energy surface is the sum $V_{nn}(R) + E(R)$.

If it is possible to solve the Schrödinger equation for a molecule, i.e. solve differential equations (2.5) and (2.6), it is possible to obtain all information about the molecule within the postulates of quantum mechanics. Unfortunately, at present an exact solution of these can only be done for one electron systems. Approximations are therefore necessary. In this respect ab initio methods are commonly used approximate methods.

Electronic Structure Theories

In ab initio methods, an appropriate quantum mechanical scheme for the molecular electronic wave function is selected. The scheme selected is then used without further approximations to obtain the desired information about the system. Thus the approximations in the ab initio methods have to do with the choice of the model. Even though these are termed ab initio methods, the selected model can be inappropriate and lead to an inaccurate result. We will here give a short description of the principal directions in the field of ab initio methods. We will outline four methods,

which can be grouped into two main groups: methods based on the variation principle (Self-Consistent Field/Hartree-Fock (SCF/HF) and Configuration Interaction (CI) methods) and those which are not (Many-Body Perturbation Theory (MBPT) and Coupled Cluster (CC) methods).

1. *SCF/HF methods.* The SCF/HF method uses the HF formalism. Because the Fock matrix depends on its own solutions the Roothaan-Hall equation, it must be solved iteratively. This results in the following procedure: firstly, calculate all one- and two-electron integrals; secondly, generate a suitable first guess of the Molecular Orbitals (MO); thirdly, make the initial density matrix; fourthly, make the initial Fock matrix as the core (one-electron) integrals + density matrix \times the two-electron integrals; then diagonalize the Fock matrix, the eigenvectors will then contain the new MO coefficients; lastly, on the basis of the new density matrix, if it is sufficiently close to the old density matrix the calculation is complete, otherwise go back to step three.
2. *CI methods.* These methods are based on the variational principle just as the SCF/HF methods. The trial wave function is expanded in linear Slater Determinants (SD), and the excited SDs are constructed by MOs taken from an SCF/HF calculation.

SCF/HF methods do not take non-dynamical correlation effects into account. Therefore these methods give incorrect dissociative behavior of the MO wave function. An improvement is the Multi-Configurational SCF (MC-SCF) method, where both the CI coefficients and the molecular-orbital expansion coefficients are simultaneously optimized for the wave function. Examples of these methods are the Complete Active-Space Self-Consistent Field (CASSCF) method, the CASSCF-Single Excitation Configuration Interaction (-SECI) method, and the CASSCF-SECI+Higher-order Correction based on the formula of Feller and Davidson[126] (+HC).

1. *MBPT.* In perturbation theory the Hamiltonian consists of two parts: a reference and a perturbation Hamiltonian where the perturbed Hamiltonian is small compared to the reference Hamiltonian. Based on this approximation, the wave function is corrected by the perturbed Hamiltonian. The most commonly used perturbation theory is Møller Plesset perturbation theory (MP). In this theory the unperturbed Hamilton operator is chosen as a sum over Fock operators. This sum counts the electron-electron repulsion twice, and the perturbation becomes the exact V_{ee} minus twice the $\langle V_{ee} \rangle$ operator. In this thesis the electronic structure theory used is many-body Møller Plesset second order perturbation theory (MP2) for the treatment of electron correlation. Second order means that up to second order corrections to the energy are made. The advantage of using many-body perturbation theory is that the numeric work can be decreased tremendously. If for example the CI method for the treatment of electron correlation is used, it is necessary to include a very large number of configurations, and the method converges slowly. This can be improved using many-body perturbation theory.

2. *CC methods.* Contrary to many-body perturbation theories, where all types of corrections to the reference wave function to a given order are included, the CC method includes only all corrections of a given type to infinite order. Therefore, the CC method is closely connected to MBPT.

In general, MBPT gives very good results when the Hartree-Fock function is the dominant contributor to the wave function. Hence, for the methods described above, CI methods are only suitable for small molecular systems in contrast with SCF/HF, MBPT and CC. But these are on the other hand only suitable for systems in the equilibrium configuration. SCF/HF are the least computationally expensive methods and can be used for very large systems.

Gaussian Type Orbitals (GTO) Basis Set

A large variety of basis sets have been developed over the years[126]. In what follows we will only focus on the Gaussian Types Orbitals (GTO) basis set, since this is the one used in this thesis. This basis set is the simplest type of basis set, therefore the required integrals can be calculated relatively easy. That means GTO are the preferred basis functions for electronic structure calculations. This basis set uses the nomenclature *klmG*. An example is the 6-31G basis set: here the first-row atoms consist of an s-type inner shell function expressed as a combination of six Gaussian functions; a set of valence s- and p-type functions, each expressed as a combination of three Gaussian functions, and an outer set of s- and p-functions, each consisting of one Gaussian function.

Polarization functions are added to the chosen sp-basis, p-functions on the hydrogen and d-functions on the heavier atoms. Hydrogen atoms often have a “passive” role, because they are terminal atoms in the molecule, i.e. they have no active part in the property of interest. Therefore, the error introduced by not including hydrogen polarization functions is often rather constant, and as the interest usually is in energy differences, this missing polarization tends to cancel out. Hydrogen often accounts for a large number of atoms in organic molecules, therefore saving three basis functions for each hydrogen can be significant. If hydrogen play an important role in the property of interest, the polarization functions on hydrogen atoms of course cannot be neglected.

The basis set (6-31G*) is the same as the 6-31G basis set except that d-polarization functions on the heavy atoms (i.e. all atoms other than hydrogen) are added to the basis set. If the basis set is extended so that both d-polarization functions on the heavy atom and p-polarization on hydrogen atoms is included, the basis set is denoted 6-31G**.

Other examples of basis sets are even-tempered, well-tempered, contracted consistent, MINI, MIDI, MAXI, DZ, TZ, QZ, PZ, DZP, and atomic natural orbitals basis sets. These are described by Jensen[126].

2.2.2 Results

We have performed MP2 calculations on CH₃CHO, CH₃CO, CH₃OOH, CH₃O₂, CH₂OOH, OH and H₂O. Two types of basis sets have been used for each MP2 calculation 6-31G and 6-31G*. The results are calculated on the basis of the molecular electronic structure program Gaussian 94[64]. In Table 2.7 the convergence scheme for the performed ab initio calculations is presented. The vibrational frequencies and moments of inertia for the molecules of interest are given in Tables 2.8-2.11. Finally, the available experimental vibrational frequencies and moments of inertia for HO and H₂O are given in Tables 2.9 and 2.11.

Molecule	Basis	Max. Force amu a_0 s ⁻²	RMS Force amu a_0 s ⁻²	Max. Displc. a_0	RMS Displc. a_0	Electronic + Zero-Point Energy Hartree
HO	6-31G	0.000011	0.000006	0.000012	0.000007	-75.443679
	6-31G*	0.000110	0.000063	0.000109	0.000063	-75.512512
H ₂ O	6-31G	0.000259	0.000145	0.000508	0.000256	-76.092309
	6-31G*	0.000001	0.000000	0.000001	0.000001	-76.175372
CH ₃ CHO	6-31G			Not converged		
	6-31G*	0.000005	0.000003	0.000201	0.000101	-153.289963
CH ₃ CO	6-31G	0.000058	0.000021	0.001671	0.000887	-152.470630
	6-31G*	0.000052	0.000031	0.001110	0.000466	-152.666321
CH ₃ OOH	6-31G	0.000217	0.000088	0.000435	0.000206	-190.016764
	6-31G*	0.000119	0.000047	0.001563	0.000615	-190.234285
CH ₃ O ₂	6-31G	0.000327	0.000103	0.000991	0.000445	-189.394931
	6-31G*	0.000001	0.000001	0.000006	0.000003	-189.614032
CH ₂ OOH	6-31G			Not converged		
	6-31G*	0.000013	0.000007	0.001054	0.000340	-189.593591

Table 2.7: Convergence scheme for the ab initio calculations performed using the ab initio program Gaussian 94. The electronic structure calculation theory used is MP2. The thresholds for convergence are: maximum force = 0.000450 amu a_0 /s⁻², RMS force = 0.000300 amu a_0 /s⁻², maximum displacement = 0.001800 a_0 , and RMS displacement = 0.0012 a_0 . RMS means Root Mean Square.

For the organic molecules investigated, no experimental or theoretical esti-

Molecule	Basis Set	Vibrational Frequencies					Zero-Point Vib. Energy eV
		cm ⁻¹					
CH ₃ CHO	6-31G*	146.7511	514.1492	797.4062	924.9322	1166.5823	1.54988
		1168.5543	1438.2875	1466.3160	1526.8802	1534.5093	
		1796.0517	2993.1207	3105.6122	3186.0038	3235.8004	
CH ₃ CO	6-31G	64.2021	458.7839	834.9811	1008.4167	1082.1145	1.23440
		1445.0091	1532.5538	1536.5456	2530.5122	3068.9785	
		3172.7845	3177.1373				
	6-31G*	74.9063	468.2364	896.2528	989.0270	1090.7346	1.20947
		1419.0643	1524.2245	1524.7236	1975.0279	3110.7074	
		3216.8833	3220.1151				
CH ₃ OOH	6-31G	112.7119	226.8932	392.0891	754.0897	967.1069	1.47056
		1159.6947	1174.0112	1308.4092	1494.5570	1536.1737	
		1581.7284	3078.6515	3180.5069	3193.0311	3561.9250	
	6-31G*	163.9007	267.4136	449.6503	870.1238	1075.9826	1.51803
		1202.9520	1228.8231	1387.7548	1504.0619	1531.0604	
		1575.1040	3098.5416	3190.8225	3217.7048	3723.3324	
CH ₃ O ₂	6-31G	119.2765	467.1861	870.3638	1149.9065	1180.2817	1.19331
		1301.3065	1498.4983	1546.9525	1560.5815	3102.8319	
		3215.0620	3236.9282				
	6-31G*	136.7289	505.4583	962.3522	1169.6074	1219.1993	1.20947
		1273.9627	1500.4946	1539.2591	1549.7274	3137.2523	
		3253.5982	3262.2009				
CH ₂ OOH	6-31G*	168.1917	398.0940	478.7843	791.8959	918.9194	1.13933
		1194.9480	1213.0104	1418.0523	1495.9503	3214.7925	
		3365.0035	3720.8709				

Table 2.8: Table of vibrational frequencies for the organic molecules from the ab initio calculations performed using Gaussian 94. The electronic structure calculation theory used is MP2.

mated spectroscopic data exists, and we have to evaluate the results on the background of the results given in Tables 2.7, 2.8 and 2.10. These tables show the importance of including polarization functions. Moreover, Table 2.7 shows that it is not possible to obtain convergence for two of the molecules (CH₃CHO and CH₂OOH) using the unpolarized 6-31G basis set. The CH₃CHO, run repeatedly, calculated the same five steps. The oscillation has to do with the H atom attached to the C atom

Molecule	Basis Set	Vibrational Frequencies cm ⁻¹			Zero-Point Vib. Energy eV
HO	6-31G	3551.43			0.22016
	6-31G*	3740.42			0.23187
H ₂ O	6-31G	1662.63	3660.27	3836.32	0.56780
	6-31G*	1735.53	3774.83	3916.26	0.58438
Molecule		Vibrational Frequencies cm ⁻¹			Zero-Point Vib. Energy eV
HO	Experiment	3737.76			0.23171
H ₂ O	Experiment	1594.7	3657.0	3755.7	0.55839

Table 2.9: The first part of the table shows vibrational frequencies for HO and H₂O from the ab initio calculations performed using Gaussian 94. The electronic structure calculation theory used is MP2. The second part shows experimental vibrational frequencies for HO and H₂O from Refs. [127] and [128].

which is bound to the O atom. The electron attached to that H atom is described by an s-orbital. The electron cloud from this orbital tries to reject the other electron clouds close to that orbital. If a polarization function were used that rejection could be spread out in other orbitals. This is not possible and therefore convergence is not achieved. For the CH₂OOH run it is not possible to come under the threshold of convergence, and therefore the run stops. This can be explained from the fact that the lone electron in the radical want to move in other orbits or the electron wants to run closer to the O atom. If the basis set were polarized that would have been possible, but now it is forced to move in the p_z-orbital only.

Two conditions can be drawn from Table 2.7. First when the basis set 6-31G* is used, the four convergence checks used in Gaussian 94 are lower than the convergence checks for the 6-31G basis set. Second that the electronic+zero-point energy becomes lower for the basis set using polarization functions compared to the basis set where polarization functions are not used. That means the calculation performed with the 6-31G* basis set comes closer to the molecule's equilibrium configuration, i.e. it is better optimized. Both of these points are logical because the 6-31G* basis set has a better functional description of a given molecule than the 6-31G basis set.

The results obtained for the vibrational frequencies of the organic molecules are given in Table 2.8 and for H₂O and HO in Table 2.9. The vibrational frequencies

Molecule	Basis Set	Momentum of Inertia		
		amu a_0^2		
CH ₃ CHO	6-31G*	31.97598	179.14306	199.93407
CH ₃ CO	6-31G	21.96234	187.39220	198.05468
	6-31G*	22.02844	181.89390	192.73563
CH ₃ OOH	6-31G	46.36383	183.71986	218.41817
	6-31G*	43.14872	171.70958	199.01502
CH ₃ O ₂	6-31G	36.45736	170.15645	194.89269
	6-31G*	34.82749	157.80645	181.02188
CH ₂ OOH	6-31G*	34.52317	160.25876	190.22406

Table 2.10: Table of moments of inertia for the organic molecules from the ab initio calculations performed using Gaussian 94. The electronic structure calculation theory used is MP2.

are calculated from the force constant, i.e. the second derivative of the energy, at the equilibrium geometry and utilizing the harmonic approximation for vibrational motion. The equilibrium geometry and the shape of the PES depend on the electronic structure model used and on the chosen basis set. In general the vibrational frequencies will decrease as the bond length increases. When comparing the calculations using the two basis sets, it is seen that in general the vibrational frequencies calculated using the 6-31G* basis are larger compared with the calculations where the 6-31G basis set is used. But this can be understood from the fact that the 6-31G* basis set calculations are closer to the molecule's equilibrium configuration than the 6-31G calculations where the internal distances in the molecule are a little bit larger. Experimental data is only available for HO and H₂O. In general ab initio calculations have a tendency to give results with an uncertainty between 10 % and 15 % compared to experimental results[126]. In Table 2.9, we see that the result for HO using the 6-31G* basis set is in extremely good agreement with the experimental data, but the size of the system is not very large compared with the organic molecules. For H₂O all the vibrational frequencies are in reasonable agreement with the experimental data.

Calculation of the moment of inertia for a molecule is fairly easy because it depend only on its configuration, i.e. reduced mass and internal distances. For most of the ab initio calculations, the moment of inertia (Tables 2.10 and 2.11) decreases

Molecule	Basis Set	Momentum of Inertia amu a_0^2		
HO	6-31G	0.00000	3.32435	3.32435
	6-31G*	0.00000	3.24480	3.24480
H ₂ O	6-31G	2.03305	4.54404	6.57709
	6-31G*	2.27513	4.19273	6.46787
Molecule		Momentum of Inertia amu a_0^2		
HO	Experiment	0.00000	3.16015	3.16015
H ₂ O	Experiment	2.20212	4.12898	6.33750

Table 2.11: First part of the table: moments of inertia for HO and H₂O from the ab initio calculations performed using Gaussian 94. The electronic structure calculation theory used is MP2. Second part: table of experimental moments of inertia for HO and H₂O from Refs. [127] and [128].

going from basis set 6-31G to 6-31G*, i.e. the internal configuration (distances in the molecule) is larger for the 6-31G calculation than the 6-31G* calculation (farther from equilibrium). Table 2.11 also shows that the internal distances in HO and H₂O still are a little bit too large, but the agreement with the experimental data is fairly good.

2.3 Phase-Space Methods

In order to apply phase-space methods to reactions 2.1 and 2.2 the long-range potential for these two molecular systems must be calculated. Therefore, this section is split in two:

- estimations of long-range potentials (*Section 2.3.1*), and
- calculations of rate constants using phase-space theory (*Section 2.3.2*).

2.3.1 Long-Range Potentials

The long-range potential describes the potential energy when the electron clouds for the interacting molecules do not overlap. Since the electron clouds do not overlap, the dipole and polarization for the molecules can be calculated independently. Since

ab initio calculations with good accuracy can be used for molecules close to their equilibrium configurations, it is a much simpler task to calculate the long-range potential than the short-range potential (i.e. potential where the electron clouds overlap, in that case MP is not a suitable method). Perturbation studies have shown that the intermolecular forces describing the long-range potential obey the expression[129]

$$V_{LR} = -(CR^{-6} + C_8R^{-8} \dots) \approx -CR^{-6} \quad (2.8)$$

where the magnitude of C depends on the dipole-dipole, dipole-induced dipole and dispersion interactions between the two molecules. The higher terms in the equation considering dipole-quadrupole, quadrupole-quadrupole interactions, etc.

The first type of interaction can be described as follows: consider two molecules A and B, and assume they have permanent dipole moments u_A and u_B . From classical electrostatic theory, the interaction between the two molecules dipoles is given by[131]

$$w_{dd}(r) = \frac{1}{4\pi\epsilon_0} [\bar{u}_A \cdot \bar{u}_B - 3(\bar{u}_A \cdot \bar{r})(\bar{u}_B \cdot \bar{r})] r^{-3} \quad (2.9)$$

where r is the distance between the two dipoles, \bar{r} is a unit vector defining the direction of the center of dipole from molecule B with respect to the dipole from molecule A and ϵ_0 is the permittivity of vacuum. If all orientations of the dipole-dipole interaction are equally probable, $w_{dd}(r)$ will average to zero. But if each relative orientation is weighted by a Boltzmann factor (k_b), and assuming that the intermolecular potential is negligible compared to $k_b T$ (T is the temperature), one can obtain the following equation for the interaction between the two dipoles[131]

$$W_{dd}(r) = -\frac{2}{3} \frac{u_A^2 u_B^2}{k_b T (4\pi\epsilon_0)^2} r^{-6} \quad (2.10)$$

The next type of interaction is due to the dipole moment that one molecule (e.g. A) will induce on the other (e.g. B) (independent of whether B is polar or non-polar). An expression for this interaction can be evaluated using $w_{di}(r) = -\frac{1}{2} \alpha_B \|\bar{E}\|^2$, (α_B is molecule B's isotropic polarization and \bar{E} is the electric field at B due to u_A). Using classical electrostatic and averaging over all orientations we get[131]

$$W_{di}(r) = -\frac{u_A^2 \alpha_B}{(4\pi\epsilon_0)^2} r^{-6} \quad (2.11)$$

If both molecules are polar the equation becomes[131]

$$W_{di}(r) = -\frac{u_A^2 \alpha_B + u_B^2 \alpha_A}{(4\pi\epsilon_0)^2} r^{-6} \quad (2.12)$$

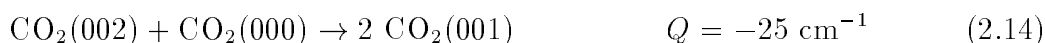
The final intermolecular interaction is also active when both molecules are non-polar. This force is called the London dispersion force. It cannot be understood within classical electrostatics. Consider the interaction between two non-polar molecules: each molecule has a charge distribution and the electronic distribution

is fluctuating. At a particular instant in time, one of the molecules may have an instantaneous dipole. This instantaneous dipole can induce a dipole moment on the other molecule. Therefore dispersion interaction requires a quantum mechanical treatment in which the interaction is taken into account by second order perturbation theory. London developed the following approximate formula for the dispersion potential

$$W_{ii}(r) = -\frac{3}{2} \frac{\alpha_A \alpha_B}{(4\pi \epsilon_0)^2} \frac{E_A^I E_B^I}{E_A^I + E_B^I} r^{-6} \quad (2.13)$$

where E_x^I is the ionization energy of molecules A and B. The ionization energy can be calculated using Koopmans theorem. In this approximation the ionization energy is given as minus the highest orbital energy. This value can be extracted from the ab initio calculations.

If both molecules are polar, the long-range potential is a summation of these three intermolecular interactions. In some cases the dispersion can give the largest contribution to the long-range potential. One important example of a system with large dispersion interaction is the $V-T$ transition of CO_2 [129]



When the wave function for a molecule in a specific configuration is known, a wide range of molecular properties can be calculated. Gaussian 94 gives as output the dipole momentum vector, the symmetric polarization matrix (columns two and three in Tables 2.12 and 2.13) and the ionization energy. We can obtain the molecules dipole moment by calculating the length of its vector and the polarization of the molecule by estimating the trace of the diagonalized symmetric polarization matrix. This is given in columns four and five in Tables 2.12 and 2.13.

Results

Only one set of experimental data for the investigated molecules polarization and dipole moment exists, that being the dipole moment for H_2O (Table 2.13). We see that Gaussian 94 predicts a dipole moment which is only slightly larger than the experimental measurement, and that the run with basis set 6-31G* gives the best result.

The polarizability of a molecule depends on the type of functional groups and the number of electrons that are present in the molecule. The calculations performed on the organic molecules give polarizations of around $20 (a_0 \text{ C})^2/\text{Ha}$ (Table 2.12) where the calculations done on H_2O and HO only have polarizations of around $3-5 (a_0 \text{ C})^2/\text{Ha}$. This is because the number of electrons in the molecule within these two groups is almost the same, thus the size of the electronic cloud is almost the same. The large difference between the two groups polarization is due to the large difference between the size of the electronic clouds of these two groups. The number of electrons in the organic molecules is between 43-48 while it is between 17-18 for the other group. The size of the dipole moment in a molecule has to do with the

Molecule Basis Set	Dipole Vector	Polarization Matrix			Polarization	Dipole	Ionization
	$e a_0$	$(a_0 C)^2/\text{Ha}$			$(a_0 C)^2/\text{Ha}$	$e a_0$	Energy Ha
CH ₃ CHO 6-31G*	0.220684 -0.379133 0.933483	20.5197 -3.66822 0.542298	-3.66822 21.1518 -2.33154	0.542298 -2.33154 27.8242	23.1652	1.03142	0.42370
CH ₂ OOH 6-31G*	0.286176 0.571986 -0.120396	15.8625 -2.36175 0.974793	-2.36175 12.0803 -0.0969484	0.974793 -0.0969484 27.3786	18.4405	0.650815	0.35599
CH ₃ CO 6-31G	-0.172214 -0.0119825 1.14413	19.2837 -2.73303 3.87320	-2.73303 20.5092 -2.92559	3.87320 -2.92559 10.9605	16.9178	1.15708	0.036987
CH ₃ CO 6-31G*	-0.126874 -0.0218898 0.922456	18.6342 -1.49973 1.14752	-1.49973 19.3487 -2.78451	1.14752 -2.78451 27.1416	21.7082	0.931397	0.36601
CH ₃ O ₂ 6-31G	-0.427158 ≈ 0.0 1.09072	15.7314 ≈ 0.0 3.23561	≈ 0.0 13.4917 ≈ 0.0	3.23561 ≈ 0.0 26.4226	18.5486	1.17138	0.46644
CH ₃ O ₂ 6-31G*	-0.261520 ≈ 0.0 1.05151	16.5724 ≈ 0.0 3.29620	≈ 0.0 14.7994 ≈ 0.0	3.29620 ≈ 0.0 26.5513	19.3077	1.08354	0.45637
CH ₃ OOH 6-31G	0.0277153 0.000174607 0.155655	18.5840 -0.00689651 0.878759	-0.00689651 13.1691 -0.0241449	0.878759 -0.0241449 27.3846	19.7126	0.158103	0.45114
CH ₃ OOH 6-31G*	-0.149029 -0.599099 0.207359	17.6031 -0.607352 1.587759	-0.607352 16.8866 1.08723	1.58776 1.08723 25.4935	19.9944	0.651250	0.44609

Table 2.12: Table of polarization, dipole moments and ionization energies for the organic molecules from the ab initio calculations performed using Gaussian 94. The electronic structure calculation theory used is MP2. Ha = Hartree.

difference between the different atoms' electronegativity in the molecule and their symmetry. Therefore the size of a molecule does not have any influence on its dipole moment. Calculating the dipole moment vectors and polarizability tensors using the

Molecule Basis Set	Dipole Vector	Polarization Matrix			Polarization	Dipole	Ionization
	$e a_0$	$(a_0 C)^2/\text{Ha}$			$(a_0 C)^2/\text{Ha}$	$e a_0$	Energy Ha
H ₂ O 6-31G	0.378610	6.79602	-1.00694	≈ 0.0	4.36473	0.969786	0.49799
	0.892826	-1.00694	4.84834	≈ 0.0			
	≈ 0.0	≈ 0.0	≈ 0.0	1.44984			
H ₂ O 6-13G*	0.337817	6.78525	-0.659751	≈ 0.0	5.04227	0.865304	0.49736
	0.796637	-0.659751	5.50920	≈ 0.0			
	≈ 0.0	≈ 0.0	≈ 0.0	2.83231			
HO 6-31G	-0.817600	6.09100	≈ 0.0	≈ 0.0	3.15552	0.817600	0.49920
	≈ 0.0	≈ 0.0	1.06964	≈ 0.0			
	≈ 0.0	≈ 0.0	≈ 0.0	2.30594			
HO 6-31G*	-0.732205	6.01730	≈ 0.0	≈ 0.0	3.74447	0.732205	0.50384
	≈ 0.0	≈ 0.0	2.42877	≈ 0.0			
	≈ 0.0	≈ 0.0	≈ 0.0	2.78738			
Molecule					Polarization $(a_0 C)^2/\text{Ha}$	Dipole $e a_0$	
H ₂ O	Experiment					0.724277	

Table 2.13: First part of the table: polarization, dipole moment and ionization energy for HO and H₂O from the ab initio calculations performed using Gaussian 94. The electronic structure calculation theory used is MP2. Second part of table: experimental dipole moment for H₂O from Refs. [130]. Ha = Hartree.

Gaussian 94 program package can have uncertainties of up to roughly 30 % [126].

In light of the theory described in this section, we have plotted the three interaction potentials and the total long-range potential of the different reaction and product channels for reactions 2.1 and 2.2 at 298 K in Figures 2.1 and 2.2. The general trend in the figures is that the dipole-dipole momentum (W_{dd}) has by far the largest contribution to the long-range potential, and the dispersion interaction is larger than the dipole-induced dipole interaction.

Eq. (2.8) is temperature dependent since Eq. (2.10) depends on the temperature. The temperature dependence of C is shown in Table 2.14. As the temperature increases W_{dd} decreases and the dipole-induced dipole moment will be increasingly important. In the cases studied in this chapter, the temperature must be around 1000 K to 6000 K before W_{dd} and $(W_{di} + W_{ii})$ contribute equally to the long-range potential. For the temperatures we are interested in, W_{dd} is the essential contributor to the long-range potential.

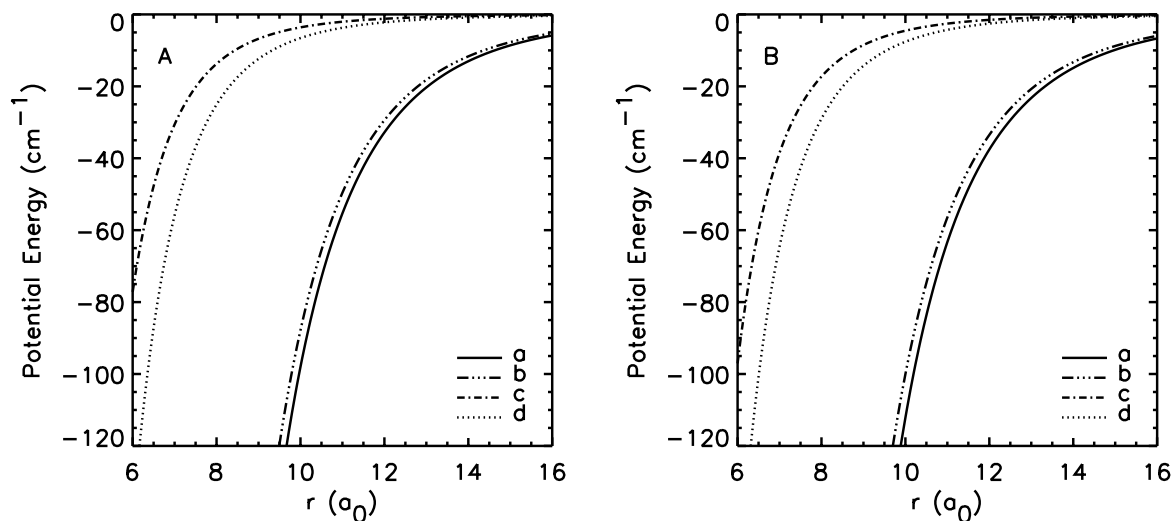


Figure 2.1: W_{dd} , W_{di} , W_{ii} and V_{LR} at 298 K for the molecules in the reactant (**Figure A**) and product channel (**Figure B**) for reaction 2.1. The dipole moments, ionization energies and polarization used in these functions are calculated using the 6-31G* basis set and given in Tables 2.12 and 2.13. **Curve a:** V_{LR} potential, **curve b:** W_{dd} potential, **curve c:** W_{di} potential, and **curve d:** W_{ii} potential.

Molecule System	Basis Set	C Hartree a_0^6
HO + CH ₃ CHO	6-31G*	120073./T + 51.3261
H ₂ O + CH ₃ CO	6-31G*	136746./T + 55.2491
HO + CH ₃ OOH	6-31G*	47870.7/T + 43.4403
H ₂ O + CH ₃ O ₂	6-31G*	185070./T + 55.1334
H ₂ O + CH ₂ OOH	6-31G*	66767.0/T + 44.8832

Table 2.14: Table of the constant C given in Eq. (2.8) from the ab initio calculations performed using Gaussian 94. The electronic structure calculation theory used is MP2.

2.3.2 Phase-Space Theory

Let us look at a general chemical reaction system: a molecule, A, composed of N atoms colliding with a molecule, B, composed of M atoms,



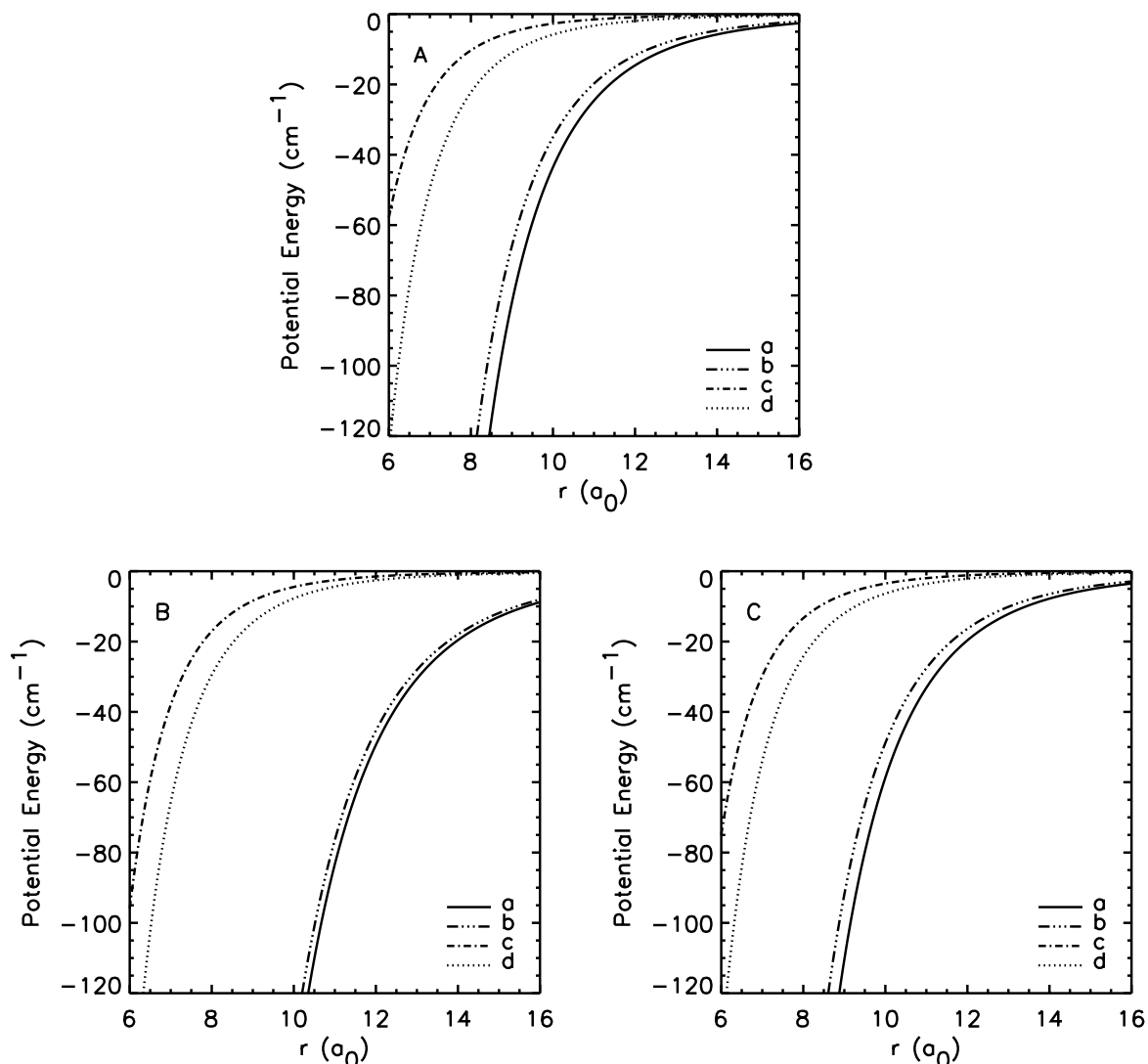


Figure 2.2: W_{dd} , W_{di} , W_{ii} and V_{LR} at 298 K for the molecules in the different reaction and product channels for reaction 2.2, **Figure A:** for HO + CH₃OOH, **Figure B:** for CH₃O₂ + H₂O, and **Figure C:** for CH₂OOH + H₂O. The dipole moments, ionization energies and polarization used in these functions are calculated using the 6-31G* basis set and given in Tables 2.12 and 2.13. **Curve a:** V_{LR} potential, **curve b:** W_{dd} potential, **curve c:** W_{di} potential, and **curve d:** W_{ii} potential.

and assume that the process described by this reaction takes place through different channels denoted α , β , γ etc. α describes the channel from the reactants to the complex $[A \cdots B]^\ddagger$, β , γ etc. are accessible channels for forming products from the complex.

The molecules in the different channels can be in different states. The states of such a system are specified by the molecules' vibrational quantum numbers, $\bar{\nu}_i$ and $\bar{\nu}_f$ ³, rotational quantum numbers, (\bar{j}^i, \bar{j}_z^i) and (\bar{j}^f, \bar{j}_z^f) , the relative translation

³ i relates to the quantum numbers of reactants A and B and f relates to the quantum numbers

energy (E_{trans}^i, E_{trans}^f), and finally the orbital angular momentum quantum numbers (l^i, l_z^i) and (l^f, l_z^f). The motion of the center of mass of A relative to B does not affect the statistics, therefore it is ignored.⁴

The theory of phase-space methods can be derived in several ways; here a derivation based upon quantum mechanics is given. Phase-space methods are based on three assumptions:

- conservation rules and detailed balance (Assumption I),
- formation (Assumption III) of a CoCo, and
- decomposition (Assumption II) of a CoCo ($[A \cdots B]^\ddagger$).

Assumption I – the conservation laws and detailed balancing must be obeyed. Thus, energy, total angular momentum and its projection on one axis, and linear momentum must be conserved.

The total energy of the reactants in reaction 2.15 is

$$E_{tot} = E_{trans}^{A,B} + E_{vib}^A + E_{vib}^B + E_{rot}^A + E_{rot}^B + V \quad (2.16)$$

The first term is the kinetic energy of the relative translational motion between the center of masses of molecules A and B. The second and third terms are the vibrational energies of A and B, respectively. The fourth and fifth terms are the rotational energies of A and B, respectively. Different molecules can possess different kinds of ro-vibrational motion. Expressions for these energies can be found in Tables 2.15 and 2.16. The last term in Eq. (2.16) is the potential energy of the system.

The total angular momentum is a sum of the orbital angular momentum and the rotational angular momenta for the reactants in reaction 2.15,

$$\bar{J} = \bar{l}^{A,B} + \bar{j}^A + \bar{j}^B \quad (2.17)$$

The first term is the orbital angular momentum, and the second and third terms are the rotational angular momenta of A and B, respectively.

Assumption II – two conditions must be fulfilled for a CoCo to be formed: the total energy of the reacting molecules can exceed the barrier of the effective potential energy⁵ and if the kinetic energy of the A-B system is sufficient to cross the barrier,

of their products.

⁴The number of quantum numbers that are required to describe a molecular state depend on the symmetry of the molecule. The description given in this section can be applied to every molecular system. Therefore, in order to give a general description we have used the compact form $\bar{v}r^x$, where x is either i or f , to describe the total number of rotational and vibrational quantum numbers for all the molecules in the reaction channels.

⁵The effective potential energy is the sum of the inter-molecular potential and centrifugal energy $[(L^i)^2 / 2\mu_{A,B}R^2]$, where $\mu_{A,B}$ is the reduced mass of the A-B system, R is the distance between the center of mass of the molecules, and L^i is the orbital angular momentum given by $(L^i)^2 = l^i(l^i + 1)\hbar^2$ (\hbar is Planck's constant divided by 2π)

Diatomic Molecule (one oscillator).
$E_{vib} = (v + \frac{1}{2}) \hbar\omega$
where ω is the vibrational frequency for the diatomic molecule and $v = 0, 1, 2, \dots$
Linear Triatomic Molecule (BCD) : (four oscillators).
$E_{vib} = (v_1 + \frac{1}{2}) \hbar\omega_1 + (v_{2a} + v_{2b} + 1) \hbar\omega_2 + (v_3 + \frac{1}{2}) \hbar\omega_3 = E_1 + E_{2a} + E_{2b} + E_3$
where ω_i are the four vibrational frequencies, $v_i = 0, 1, 2, \dots$ and $i = 1, 2a, 2b$ or 3
Spherical, Symmetric and Asymmetric Top Molecule : $s = 3n - 6$ oscillators.
$E_{vib} = \sum_i^s (v_i + \frac{1}{2}) \hbar\omega_i = \sum_i^s E_i$
where ω_i is the vibrational frequencies for the s oscillators and $v_i = 0, 1, 2, \dots$

Table 2.15: Expressions for the quantum mechanical vibrational energy for various molecules using the harmonic oscillator approximation. \hbar is Planck's constant divided by 2π .

a maximum value of L^i , L_{max}^i , for which scattering occurs will exist. Based upon these assumptions, the probability of forming CoCo from every channel is one if the energy of reacting molecules exceed the barrier of the effective potential energy and L^i is less than or equal to L_{max}^i . Otherwise it is zero. Thus the total cross section for formation of a CoCo can be written as

$$\sigma_{CoCo} = \frac{\pi \hbar^2}{2\mu_{A,B} E_{trans}^i} \sum_{l^i}^{l_{max}^i} (2l^i + 1) = \frac{\pi \hbar^2}{2\mu_{A,B} E_{trans}^i} (l_{max}^i + 1)^2 \quad (2.18)$$

Assumption III – decomposition of CoCo is uncorrelated with the modes of the reactants except through conservation laws and detailed balancing. Hence, there is an equal probability to decompose CoCo into the different channels.

Assumption I is required because energy and momentum must be conserved and the condition of detailed balance must be fulfilled to have a meaningful model of a chemical system. On the other hand Assumptions II and III are rather rough approximations – classical, quantum-classical and quantum mechanical dynamical simulations clearly show that the formation and decomposition of a CoCo cannot be considered to be that simple. CoCo can also be formed when the system's kinetic energy is lower than the effective potential energy. One example is that a CoCo is formed due to resonance behavior of the collision between A and B, e.g. due to tunneling through the barrier[133]. Another alternative under these conditions is the formation of non-resonance complexes. A CoCo formed under this condition has a very small probability of tunneling through the barrier[133]. These two cases will not contribute significantly to the reaction probability around room temperature,

Diatomic, Triatomic and Spherical Top Molecule
$E_{rot} = C j(j+1)$ <p>where $C = \frac{\hbar^2}{2I} j(j+1)$, I is the moment of inertia for a diatomic, triatomic or spherical top molecule, and $j = 0, 1, 2, \dots$</p>
Symmetric Top Molecule
$E_{rot} = C_a j(j+1) + (C_c - C_a)k^2 = E_{rot_j} + E_{rot_k}$ <p>where $C_a = \frac{\hbar^2}{2I_a}$ and $C_c = \frac{\hbar^2}{2I_c}$. If the symmetric top is prolate the principal moments of inertia are $I_a < I_b = I_c$, and if the top is an oblate the principal moments of inertia are $I_a = I_b < I_c$. $j = 0, 1, 2, \dots$ and $k = 0, \pm 1, \pm 2, \dots, \pm j$</p>
Asymmetric Top Molecule[132]
$E_{rot} = C_1 j(j+1) + C_2 k^2$ $+ C_2 (k^2 \sum_{n=2}^{\infty} \varepsilon_{0n} C_3^n + j(j+1) \sum_{n=1}^{\infty} \varepsilon_{1n} C_3^n + j^2(j+1)^2 \sum_{n=2}^{\infty} \varepsilon_{2n} C_3^n + \dots)$ $= E_{rot_j}^1 + E_{rot_k}^1 + E_{rot_k}^2 + E_{rot_j}^2 + E_{rot_j}^3 + \dots$ <p>where $I_c > I_b > I_a$, $a = \frac{\hbar^2}{2I_a}$, $b = \frac{\hbar^2}{2I_b}$, and $c = \frac{\hbar^2}{2I_c}$. The ε constants are given in Ref. [132]. For the near-prolate case ($b \approx c$) $C_1 = (b+c)/2$, $C_2 = a - (b+c)/2$, and $C_3 = \frac{b-c}{2(2a-b-c)}$. For the near-oblate case ($a \approx b$) $C_1 = (a+b)/2$, $C_2 = c - (a+b)/2$, and $C_3 = \frac{a-b}{2(a+b-2c)}$. $k_c = j$ when $k = 0$, $k_c = j - k$ when lower and $k_c = j - k + 1$ when upper.</p>

Table 2.16: Expressions for the quantum mechanical rotational energy for various molecules using the rigid rotor approximation. \hbar is Planck's constant divided by 2π . For the polyatomic molecules, a, b and c describe the three mutually perpendicular principal axes.

if the atoms taking part in the collision are heavy particles. Assumption II is a reasonable approximation for most of the large molecule systems that we wish to investigate with phase-space methods. Assumption III is reasonable for reactions where the lifetime of a CoCo is long, since then there is an equal probability of the CoCo decomposing into the available manifolds of the different reaction channels. On the other hand, if the reaction is very fast our method will overestimate the rate constant.

In statistical theory the CoCo is specified by J and J_z and E_{tot} . Therefore, the probability of forming a complex at a specific (J, J_z, E_{tot}) from the initial state $(\bar{v}j^i, l^i, E_{trans}^i)$ will be

$$\frac{1}{(2l^i + 1) \prod_k^{A,B} (2j^k + 1)} \quad \text{if } \bar{J} \text{ and } E_{tot} \text{ is conserved}$$

$$0 \quad \text{otherwise} \quad (2.19)$$

which gives

$$\sigma(\bar{v}r^i, l^i; J, J_z, E_{tot}) = \frac{\pi \hbar^2}{2\mu_{A,B} E_{trans}^i} \sum_{\left\{ \begin{array}{l} l^i \\ J \text{ and } E_{tot} \text{ conserved} \\ l^i \leq l_{max}^i \end{array} \right\}} (2l^i + 1) \frac{(2J + 1)}{(2l^i + 1) \prod_k^{A,B} (2j^k + 1)} \quad (2.20)$$

In Eq. (2.20) the summation over l^i is restricted to three constraints: first, conservation of total energy (Assumption I); second, conservation of total angular momentum (Assumption I); and third, the constraint $l^i \leq l_{max}^i$ (Assumption II). Although for atom-diatomic systems the “triangular” inequality $\left| l^{atom-diatom} - j^{diatom} \right| \leq J \leq \left| l^{atom-diatom} + j^{diatom} \right|$ will ensure conservation of angular momentum, the conservation of angular momentum in general cannot be treated in such a simple manner because we are dealing with systems composed of a larger number of atoms; this problem will be discussed in *Section 2.3.2.1*.

The three assumptions make it possible to write the cross section, for the process described by reaction 2.15, as a product of the cross section for formation of the CoCo (Eq. (2.20)) multiplied by the probability that it decomposes into products. This leads to the following state-to-state cross section

$$\sigma(\bar{v}r^i, E_{trans}^i; \bar{v}r^f, E_{trans}^f) = \frac{\pi \hbar^2}{2\mu_{A,B} E_{trans}^i \prod_k^{A,B} (2j^k + 1)} \sum_{l^i=0}^{l_{max}^i} \left\{ \sum_{\left\{ \begin{array}{l} J \\ J \text{ and } E_{tot} \text{ conserved} \end{array} \right\}} \sum_{\left\{ \begin{array}{l} l^f \\ J \text{ and } E_{tot} \text{ conserved} \end{array} \right\}} (2J + 1) P(J, E_{tot}; \bar{v}r^f, l^f, E_{trans}^f) \right\} \quad (2.21)$$

The conservation of energy (Assumption I) is ensured because the probability of decomposing the CoCo depends on E_{tot} .

The next step in the derivation of the cross section is to apply the principle of detailed balancing to Eq. (2.21). We consider the reactive collision $A+BC \rightarrow AB+C$, and let $P_{A+BC \rightarrow AB+C}$ be the reaction probability. The concept of detailed balancing is that $P_{A+BC \rightarrow AB+C} = P_{AB+C \rightarrow A+BC}$. In our model the principle of detailed balancing requires that

$$\prod_k^i (2j^k + 1) \mu_{A,B} E_{trans}^i \sigma(\bar{v}r^i, E_{trans}^i; \bar{v}r^f, E_{trans}^f) = \prod_k^f (2j^k + 1) \mu_f E_{trans}^f \sigma(\bar{v}r^f, E_{trans}^f; \bar{v}r^i, E_{trans}^i) \quad (2.22)$$

If we set

$$\sum_{\left\{ \begin{array}{c} l^x \\ \bar{J} \text{ and } E_{tot} \text{ conserved} \end{array} \right\}} P(J, E_{tot}; \bar{v}r^x, l^x, E_{trans}^x) =$$

$$P(J, E_{tot}; \bar{v}r^x, E_{trans}^x) \quad (2.23)$$

combine Eq. (2.22) with Eq. (2.21), and use the fact that $P(J, E_{tot}; \bar{v}r^f, l^f, E_{trans}^f)$ is independent of the final states and vice versa (Assumption III), we obtain

$$\sum_{J=0}^{\infty} (2J+1) P(J, E_{tot}; \bar{v}r^i, E_{trans}^i) \sum_{\left\{ \begin{array}{c} l^f \\ \bar{J} \text{ and } E_{tot} \text{ conserved} \\ l^f \leq l_{max}^f \end{array} \right\}} 1 =$$

$$\sum_{J=0}^{\infty} (2J+1) P(J, E_{tot}; \bar{v}r^f, E_{trans}^f) \sum_{\left\{ \begin{array}{c} l^i \\ \bar{J} \text{ and } E_{tot} \text{ conserved} \\ l^i \leq l_{max}^i \end{array} \right\}} 1 \quad (2.24)$$

The last summations in this equation are the total number of states accessible from a CoCo with a given (J, E_{tot}) , therefore we write

$$\sum_{\left\{ \begin{array}{c} l^x \\ \bar{J} \text{ and } E_{tot} \text{ conserved} \\ l^x \leq l_{max}^x \end{array} \right\}} 1 = N(\bar{v}r^x, E_{tot}, J) \quad (2.25)$$

Light[107] has shown that the probability for the decomposition of a CoCo is proportional to the number of states that can be formed from a given channel. That means the solution of Eq. (2.24) is

$$\frac{P(J, E_{tot}; \bar{v}r^i, E_{trans}^i)}{N(\bar{v}r^i, E_{tot}, J)} = \frac{P(J, E_{tot}; \bar{v}r^f, E_{trans}^f)}{N(\bar{v}r^f, E_{tot}, J)} = \text{constant} \quad (2.26)$$

Because the summation over the probabilities from all the (reactant and product) channels must be unity, the constant in Eq. (2.26) must be $(\sum_{x=\alpha, \beta, \dots} N(\bar{v}r^x, E_{tot}, J))^{-1}$, therefore

$$P(J, E_{tot}; \bar{v}r^f, E_{trans}^f) = \frac{N(\bar{v}r^f, E_{tot}, J)}{\sum_{x=\alpha, \beta, \dots} N(\bar{v}r^x, E_{tot}, J)} \quad (2.27)$$

The probability P in Eq. (2.21) does not depend on the initial quantum numbers, therefore the summation over l^i in Eq. (2.21) can be written according to Eq. (2.25) as $N(\bar{v}r^i, E_{tot}, J)$. The summation of P over l^f in Eq. (2.21) is written in Eq. (2.27). Thus, the total cross section, Eq. (2.21), becomes

$$\sigma(\bar{v}r^i, E_{trans}^i; \bar{v}r^f, E_{trans}^f) =$$

$$\frac{\pi \hbar^2}{2\mu_{A,B} E_{trans}^i \prod_k^{A,B} (2j^k + 1)} \sum_{J=0}^{\infty} (2J+1) \frac{N(\bar{v}r^i, E_{tot}, J) N(\bar{v}r^f, E_{tot}, J)}{\sum_{x=\alpha, \beta, \dots} N(\bar{v}r^x, E_{tot}, J)} \quad (2.28)$$

The reaction cross section given here depends on a specific chosen initial and final relative velocity between the molecules and their ro-vibrational state. This cross section can be summed in different ways to get less complete distributions. For example, assuming a Boltzmann distribution over the initial ro-vibrational states and then summing up over the initial and final ro-vibrational quantum numbers. This gives the total reaction cross section for the process

$$\sigma(E_{tot}, T) = \frac{\pi \hbar^2}{2\mu_{A,B}} \frac{1}{\prod_k^{A,B} Q_{rot}^k Q_{vib}^k} \sum_{J=0}^{\infty} (2J+1) \sum_{\bar{v}r^i} \left(\frac{N(\bar{v}r^i, E_{tot}, J)}{E_{trans}^i} \right) \frac{\sum_{\bar{v}r^f} N(\bar{v}r^f, E_{tot}, J)}{\sum_{x=\alpha, \beta, \dots} \sum_{\bar{v}r^x} N(\bar{v}r^x, E_{tot}, J)} \quad (2.29)$$

That means in Eq. (2.29), the different $(\bar{v}r^i)$ -cross sections are weighted with the rotational degeneracy of the two molecules divided by the rotational, Q_{rot}^k , and vibrational, Q_{vib}^k , partition functions of molecule A and B, respectively.

Our primary goal here is to calculate the overall rate constant. This can be done with the following procedure. The thermal rate constant from a given initial to final ro-vibrational state is found by averaging the total state to state reaction cross sections with respect to the Boltzmann distribution

$$k(\bar{v}r^i; \bar{v}r^f; T) = S \sqrt{\frac{8k_b T}{\pi \mu_{A,B}}} \int_0^{\infty} d(E_{trans}^i/k_b T) \exp(-E_{trans}^i/k_b T) \sigma(\bar{v}^i, \bar{j}^i, E_{trans}^i; \bar{v}^f, \bar{j}^f, E_{trans}^f) \quad (2.30)$$

where k_b is the Boltzmann constant, S is the symmetry factor for the reaction and T is the temperature. Again, the overall rate constant can be estimated by assuming a Boltzmann distribution over the initial ro-vibrational states and then summing up over all the possible ro-vibrational quantum numbers. This gives

$$k(T) = S \sqrt{\frac{8k_b T}{\pi \mu_{A,B}}} \int_0^{\infty} d(E_{tot}/k_b T) \exp\left(\frac{-E_{tot}}{k_b T}\right) P(E_{tot}, T) \quad (2.31)$$

where

$$P(E_{tot}, T) = \frac{\pi \hbar^2}{2\mu_{A,B} k_b T} \frac{1}{\prod_k^{A,B} Q_{rot}^k Q_{vib}^k} \sum_{J=0}^{\infty} (2J+1) \frac{\sum_{\bar{v}r^i} N(\bar{v}r^i, E_{tot}, J) \sum_{\bar{v}r^f} N(\bar{v}r^f, E_{tot}, J)}{\sum_{x=\alpha, \beta, \dots} \sum_{\bar{v}r^x} N(\bar{v}r^x, E_{tot}, J)} \quad (2.32)$$

The next step is to sum $\sum_{\bar{v}r^x} N(\bar{v}r^x, E_{tot}, J) = N(E_{tot}, J)$. Note that Eqs. (2.28)-(2.32) only apply to collisions between two molecules. However, Eqs. (2.28) and (2.29) can also be used for atom-molecule reactions by removing all the ro-vibrational terms of the species that corresponds to the atom.

2.3.2.1 Evaluation of $N(E_{tot}, J)$

In this section we describe how the total number of states, $\sum_{\bar{v}r^x} N(\bar{v}r^x, E_{tot}, J) = N(E_{tot}, J)$, accessible from a CoCo can be calculated for different kind of molecular systems[62].

We use the following notation: v_{max} = largest allowed vibrational quantum number (see Table 2.17), j_{max} = largest allowed rotational quantum number (see Table 2.18), and l_{max} = largest allowed orbital angular momentum quantum number (see Section 2.3.2.2).

Diatomic Molecule
$v_{max} = \frac{E_{tot} - V}{\hbar\omega} - \frac{1}{2},$ <p>where ω is the vibrational frequency for the diatomic molecule.</p>
Linear Triatomic Molecule
$v_{max_1} = \frac{E_{tot} - V}{\hbar\omega_1} - \frac{1}{2}$ $v_{max_{2a}}(v_1) = \frac{E_{tot} - E_{1a} - V}{\hbar\omega_2} - \frac{1}{2}$ $v_{max_{2b}}(v_1, v_{2a}) = \frac{E_{tot} - E_{1a} - E_{2a} - V}{\hbar\omega_2} - \frac{1}{2}$ $v_{max_3}(v_1, v_{2a}, v_{2b}) = \frac{E_{tot} - E_{1a} - E_{2a} - E_{2b} - V}{\hbar\omega_3} - \frac{1}{2}$ <p>where ω_i are the four vibrational frequencies and $i = 1, 2a$ or $2b$. E_{1a}, E_{2a} and E_{2b} are defined in Table 2.15.</p>
Spherical, Symmetric and Asymmetric Top Molecule
$v_{max_1} = \frac{E_{tot} - V}{\hbar\omega_1} - \frac{1}{2}$ $v_{max_2} = \frac{E_{tot} - V - E_1}{\hbar\omega_2} - \frac{1}{2}$ \vdots $v_{max_{s-1}} = \frac{E_{tot} - V - \sum_{i=1}^{s-2} E_i}{\hbar\omega_{s-1}} - \frac{1}{2}$ $v_{max_s} = \frac{E_{tot} - V - \sum_{i=1}^{s-1} E_i}{\hbar\omega_s} - \frac{1}{2}$ <p>where ω_i is the vibrational frequencies for the s oscillators. E_i is defined in Table 2.15.</p>

Table 2.17: Expressions describing how to select the maximum vibrational quantum number v_{max} for various molecules taking part in a molecular collision. E_{tot} and V are the total energy and the potential energy for the system under investigation.

Diatomic, Linear Triatom, Spherical Top Molecule
$j_{max} (j_{max} + 1) = \frac{E_a}{C}$
Symmetric Top Molecule
$j_{max} (j_{max} + 1) = \frac{E_a}{C_a}$
$(k_{max})^2 = \frac{E_a - C_a j(j+1)}{C_c - C_a}$
Asymmetric Top Molecule
$j_{max} (j_{max} + 1) = f(E_a) =$ the inverse of the expression for the energy of the asymmetric top molecule at $k = 0$
$k_{max}^2 = \frac{E_a - C_1 j(j+1) - C_2 j(j+1) \sum_{n=1}^{\infty} \varepsilon_{1n} C_3^n - C_2 j^2(j+1)^2 \sum_{n=2}^{\infty} \varepsilon_{2n} (C_3)^n + \dots}{(C_2 + C_2 \sum_{n=2}^{\infty} \varepsilon_{0n} (C_3)^n)^{-1}}$

Table 2.18: Expressions describing how to select the maximum rotational quantum number j_{max} and k_{max} for various molecules taking part in a molecular collision. E_a is the available energy for the vibrational degrees of freedom. The C and ε constants are defined in Table 2.16. \hbar is Planck's constant divided by 2π .

In the following, for systems with two or three reaction partners, the equations for the total number of states, $N(E_{tot}, J)$, at a given total energy and total angular momentum, are evaluated. The chemical systems involve atoms, diatomic molecules, linear triatomic molecules, and molecules having spherical, symmetric or asymmetric top symmetry.

Atom + Molecule Collisions

Consider the case where A represents an atom and B a molecule composed of N atoms. The total energy of such a system is

$$E_{tot} = E_{trans}^{A,B} + E_{vib}^B + E_{rot}^B + V \quad (2.33)$$

and the total angular momentum is

$$\bar{J} = \bar{l}^{A,B} + \bar{j}^B \quad (2.34)$$

From Eq. (2.33) we define the available energy as

$$E_{avab} = E_{tot} - E_{vib}^B - V \quad (2.35)$$

The first step in the evaluation of $N(E_{tot}, J)$ is to calculate the number of accessible states when the vibrational motion of the molecule is constant $N(\bar{v}^B, E_{tot}, J)$. From the equations for the quantum mechanical rotational energy in Table 2.16 we see that if B is a diatomic, linear triatomic or spherical symmetric top molecule the

rotational energies are identical. Therefore in this case the number of accessible states is written as

$$N(\bar{v}^B, E_{avab}, J) = \sum_{j^B=0}^{j_{max}^B} \sum_{\substack{J+j^B \\ l^{A,B} = |J-j^B| \\ l^{A,B} \leq l_{max}^{A,B}}} 1 \quad (2.36)$$

where $l_{max}^{A,B}$ is given in *Section 2.3.2.2*. On the other hand, if B is a molecule with symmetric top symmetry the expression of $N(\bar{v}^B, E_{avab}, J)$ becomes

$$N(\bar{v}^B, E_{avab}, J) = \sum_{j^B=0}^{j_{max}^B} \sum_{k^B=-j^B}^{j^B} \sum_{\substack{J+j^B \\ l^{A,B} = |J-j^B| \\ l^{A,B} \leq l_{max}^{A,B}}} 1 \quad (2.37)$$

When B is an asymmetric top molecule[132] it has three quantum numbers j , k and k_c , where j and k correspond to the same quantum numbers as for the symmetric case. When $k=0$, $k_c=j$, otherwise k_c is equal to $j-k$ or $j-k+1$. Let $\uplus_{k_c^B}$ describe the summation over k_c as described above, then the number of accessible states when B is an asymmetric top molecule is given by

$$N(\bar{v}^B, E_{avab}, J) = \sum_{j^B=0}^{j_{max}^B} \sum_{k^B=-j^B}^{j^B} \uplus_{k_c^B} \sum_{\substack{J+j^B \\ l^{A,B} = |J-j^B| \\ l^{A,B} \leq l_{max}^{A,B}}} 1 \quad (2.38)$$

The final step is to perform the summation over the vibrational motion of the molecules. If we define the following terms:

$$\begin{aligned} S_1^{diatom} &= \sum_{v^{diatom}=0}^{v_{max}^{diatom}} 1 \\ S_4^{triatom} &= \sum_{v_1^{triatom}=0}^{v_{max1}^{triatom}} \sum_{v_{2a}^{triatom}=0}^{v_{max2a}^{triatom}} \sum_{v_{2b}^{triatom}=0}^{v_{max2b}^{triatom}} \sum_{v_3^{triatom}=0}^{v_{max3}^{triatom}} 1 \\ S_s^{Sp} &= \left(\prod_{l=1}^s \sum_{v_l^{Sp}=0}^{v_{maxl}^{Sp}} \right) 1 \\ S_s^{Sy} &= \left(\prod_{l=1}^s \sum_{v_l^{Sy}=0}^{v_{maxl}^{Sy}} \right) 1 \\ S_s^{Asy} &= \left(\prod_{l=1}^s \sum_{v_l^{Asy}=0}^{v_{maxl}^{Asy}} \right) 1 \end{aligned} \quad (2.39)$$

we can write N for all the molecules in the following way:

$$N(E_{tot}, J) = S_t^B N(\bar{v}^B, E_{avab}, J) \quad (2.40)$$

where t is either one, four or s , and B is either a diatomic, triatomic, spherical top (Sp), symmetric top (Sy) or asymmetric top (Asy).

Molecule + Molecule Collisions

The expression for the number of accessible states for the collisions between two molecules is more complicated. This arises from the fact that the total angular momentum depends on two rotational angular momenta, one from molecule A and one from molecule B. The total angular momentum is

$$\bar{J} = \bar{l}^{A,B} + \bar{j}^A + \bar{j}^B \quad (2.41)$$

For the atom-molecule case we should find vectors of $\bar{l}^{A,B}$ and \bar{j}^B where their sum was equal to \bar{J} . Since \bar{J} consists of only two vectors we could place them in the two dimensional space and then find the necessary vectors. In the case of a molecule-molecule collision we must consider three vectors and the vectors must be placed in the three dimensional space to calculate the total angular momentum. Handling such a problem is rather complicated and not very practical. We can avoid this problem by simply rewriting Eq. (2.41)

$$\bar{J} = \bar{l}^{A,B} + \bar{w} \quad \text{and} \quad \bar{w} = \bar{j}^A + \bar{j}^B \quad (2.42)$$

Thus, if we find all possible vectors, \bar{w} , with the only restriction that $j^A \leq j_{max}^A$ and $j^B \leq j_{max}^B$ and then find the vectors that fulfill $\bar{J} = \bar{l}^{A,B} + \bar{w}$, we have circumvented the problem by reformulating the molecule-molecule case to be the same as the atom-molecule case. Therefore

$$N'(\bar{v}^A, \bar{v}^B, E_{avab}, J) = \sum_{j^A=0}^{j_{max}^A} \sum_{j^B=0}^{j_{max}^B(j^A)} 1 \quad (2.43)$$

if A and B are either diatomic, triatomic or spherical top molecules. If one of the molecules (e.g. A) is a symmetric top Eq. (2.43) becomes

$$N'(\bar{v}^A, \bar{v}^B, E_{avab}, J) = \sum_{j^A=0}^{j_{max}^A} \sum_{k^A=-j^A}^{j^A} \sum_{j^B=0}^{j_{max}^B(j^A)} 1 \quad (2.44)$$

and if both A and B are symmetrical top molecules, we have

$$N'(\bar{v}^A, \bar{v}^B, E_{avab}, J) = \sum_{j^A=0}^{j_{max}^A} \sum_{k^A=-j^A}^{j^A} \sum_{j^B=0}^{j_{max}^B(j^A)} \sum_{k^B=-j^B}^{j^B} 1 \quad (2.45)$$

where w in Eqs. (2.43)-(2.45) is given by $\sqrt{j^A{}^2 + j^B{}^2 - 2j^A j^B \cos(\theta)}$ ⁶, and θ is the angle between $\bar{l}^{A,B}$ and \bar{w} . Now adding the $\bar{l}^{A,B}$ vector to the equations and integrating over w , we can write the total number of accessible states as

$$N(\bar{v}^A, \bar{v}^B, E_{avab}, J) = N'(\bar{v}^A, \bar{v}^B, E_{avab}, J) \int_{w_{min}}^{w_{max}} \sum_{\substack{J+w \\ \{ \begin{array}{l} l^{A,B} = |J-w| \\ l^{A,B} \leq l_{max}^{A,B} \end{array} \}}} dw \quad (2.46)$$

where the last sum removes all the “forbidden” states. If the summation in Eq. (2.46) is replaced by an integral, the resulting double integral can easily be integrated analytically. The shaded and hatched area shown in Figure 2.3 illustrates the volume of integration.

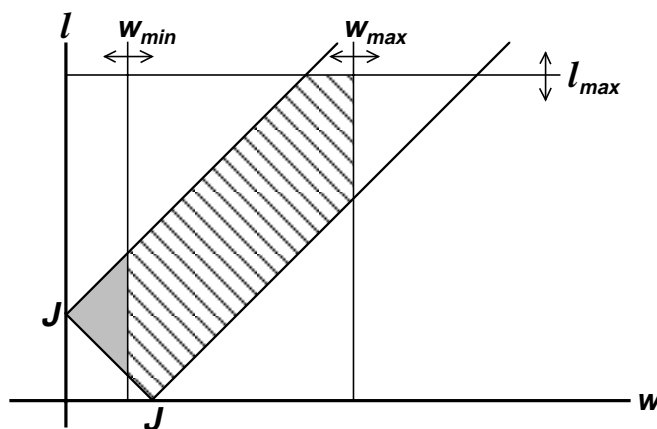


Figure 2.3: Region of integration in the l - w plane given by the double integral in Eq. (2.46), if the summation in Eq. (2.46) is exchanged with an integral.

Finally, we have to sum over the vibrational motion of the molecules. Because of the definitions given in Eq. (2.39) this will be

$$N(E_{tot}, J) = S_{t_1}^A S_{t_2}^B N(\bar{v}^A, \bar{v}^B, E_{avab}, J) \quad (2.47)$$

A + B + C Molecule Collisions

Here we will not derive the equations for all three molecule/atom cases, instead we will present the equations for the case where the three molecules are treated as asymmetric tops. It is relatively easy to revise the equations for asymmetric tops to apply them to simpler systems with different symmetry point groups or to an

⁶We do not give the three expressions for the cases where B or both A and B can be asymmetric top molecules, but comparing Eqs. (2.43-2.45) with Eqs. (2.36-2.38) and (2.52-2.53) these expressions are easily obtained.

atom. Following the concept used for the molecule-molecule case we write the total angular momentum

$$\bar{J} = \bar{l}^{A,B} + \bar{l}^{AB,C} + \bar{j}^A + \bar{j}^B + \bar{j}^C \quad (2.48)$$

and the total energy as

$$E_{tot} = E_{trans}^{A,B} + E_{trans}^{AB,C} + E_{vib}^A + E_{vib}^B + E_{vib}^C + E_{rot}^A + E_{rot}^B + E_{rot}^C + V \quad (2.49)$$

Making the same vector splitting as before, e.g.

$$\bar{J} = \bar{l}^{A,B} + \bar{w}_1, \quad \bar{w}_1 = \bar{l}^{AB,C} + \bar{w}_2, \quad \bar{w}_2 = \bar{j}^A + \bar{w}_3 \quad \text{and} \quad \bar{w}_3 = \bar{j}^B + \bar{j}^C \quad (2.50)$$

and denoting the angles between the vectors as

$$\theta_1 = \angle(\bar{l}^{AB,C}, \bar{w}_2), \quad \theta_2 = \angle(\bar{j}^A, \bar{w}_3) \quad \text{and} \quad \theta_3 = \angle(\bar{j}^B, \bar{j}^C) \quad (2.51)$$

we obtain for the total number for accessible states

$$N(\bar{v}^A, \bar{v}^B, \bar{v}^C, E_{tot}, J) = \sum_{j^A=0}^{j_{max}^A} \sum_{k^A=-j^A}^{j^A} \uplus_{k_c^A} \sum_{j^B=0}^{j_{max}^B(j^A)} \sum_{k^B=-j^B}^{j^B} \uplus_{k_c^B} \sum_{j^C=0}^{j_{max}^C(j^A, j^B)} \sum_{k^C=-j^C}^{j^C} \uplus_{k_c^C} \sum_{l^{A,B,C}=0}^{l_{max}^{A,B,C}} \int_0^{2\pi} d\theta_2 \int_0^{2\pi} d\theta_3 \int_0^{2\pi} d\theta_4 \sum_{\substack{J+w_1 \\ l^{A,B} \leq l_{max}^{A,B}}} \quad (2.52)$$

If the vibrational motion of the molecules is also included we get

$$N(E_{tot}, J) = S_{t_1}^A S_{t_2}^B S_{t_3}^C N(\bar{v}^A, \bar{v}^B, \bar{v}^C, E_{avab}, J) \quad (2.53)$$

Using this methodology it is simple to extend the equations to more advanced systems.

2.3.2.2 Assignment of Maximum Orbital Angular Momentum

The most critical part of the theory lies in the choice of the requirements for a CoCo. As stated in a previous section, a CoCo is formed when the kinetic energy of the A-B system can exceed the barrier of the effective potential, and the orbital angular momentum is less than or equal to the maximum orbital angular momentum when N is calculated. In this section two kinds of chemical reactions will be discussed:

- reactions with, and
- without potential energy barriers.

The methodology to calculate the maximum orbital angular momentum is taken from the work by Light and co-workers[107].

Reactions Without Potential Energy Barriers

Reactions without energy barriers are the simplest type to handle. The impact parameter, b , and l are related through the relationship $b^2 = \frac{l(l+1)\hbar^2}{2\mu E_{trans}}$. For reactions without energy barriers there exists a distance r^* where the molecule/atom-molecule is strongly coupled. If the reaction has no energy barrier it is reasonable to believe that r^* is approximately independent of the two species' internal energy, relative translational energy between them, and their rotational angular momenta. If it is assumed that the maximum of the effective potential occurs in that attractive region of the PES, the short-range part of the potential can be neglected. Therefore, the effective potential between the molecules in the channels is

$$V_{eff} = V_{LR} + \frac{l(l+1)\hbar^2}{2\mu} R^{-2} \quad (2.54)$$

where V_{LR} is given by Eq. (2.8). From this potential we can evaluate at which R the effective potential has its maximum value. The maximum angular momentum, $l_{max}(l_{max}+1)\hbar^2$, is then fixed by

$$l_{max}(l_{max}+1)\hbar^2 = n\mu C^{2/n}(2E_{trans}/(n-2))^{1-2/n} \quad (2.55)$$

This equation is most applicable to low energy conditions, but at higher energies the maximum impact parameter, b_{max} , given by this equation can be lower than r^* . This should not be allowed, therefore it is more reasonable to let b_{max} be the maximum of these two values. The result, expressed in maximum orbital angular momentum, is

$$l_{max}(l_{max}+1)\hbar^2 = \max \begin{cases} n\mu C^{2/n}(2E_{trans}/(n-2))^{1-2/n} \\ 2\mu E_{trans}(nC-2C)^{2/n}(2E_{trans})^{2/n} \end{cases} \quad (2.56)$$

Reactions With Potential Energy Barriers

It is more difficult to make an unambiguous theory for reactions with energy barriers. In this case, it is reasonable to assume that the formation of a CoCo depends on the energy barrier (E_b), r^* , the translational energy, the molecules' ro-vibrational energy etc. For the systems we are interested in it is not possible to make calculations of these items directly because this would demand too detailed PES information. The model is therefore developed from a reasonable guess, see *Section 4.2*. We set

$$l_{max}(l_{max}+1)\hbar^2 = \begin{cases} \left(E_{avab} - E_b - \frac{j_B(j_B+1)\hbar^2}{2I_B} - \frac{j_A(j_A+1)\hbar^2}{2I_A} \right) 2\mu_{A,B} r^{*2} & \text{if } E_b \geq 0 \\ \left(E_{avab} - \frac{j_B(j_B+1)\hbar^2}{2I_B} - \frac{j_A(j_A+1)\hbar^2}{2I_A} \right) 2\mu_{A,B} r^{*2} & \text{if } E_b < 0 \end{cases} \quad (2.57)$$

l_{max} for N-molecule/atom Systems

From a theoretical point of view a reaction can always be split up in a number of bi-molecular elementary reactions, therefore a theoretical description of atom-molecule and molecule-molecule reactions should be a complete description of all chemical reactions. The systems we are interested in are molecular collisions of large molecular systems. Experiments can be used to estimate reactants and products for some of these systems but finding the reaction mechanism and the transition state is very difficult. One example is the self reactions of the simplest peroxy radicals. This reaction has been investigated by Lightfoot et al.[75]. They could not estimate the reaction pathway but they were able to predict the products. This creates some problems because even though the reaction starts with the collision of two molecules, the products result from the composition of three molecules and the mechanism by which the molecules interact to form these products is unknown. Therefore, we also have to discuss what kind of concept that can be used to estimate l_{max} for N-molecule/atom systems. We will not discuss the general case even though it is possible because it will be much more illustrative to present the model for the three-molecule/atom case (A+B+C). From this case, it is simple to expand the model to more advanced systems.

For an A+B+C system we can have the following orbital angular momenta ($l^{A,B}$, $l^{C,AB}$), ($l^{A,C}$, $l^{B,AC}$) or ($l^{B,C}$, $l^{A,BC}$). Let us assume that we have sufficient information to calculate l_{max} for each of these orbital angular momenta, then we define[62]

$$l_{max}(l_{max} + 1) = \max \begin{cases} \min \{l_{max}^{A,B}(l_{max}^{A,B} + 1), l_{max}^{C,AB}(l_{max}^{C,AB} + 1)\} \\ \min \{l_{max}^{A,C}(l_{max}^{A,C} + 1), l_{max}^{B,AC}(l_{max}^{B,AC} + 1)\} \\ \min \{l_{max}^{B,C}(l_{max}^{B,C} + 1), l_{max}^{A,BC}(l_{max}^{A,BC} + 1)\} \end{cases} \quad (2.58)$$

The orbital angular momenta of the channel bottlenecks are found by taking $\min \{l_{max}^{N_1, N_2, N_3}(l_{max}^{N_1, N_2, N_3} + 1), l_{max}^{N_3, N_1, N_2}(l_{max}^{N_3, N_1, N_2} + 1)\}$ for each channel. The reaction bottleneck is defined as the maximum value of these channel bottlenecks, l_{max} ; the reaction bottleneck has the highest reaction probability to form a CoCo. By making such a definition of l_{max} , the expression of l_{max} is the same as we have found for bi-molecular reactions.

2.3.2.3 Calculations

In order to calculate the rate constant for reactions 2.1 and 2.2 using phase-space theory[63] spectroscopic data and potential energies are required. Furthermore, because the two reactions do not have an activation energy barrier⁷ information

⁷According to the experimental investigations these two reactions have a negative activation energy barrier. Therefore we have assumed that these reactions have no energy barrier.

about the dipole moments, isotropic polarizabilities and ionization energies for the molecules are required too. The electronic structure calculations needed have been presented and discussed in *Section 2.2.2*. Based on these ab initio calculations the long-range potentials for the five molecular systems were calculated and presented in *Section 2.3.1*.

The ab initio calculations showed that the exothermicity of the two reactions is around 0.6294 to 1.116 eV, see Table 2.7. Because of the theoretical concept used in the theoretical model and the high exothermicity of the reactions it is reasonable to assume that the non-reactive phase-space is very small compared to the reactive phase-space and as a result we perform the following and reasonable approximation

$$\frac{\sum_{\bar{v}^f} \sum_{\bar{j}^f} N(\bar{v}^f, \bar{j}^f, E_{tot}, J)}{\sum_{x=\alpha, \beta, \dots} \sum_{\bar{v}^x} \sum_{\bar{j}^x} N(\bar{v}^x, \bar{j}^x, E_{tot}, J)} \approx 1 \quad (2.59)$$

Direct counting is used to obtain $\sum_{\bar{v}^i} \sum_{\bar{j}^i}$.

Using dynamical simulation to solve the equations of motion of molecular collisions, the calculated cross sections only depend on the energy. So far this has also been the case for the different theoretical phase-space treatments. In the model presented in this chapter the long-range potential must be calculated in order to estimate the maximum reaction orbital angular momentum. Contrary to other phase-space treatments of bi-molecular reactions, we apply the theory to bi-molecular systems where both molecules are polar, therefore the cross section also becomes temperature dependent because of the dipole-dipole interaction, since Eq. (2.10) is temperature dependent. In Figure 2.4 the calculated phase-space at different temperatures and energies for the two reactions is plotted. The phase-space is calculated in each of the surfaces node-points. Two trends in the figures are seen: (i) the phase-space is increasing with the energy. This is obvious since increasing energy leads to more energy to be distributed between the different degrees of freedom of the molecular systems. (ii) the phase-space is decreasing with the temperature. In Table 2.14 we see that C decreases with the temperature therefore the maximum orbital angular momentum decreases with the temperature, which means the available phase-space will decrease with temperature.

Using the phase-space shown in Figure 2.4 we have calculated the rate constant for reactions 2.1 and 2.2. The results from these calculations will be presented and discussed together with the experimental results in the following sections.

Furthermore, we have made three additional phase-space calculations for both reactions[63]: First – we have taken the largest possible error of the zero-point vibrational energy $\approx 15\%$ and added it to the zero-point vibrational energy. Second – we have taken the largest possible error of $C \approx 30\%$ and subtracted it from C . Third – taking point one and two together, then calculating the rate constants on the basis of these phase-spaces.

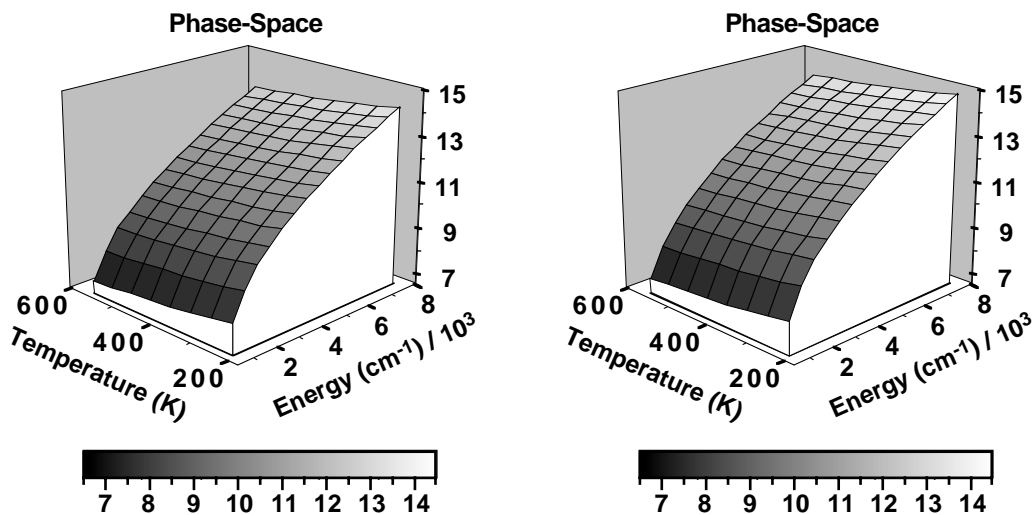


Figure 2.4: Figure on the left: the logarithm of the calculated phase-space $N(E_{tot}, T)$ for the HO + CH₃CHO system. Figure on the right: the logarithm of the calculated phase-space $N(E_{tot}, T)$ for the HO + CH₃OOH system.

2.3.2.4 Discussion of the Results

Reaction 2.1, Experiments

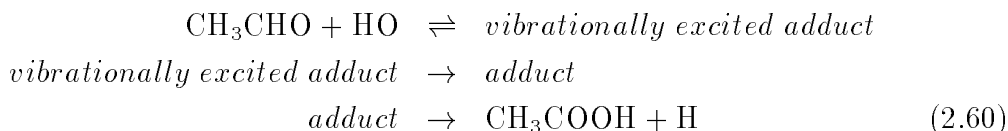
Aldehydes play an important role in tropospheric chemistry and combustion and the HO radical is an important oxidizing agent in these applications, therefore the reaction between hydroxy radicals and acetaldehyde has been investigated by many experimental groups[134, 135, 136, 137, 138, 139, 140, 141, 142, 143, 144]. In Tables 2.19 and 2.20 the rates given in Refs. [134, 135, 136, 137, 138, 139, 140, 141, 142, 143, 144] are summarized. In three of the experiments the temperature dependence of the reaction rate constant is measured[137, 140, 141] and all predict a negative activation energy.

The experiments performed on the system give an ambiguous answer of how the interaction between these two molecules take place. Since the bond dissociation energy of the H-atom attached to the carbonyl group (≈ 3.747 eV) is much lower than that attached to the methyl group (≈ 4.250 eV) it is reasonable to believe that the H-atom attached to the carbonyl group is the reactive one. Generally, it has been accepted that reactions between the HO radical and aldehydes take place via hydrogen abstraction of the H-atom placed on the carbonyl group[140, 141]. The majority of these reactions show positive activation energies. Atkinson and Pitts Jr.[137] argue that the measured negative activation energy for reaction 2.1 is an unusual feature for reactions occurring via H-atom abstraction, but negative temperature dependencies for reactions between HO radicals and CH₃SH, CH₃SCH₃, CH₃NH₂, C₂H₅NH₂, (CH₃)₂SNH, and (CH₃)₃N, and for Cl atoms with propane and *n*-butane are observed, and these are all H-atom abstraction reactions[137]. Semmes et al.[140] claimed that the negative temperature dependence they calculated for

Ref.	Temp. (K)	Rate Constant ($10^{-11}\text{cm}^3\text{s}^{-1}$)
[134]	300	1.6 ± 0.4
[134]	300	1.5 ± 0.375
[135]	300	≥ 2.0
[136]	298	1.9 ± 0.2
[137]	299.4	1.60 ± 0.16
[138]	298	1.5 ± 0.5
[138]	298	1.2 ± 0.50
[139]	300	1.6
[140]	298	1.22 ± 0.27
[141]	298	1.47 ± 0.28
[141]	298	1.42 ± 0.10
[142]	298	1.69 ± 0.35
[143]	298	1.7 ± 0.3
[144]	298	1.62 ± 0.10
This Work ^a [63]	300	19.7
This Work ^b [63]	300	18.5
This Work ^c [63]	300	12.2
This Work ^d [63]	300	11.5
This Work ^e [63]	300	0.820
This Work ^f [63]	300	0.771
This Work ^g [63]	300	0.510
This Work ^h [63]	300	0.479

Table 2.19: Rate constants for $\text{CH}_3\text{CHO} + \text{HO} \rightarrow \text{CH}_3\text{CO} + \text{H}_2\text{O}$. **a:** the theoretical results obtained using the model described in this chapter[62], **b:** the theoretical results obtained using the model described in this chapter under the assumption that the zero-point vibrational energy for all the molecules in the reaction is 15 % higher (within the uncertainty of the ab initio calculations), **c:** the theoretical results obtained using the model described in this chapter under the assumption that the maximum orbital angular momentum is 21 % lower (within in the uncertainty of the ab initio calculations), and **d:** the theoretical results obtained using the model described in this chapter under the assumption that the maximum orbital angular momentum is 21 % lower and the zero-point vibrational energy for all the molecules in the reaction is 15 % higher. **e-h:** same as for points **a-d** but where the rate constant is multiplied with the GSLCC factor, Eq. (2.62). For reaction 2.1 this factor is 1/24.

reaction 2.1 is within the possibilities of abstraction reactions. Michael et al.[141] suggested a new possible reaction mechanism occurring via an addition reaction, because of the negative temperature dependence:



and concluded that if this addition reaction is important, it is probable that the major product is the stabilized *adduct* radical, and the reaction process 2.60 will primarily occur in the high pressure limit. They also stated that reaction 2.1 is the most likely reaction because the dissociation energy needed to remove the H-atom on the carbonyl group is much lower compared with that of the methyl group.

Ref.	Temp. (K)	Rate Constant ($10^{-11}\text{cm}^3\text{s}^{-1}$)							
[137]	299.4	1.60 ± 0.16							
[137]	355.0	1.44 ± 0.15							
[137]	426.1	1.24 ± 0.13							
[141]	244.0	2.01 ± 0.10							
[141]	259.0	1.84 ± 0.13							
[141]	273.0	1.7325 ± 0.095							
[141]	298.0	1.47 ± 0.28							
[141]	298.0	1.42 ± 0.10							
[141]	333.0	1.3 ± 0.12							
[141]	355.0	1.4 ± 0.08							
[141]	367.0	1.415 ± 0.07							
[141]	373.0	1.5 ± 0.10							
[141]	393.0	1.16 ± 0.06							
[141]	420.0	1.17 ± 0.08							
[141]	424.0	1.06 ± 0.06							
[141]	433.0	1.10 ± 0.06							
[141]	466.0	1.15 ± 0.08							
[141]	468.0	1.04 ± 0.04							
[141]	492.0	1.04 ± 0.14							
[141]	499.0	0.92 ± 0.04							
[141]	528.0	0.99 ± 0.04							
[140]	253.0	1.4 ± 0.31							
[140]	298.0	1.22 ± 0.27							
[140]	356.0	1.07 ± 0.25							
[140]	424.0	1.10 ± 0.23							
		This Work[63]							
Temp. (K)	Rate Constant ($10^{-11}\text{cm}^3\text{s}^{-1}$)								
	<i>a</i>	<i>b</i>	<i>c</i>	<i>d</i>	<i>e</i>	<i>f</i>	<i>g</i>	<i>h</i>	
250	20.2	19.6	12.6	12.2	0.843	0.817	0.524	0.508	
300	19.7	18.5	12.2	11.5	0.820	0.771	0.510	0.479	
350	19.1	17.4	11.9	10.8	0.797	0.724	0.495	0.450	
400	18.6	16.3	11.5	10.1	0.773	0.678	0.481	0.421	
450	18.0	15.2	11.2	9.42	0.748	0.632	0.465	0.393	
500	17.3	14.1	10.8	8.76	0.723	0.587	0.449	0.365	
550	16.7	13.1	10.4	8.12	0.697	0.545	0.433	0.338	

Table 2.20: Rate constants for $\text{CH}_3\text{CHO} + \text{HO} \rightarrow \text{CH}_3\text{CO} + \text{H}_2\text{O}$. **a:** the theoretical results obtained using the model described in this chapter[62], **b:** the theoretical results obtained using the model described in this chapter under the assumption that the zero-point vibrational energy for all the molecules in the reaction is 15 % higher (within the uncertainty of the ab initio calculations), **c:** the theoretical results obtained using the model described in this chapter under the assumption that the maximum orbital angular momentum is 21 % lower (within the uncertainty of the ab initio calculations), and **d:** the theoretical results obtained using the model described in this chapter under the assumption that the maximum orbital angular momentum is 21 % lower and the zero-point vibrational energy for all the molecules in the reaction is 15 % higher. **e-h:** same as for the points **a-d** but where the rate constant is multiplied with the GSLCC factor, Eq. (2.62). For reaction 2.1 this factor is 1/24.

Recently D’Anna and Nielsen[145][146] discussed the HO-acetaldehyde reaction mechanism again, and they showed that reaction 2.1 could be an addition

reaction occurring via first an exothermic adduct formation before the H-C bond on the carbonyl group is cleaved:



They claim that the transition state for the formation of the adduct is very loose with a high density of states and a low energy threshold compared with the second transition state.

Reaction 2.1, Theoretical Derivations

Our results shows a negative temperature dependence which is also seen in the experimental measurements[137][140][141] (see Table 2.20), but the phase-space model overestimates the rate constants by a factor of 10-16 at 300 K (see Table 2.19). One of the main assumptions in the developed phase-space model is that all of the different decomposition channels of the collision complex are of equal probability. This favors reactions that occur via long-lived complexes. Therefore, it is reasonable that the model overpredicts rather than underpredicts the rate constants and that the model will give the best agreement with experiments if the reaction takes place through the formation of an adduct as suggested by D'Anna and Nielsen[145][146].

To improve the illustration of the difference between the experimental measurements and the theoretically determined rates, ratio plots between the theoretically calculated rates under different approximations and the NASA[29]/IUPAC[28] recommendations are shown in Figure 2.5⁸.

The curves in Figures 2.5A and 2.5B show that the theoretical model predicts the temperature dependence reasonably well, especially at high temperatures (the limit of no tunneling). Two trends are clear in the figures, first, when only the maximum angular momentum is decreased the rate constants decrease with the same factor at all temperatures. That means that the double integral illustrated in Figure 2.3 decreases with the same factor at all temperatures. Second, the number of vibrational states of an s -dimensional harmonic vibrator increases exponentially with the energy, therefore when the zero-point vibrational energy is increased by 15 % (as it is the case for *curve b* and *d*; compare with *curve a* in Figure 2.5) the phase-space decreases as the energy increases. Therefore, the rate constants will decrease compared to *curve a* with increasing temperature. These two trends are illustrated in Figure 2.6, where it is observed that the ratio is constant with increasing temperature but increases with increasing energy.

According to Semmes et al.[140] the energy barrier height should be zero and not all the vibrations should contribute to the formation of the transition state i.e.

⁸The NASA recommendation is based upon an average value from six of the experimental measurements mentioned in the beginning of this section as the rate for the reaction at 298 K. As activation energy NASA recommended the average value of the activation energy from the studies of Atkinson and Pitts Jr.[137], Semmes et al.[140] and Michael et al.[141]. IUPAC used the data from Niki et al.[136], Atkinson and Pitts Jr.[137] and Michael et al.[141] in their recommendation. The preferred value of IUPAC was obtained from a least-square analysis of the absolute rate coefficient from these studies.

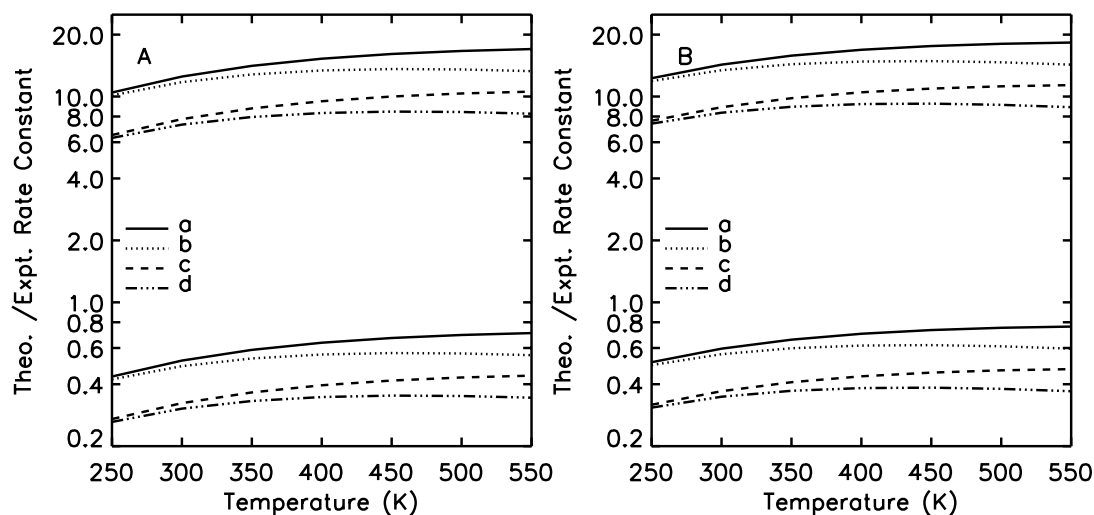


Figure 2.5: Ratio between theoretically calculated rate constants (this work[63]) and the rate constants recommended by NASA[29] and IUPAC[28] for reaction 2.1. In **Figure A**: the experimental values are those recommended by IUPAC[28], and in **Figure B**: the experimental values are those recommended by NASA[29]. **Upper curve a**: the theoretical results obtained using the model described in this chapter, **upper curve b**: the theoretical results obtained using the model described in this chapter under the assumption that the zero-point vibrational energy for all the molecules in the reaction is 15 % higher (within the uncertainty of the ab initio calculations), **upper curve c**: the theoretical results obtained using the model described in this chapter under the assumption that the maximum orbital angular momentum is 21 % lower (within the uncertainty of the ab initio calculations), and **upper curve d**: the theoretical results obtained using the model described in this chapter under the assumption that the maximum orbital angular momentum is 21 % lower and the zero-point vibrational energy for all the molecules in the reaction is 15 % higher. **Lower curves a-d**: same as for the upper curves but where the rate constants are multiplied with the GSLCC factor, Eq. (2.62). For reaction 2.1 this factor is 1/24.

the vibrational partition functions of the reactants and the transition state should be almost the same. Therefore, they believe that the reaction proceeds via a long-lived complex. This idea is supported by the work of D'Anna and Nielsen[145][146], but they also state that both addition and abstraction of reaction 2.1 could lead to the products H_2O and CH_3CO . It is impossible to consider this possibility in our model. Instead we have made a simple geometric assumption to include a short-lived complex in the model. This assumption is based on defining a Geometric Short-Living CoCo (GSLCC) factor. This is done by calculating electrostatic potentials for the reactants. The electrostatic potential of a molecule provides information about the electrostatic attractive regions of a molecule interacting with a positive or negative charge. The electrostatic potentials of each reactant are obtained from the electronic structure calculations and the potentials are visualized through the use of the quantum chemical program package SPARTAN[147].

For each reactant there are positive and negative electrostatic regions. For two reactants to interact and form bonds it is crucial that we have positive and negative regions approaching each other. For a given electrostatic surface we calculate the surface area of the reactants' attractive parts and we relate that to the total surface

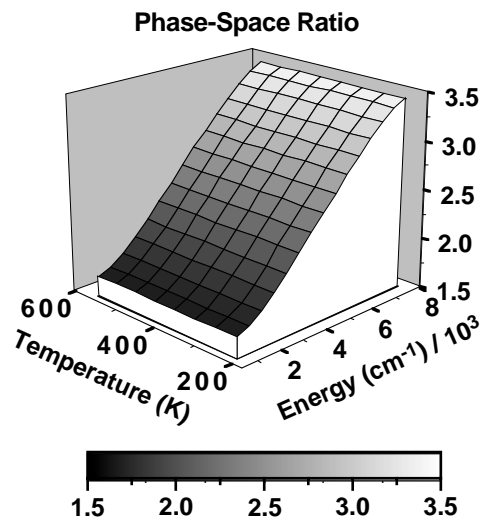


Figure 2.6: Ratio between two phase-spaces for the HO + CH₃CHO system. The numerator is the phase-space calculated using the model described in this chapter, the denominator is the phase-space calculated using the model described in this chapter under the assumption that the maximum orbital angular momentum is 21 % lower and the zero-point vibrational energy for all the molecules in the reaction is 15 % higher.

area of the contour electrostatic surfaces. The geometrical factor is then given as

$$\text{GSLCC} = \frac{\sigma_{\text{CH}_3\text{CHO}} + \sigma_{\text{HO}}}{T_{\text{CH}_3\text{CHO}} + T_{\text{HO}}} \quad (2.62)$$

where σ_x and T_x are the attractive and total electrostatic surface area of reactant x , respectively. Using this methodology we find that $\text{GSLCC} = 1/24$ for reaction 2.1. Results are plotted as the lower curves in Figure 2.5 and written in Tables 2.19 and 2.20.

We obtain a rate constant range from $k/24$ (short lived-complex) to k (long-lived complex), and the calculated/measured rate constants should be within this range. Figure 2.5 shows that a factor of $1/24$ multiplied to the rate constant under predicts the rate constants for reaction 2.1, but also that the calculated rate constants are closer to that of the short-lived complex than to that of the long-lived complex.

Reaction 2.2, Experiments

Methyl hydroperoxide is believed to be formed in the low temperature range of hydrocarbon combustions, and it is an important intermediate in the atmospheric oxidation of methane and non-methane hydrocarbons. We have tested the model on the atmospheric methyl hydrogen peroxide removal reaction, i.e. its reaction with hydroxid radicals, reaction 2.2. The two experimental measurements that have been conducted on this reaction[148, 149] show certain similarities – two H-atom abstraction reaction channels are observed: -OOH abstraction and -CH abstraction.

The dissociation energy of the $\text{CH}_3\text{OO-H}$ bond is ≈ 3.586 eV and ≈ 4.250 eV for the $\text{H-CH}_2\text{OOH}$ bond indicating that the $-\text{OOH}$ abstraction is the dominant channel, in contrast the other channel has three possible H-atoms that can participate in the abstraction reaction. However, both experiments indicate that the $-\text{OOH}$ abstraction is the dominant channel.

On the other hand, the values measured by the two experimental groups are quite different. Niki et al.[148] obtained a rate constant at 300 K that was approximately a factor of two higher than the results by Vaghjiani and Ravishankara[149], see Table 2.21.

Moreover, the branching ratio measured by Nike et al. was 1.30 ± 0.26 while Vaghjiani and Ravishankara found the ratio to be 2.52 ± 0.36 and they determined the ratio to be temperature independent. Recently, Junkermann and Stockwell[150] used these experimental results in two independent simulations in a study of photooxidants in the marine boundary layer of the tropical southern Atlantic Ocean. They found that using the measurements from Vaghjiani and Ravishankara lead to a loss of CH_3OOH that is far higher than that of H_2O_2 . This is not very likely because CH_3OOH is a heavier and less soluble molecule than H_2O_2 . This was not the case when results from Niki et al. were used and this favors the measurements by Niki et al.

The compound CH_2OOH , formed in the second reaction channel, is very unstable and breaks apart into HCHO and HO within a few microseconds. In the calculations we have assumed that the exothermicity is so large that no back reflection in the reaction can occur. This additional channel will not affect this fact because it is reasonable to believe that these two new species are more stable and therefore have a lower potential energy.

Even though Vaghjiani and Ravishankara measure a negative temperature dependence of the rate constants for both reaction channels, the possibility of a complex reaction pathway with an attractive part to the $\text{CH}_3\text{OOH-OH}$ interaction, rather than a simple H-atom abstraction mechanism, cannot be excluded.

Reaction 2.2, Theoretical Derivations

When using theoretical models to calculate for example rate constants, identical reaction pathways must be considered. For reaction 2.2a HO can only attack the methyl peroxide at the H-atom placed on the hydroxid, therefore the symmetry factor for this channel is one. This is not the case for the other channel. Here HO can attack one of the three identical H-atoms placed on the methyl group and the symmetry factor for this reaction is three. Using that the branching ratio for reaction 2.2 is temperature independent[149] and taking the ratio evaluated by Niki et al.[148]⁹ we find that the evaluated rate constants must be multiplied by a symmetry factor of

$$\frac{1.30}{1.00 + 1.30} + \frac{1.00}{3.00(1.00 + 1.30)} \approx 0.71 \quad (2.63)$$

In Table 2.21 the theoretically calculated rate constants are shown together with

⁹Using this result on the basis of the work by Junkermann and Stockwell[150]

Ref.	Temp. (K)	Rate Constant ($10^{-11}\text{cm}^3\text{s}^{-1}$)							
[149]	200	0.758 $\left\{ \begin{array}{l} +0.0832 \\ -0.0723 \end{array} \right.$							
[149]	250	0.627 $\left\{ \begin{array}{l} +0.0832 \\ -0.0723 \end{array} \right.$							
[149]	300	0.552 $\left\{ \begin{array}{l} +0.0592 \\ -0.0539 \end{array} \right.$							
[148]	300	1.0							
[149]	350	0.504 $\left\{ \begin{array}{l} +0.0537 \\ -0.0496 \end{array} \right.$							
[149]	400	0.471 $\left\{ \begin{array}{l} +0.0500 \\ -0.0466 \end{array} \right.$							
[149]	450	0.447 $\left\{ \begin{array}{l} +0.0472 \\ -0.0444 \end{array} \right.$							
		This Work[63]							
Temp. (K)		Rate Constant ($10^{-11}\text{cm}^3\text{s}^{-1}$)							
		<i>a</i>	<i>b</i>	<i>c</i>	<i>d</i>	<i>e</i>	<i>f</i>	<i>g</i>	<i>h</i>
200		15.4	15.2	9.54	9.41	0.495	0.489	0.308	0.303
250		15.0	14.4	9.32	8.97	0.484	0.466	0.301	0.289
300		14.6	13.5	9.04	8.38	0.469	0.435	0.292	0.270
350		14.1	12.5	8.75	7.75	0.454	0.403	0.282	0.250
400		13.6	11.5	8.47	7.14	0.440	0.371	0.273	0.230
450		13.2	10.6	8.21	6.57	0.426	0.341	0.265	0.212

Table 2.21: Rate constants for $\text{CH}_3\text{OOH} + \text{HO} \rightarrow \text{products}$. **a:** the theoretical results obtained using the model described in this chapter[62], **b:** the theoretical results obtained using the model described in this chapter under the assumption that the zero-point vibrational energy for all the molecules in the reaction is 15 % higher (within the uncertainty of the ab initio calculations), **c:** the theoretical results obtained using the model described in this chapter under the assumption that the maximum orbital angular momentum is 21 % lower (within the uncertainty of the ab initio calculations), and **d:** the theoretical results obtained using the model described in this chapter under the assumption that the maximum orbital angular momentum is 21 % lower and the zero-point vibrational energy for all the molecules in the reaction is 15 % higher. **e-h:** same as for the points **a-d** but where the rate constant is multiplied with the GSLCC factor, Eqs. (2.62) and (2.64). For reaction 2.2 this factor is 1/31.

the experimentally measured rate constants, we see that the theoretical model over predicts the rate constant for the process by a factor of 15-25 at 300 K, but this is quite natural because in the development of the theoretical model it was assumed that the process occur via a long lived complex. However, if the results by Niki et al. are considered to be more correct than the results measured by Vaghjiani and Ravishankara, as suggested by Junkermann and Stockwell, the model only over predicts the experimental results by a factor of 15 at 300 K.

For reaction 2.2 the GSLCC factor for channel a is calculated to be $1/38$ and $1/18$ for channel b . From that we get the following GSLCC factor for reaction 2.2:

$$\text{GSLCC} = \frac{1.30}{38 \times 0.71 \times 2.30} + \frac{1.00}{18 \times 0.71 \times 3.00 \times 2.30} \approx \frac{1}{31} \quad (2.64)$$

To compare the theoretical and experimental results, as we did for reaction 2.1, we plot the ratio between the theoretical calculation and the rates recommended by NASA[29] and IUPAC[28]¹⁰ in Figure 2.7. We see that the behavior of the curves

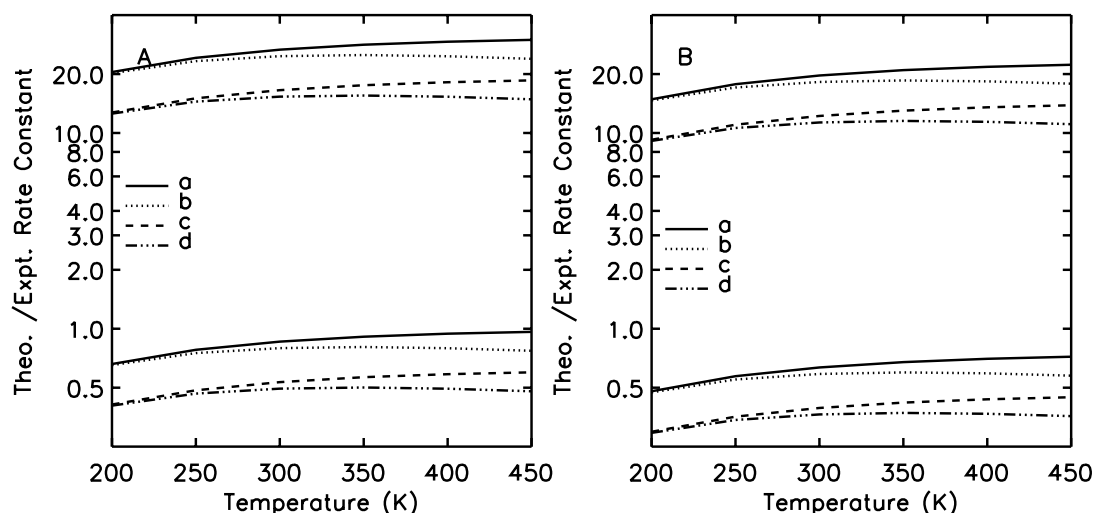


Figure 2.7: Ratio between theoretically calculated rate constants (this work) and the rate constants recommended by NASA[29] and IUPAC[28] for reaction 2.2. In **Figure A**: the experimental values are those recommended by IUPAC[28], and in **Figure B**: the experimental values are those recommended by NASA[29]. **Upper curve a**: the theoretical results obtained using the model described in this chapter, **upper curve b**: the theoretical results obtained using the model described in this chapter under the assumption that the zero-point vibrational energy for all the molecules in the reaction are 15 % higher (within the uncertainty of the ab initio calculations), **upper curve c**: the theoretical results obtained using the model described in this chapter under the assumption that the maximum orbital angular momentum are 21 % lower (within the uncertainty of the ab initio calculations), and **upper curve d**: the theoretical results obtained using the model described in this chapter under the assumption that the maximum orbital angular momentum are 21 % lower and the zero-point vibrational energy for all the molecules in the reaction are 15 % higher. **Lower curves a-b**: same as for the upper curves but where the rate constants are multiplied with the GSLCC factor, Eqs. (2.62) and (2.64). For reaction 2.2 this factor is $1/31$.

in Figure 2.7 is identical with that of the curves in Figure 2.5 for reaction 2.1, and the discussion therefore is identical with that in Section *Reaction 2.1, Theoretical Derivations*.

¹⁰NASA[29] recommended the average of the rates given by Nike et al.[148] and Vaghjiana and Ravishankara[149] at 298 K and they recommended the activation energy given by Vaghjiana and Ravishankara. IUPAC[28] only used the work by Vaghjiana and Ravishankara in their recommendation.

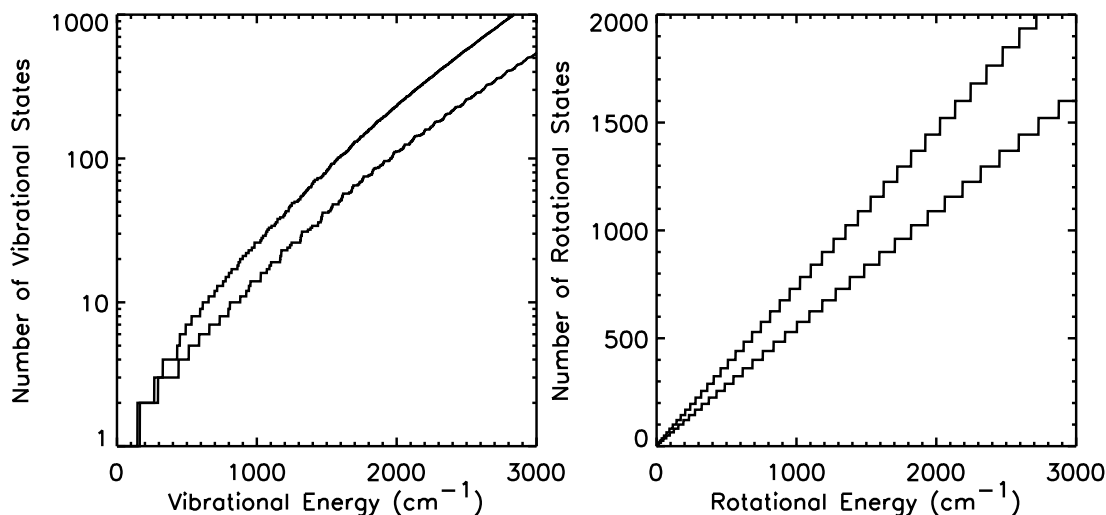


Figure 2.8: Figure on the left: Comparison between the number of vibrational states for CH_3OOH (**upper curve**) and CH_3CHO (**lower curve**) at energies from 1 to 3000 cm^{-1} . Figure on the right: Comparison between the number of rotational states for CH_3OOH (**upper curve**) and CH_3CHO (**lower curve**) at energies from 1 to 3000 cm^{-1} .

Comparison of the Results Derived for Reactions 2.1 and 2.2

Even though the input data for the model is quite different for reactions 2.1 and 2.2, we will try to make comparisons of the results obtained. In Figure 2.8 the rotational and vibrational number of states as a function of energy for the organic molecules CH_3OOH and CH_3CHO are plotted. Both graphs show that the number of rotational and vibrational states for methyl peroxide is higher than for acetaldehyde, while the C -constants have the opposite effect, see Figure 2.9. All in all, the calculated rates

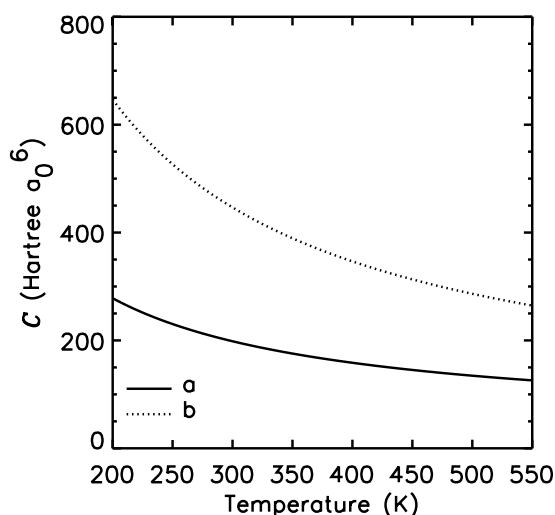


Figure 2.9: Comparison between the $C(T)$ -constants results obtain for reactions 2.1 and 2.2. **Curve a:** for the $\text{HO} + \text{CH}_3\text{OOH}$ system. **Curve b:** for the $\text{HO} + \text{CH}_3\text{CHO}$ system.

for reactions 2.1 and 2.2 are not very different. Figure 2.10 shows that the ratio between the theoretical rate constants calculated for reaction 2.1 divided by the

rate constant for reaction 2.2 varies between 0.70 to 0.75. This is in good agreement

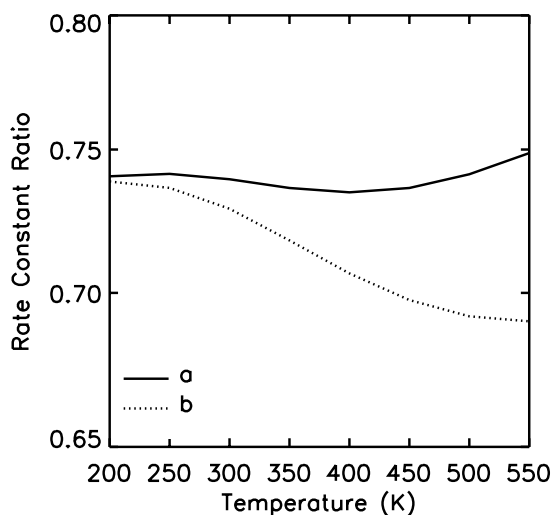


Figure 2.10: Ratio plots of the calculated rate constants obtain for reactions 2.1 and 2.2. Numerator: theoretical obtained rate for reaction $\text{HO} + \text{CH}_3\text{OOH} \rightarrow \text{products}$; denominator: theoretical obtained rate for reaction $\text{HO} + \text{CH}_3\text{CHO} \rightarrow \text{products}$. **Curve a:** the theoretical rate constants are obtained in the same manner as **Figures 2.5** and **2.7** curves **a** and **c**. **Curve b:** the theoretical rate constants are obtained in the same manner as **Figures 2.5** and **2.7** curves **b** and **d**.

with the result measured by Niki et al.[148] divided by the averaged value of the fifteen experimental measured rate constants at 300 K for reaction 2.1. This gives a ratio of 0.65.

2.4 Conclusion

Electronic structure calculations converge relatively easily when calculations of molecular properties for equilibrium configurations are performed. Already for self consistent field theory with a double zeta plus polarization type basis set the “geometry error” is often around ~ 1 kcal/mol or less. For most applications an MP2/(double zeta plus polarization type basis set) optimized geometry is normally sufficient. Translational and rotational contributions are easy to calculate, as they only depend on the molecular mass and the geometry, and are usually calculated with good accuracy. The vibrational effect is mainly the zero point energies, and it requires calculations of the frequencies. An accurate prediction of frequencies is fairly difficult, and in general values within 10 % to 15 % of the experimental measured values are obtained. But since the absolute value of the zero point energy is small, a large relative error is tolerable. Furthermore, the errors in calculated frequencies are to a certain extent systematic, and therefore can be improved by a uniform scaling.

The self consistent field theory error depends on the size of the basis set. The energy error, however, behaves asymptotically as $\sim L^{-6}$, where L is the highest angular momentum in the basis set, i.e. already with a basis set of triple zeta plus

double polarization function, the quality of the results are quite stable. Combined with the fact that an SCF/HF calculation is the least expensive ab initio method, this means that the SCF/HF error normally is not the limiting factor.

The molecular electronic structures used for calculations presented are based on the molecular-orbital method. Although this approach does not give a correct description of the dissociative processes in chemical reactions, we can conclude that it gives very accurate calculations of molecular properties near the molecules equilibrium configurations. And the model introduced in this chapter[62] only requires these equilibrium calculations. In general, we can conclude that the results given by the two different basis set have errors that are so small that we assume it to have very little influence when it is used on the phase-space model[62] presented.

The advantage of the phase-space model presented is that only a very limited number of input parameters are needed to calculate the rate constants for a reaction if the reactant/product channels are known. Spectroscopic data for the molecules existing in the reactant/product channels and their potential energy are required to calculate the number of states. To calculate the maximum impact parameter either the energy barrier is required or if the reaction channels do not have a barrier the dipole moments, polarization and ionization energy for the molecules are required. All these parameters can with good accuracy be calculated using electronic structure theory.

The presentation of phase-space theory given in this chapter is based upon a discrete expression of the theory unlike other applications of phase-space theory which have all used a continuous description[107, 151, 152, 153, 154, 155, 156]. This is possible today due to the increased capability of present computer technology. A continuous description of the interacting species' vibrational energy if the reaction does not have an energy barrier is physically wrong, as the spacing between the low lying vibrational energy levels is too large.

If it were possible to use full reaction dynamics, reaction path dynamics or transition state theory to calculate the rate constant for a molecular system, then these theoretical methods would of course be preferable. Unfortunately, for these methods the PES, the reaction path or information on the transition state are available for only a very limited number of molecular systems, and usually these are systems composed only of light elements.

The greatest approximation in our phase-space model concerns the formation and decomposition of the CoCo into the reaction channels. Even though Assumptions II and III appear to be logical from a classical point of view, classical dynamical simulations show[58, 59, 60, 61] that not every trajectory in compliance with Assumption II actually leads to the formation of a CoCo. Therefore, this method will tend to overestimate the probability of forming a CoCo unless there are competing quantum effects such as tunneling. Furthermore, many full dynamical simulations indicate that for triatomic systems most of the reactive collisions are almost collinear (see e.g. Ref. [59]) meaning that Assumption III also overestimates the reaction probability. Such considerations have not been taken in our model because we wanted the model to require the fewest possible number of potential energy points or

data concerning molecular properties as possible. Consideration of the two problems described requires further information about potential energy surfaces or molecular properties.

As well as predicting the distribution of product states from thermal reactions, ionic fragmentation and photochemical uni-molecular dissociation, the phase-space theory can be used to calculate state-to-state cross sections and rate constants, and total cross sections and rate constants for bi-molecular reactions proceeding through long-lived complexes, as we have shown.

Even though the model without the adjustments overestimates the rate constants for both reactions tested in this chapter compared with the results recommended by IUPAC and NASA, this is only by a factor of 10-25 at 300 K. This is a fairly good result considering the simplicity of the model. However, these recommendations are average values taken from the experimental measurements, thus for some of the experimental measurements our theoretical estimates are in better agreement than a factor of 10-25.

However, we have only performed a few tests of the model. Additional tests of other kinds of chemical reactions must be performed in order to confirm how well the model performs. We believe that our model can be applied to a large number of important reactions because if the reaction channels are known no other additional information about the system is needed to calculate a rate constant. Furthermore, the tests performed on reactions 2.1 and 2.2 show that even though the model overpredicts the rate constant for both reactions, it is by almost the same factor, and the model more or less reproduces the temperature dependence, i.e. the model reproduces important identical trends of the reactions.

In conclusion, our model is a good tool to estimate an approximate value of an unknown rate constant. Furthermore, multiplying the theoretically derived rate constants with the GSLCC factor, we obtained an interval ($[k/\text{GSLCC}, k]$) which is in the range of all the experimental measurements of the two reactions. This indicates the utility of the model, since the model is superior to the traditional correlation methods that can give errors with a factor between 10^2 and 10^4 . But if experimental measurements are available for a system of interest are these superior to the presented phase-space method.

Chapter 3

Air Quality Modeling

The atmosphere is a dynamic system with its gas particles continuously interacting with vegetation, oceans, biological and anthropogenic sources. Modeling of long-range transport of air pollutants involve four major stages:

- *emissions* from anthropogenic and natural sources, see introduction to *Chapter 1*,
- *transport* of air pollutants due to the wind field (advection),
- *diffusion*, horizontal and vertical, and
- *transformation of chemical compounds during transport*, which can be subdivided into:
 - *deposition*, dry and wet, and
 - *chemical reactions*, homogeneous and heterogeneous.

It is possible to establish and solve a partial differential equation system for each chemical species based on these different concepts. Traditionally, two methods have been used in relation to this: the Lagrangian and the Eulerian approach. In ACTM, the Lagrangian approach describes an air parcel of a chemical box that is advected according to the average wind speed and direction. In the Eulerian modeling framework a fixed grid domain is used where the number of species entering and leaving the grid cells through the walls are determined.

All physical processes are incorporated when using Eulerian models to solve long-range transport problems. Similar theoretical completeness is not the case for conventional Lagrangian models, because in these models it is for example not possible to incorporate the diffusion process into the dynamics. Attempts have been made to include diffusion into Lagrangian models, but it is not possible to do in a realistic manner. Even though Lagrangian models have these shortcomings, they also have some advantages over Eulerian models. Lagrangian models are much less computer time consuming and simpler to implement than Eulerian models. Due to these advantages Lagrangian models still have their legitimacy especially for

forecasting purposes. For such purposes a Lagrangian model makes it possible to implement more detailed chemical mechanisms, more accurate chemical solvers etc.¹ than in Eulerian models.

In this chapter the air quality model used to model surface ozone is Lagrangian and a Gear algorithm is used to solve the temporal and spatial concentration profiles of the chemical compounds. Based on the discussion above, it is natural to ask the question:

- which model is appropriate to use?

Several comparison studies between Lagrangian and Eulerian models have been made. The European Modelling of Atmospheric Constituents (EUMAC) sub-programme under EUROTRAC[41] has compared the Lagrangian EMEP model[16, 17, 18] with three Eulerian models: EURAD[39], LOTUS[38] and REM3[41] (see Table 0.3 in the *Introduction*). This study compared surface ozone, NO and NO₂ over Europe. The report concluded that for ozone all four models show reasonable agreement with measurements, and they found that the EURAD model overestimates while the three other models underestimate NO and NO₂. Another example is the comparison between the Eulerian Multi-layer Atmospheric CHEMistry Model (MACHO) and the Lagrangian EMEP model[157]. This work also showed insignificant differences between the ability of the models to estimate surface ozone.

In general, a large variety of Lagrangian and Eulerian model studies have been performed over Europe. All of these studies claim to have some success in reproducing some trends of regional surface ozone[11]. These examples clearly indicate that the Eulerian modeling concept has not shown any superior qualities in modeling surface ozone over the Lagrangian modeling concept.

Several meteorological conditions have an influence on the formation of surface ozone on a regional scale[2, 11, 103]:

- *large amounts of sunlight* to activate the photolysis processes,
- *warm temperatures* to increase the chemical processes and the evaporation of emissions from VOC,
- *low wind speed* (0-5 m/s will prevent dispersion), and
- *low ABL height* (will ensure a build up of precursors).

These conditions are fulfilled under stable summer anticyclones².

The opposite relationship between wind speed and high surface ozone concentration occurs[11] in autumn, winter and spring at some locations in Europe. These trends have been explained as a transport of air down to the surface with increased vertical exchange. Especially for the spring, the larger wind speed could be caused

¹Hence the chemistry is a very important issue in RAQM, see *Introduction* and *Section 1.1*.

²Anticyclones: the air moves clockwise slowly around a high pressure.

by sources from the free troposphere, probably due to an enhanced tropopause exchange.

Together with regional scale surface ozone episodes, mesoscale processes (small scale meteorology) are able to influence the concentration of surface ozone. These mesoscale processes influence the ozone on a local basis and do not lead to long-range transport of air pollutants. The mesoscale processes are[11]:

- land and sea breezes, an example of this exchange of polluted air between the inland and coastal is Los Angeles[158],
- local circulations of air from mountains down to valleys,
- the rougher and drier urban areas next to the surrounding rural regions can lead to mechanically driven turbulence and a deeper mixed layer, and
- during the night a stable layer can develop close to the surface shielding the air above from effects of surface drag and air. This creates an inertial oscillation with a maximum speed located around 100-300 meters above the surface.

In this chapter we will not focus on how different regional and small scale meteorological conditions influence the concentration levels of tropospheric ozone. Instead, the main focus of this chapter is to investigate how the two Lagrangian models, DACFOS and the newly developed MOON model, perform with respect to modeling surface ozone. This task is accomplished as follows:

- in *Section 3.1* a theoretical description of the MOON model is given. It covers:
 - the transport concept,
 - meteorological parameters,
 - dry and wet depositions,
 - emission inventories, and
 - a description of the differences between DACFOS and the MOON model,
- in *Sections 3.2* and *3.3* a comparison of the two models is performed
 - without transport (0-dimensional simulations), *Section 3.2*, and
 - with and without transport (3-dimensional simulations), *Section 3.3*.

The purpose of the 0-dimensional simulations is to test

1. the utility of parameterized photolysis rates versus “exact” photolysis rates, and
2. the differences between the VOC emission distribution key used in DACFOS versus that described in *Appendix B* and used in the MOON model.

The intention with the 3-dimensional simulations is to compare DACFOS with the MOON model in order to

1. test the utility of the QSSA solver versus a Gear algorithm,
2. test the utility of parameterized photolysis rates versus “exact” photolysis rates, and
3. validate the two models for 25 locations in Europe for the period of August 11 to August 24 1995,

and answer two questions:

1. does the MOON model model surface ozone better than DACFOS?
2. can a Gear based model, i.e. the MOON model, be used as a forecast model?
We present the computer time of the MOON model for 1000×14 trajectories on DMI’s supercomputer, an NEC SX-4.

Even though we have made the MOON model such that the RADM2, RACM, EMEP and Jacobson’s MCHs all can be used, only the results from the MOON model using the RACM MCH will be presented in this chapter.

We want to emphasize that the advantages of using a Gear algorithm to solve the chemistry are related to the fact that it is considered to be a benchmark solver. Furthermore, the Gear algorithm is a very robust method. Therefore, it is very easy to develop chemical compilers that make it very simple to implement chemical reactions into a given ACTM. This makes such a solver highly workable for scientific purposes in the field of atmospheric chemistry. These advantages, in the MOON model, have been extended such that new emission inventories, deposition parameters and initial concentrations can easily be changed or improved.

Traditional Lagrangian models are single-trajectory models which means that the entire trajectory is run to completion before the next is started. Such a numerical approach would be too computationally time consuming for our purposes, because we want to benefit from the advantages of a Gear algorithm. Therefore we have developed a multi-trajectory model, the MOON model, based on the “Eulerian” SMVGEAR solver developed by Jacobson[56]. This model can run a large number of trajectories simultaneously. The primary advantage of this model is that the algorithm is vectorizable with respect to trajectories. Tests performed by Jacobson[56] show that such a vectorization is highly preferable compared with codes that vectorize around the chemical species, see *Appendix C.2*. In *Appendix C.2* we have outlined the numerical concept used to solve the chemistry in the MOON model. In *Appendix D* we present a complete description of all input parameters, input files and subroutines necessary to run the model. Finally, in *Appendix C.1* a description of the chemistry solver in DACFOS is outlined.

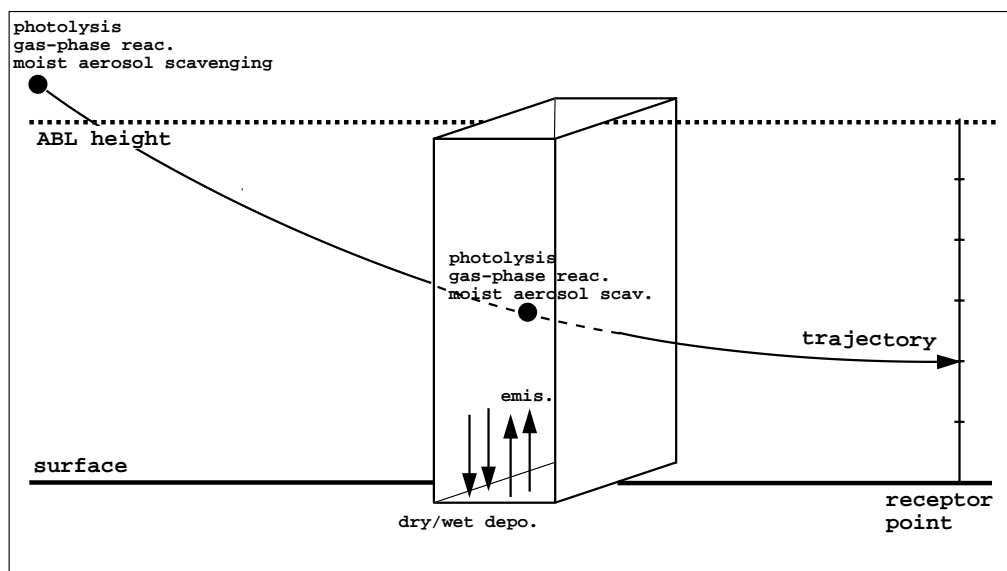


Figure 3.1: Schematic description of the MOON model. During the period of time the particle spends above the ABL the emission uptake and deposition processes are suspended. When the particle enters the ABL, a squared chemical box is assumed in which dry and wet depositions and emission from anthropogenic and natural sources enter and exit the box.

3.1 MOON Model: Theory

For Lagrangian models the major stages described in the introduction to this chapter can be split in two tasks the solution of³:

1. the transport of air pollutants, *Section 3.1.1*, and
2. the emission and transformation of chemical compounds along the line of transport calculated under the first task, *Section 3.1.2*.

In Figure 3.1 a simplified illustration of the model is presented. When the trajectory is in the free troposphere, we suspend the emission uptake and the deposition processes. When it is inside the ABL, a squared chemical box from the Earth surface up to the ABL height is considered. Inside this squared box full vertical mixing is assumed.

The meteorological data used to run the model are based upon data from the high-resolution numerical weather prediction model DMI-HIRLAM, which is operational at DMI. In 1995, DMI-HIRLAM was run over two different areas. The large version covered Greenland and Europe, the middle of the North American continent in the west and extended into Russia in the east. The small-area version,

³The different theoretical aspects for the MOON model described in this section are identical with DACFOS if nothing else is stated.

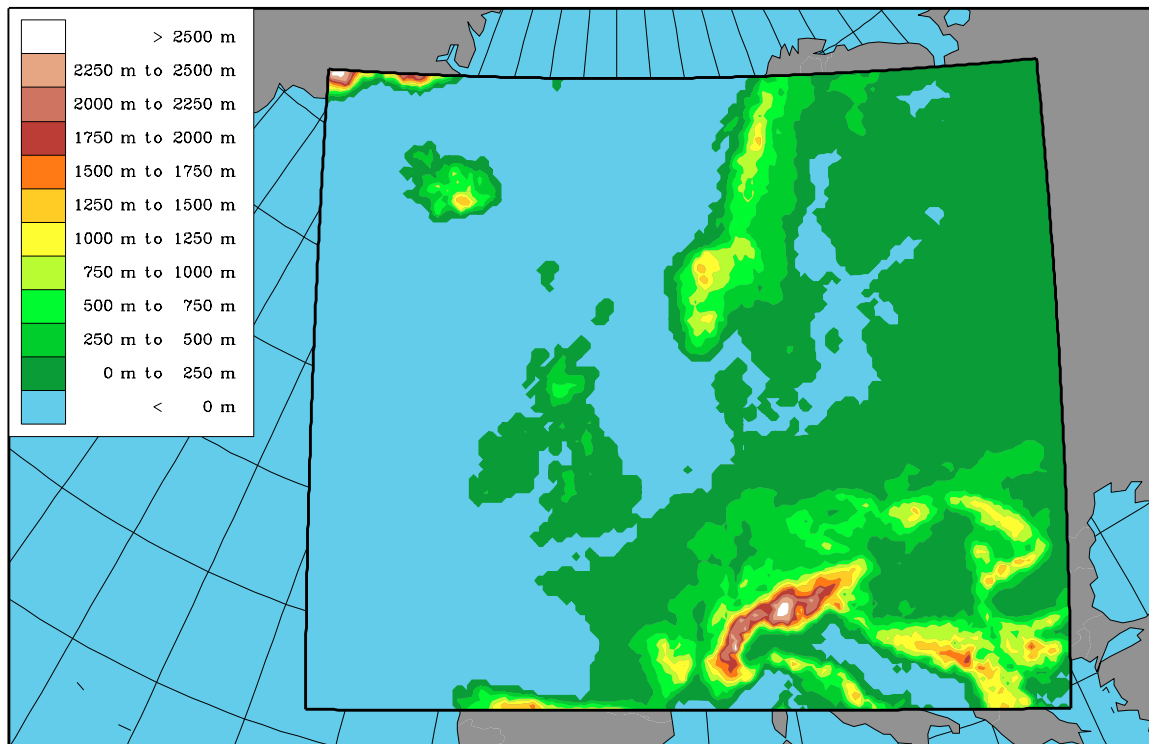


Figure 3.2: Orography of the small-area version of DMI-HIRLAM in 1995.

illustrated in Figure 3.2, covers Europe and is the one used in this study. The grid resolution for the small-area is horizontally $16 \times 16 \text{ km}^2$ with a vertical resolution of 31 layers, see the illustration in Figure 3.3. Below and in *Appendix D*, the required meteorological data for running the MOON model are outlined.

3.1.1 Transport

The MOON model is a 3-dimensional single-layer backward trajectory model. The 3-dimensions are related to the wind field. This is different from other backward trajectory models where the trajectories are derived from a 2-dimensional wind field at a given pressure level, see *Introduction, Danish Atmospheric Chemistry Forecasting System*. The advantage of the 3-dimensional description is that the trajectories follow the orography, while in the 2-dimensional description in a given pressure level, the trajectories may pass through for example mountains.

The advection of a Lagrangian model is given by

$$\frac{d\bar{r}}{dt} = \bar{v} \quad (3.1)$$

where \bar{r} is the position vector, \bar{v} is the three dimensional wind field vector and t is the time. The Lagrangian 3-dimensional advection equation is solved by an iterative method involving linear spatial and temporal interpolation.

The meteorological data used in the MOON model (and DACFOS) are averaged meteorological data calculated by linear interpolation from the four closest

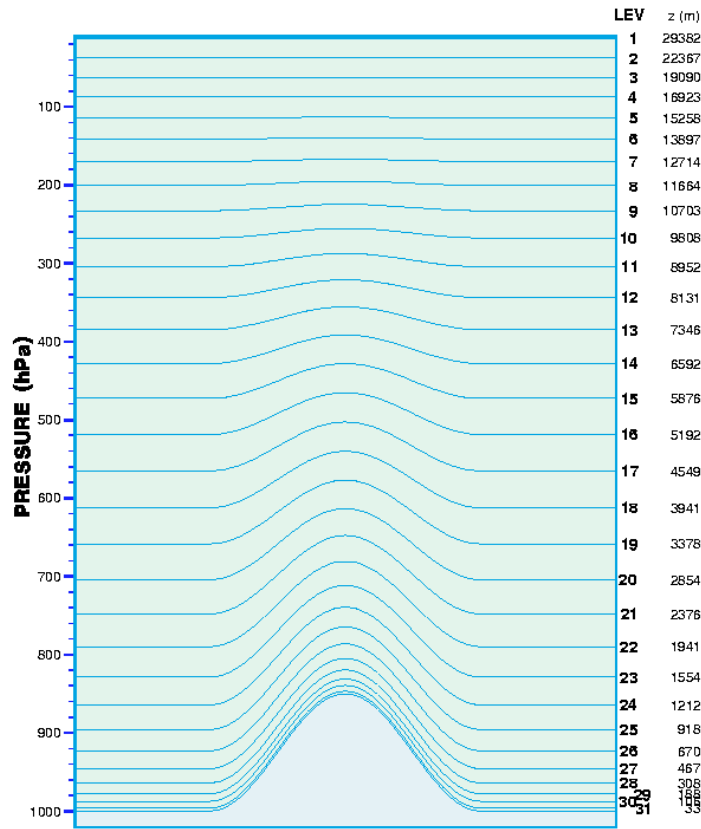


Figure 3.3: Vertical resolution of DMI-HIRLAM.

DMI-HIRLAM grid points.

3.1.2 Emissions and Transformation of Chemical Compounds During Transport

When the trajectory is in the free troposphere the chemical box solves the problem

$$\frac{dc_i}{dt} = P_i(\bar{c}, t, \bar{k}) - L_i(\bar{c}, t, \bar{k}) c_i \quad (3.2)$$

where $i \in \{1, 2, \dots, n\}$, n is the number of chemical compounds in the model, c_i is the concentration of the i th chemical compound, $P_i(\bar{c}, t, \bar{k})$ and $L_i(\bar{c}, t, \bar{k}) c_i$ are the production and loss terms of chemical compound i , \bar{k} denotes the reaction rates, and t the time.

Inside the ABL, the mass balance of the chemical box is given by the differential equations:

$$\begin{aligned} \frac{dc_i}{dt} = & -(k_{w_depo}^i + k_{d_depo}^i) c_i(x, y, z, t) \\ & + \{c_i\} + P_i(\bar{c}, t, \bar{k}) - L_i(\bar{c}, t, \bar{k}) c_i \end{aligned} \quad (3.3)$$

The first two terms on the right hand side of Eq. (3.3) describe dry and wet depositions, the next term is the emission and the final two terms are for the chemical reaction system. In the following subsections a description of these different elements in the MOON model is given.

As explained in *Appendix D* emissions and depositions are implemented in the MOON model as chemical reactions. Therefore, the numerical problem of Eq. (3.3) can be converted into Eq. (3.2).

The ABL Height

The ABL height (h_{mix}) is in the MOON model used to turn emissions and depositions on and off. Since there is no physical isolation of the ABL from the free troposphere, the ABL height is also an important parameter when the exchange of pollutants between the free troposphere and the ABL is simulated. Therefore, a good estimate of h_{mix} is important for the MOON model. In this context h_{mix} is estimated by the bulk Richardson number approach[159] since this method is robust and reasonably accurate, and applicable for use where the vertical resolution of temperature and wind is given by numerical weather prediction models.

The Richardson number (Ri) is given by[159]

$$Ri = \frac{g z (\theta_v - \theta_s)}{\theta_s (u^2 + v^2)} \quad (3.4)$$

where g is the gravitational acceleration, z is the height above the surface, θ_v is the potential temperature at height z , θ_s is the potential temperature at the surface and (u, v) are the horizontal wind components at height z . From Eq. (3.4) h_{mix} is given by the height at which the bulk Richardson number reaches a critical value. It was found that for the DMI-HIRLAM the critical values of the bulk Richardson number are in the range of 0.15 to 0.35. This large range of values indicates the robustness of the method. A value of $Ri = 0.25$ was used to calculate h_{mix} for the trajectories.

Exchange Mechanisms Between the ABL and the Free Troposphere

The ABL has a diurnal variation and during nighttime h_{mix} is low. In the morning the ABL expands due to convection. When the ABL is expanding, an exchange with air from the free troposphere will occur. This exchange must be included in the MOON model. Since full vertical mixing is assumed, and no exchange with the free troposphere occurs when the ABL is decreasing, the following mathematical description of this problem can be written:

$$c_i = \begin{cases} c_i^{ABL} & \Delta h_{mix} \leq 0 \\ \left(\frac{\Delta h_{mix}}{h_{mix}} - 1 \right) c_i^{ABL} + \frac{\Delta h_{mix}}{h_{mix}} c_i^{BC} & \Delta h_{mix} > 0 \end{cases} \quad (3.5)$$

where c_i^{ABL} is the concentration of i th species in the ABL if no expansion of the ABL would occur, c_i^{BC} the background tropospheric concentration and Δh_{mix} the

expansion of the ABL. The term c_i^{BC} is calculated from the parameters given in Table 3.1.

The parameters in Table 3.1 are also used to initialize the concentrations in the MOON model. The initialization of chemical species and calculation of c_i^{BC} in

<i>Seasonal Dependent Background Concentration Parameters</i>												
Jan.	Feb.	Mar.	Apr.	May	Jun.	Jul.	Aug.	Sep.	Oct.	Nov.	Dec.	
<i>O₃ (ppbV, Land)</i>												
35.0	35.0	35.0	45.0	50.0	50.0	47.5	45.0	40.0	35.0	35.0	35.0	
<i>O₃ (ppbV, Sea)</i>												
28.0	28.0	28.0	36.0	40.0	40.0	38.0	36.0	32.0	28.0	28.0	28.0	
<i>PAN (pptV, Land/Sea)</i>												
45.5	45.5	45.5	262.5	350.	280.	192.5	147.	94.5	45.5	45.5	45.5	
<i>Background Concentration Parameters</i>												
Species	<i>Land</i>		<i>Sea</i>									
NO (ppbV)	0.20		0.05									
NO ₂ (ppbV)	0.50		0.05									
HNO ₃ (ppbV)	0.30		0.10									
SO ₂ (ppbV)	0.25		0.10									
HCHO (ppbV)	0.25		0.25									
H ₂ O ₂ (ppbV)	2.00		2.00									
CO (ppbV)	150.		150.									
H ₂ (ppbV)	500.		500.									
CH ₄ (ppmV)	1.40		1.40									
O ₂ (%)	20.9		20.9									
N ₂ (%)	78.1		78.1									
<i>Latitude Dependent Parameters</i>												
	O ₃	NO	NO ₂	HNO ₃	SO ₂	HCHO	PAN					
[0;32.5[1.00	0.05	0.05	1.00	0.05	1.00	0.15					
[32.5;37.5[1.03	0.15	0.15	1.00	0.15	1.00	0.33					
[37.5;42.5[1.05	0.30	0.30	1.00	0.30	1.00	0.50					
[42.5;47.5[1.02	0.80	0.80	0.85	0.80	0.85	0.80					
[47.5;52.5[1.00	1.00	1.00	0.70	1.00	0.70	1.00					
[52.5;57.5[0.92	0.60	0.60	0.55	0.60	0.55	0.75					
[57.5;62.5[0.85	0.20	0.20	0.40	0.20	0.40	0.50					
[62.5;67.5[0.82	0.12	0.12	0.30	0.12	0.30	0.30					
[67.5;90.0]	0.80	0.05	0.05	0.20	0.05	0.20	0.10					

Table 3.1: Applied background concentration parameters and latitude dependent parameters [13] used by the MOON model. The background concentrations c_i^{BC} are calculated by multiplication of the background concentration parameters with the latitude dependent parameters.

DACFOS are described in Table 3.2.

Emissions

The MOON model uses emissions from the EMEP grid from 1994, this inventory gives data for NO_x , SO_2 , non-methane VOC and isoprene[101]. The EMEP emission data are given in emission per unit mass per year in the EMEP grid covering the European continent and the Atlantic Ocean. As a first approximation, we have converted these emission data into emissions on a daily basis. The MOON model's horizontal coordinates are longitude and latitude. In order to use the emission inventory from EMEP the conversion from latitude (ϕ) and longitude (λ) to EMEP coordinates in a 50×50 km grid is made:

$$\begin{aligned} x_{EMEP} &= x_{pol} + C_{EMEP} \times \tan(\pi/4 - \phi/2) \times \sin(32 + \lambda) \\ y_{EMEP} &= y_{pol} - C_{EMEP} \times \tan(\pi/4 - \phi/2) \times \cos(32 + \lambda) \end{aligned} \quad (3.6)$$

where x_{pol} is the x_{EMEP} of the North Pole, y_{pol} is the y_{EMEP} of the North Pole, $C_{EMEP} = R_{Earth}/r_{grid} \times (1 + \sin(\pi/3))$, R_{Earth} is the radius of the Earth and r_{grid} is the grid length.

These 2-dimensional daily emissions from the 50×50 km grid are assumed to be completely mixed in the square box shown in Figure 3.1 when the air parcel is below the ABL height, otherwise the emissions are turned off. Therefore, we have

$$\{c_i\} = \begin{cases} \frac{EMIS_{c_i}}{h_{mix}} & \text{if } h_{mix} > h \\ 0.0 & \text{otherwise} \end{cases} \quad (3.7)$$

where h is the height of the trajectory and $EMIS_{c_i}$ is the two dimensional emission of c_i from a 50×50 km square adjusted with the density of the air (DMI-HIRLAM data) and surface temperature (DMI-HIRLAM data).

The emission ($EMIS_{c_i}^{EMEP}$) inventory is distributed in the MOON model ($EMIS_{c_i}^{MOON}$) as follows, for SO_2

$$EMIS_{SO_2}^{EMEP} = \begin{cases} 95\% EMIS_{SO_2}^{MOON} \\ 5\% EMIS_{sulphate}^{MOON} \end{cases} \quad (3.8)$$

for NO_x over land

$$EMIS_{NO_x}^{EMEP} = \begin{cases} 90\% EMIS_{NO}^{MOON} \\ 10\% EMIS_{NO_2}^{MOON} \end{cases} \quad (3.9)$$

over sea

$$EMIS_{NO_x}^{EMEP} = 100\% EMIS_{NO_2}^{MOON} \quad (3.10)$$

because we assume that NO_x sources over sea only arise from long transport. For isoprene we have

$$EMIS_{C_5H_8}^{EMEP} = 100\% EMIS_{C_5H_8}^{MOON} \quad (3.11)$$

The final compound, the VOC, are distributed according to the description given in *Appendix B*. The emission distribution key for NO_x and VOC in DACFOS are different than that used by the MOON model, these differences are illustrated in Table 3.2.

Depositions

Dry Deposition

Dry deposition is the removal of species (gaseous and particles) from the atmosphere to the Earth surface by vegetation or other biological or mechanical means without any interaction with precipitation[2]. Therefore, dry deposition takes place in the lower surface layers and not in the free troposphere. In the MOON model complete vertical mixing in the ABL is assumed and we obtain the following formula for the mass loss due to dry deposition:

$$k_{d_depo} = \frac{v_d}{h_{mix}} \quad (3.12)$$

where v_d is the dry deposition velocity.

Only dry depositions due to gaseous particles are considered in the MOON model. In this respect the resistance method is used to calculate v_d . This treatment of dry depositions is identical with that of DACFOS[13] and the ACDEP[23] model. The inverse of the sum of resistances in three sequential layers is equal to v_d :

$$v_d = (r_a + r_l + r_s)^{-1} \quad (3.13)$$

The first resistance r_a is the aerodynamic resistance. This resistance describes the turbulent transfer of the contaminant to the near-surface layer and depends for instance on wind speed, atmospheric stability and surface roughness. The term r_l is the laminar sublayer resistance, which is the resistance needed to penetrate across the atmospheric near-surface layer. Finally, r_s is the resistance associated with gaseous-surface interaction. Equations for these three resistances are shown in Ref. [85].

This theoretical model for handling dry deposition depends on many physical characteristics among others: meteorological parameters, surface characteristics and molecular transport. Therefore, the dry deposition will vary over different landscapes (sea, desert, grass etc.) and whether it is daytime or nighttime.

In Table 3.3, we have outlined the dry depositions utilized in the MOON model. The nighttime dry depositions come from the daytime dry depositions by reducing these with a factor 4 to allow for surface inversion.

<u>DACFOS</u>	<u>MOON model</u>
<i>Solver:</i> QSSA.	Gear.
<i>MCHs:</i> EMEP MCH.	RADM2, RACM, EMEP and Jacobson's MCHs.
<i>Photolysis:</i> Use the parameterization $A \exp(-B \sec\theta)$.	Linear interpolation between calculated three dimensional grid points. The three dimensions are local hour angle, height and latitude at specific longitude. See section <i>Chemistry and Photorates</i> below.
<i>Initial Concentrations:</i> [NO] = 0.04 ppbV [NO ₂] = [SO ₂] = 0.2 ppbV [CO] = 152. ppbV [CH ₄] = 1400. ppbV [O ₃] = 20. ppbV [C ₂ H ₆] = [n-C ₄ H ₁₀] = [C ₂ H ₄] = [C ₃ H ₆] = [OXYL] = [HCHO] = [CH ₃ CHO] = [CH ₃ COC ₂ H ₅] = 0.4 pptV	As described in Table 3.1.
<i>Background Concentrations:</i> As described in Table 3.1 except for [NO] _{land} = 0.50 ppbV [SO ₂] _{land} = 1.0 ppbV [Nitrate] = [HNO ₃] _{Table 3.1} [H ₂] = [H ₂] _{Table 3.1}	As described in Table 3.1
<i>NO_x Emissions:</i> {NO} = {NO _x }	Over land: $\begin{cases} \{NO\} = \{NO_x\} \times 0.9 \\ \{NO_2\} = \{NO_x\} \times 0.1 \end{cases}$ Over sea: {NO ₂ } = {NO _x }
<i>Dry Deposition:</i> See Table 3.3	See Table 3.3
<i>VOC Emissions:</i> {CO} = {VOC} × 2.7 {C ₂ H ₅ OH} = {VOC} × 0.13957 {C ₂ H ₆ } = {VOC} × 0.07689 {n-C ₄ H ₁₀ } = {VOC} × 0.41444 {C ₂ H ₄ } = {VOC} × 0.03642 {C ₃ H ₆ } = {VOC} × 0.03827 {o-xylene} = {VOC} × 0.24537	The distribution key is given in <i>Appendix B</i> .
<i>Rate Constant for Moist Aerosol Scavenging of Gas-Phase Particles:</i> $k = \begin{cases} 1.0 \times 10^{-4} \text{s}^{-1} & \text{if rh.} > 90\% \\ 5.0 \times 10^{-6} \text{s}^{-1} & \text{otherwise} \end{cases}$ rh. = relative humidity.	$k = \begin{cases} 1.0 \times 10^{-4} \text{s}^{-1} & \text{if rh.} > 90\% \\ 5.0 \times 10^{-6} \text{s}^{-1} & \text{if } 90\% \geq \text{rh.} > 55\% \\ 0.0 \text{ s}^{-1} & \text{otherwise} \end{cases}$

Table 3.2: Differences between DACFOS and the MOON model.

<i>Moist Aerosol Scavenging of Gas-Phase Particles:</i>				
EMEP reac./RACM reac.	Rate			
H ₂ O ₂ /H ₂ O ₂ → aerosol	see Table 3.2			
CH ₃ O ₂ H/OP1 → aerosol	see Table 3.2			
sulphate/sulfuric acid → aerosol	see Table 3.2			
HNO ₃ /HNO ₃ → nitrate	see Table 3.2			
÷/N ₂ O ₅ → 2 × nitrate	see Table 3.2			
<i>Dry Deposition:</i>				
EMEP species/RACM species	v_d (cm s ⁻¹)			
	Land		Sea	
	day	night	day	night
HNO ₃ /HNO ₃	2.00/2.00	0.50/0.50	2.00/2.00	0.50/0.50
SO ₂ /SO ₂	0.50/0.50	0.125/0.125	0.50/0.50	0.125/0.125
H ₂ O ₂ /H ₂ O ₂	0.50/0.50	0.125/0.125	0.50/0.50	0.125/0.125
NO ₂ /NO ₂	0.20/0.20	0.05/0.05	0.20/0.00	0.05/0.00
O ₃ /O ₃	0.50/0.50	0.125/0.125	0.50/0.00	0.125/0.00
PAN/PAN	0.20/0.20	0.05/0.05	0.20/0.00	0.05/0.00
MPAN/TPAN	0.20/0.20	0.05/0.05	0.20/0.00	0.05/0.00
sulphate/sulfuric acid	0.10/0.10	0.025/0.025	0.10/0.10	0.025/0.025
nitrate/÷	0.10/0.10	0.025/0.025	0.10/0.10	0.025/0.025
CH ₃ O ₂ H/OP1	0.50/0.50	0.125/0.125	0.50/0.50	0.125/0.125
organic peroxides/OP2	0.50/0.50	0.125/0.125	0.50/0.50	0.125/0.125
CH ₃ COO ₂ H/PAA	0.50/0.50	0.125/0.125	0.50/0.50	0.125/0.125
HCHO/HCHO	0.30/0.30	0.075/0.075	0.30/0.30	0.075/0.075
CH ₃ CHO/ALD	0.30/0.30	0.075/0.075	0.30/0.30	0.075/0.075
CH ₃ COC ₂ H ₅ /KET	0.30/0.30	0.075/0.075	0.30/0.30	0.075/0.075
<i>Wet Deposition:</i>				
EMEP species/RACM species	Λ (s ⁻¹)			
SO ₂ /SO ₂	$(3 + \sin(2\pi([\text{day of year}] - 80)/365.2)) \times 10^5$			
HCHO/HCHO	$(3 + \sin(2\pi([\text{day of year}] - 80)/365.2)) \times 10^5$			
HNO ₃ /HNO ₃	1.4×10^6			
H ₂ O ₂	1.4×10^6			
CH ₃ O ₂ H/OP1	1.4×10^6			
nitrate/÷	1.0×10^6			
sulphate/sulfuric acid	1.0×10^6			

Table 3.3: Moist aerosol scavenging of gas-phase particles, dry and wet depositions used in DACFOS and the MOON model. The EMEP species are used in DACFOS and the RACM species is used in the MOON model. v_d are dry deposition velocities. Λ is scavenging coefficients[13].

Wet Deposition

Wet depositions are processes where material is scavenged by atmospheric hydrom-

eters, e.g. cloud, fog drops, rain and snow, and then transferred to the Earth's surface.

The traditional way to treat wet deposition is to split it up into in-cloud and below scavenging ratios (Λ). The values of Λ for different atmospheric chemical compounds used in the MOON model are presented in Table 3.3. These scavenging coefficients are taken from DACFOS[13]. We have not explicitly calculated scavenging ratio for the MOON model but this could be done for example using the method described in Refs. [2, 23].

The wet deposition is then given by[2, 23]

$$k_{w_depo}^i = \frac{\Lambda_i P}{h} \quad (3.14)$$

where P is the precipitation and h is the height over which scavenging occur. In the MOON model k_{w_depo} is considered in the ABL that means $h = h_{mix}$. The precipitation and the ABL height values are taken from DMI-HIRLAM.

Moist Aerosol Scavenging of Gas-Phase Particles

Some gas molecules are attracted to and can adhere to existing particles, oxidize and/or combine with other gaseous particles that are more stable in particulate than in the gaseous phase. In this respect atmospheric water is an important component of suspended particulate matter. The presence of ionic species (e.g. sulphate and nitrate) will increase the liquid water uptake of adhered gas molecules to such particles. For liquid water consisting of a mixture of HNO_3 , H_2SO_4 , NH_3 and HCl , the work by Watson et al.[160] showed that up to around 55% relative humidity, the liquid content is ≈ 0.0 . Then a sharp increase in the liquid content occurs, followed by a flattening to around 90% relative humidity. Again a sharp rise in the liquid content is observed. These new experimental results together with the uptake rate from Ref. [30] are used to incorporate moist aerosol scavenging of the liquid soluble molecules H_2O_2 , $\text{CH}_3\text{O}_2\text{H}$, sulphate, HNO_3 and N_2O_5 into the MOON model. This leads to the following uptake rate for these molecular species[160]:

$$k = \begin{cases} 1.0 \times 10^{-4} \text{s}^{-1} & \text{if rh.} > 90\% \\ 5.0 \times 10^{-6} \text{s}^{-1} & \text{if } 90\% \geq \text{rh.} > 55\% \\ 0.0 \text{ s}^{-1} & \text{otherwise} \end{cases} \quad (3.15)$$

These results are summarized in Tables 3.2 and 3.3.

Chemistry and Photorates

In the simulations presented in this chapter the RACM MCH is used in the MOON model. A detailed description of the RACM MCH is given in *Chapter 1*.

Parameterized formulas are used to calculate the photolysis rates in the EMEP MCH, in the comparison of the EMEP, RADM2 and RACM MCHs performed in *Chapter 1* and in DACFOS.

The MOON model uses the photolysis program *photo_2d.f*, see *Appendix D*, developed by S. Madronich, NCAR[161]. This program calculates photolysis parameters in a three dimensional grid. The three dimensions are the local hour angle (in $[-\pi; \pi]$), height (in $[0\text{km}; 30\text{km}]$) and latitude (in $[35^\circ; 75^\circ]$) at a specific longitude (0°). This is sufficient information for calculating the photolysis at every time of day in the DMI-HIRLAM area using linear interpolation among these three variables. This way of handling the photolysis is much more exact than parameterization formulas which can lead to errors as shown in *Section 3.2*. The adsorption cross sections and photochemical quantum yields used in *photo_2d.f* are from Ref. [32].

The calculated photolysis rate grid is for clear sky conditions ($J_i^{Clear-Sky}$). The photolysis rate is then corrected for cloud cover in the following manner

$$J_i = J_i^{Clear-Sky} \times (1 - TC \times 0.5) \quad (3.16)$$

where TC is the total cloud cover fraction in a given grid square.

The fractional cloud cover (FC) is derived from DMI-HIRLAM by calculating it in each grid square in each vertical layer[162]. From that TC in a grid square from the Earth's surface to the top of the atmosphere is calculated as

$$TC = 1 - \prod_i (1 - FC_i) \quad (3.17)$$

3.2 0-Dimensional Simulations

To test the differences between the manner in which the MOON model and DACFOS treat photolysis rates and VOC emissions, we have removed the transport in these two models. The 0-dimensional simulations performed illustrate rather clean air (LAND) and moderately polluted (M_PLUME and D_PLUME) conditions[38], see Table 3.4. Note that the simulations results obtained in this section are not directly comparable with the results from the comparison studies performed in *Chapter 1*.

In Figure 3.4 the concentration levels of ozone and in Figure 3.5 the concentration levels of NO, NO₂, HO, HO₂ and RO₂ for five day 0-dimensional simulations of the LAND, D_PLUME and M_PLUME cases using DACFOS and the MOON model are plotted.

Based on the simulation setups, there are four possible explanations for the differences between the two models seen in Figures 3.4 and 3.5:

1. different chemical mechanisms,
2. solvers,
3. different emission distribution keys, and
4. different photolysis.

	LAND case	M_PLUME case	D_PLUME case
N (molecules/cm ³)	2.55×10^{19}	2.55×10^{19}	2.55×10^{19}
H ₂ O (%)	1.00	1.00	1.00
O ₃ (ppbV)	30.0	50.0	50.0
HNO ₃ (ppbV)	0.10	0.10	0.10
CO (ppbV)	100.	200.	200.
CH ₄ (ppbV)	1700.	1700.	1700.
H ₂ (ppbV)	500.	500.	500.
H ₂ O ₂ (ppbV)	2.00	2.00	2.00
HCHO (ppbV)	1.00	1.00	1.00
O ₂ (%)	20.9	20.9	20.9
N ₂ (%)	78.1	78.1	78.1
NO (ppbV)	0.10	0.20	0.20
NO ₂ (ppbV)	0.10	0.50	0.50
NO (cm ⁻³ s ⁻¹)	0.00	1.1×10^6	1.1×10^6
SO ₂ (cm ⁻³ s ⁻¹)	0.00	2.2×10^5	2.2×10^5
CO (cm ⁻³ s ⁻¹)	0.00	2.4×10^6	$2.7 \times \{\text{VOC}\}$
VOC (cm ⁻³ s ⁻¹)	0.00	3.0×10^6	3.0×10^6
Emission distribution key as described in		<i>Appendix B</i>	DACFOS (Table 3.2)

Table 3.4: Simulated 0-dimensional scenarios. All scenarios are simulated on July 1 1985, place: longitude = 0.0° and latitude = 45° north, under clear skies with ground albedo = 0.10, solar declination = 23° and altitude = 0.0 km. The temperature is chosen as 288.15 K and the pressure = 1013.25 mbar.

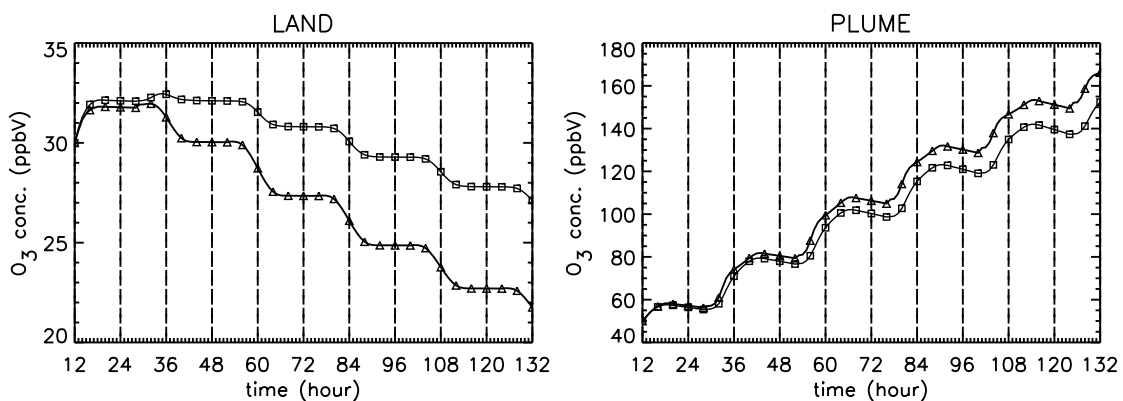


Figure 3.4: 0-dimensional box model simulation of the MOON model and DACFOS. Comparison of the ozone concentration from these two runs. The LAND case is without VOC emission, while in the PLUME cases $\{\text{VOC}\} = 3 \times 10^6 \text{ cm}^{-3} \text{ s}^{-1}$. The simulations are started at noon local time with output every 15 min. □: The MOON model (where PLUME case = M_PLUME case). Δ: DACFOS (where PLUME case = D_PLUME case).

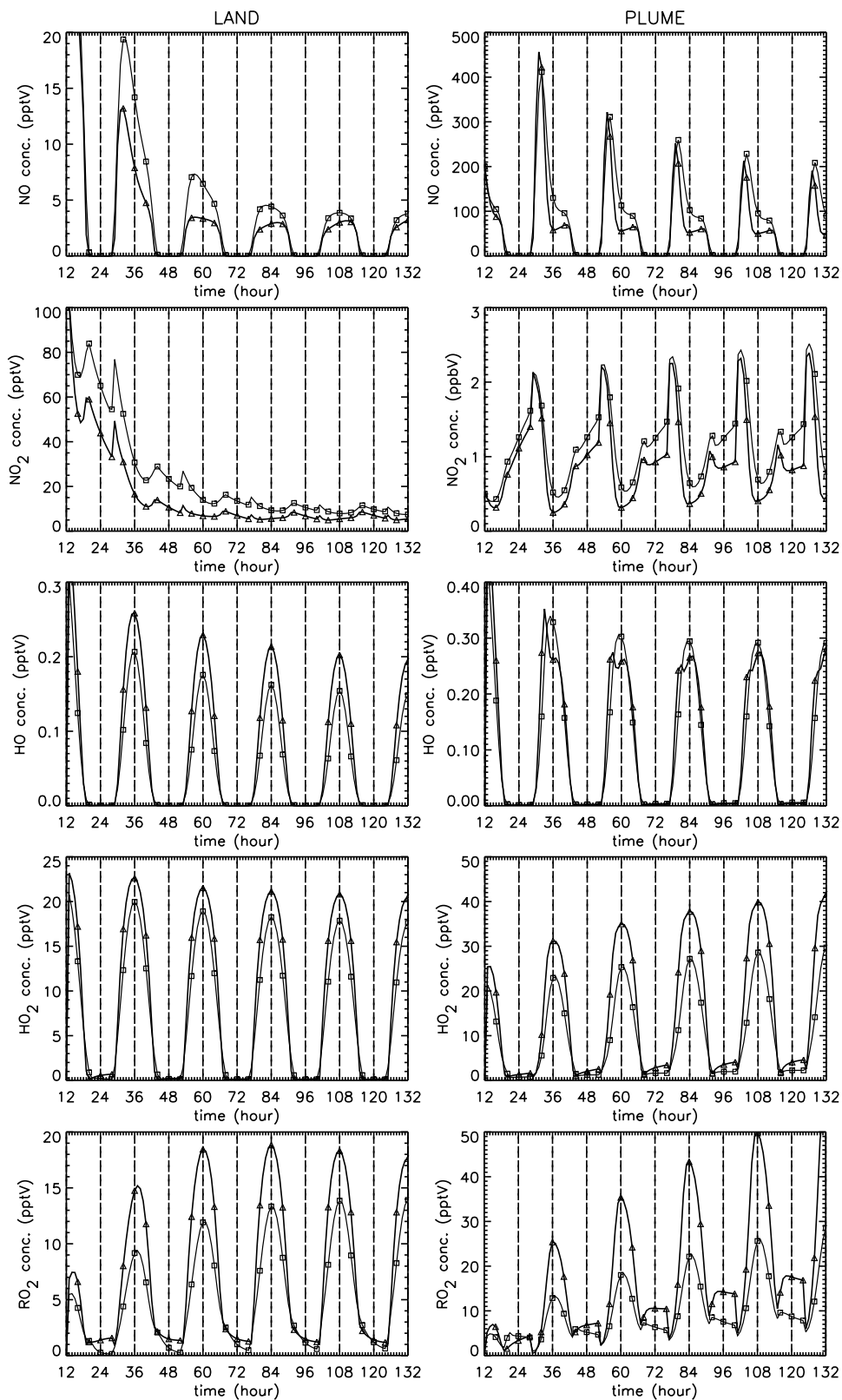


Figure 3.5: 0-dimensional box model simulation of the MOON model and DACFOS. Comparison of the NO, NO₂, HO, HO₂ and RO₂ concentrations from these two runs. For further explanation of the different simulations see the figure caption for Figure 3.4.

The RACM MCH is implemented in the MOON model while the EMEP MCH is used by DACFOS. We observe that the trends seen in Figures 3.4 and 3.5 are identical with the trends seen in Figures 1.22-1.27, but larger differences for these runs are observed than those from *Chapter 1*. We find that after a five day simulation DACFOS gives 25 % less ozone than the MOON model in the LAND case and for the PLUME case the MOON model gives 10 % less ozone than DACFOS. A description of how the different concentration levels plotted in Figure 3.5 affect the concentration of ozone will not be given here because that is explained in *Chapter 1*. Based on *Chapter 1* we find that the concentration levels of NO, NO₂, HO, HO₂ and RO₂ compared with the concentration levels of ozone reflect the discussion in *Chapter 1*.

Therefore, the use of the two different mechanisms is not a sufficient explanation of the difference between the results presented in Figures 3.4 and 3.5. Moreover, when tests of the two model systems are based on scenarios such as those presented in this section (clean and moderately polluted scenarios), large differences between the QSSA solver and the Gear algorithm should not appear. Since simple solvers such as the QSSA solver are specially constructed to model such environmental conditions.

In the following we will focus on the effects the different utilized emission distribution keys and photolysis rates have on the results presented in Figures 3.4 and 3.5. A comparison of the chemical mechanisms is made in *Chapter 1* and the two solvers performance will be discussed in *Section 3.3.1*.

The Effect of the Different Emission Distribution Keys Used

The investigations have been performed making 0-dimensional box model simulations using DACFOS and the MOON model plus the following two “variants” of DACFOS:

1. a 0-dimensional box model using the EMEP MCH integrated by a Gear algorithm and photolysis from DACFOS (Eq. (1.90)) (this model will be denoted DACFOS_{s-M,p-D}), and
2. a 0-dimensional box model with the EMEP MCH integrated by a Gear algorithm and photolysis from the *photo_2d.f* program (this model will be denoted DACFOS_{s-M,p-M}).

In Figure 3.6 the effect the two different emission distribution keys have on the ozone concentrations is illustrated. We find that the distribution key used in DACFOS gives approximately 6-8 ppbV more ozone after a five day simulation than the distribution key used in the MOON model. In general, the differences between the model simulations are relatively small, but as the simulations go from day one to day five, the differences between the simulations increases monotonically.

The Effect of the Different Photolysis Rates used

In Figure 3.7 we have focused on how the two different methods of calculating photolysis rates, that in DACFOS and that in the MOON model, influence the ozone

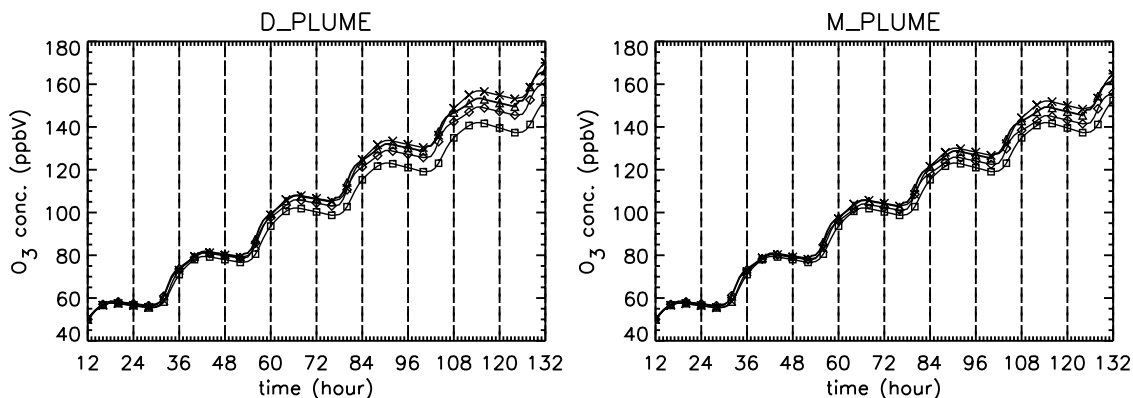


Figure 3.6: 0-dimensional box model simulations of the MOON model, DACFOS, DACFOS_{s_M_p_M} and DACFOS_{s_M_p_D}. Comparison of the ozone concentration from these four runs. The simulations are started at noon local time with output every 15 min. In all the simulations $\{\text{VOC}\} = 3 \times 10^6 \text{ cm}^{-3} \text{ s}^{-1}$. \square : The MOON model, D_PLUME case = M_PLUME and M_PLUME case = M_PLUME. \times : DACFOS_{s_M_p_M}, D_PLUME case = D_PLUME and M_PLUME case = M_PLUME. \diamond : DACFOS_{s_M_p_D}, D_PLUME case = D_PLUME and M_PLUME case = M_PLUME. \triangle : DACFOS, D_PLUME case = D_PLUME and M_PLUME case = M_PLUME.

concentration. Figure 3.7 shows that the different treatments of calculating photolysis rates have a large impact on the ozone concentration in the LAND case. The same trend is not observed in the PLUME case since the EMEP MCH, under polluted conditions, gives more ozone than the RACM MCH (see *Section 1.2.2*). This affects the ozone concentration in the opposite direction than DACFOS's treatment of photolysis rates compared with the MOON model.

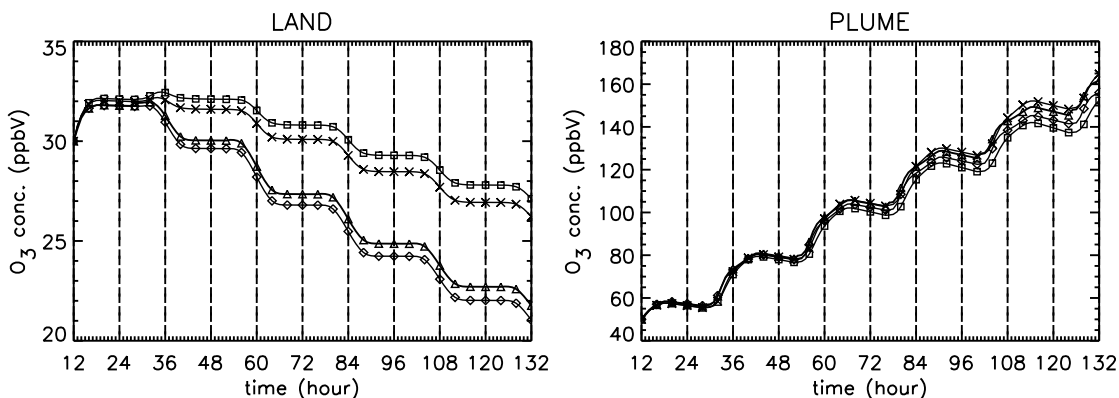


Figure 3.7: 0-dimensional box model simulations of the MOON model, DACFOS, DACFOS_{s_M_p_M} and DACFOS_{s_M_p_D}. Comparison of the ozone concentration from these four runs. The LAND case is without VOC emissions, while in the PLUME simulations $\{\text{VOC}\} = 3 \times 10^6 \text{ cm}^{-3} \text{ s}^{-1}$. The simulations are started at noon local time with output every 15 min. \square : The MOON model (where PLUME case = M_PLUME case). \times : DACFOS_{s_M_p_M} (where PLUME case = M_PLUME). \diamond : DACFOS_{s_M_p_D} (where PLUME case = M_PLUME). \triangle : DACFOS (where PLUME case = M_PLUME).

Figure 3.8 presents a comparison of the photolysis parameterization used by

DACFOS and the MOON model for reactions: $O_3 + h\nu \rightarrow O_2 + O(^1D)$ and $NO_2 + h\nu \rightarrow NO + O(^3P)$. This figure illustrates that the parameterization used in DAFOS overpredicts the photolysis during the day. This is the reason for the difference is seen in Figure 3.7 for the LAND case. For the three DAFOS simulations the lowest ozone concentrations are obtained when the highest photolysis rates of ozone are used. Therefore, both in the LAND case and PLUME case in Figure 3.7, the largest similarity is observed between the DAFOS and DAFOS_{s_M,p-D} simulations.

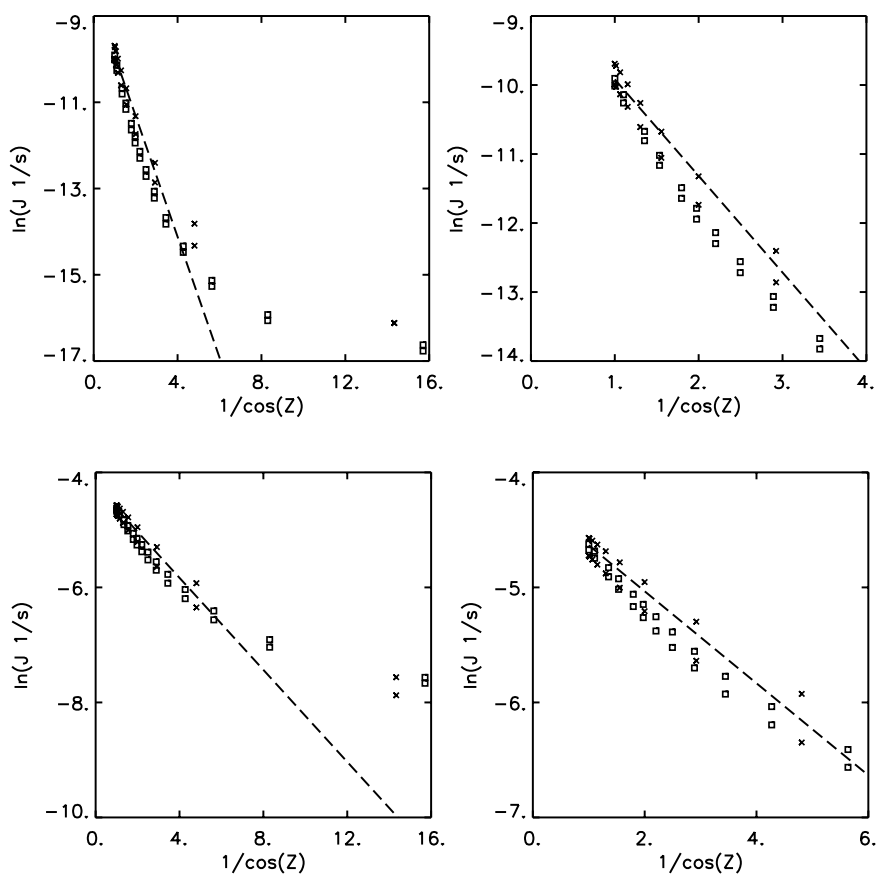


Figure 3.8: Comparison of the photolysis parameterization used in DAFOS (broken line) with the calculated photolytic rate constants at the Earth's surface from Demerjian et al.[163] (x) and the photolysis program *photo_2d.f* (□). Upper figures are for reac. $O_3 + h\nu \rightarrow O_2 + O(^1D)$. Lower figures $NO_2 + h\nu \rightarrow NO + O(^3P)$. Z is the solar zenith angle.

Summary

In summary, we have in Table 3.5 calculated different ratios of the final ozone concentrations obtained in the simulations. Table 3.5 shows, as discussed above, that the different treatments of the photolysis are the primary reason for the different concentration levels of ozone in the LAND case. For the PLUME case, no pronounced trends are observed since the chemical mechanisms used, the treatment

of photolysis and emission all go in different directions, resulting in cancelation of errors/effects. At present nothing conclusive can be said about the solvers used.

[O ₃]	LAND case	[O ₃]	PLUME case
[O ₃] _{MOON}	1.00	[O ₃] _{p_M,s_M,e_D}	1.29
[O ₃] _{p_M,s_M}	0.81	[O ₃] _{DACFOS}	1.00
[O ₃] _{DACFOS}	0.00	[O ₃] _{p_M,s_M,e_M}	0.88
[O ₃] _{p_D,s_M}	-0.15	[O ₃] _{p_D,s_D,e_M}	0.67
		[O ₃] _{p_D,s_M,e_D}	0.61
		[O ₃] _{p_D,s_M,e_M}	0.20
		[O ₃] _{MOON}	0.00

Table 3.5: Ratios of the ozone concentration after five days of the simulations shown in Figure 3.4, 3.6 and 3.7. For the LAND case the numbers in the table are calculated as follows $([O_3] - [O_3]_{DACFOS}) / ([O_3]_{MOON} - [O_3]_{DACFOS})$, and for the PLUME case as follows $([O_3] - [O_3]_{MOON}) / ([O_3]_{DACFOS} - [O_3]_{MOON})$. The subscripts indicate the following: *p_M* photolysis from photolysis program *photo_2df*, *p_D* photolysis from the photolysis parameterization used in DACFOS, *s_M* solver Gear algorithm, *s_D* solver QSSA, *e_M* emissions handled as in the MOON model, and *e_D* emissions handled as in DACFOS. Note, the RACM MCH is only used to calculate $[O_3]_{MOON}$. For all the other simulations the ozone concentrations are calculated using the EMEP MCH.

Due to the opposing effects the two model systems have whether the chemical box is placed in a clean or polluted environment, we note that it is not possible to conclude whether DACFOS or the MOON model in general will predict higher or lower ozone concentrations.

3.3 3-Dimensional Simulations

In this section DACFOS and the MOON model is compared on the basis of 3-dimensional simulations. This comparison is performed every third hour over a two week period from August 11 to August 24 1995 for 25 locations in Europe. At each arrival time and location trajectories are run in five heights⁴. This means that 1000 trajectories are run each day. All of these trajectories are at least four days long. In Table 3.6 the 25 different locations of measurement sites used for the 3-dimensional simulations are shown, and in Figure 3.9 the geographical locations for these 25 locations in Europe are indicated.

⁴All five arriving trajectories are used to calculate the surface ozone concentration at a receptor point (for the simulations described in *Section 3.3.2, Comparison 2*), since trajectories arriving at different heights can vary considerably due to the dependence of the wind on the height above ground. Therefore, even though full vertical mixing is assumed inside the squared box illustrated in Figure 3.1, the chemical composition of the arriving chemical boxes along the trajectories at different heights at a given receptor point can diverge a lot. These 5 trajectories arrive at a given receptor point at equidistant heights between the ground and the top of the ABL.

Station Codes	Station Name	Country	Location		Height Above Sea (m)	Station Category
			Latitude	Longitude		
CS01	Kosetice	Czech Rep.	49.58 N	15.08 E	633	EMEP
DK02	Keldsnor	Denmark	54.73 N	10.72 E	9	EMEP
DK03	Ulborg	Denmark	56.29 N	8.43 E	10	EMEP
DK04	Frederiksborg	Denmark	55.97 N	12.33 E	10	EMEP
DK05	Lille Valby	Denmark	55.70 N	12.10 E		Danish NERI
DK06	Jægersborg	Denmark	55.76 N	12.53 E	39	DMI
SF07	Virolahti	Finland	60.52 N	27.68 E	8	EMEP
SF08	Uto	Finland	59.78 N	21.38 E	2	EMEP
DE09	Westerland	Germany	54.93 N	8.31 E	12	EMEP
DE10	Deuselbach	Germany	49.76 N	7.05 E	480	EMEP
DE11	Brotjacklriegel	Germany	48.82 N	13.22 E	1016	EMEP
DE12	Neuglobsow	Germany	53.17 N	13.03 E	65	EMEP
DE13	Zingst	Germany	54.43 N	12.73 E	1	EMEP
DE14	Meinerzhagen	Germany	51.12 N	7.63 E	510	EMEP
NL15	Witteveen	Netherlands	52.82 N	6.67 E	16	EMEP
NL16	Bilthoven	Netherlands	52.12 N	5.20 E	5	EMEP
NO17	Birkenes	Norway	58.38 N	8.25 E	190	EMEP
NO18	Osen	Norway	61.25 N	11.78 E	440	EMEP
SK19	Stara Lesna	Slovakia	49.15 N	20.28 E	808	EMEP
SE20	Rörvik	Sweden	57.42 N	11.93 E	10	EMEP
SE21	Vavihill	Sweden	56.02 N	13.15 E	175	EMEP
SE22	Norra-Kvill	Sweden	57.82 N	15.57 E	261	EMEP
UK23	Strath Vaich	United Kingdom	57.73 N	4.78 W	270	EMEP
UK24	Harwell	United Kingdom	51.57 N	1.32 W	137	EMEP
UK25	Ladybower	United Kingdom	53.33 N	1.75 W	420	EMEP

Table 3.6: Locations of the measurement sites used for the 3-dimensional simulations.

Two types of comparisons between the models have been carried out for these 25 locations:

Comparison 1: 1000 (= 25 sites \times 8 arrivals times \times 5 heights at each site) 3-dimensional simulations of DACFOS and the MOON model without any sources and sinks using the trajectories for August 11 1995 to calculate the photolysis under clear sky conditions. The initial conditions for these simulations are the LAND case (see Table 3.4) and Urban case (see *Section 1.2.2*).

Comparison 2: 14 \times 1000 3-dimensional simulations of DACFOS and the MOON model from August 11 to August 24 1995 with sources and sinks etc. as described in Tables 3.1-3.3 and *Section 3.1*.

Since DACFOS and the MOON model are one-layer models which calculate the ABL average concentrations of chemical compounds treated in the models, the simulation results must be compared with measurements carried out at ground level. In Comparison 2 the model results are therefore also compared with available measurement

data from the EMEP stations, and the DMI and Danish NERI station described in Table 3.6 and Figure 3.9. For Keldsnor, Lille Valby, Witteveen, Bilthoven and Ladybower, measurement data for the simulation period are either missing or very sparse, therefore the simulation results from these stations will not be discussed further in what follows.



Figure 3.9: The geographical locations of the 25 sites given in Table 3.6.

3.3.1 Comparison 1

LAND Case Simulations

As observed in *Section 3.2* the MOON model simulates higher ozone concentrations than DACFOS for the 0-dimensional LAND case. This is also illustrated by Figure 3.10 where we have grouped the final ozone concentrations obtained in the two models. Figure 3.10 indicates that approximately 5 ppbV more ozone is obtained in the MOON model than DACFOS. For DACFOS, final ozone concentrations in interval 25-30 ppbV have the highest frequency, while for the MOON solver this interval is 30-35 ppbV. Furthermore, we find that the ozone concentration after the 5 day simulation is almost constant for all 2×1000 simulations, as it should be the case for rural scenarios.

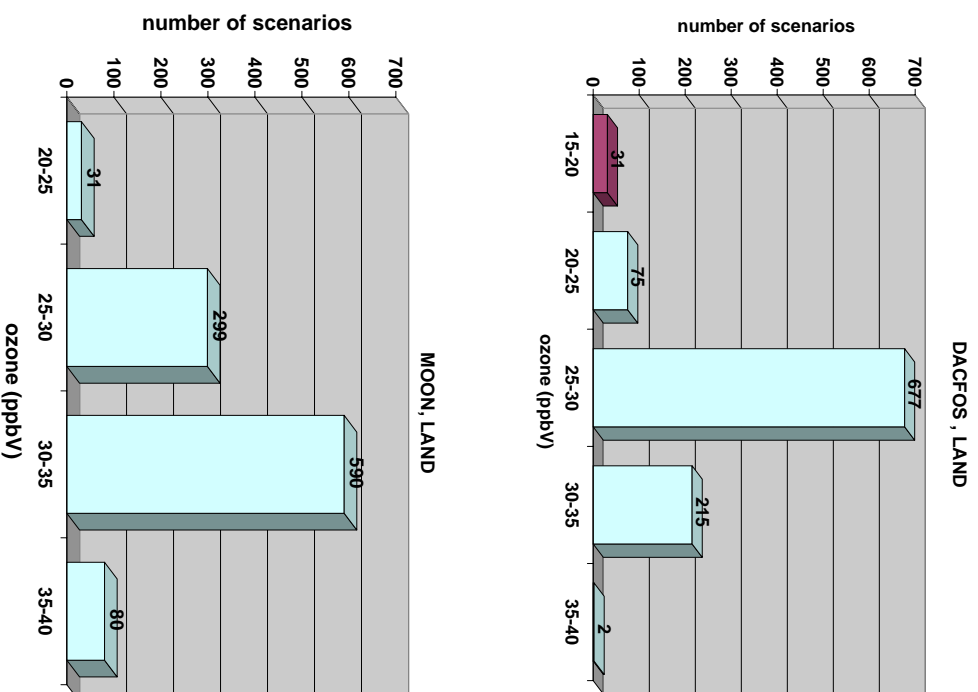


Figure 3.10: 1000 simulations of DACFOS and the MOON model for August 11 1995 grouped according to their final ozone concentration. The simulations are performed without any sources and sinks. Initial concentrations are according to the LAND scenario described in Table 3.4.

Detailed analysis of the single trajectories show that those coming from east in relation to the location of the measurement site gives less ozone (they experience more sunlight) than those coming from west (they experience less sunlight). This result is identical with what we observed in Figure 3.4. This figure shows that sunlight has a destructive effect on ozone for rural sites.

Urban Case Simulations

In Figure 3.11 the performance of DACFOS and the MOON model for the Urban case simulated as a 0-dimensional box at longitude = 0.0° and latitude = 45.0° is illustrated. This simulation shows that both models perform as expected. In contrast to the 0-dimensional LAND case (Figure 3.4), the 0-dimensional Urban case produces ozone during the daytime (Figure 3.11) while a small loss of ozone is observed during the nighttime. However, ozone is produced throughout the simulation. According to this figure we can expect that the 1000 3-dimensional Urban case simu-

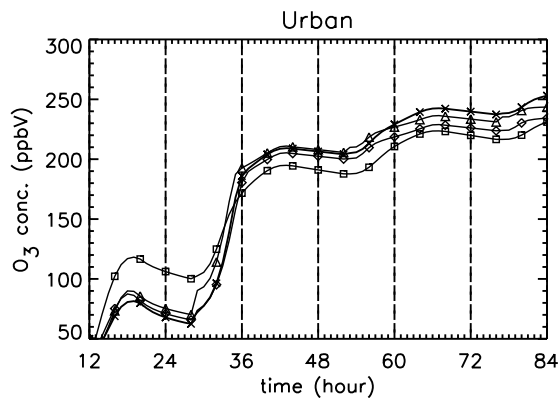


Figure 3.11: 0-dimensional box model simulations of the MOON model, DACFOS, DACFOS_{s_M_p_M} and DACFOS_{s_M_p_D}. Comparison of the ozone concentration from these four runs. The simulations are started at local noon (12 hour), output every 15 min. □: The MOON model, Urban case. ×: DACFOS_{s_M_p_M}, Urban case. ◇: DACFOS_{s_M_p_D}, Urban case. △: DACFOS, Urban case.

lations for DACFOS and the MOON model ought to give final ozone concentrations roughly in the range of 100 ppbV to 350 ppbV.

In Figure 3.12 we have grouped the final ozone concentration for the 1000 Urban simulations using DACFOS and the MOON model. This arrangement of the ozone concentrations shows dramatic differences between the two models. 41.4% of the chemical boxes from DACFOS gives a too high ozone concentration. We have observed differences between the models due to the different treatment of photolysis (Figures 3.4, 3.10 and 3.11), and we can see that for the MOON model the trajectories coming from east in relation to the receptor point site gives more ozone than those coming from west. This correlation is not observed for DACFOS.

The unrealistically high final ozone concentrations calculated by DACFOS when compared with the results obtained by the MOON model must be a consequence of the QSSA solver in DACFOS forced by the variation of the photolysis rates during the day. For the MOON model there is an excellent correlation between Figures 3.4 (LAND) and 3.10, Figures 3.11 and 3.12, and the trajectories' behavior.

3.3.2 Comparison 2

In this section 14000 trajectories are run for DACFOS and the MOON model in order to:

- test whether the MOON model can be used as a surface ozone forecast model (discussed in section *Discussion of Elapsed Time*), and
- evaluate the two models against each other and measurement data (discussed in section *Discussion of the Simulation Results*).

Note, DACFOS is today used as a surface ozone forecast model at DMI. Given the model concepts of DACFOS and the MOON model, the MOON model either should

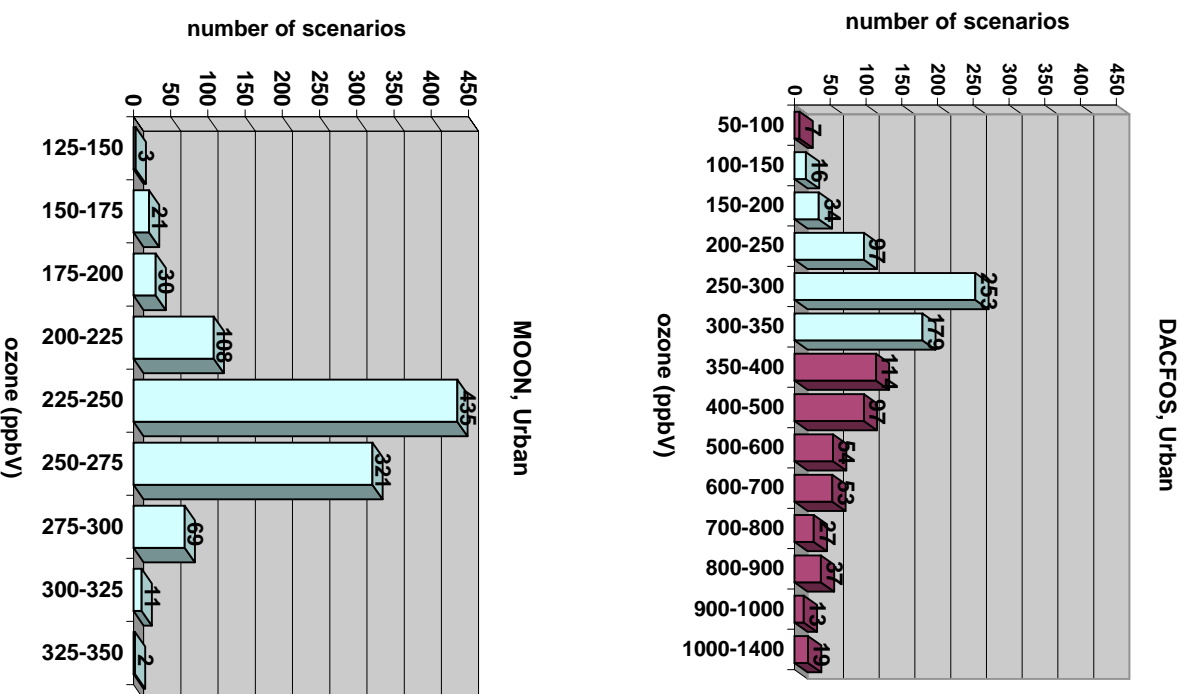


Figure 3.12: 1000 simulations of DACFOS and the MOON model for August 11 1995 grouped according to their final ozone concentration. The simulations are performed without any sources and sinks. Initial concentrations are according to the Urban scenario described in *Section 1.2.2*.

model surface ozone just as well or better than DACFOS. Therefore, it is enough to evaluate the MOON model's computer time in order to decide whether it can be used as a surface ozone forecast model.

Discussion of Elapsed Time

In Table 3.7 the computational speed of DACFOS and the MOON model is displayed. The computational speed of DACFOS and the MOON model is compared

<i>Simulation Days, Dates</i>													
11	12	13	14	15	16	17	18	19	20	21	22	23	24
<i>DACFOS on a Silicon Graphics 180 MHZ IP32 Processor</i>													
CPU time for 14×1000 trajectories													
298	296	290	234	235	261	300	306	311	298	297	297	307	279
<i>The MOON Model on an NEC SX-4 using one Processor</i>													
CPU time for 14×1000 trajectories													
322	390	380	356	328	331	363	360	344	348	340	323	375	362
MFLOPS for 14×1000 trajectories													
489	529	536	526	511	507	517	512	507	512	504	490	525	524

Table 3.7: Computational speed of DACFOS and the MOON model. Scenarios are 3 dimensional simulations at the 25 locations denoted in Table 3.6 for the period August 11 to August 24 1995. The set up of DACFOS and the MOON model is described in Tables 3.1-3.3 and *Section 3.1*. The MOON model program vectorizes 96% in its present version.

on the basis of runs on two different computers. The MOON model consists of code especially developed to run on a vector machine while DACFOS does not. DACFOS today is run on a Silicon Graphics 180 MHZ IP27 (R10000) Processor.

Table 3.7 shows that there are no large differences in the elapsed time of the two models. The average elapsed time for one trajectory using the MOON model takes 0.35 sec. and for DACFOS 0.29 sec. However, the RACM MCH used by the MOON model consists of a more comprehensive chemical mechanism than the EMEP MCH used by DACFOS (see *Section 1.2.1*), therefore the MOON model will run faster if the EMEP MCH is used instead of the RACM MCH.

Runs of the MOON model on a Silicon Graphics 180 MHZ IP32 (R10000) processor show that four to five day long trajectories takes approximately 44 seconds per trajectory, i.e. a factor of 125 is gained when it is run at NEC SX-4 (using one processor) for the present version of the MOON model.

Development of solvers to integrate numerical CRSs is a scientific discipline in its own right. Many solvers have been presented and tested, especially against the Gear algorithm and the QSSA solver. For example the computational speed of the EBI solver[48] is approximately identical with the QSSA solver[48], while the IEH solver[49] is 6.5 to 10 times slower than the QSSA solver[49]. Both of these solvers together with the QSSA solver are developed with the aim of being applied to 3-dimensional RAQMs. A comparison of these facts with the results reported in Table 3.7 show that the MOON model is much faster than the IEH solver⁵ and almost as fast as the Eulerian backward and QSSA solver. That means, the MOON model can easily be used as a solver in 3-dimensional RAQMs, and therefore also as an ozone forecast model at DMI.

⁵The IEH solver at present does not consist of vectorized code[164].

Discussion of the Simulation Results

2 week runs for 25 locations give a total of 2×2800 modeling points. All of these modeling points together with accessible measurement data for the 25 locations are plotted in the Figures F.1-F.25 (see *Appendix F*). Considerable differences between the 20 of the 25 locations⁶ is observed. We can roughly group the 20 locations in five classes⁷:

1. “high” photochemical activity and “high” ozone concentration (Kosetice, Deuselbach, Neuglobsow, Meinerzhagen, Stara Lasna and Harwell). A representative of the class, Kosetice, is plotted in Figure 3.13,
2. “high” photochemical activity and “low” ozone concentration (Jægersborg, Frederiksborg, Zingst, Birkenes, Osen and Rörvik). A representative of the class, Jægersborg, is plotted in Figure 3.14,
3. “low” photochemical activity and “high” ozone concentration (Brotjacklriegel). A representative of the class, Brotjacklriegel, is plotted in Figure 3.15,
4. “low” photochemical activity and “low” ozone concentration (Virolahti and Uto). A representative of the class, Uto, is plotted in Figure 3.16,
5. both “high” and “low” photochemical activity and “high” and “low” ozone concentration (Ulborg, Westerland, Vavihill, Norra-Kvill and Strath Vaich). A representative of the class, Ulborg, is plotted in Figure 3.17. The plot from Ulborg show that it the first two days has a “high” photochemical activity then five days with almost no photochemical activity then an increasing photochemical activity again.

The general trend in these figures are that the MOON model predicts higher surface ozone concentrations than DACFOS and, as we observed in Figure 3.17, that the MOON model nicely follows the measurement data for Ulborg when it goes from “high” photochemical activity to “low” photochemical activity.

In what follows we will examine how well the model results reproduce

- the daily maximum surface ozone concentration,
- the 24 hour periodicity of surface ozone concentration, and
- the total daily surface ozone concentration exposure.

⁶As mentioned before Keldsnor, Lille Valby, Witteven, Bilthoven and Ladybower are not considered.

⁷This classification is based on a rough valuation of the measurement data plotted at Figures F.1-F.25 and the discussions throughout this section. The definition “high” photochemical activity refers to locations having an evident diurnal surface ozone cycle with a high amplitude.

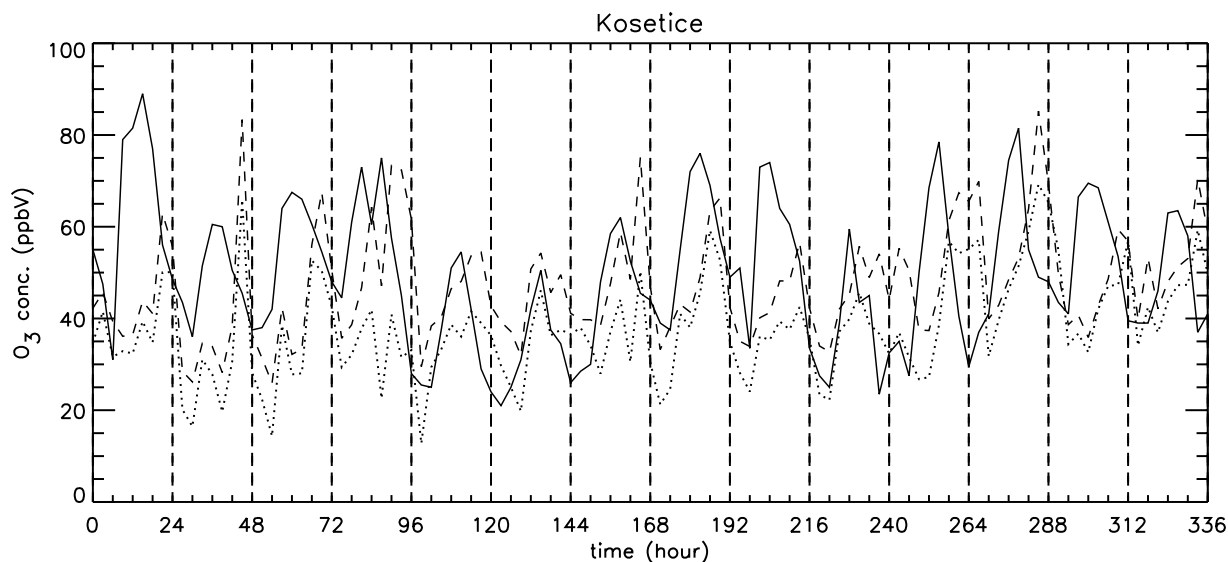


Figure 3.13: Model and observed ozone concentrations for the period August 11 to August 24 1995. Measured data is the solid line, DACFOS's results the dotted line, and the MOON model the dashed line.

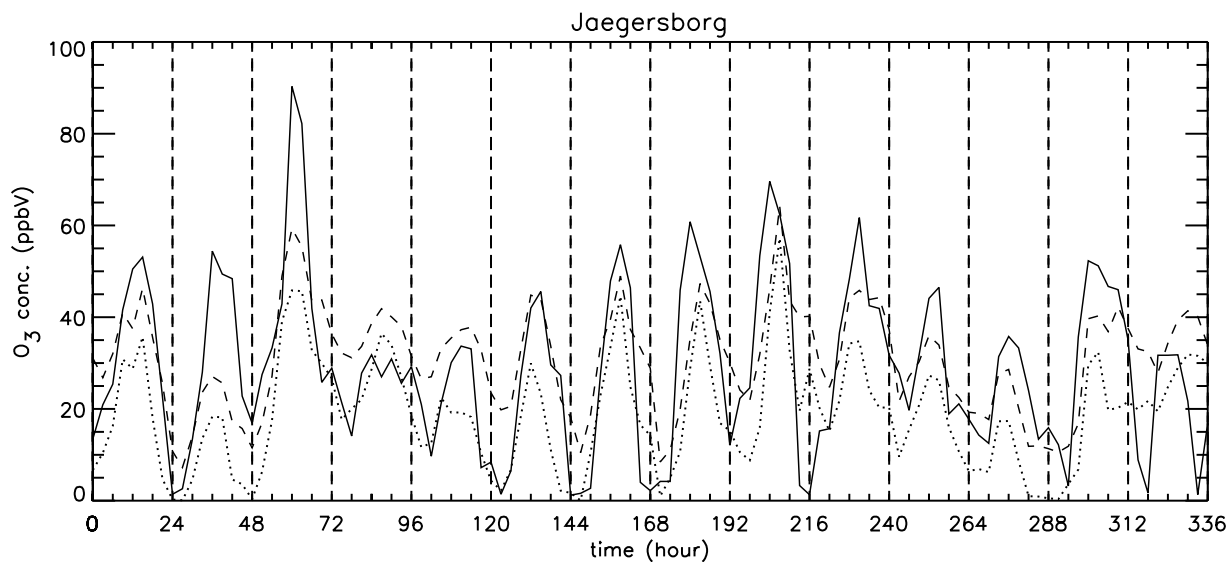


Figure 3.14: Model and observed ozone concentrations for the period August 11 to August 24 1995. Measured data is the solid line, DACFOS's results the dotted line, and the MOON model the dashed line.

These three aspects are important for 3-dimensional RAQMs since they are closely related to different types of exposure.

Since very different ozone concentration behaviors are observed for the 20 locations, a comparison of these model simulations with the measurement data is a reasonable good method for evaluating the MOON model and DACFOS. However,

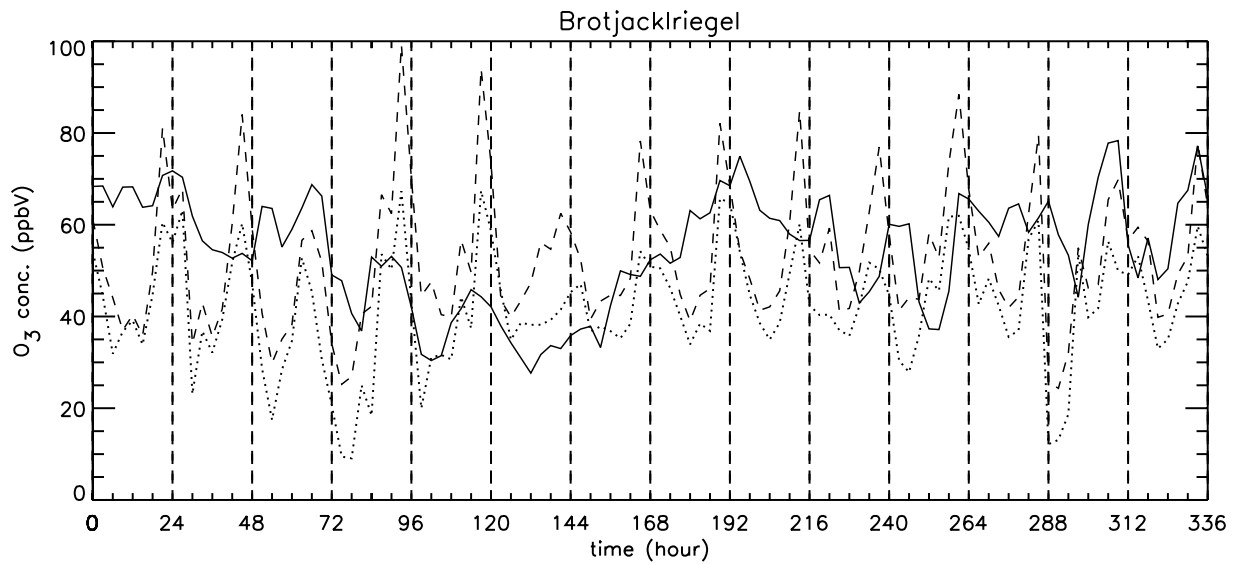


Figure 3.15: Model and observed ozone concentrations for the period August 11 to August 24 1995. Measured data is the solid line, DACFOS's results the dotted line, and the MOON model the dashed line.

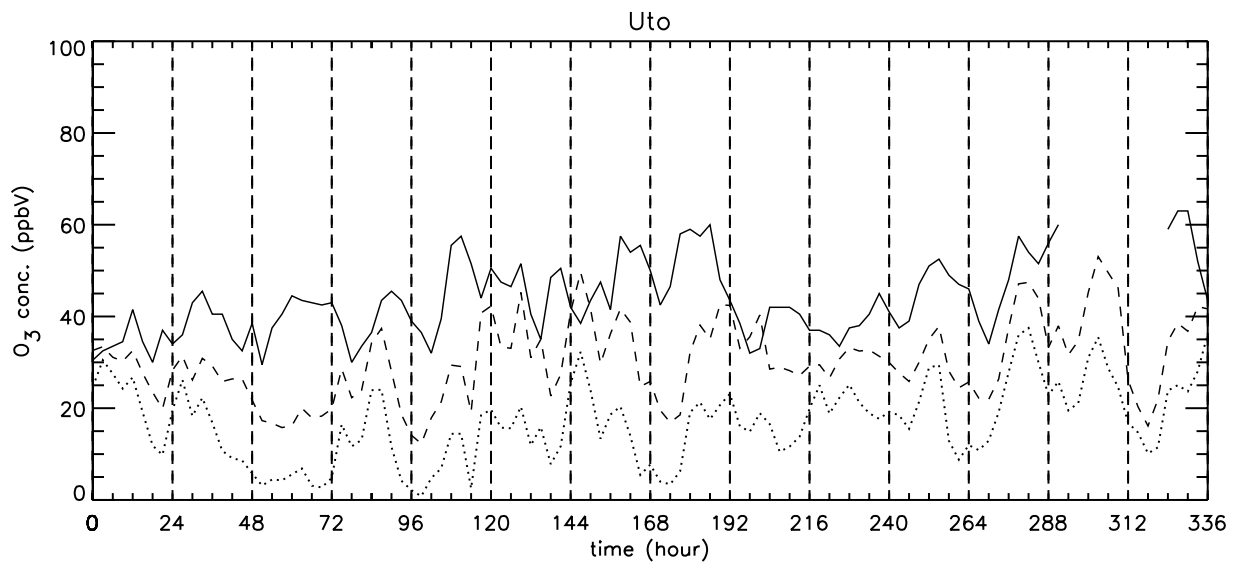


Figure 3.16: Model and observed ozone concentrations for the period August 11 to August 24 1995. Measured data is the solid line, DACFOS's results the dotted line, and the MOON model the dashed line.

due to the large number of calculated points it is a very extensive task to analyze the models performances properly without making any kind of data reduction. Therefore, in the following the models' performance is primarily discussed on the basis of the five class representatives plotted in Figures 3.13-17.

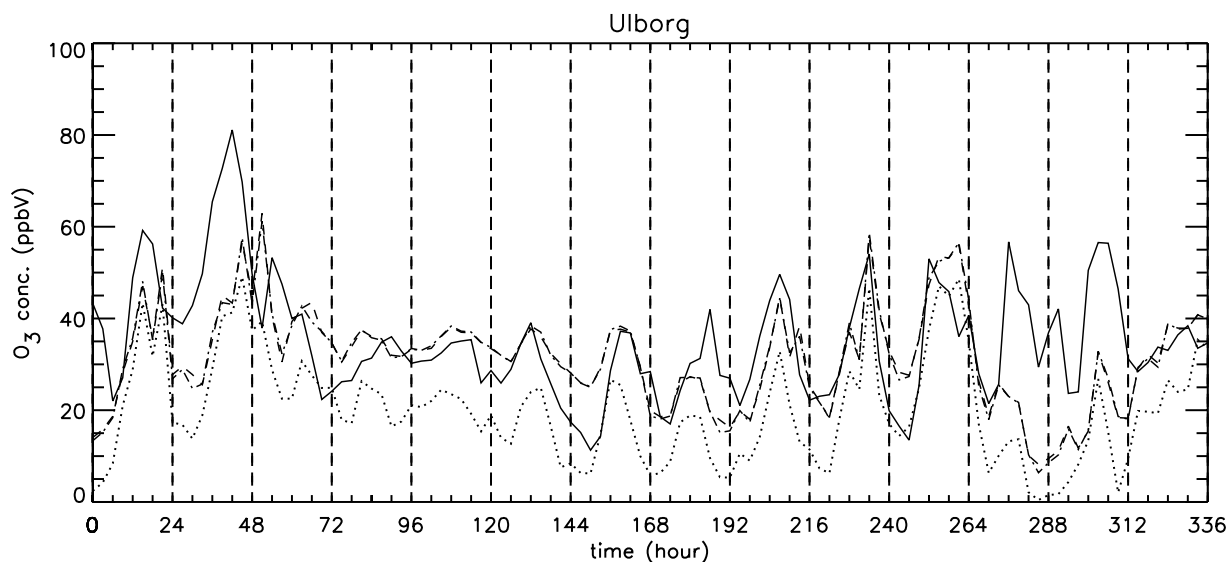


Figure 3.17: Model and observed ozone concentrations for the period August 11 to August 24 1995. Measured data is the solid line, DACFOS's results the dotted line, and the MOON model the dashed line.

Daily Maximum Surface Ozone Concentration

Ozone affects the plants (*Introduction, The Impact of Ozone on the Environment*). Since plants respond directly to ozone[165] it is natural to investigate the model's ability to model the daily maximum ozone concentration. The EU has introduced vegetation projection as well as population information and warning thresholds for surface ozone[3], see Table 0.2. These thresholds are averages for a period of 1 hour. Thus, it is important that a forecasting model are able to predict the maximum concentration of surface ozone reasonably well. In Table 3.8 these values are given for the five class representatives.

Table 3.8 shows that the MOON model in general simulates the daily maximum ozone concentration peak reasonably well for Kosetice, Jægersborg, Uto and Ulborg. The same good results are not achieved by DACFOS. We find that the MOON model in 11 out of 14, 12 out of 14, 12 out of 12 and 14 out of 14 days for Kosetice, Jægersborg, Uto and Ulborg, respectively, agrees better with the measurement data than DACFOS. For Brotjacklriegel DACFOS gives better results than the MOON model, but the correlation and the ozone concentration values between the model results and the measurements do not agree very well for this location. Contrary to the measurement data, the model results for Brotjacklriegel show "high" photochemical activity (see next subsection *Periodicity of Surface Ozone Concentration*). For days 4 and 5 differences up to 50 ppbV more ozone is exhibited by the models (see Figure 3.15).

Table 3.9 shows also that the MOON model outperforms DACFOS in simulating the height of the daily surface ozone concentration peak for all the measurement locations except for Brotjacklriegel and Virolahti. However, in DACFOS and the

<i>Simulation Day, Date</i>													
11	12	13	14	15	16	17	18	19	20	21	22	23	24
<i>Kosetice</i>													
Measurement Data													
89.0	60.5	67.5	75.0	54.5	50.5	62.0	76.0	74.0	59.5	78.5	81.5	69.5	63.5
DACFOS													
50.1	65.9	52.6	41.9	41.5	46.1	50.3	59.2	42.5	45.6	56.8	69.2	36.7	59.3
The MOON Solver													
62.9	83.3	67.5	73.3	54.5	54.3	75.1	66.3	56.6	55.7	67.4	85.2	59.4	70.4
<i>Jægersborg</i>													
Measurement Data													
53.2	54.4	90.4	31.8	33.8	45.6	55.8	60.8	69.6	61.8	46.6	35.8	52.4	31.8
DACFOS													
35.7	18.3	45.8	36.5	22.4	29.9	44.6	43.6	57.2	34.8	27.3	17.4	32.4	31.9
The MOON Model													
46.3	27.1	59.3	41.8	37.8	44.8	49.0	47.3	64.2	45.8	37.0	28.6	42.3	41.4
<i>Brotjacklriegel</i>													
Measurement Data													
70.8	71.8	68.8	53.1	45.9	33.7	50.0	69.7	75.0	66.4	66.8	65.6	78.4	77.2
DACFOS													
60.5	63.1	52.7	67.3	67.4	38.7	54.2	65.7	60.1	51.7	62.0	60.9	56.4	59.7
The MOON Model													
81.1	84.0	59.2	99.2	94.0	62.5	78.3	82.1	84.8	76.9	88.4	79.6	69.8	77.8
<i>Uto</i>													
Measurement Data													
41.5	45.5	44.5	45.5	57.5	51.5	57.5	60.0	42.0	45.0	52.5	57.5	-	-
DACFOS													
30.5	26.2	6.86	24.0	18.5	20.3	32.3	21.3	23.1	25.1	29.4	37.5	35.5	28.0
The MOON Model													
33.4	31.4	21.8	37.4	40.7	45.2	49.6	42.5	40.3	33.2	37.8	47.4	53.1	42.2
<i>Ulborg</i>													
Measurement Data													
59.2	81.1	53.3	36.0	35.4	39.1	37.2	42.0	49.6	54.1	53.0	56.7	56.6	38.4
DACFOS													
43.3	49.1	39.4	26.3	24.5	24.9	26.6	18.9	32.9	46.6	48.6	13.7	26.8	35.4
The MOON Model													
51.2	56.6	62.9	37.4	38.1	37.7	37.7	27.3	44.8	57.7	56.1	25.8	32.7	40.8

Table 3.8: Maximum modeled and measured surface ozone concentration peak for different days in the period August 11 to August 24 1995 for the five class representatives. The unit for the ozone concentrations is ppbV. Note, that if measurements data are missing for a day of interest then no maximum ozone peak concentration is measured.

Location	Average Max. O ₃ Concentration From					
	Meas. Data (ppbV) (hour)		DACFOS (ppbV) (hour)		MOON (ppbV) (hour)	
Kosetice	68.7	13.9	51.3	17.8	66.6	19.3
Ulborg	49.4	15.0	32.6	14.4	43.3	14.6
Frederiksborg	53.6	15.2	37.1	14.1	46.9	15.9
Jægersborg	51.7	13.5	34.1	13.7	43.8	14.8
Violahti	36.8	13.7	34.6	16.3	43.1	18.6
Uto	50.0	14.5	24.6	10.8	38.4	10.8
Westerland	56.6	15.8	32.7	15.3	47.0	15.3
Deuselbach	71.9	15.7	52.7	15.7	65.2	18.5
Brotjacklriegel	63.8	14.4	58.6	18.0	79.8	19.5
Neuglobsow	71.4	15.0	52.7	16.1	60.7	18.8
Zingst	52.2	13.9	34.6	14.6	48.3	14.6
Meinerzhagen	65.8	14.7	56.3	19.8	68.0	20.1
Birkenes	45.9	13.0	27.6	14.4	38.2	14.8
Osen	38.7	12.1	29.2	15.2	36.3	18.2
Stara Lesna	59.8	12.9	43.8	11.6	54.0	19.7
Rörvik	52.9	14.8	28.6	11.3	39.2	13.6
Vavihill	56.2	13.9	36.2	15.2	43.6	15.2
Norra-Kvill	48.0	13.9	36.8	14.1	45.0	19.5
Strath Vaich	43.0	13.9	31.4	13.5	41.9	14.8
Harwell	62.2	13.9	44.3	18.0	54.8	17.1

Table 3.9: Average over the measured and simulated maximum ozone concentration peak and the time for the daily ozone peak. Days where at least one measurement data point is missing is not included in the average values.

MOON model full vertical mixing is assumed within the ABL. This approximation is justified in under convective conditions. Since generally one expects good thermal mixing of the ABL in the summer afternoon where the measurement and modeled surface ozone concentrations usually peak (see Table 3.9). But the model results in general have its ozone concentration peak later than the measurement data (see Table 3.9).

Periodicity of Surface Ozone Concentration

The ozone concentration in the ABL shows a diurnal pattern. In urban regions this diurnal variation is especially marked[158]. For mountainous or more remote areas, the nighttime loss of ozone is smaller and therefore a flatter diurnal variation is observed[158]. In this section we test whether periodic patterns exist and overlap between the measurement data and model results is observed. This task will be achieved by estimating the power spectra (H) of the surface ozone concentration series[166], plotted in *Appendix F*. In addition to periodic patterns, power spectra

can also show the correlation between two point series or functions if they are in phase. The surface ozone concentration series mean is removed before the power spectra is calculated to reduce spectral leakage [166]. Note, for the measurement data the power spectrum is only calculated when a complete data set in the two week period exists.

A pronounced 24 hour peak is observed in most of the power spectra for both the measurement data and the simulations. The spectrum for Jægersborg is shown as an illustration for such resemblances (see Figure 3.18). Exceptions to this are

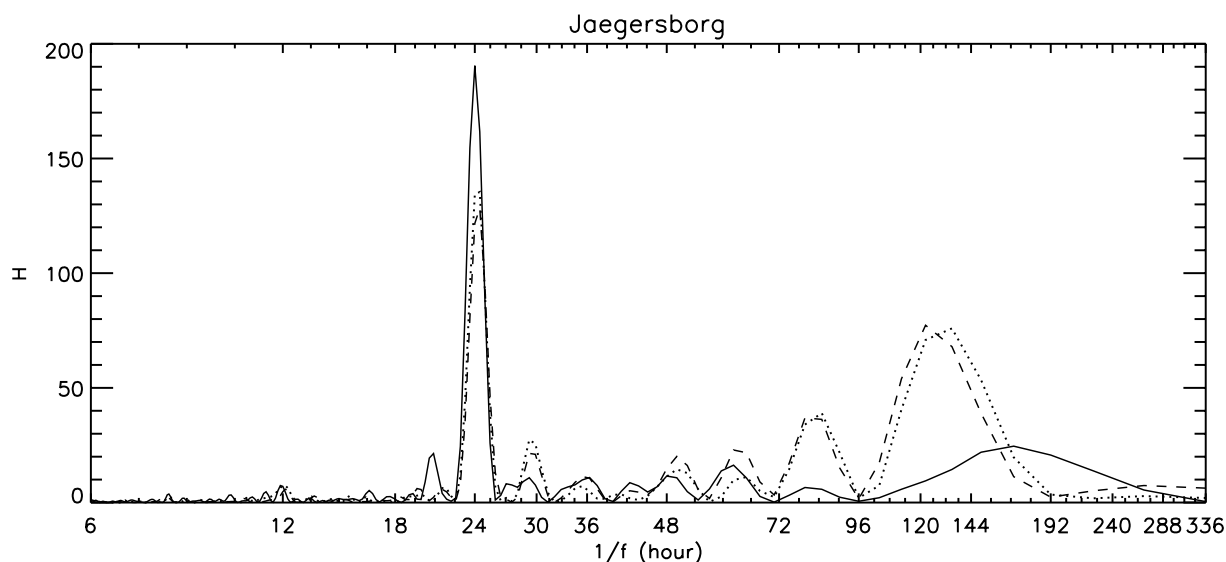


Figure 3.18: The normalized power spectrum $H(f)$ for model and observed ozone concentration data in the period August 11 to August 24 1995. Measured data is the solid line, DACFOS's results the dotted line, and the MOON model's results the dashed line.

Uto, Westerland and Strath Vaich for both the MOON model and DACFOS (as an example see the power spectrum for Uto Figure 3.19: the power spectrum of the measurement data is not calculated for these three sites), Stara Lesna for DACFOS (but a small 24 hour peak can be seen) and Brotjacklriegel (see Figure 3.20) for the measurement data. Brotjacklriegel is the only location where there is a difference between model results and measurement data (see also the discussion in previously subsection *Daily Maximum Surface Ozone Concentration*). But a comparison of the model and measured data for surface ozone shows that even though this indicates that the models can simulate a 24 hour cycle, the diurnal peak first comes around hour 18-21 for the model results in the southern and south-eastern European locations, while the peak for measurements lies in the interval 12-18 hour, see Table 3.9. What is in common for all of these locations is that they are placed in class "high" photochemical activity and "high" ozone concentration.

Moreover, for abundant power spectra periodic similarities are observed for DACFOS and the MOON model simulations, see e.g. Figure 3.18. This is natural because of the identical physical and meteorological treatments in the two models.

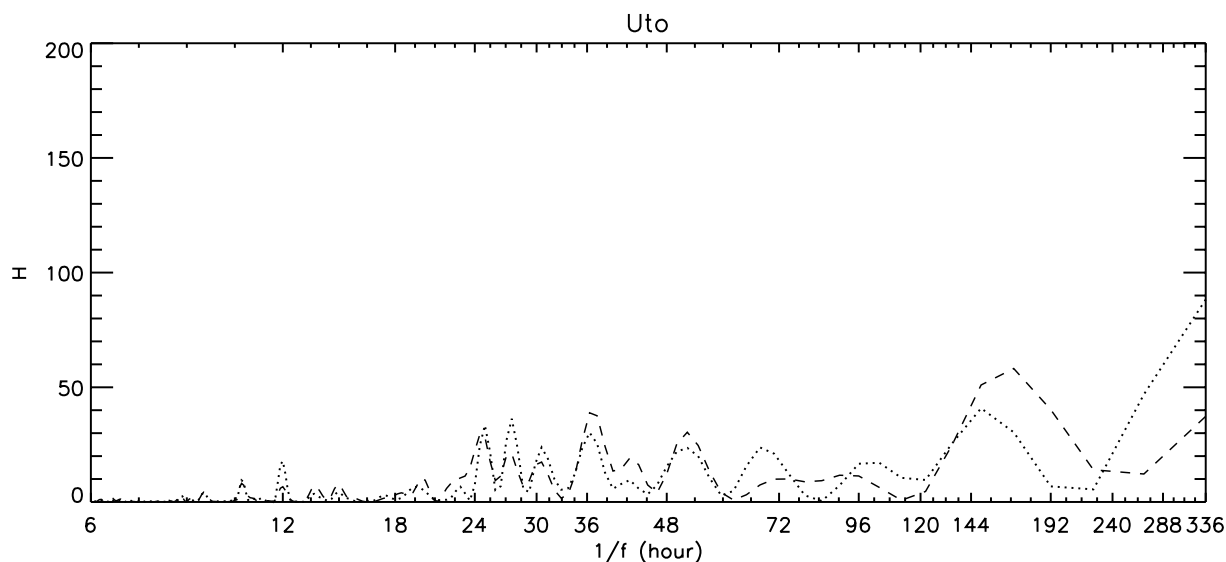


Figure 3.19: The normalized power spectrum $H(f)$ for model ozone concentration data in the period August 11 to August 24 1995. DACFOS's results is the dotted line, and the MOON model's results the dashed line.

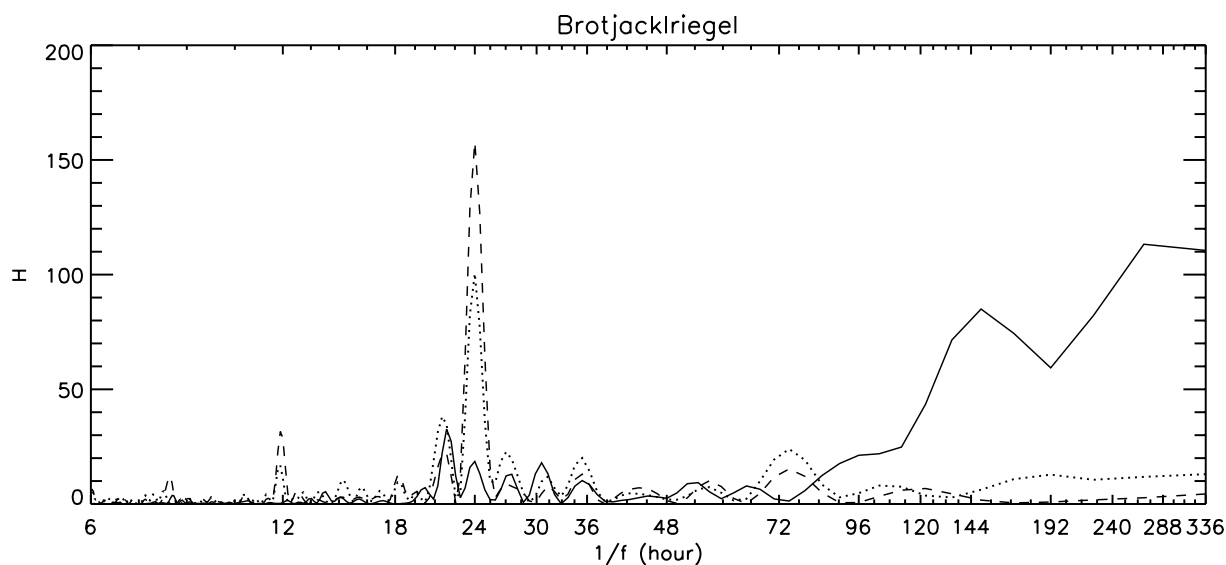


Figure 3.20: The normalized power spectrum $H(f)$ for model and observed ozone concentration data in the period August 11 to August 24 1995. Measured data is the solid line, DACFOS's results the dotted line, and the MOON model's results the dashed line.

If we calculate the area of the 24 hour peak in the normalized power spectra shown and multiply it by the variance of the different locations' corresponding ozone concentrations, it will be possible to compare the different locations' 24 hour photochemical activity. In Table 3.10 this calculation has been performed for the different locations. We observe that DACFOS and the MOON model in general have difficulties in reproducing the same high daily variation, except for Norra-Kvill and Brotjacklriegel. In general for the northern European locations, the model results

show a small diurnal variation, and this is not always reproduced by the measurements, see e.g. the locations Osen and Birkenes. This fact could maybe be explained by a trajectory analyses.

Brotjacklriegel is the site with the highest altitude of the locations. The diurnal cycle becomes less pronounced with increasing altitude[158] and this fact is therefore reasonably reproduced by the measurements for Brotjacklriegel compared to the other locations in that region, in contrast to the model results. In general we observe that for most of the locations DACFOS and the MOON model agree reasonably well.

	Measurement I_H (ppbV/hour)	MOON I_H (ppbV/hour)	DACFOS I_H (ppbV/hour)
Kosetice	19.2	9.58	5.50
Keldsnor	-	3.54	3.92
Ulborg	7.20	2.65	3.87
Frederiksborg	21.3	11.5	12.3
Lille Valby	-	9.42	10.3
Jægersborg	31.0	8.64	10.2
Virolahti	7.45	2.32	2.03
Uto	-	1.47	0.989
Westerland	-	3.33	2.41
Deuselbach	-	8.03	6.54
Brotjacklriegel	1.69	16.0	7.13
Neuglobsow	-	6.96	6.56
Zingst	-	5.19	4.55
Meinerzhagen	-	11.0	10.3
Witteveen	-	9.28	10.7
Bilthoven	-	11.4	11.9
Birkenes	17.8	2.67	3.29
Osen	13.1	1.32	2.34
Stara Lesna	14.9	4.13	2.25
Rörvik	-	2.84	2.66
Vavihill	15.6	7.05	10.9
Norra-Kvill	4.08	3.75	3.15
Strath Vaich	-	0.828	1.72
Harwell	30.4	18.3	15.3
Ladybower	-	18.5	14.6

Table 3.10: The area of the 24 hour peak in the normalized power spectra for the 25 locations multiplied with the variance for the different locations' corresponding ozone concentrations, I_H .

Note, the main purpose in calculating the power spectra for the ozone concentration series was to investigate whether they produce the 24 hour periodicity. However, many other interesting features can be observed in the spectra:

- some of the spectra have a small 12 hour peak, and

- many of the spectra have many broad lines in the low frequency range (this could merely be a Fourier resolution trend which could be filtered away, white noise),

but we will not in this context try to analyze these lines/peaks because it would be an immense task.

Finally, since a fall in anthropogenic activity take place in the weekends a 7 day peak should appear in the spectra of the measurement data, this is not observed. It could be because only measurements for two weeks is used in the analyses. Such a 7 day variation is not included in DACFOS and the MOON model.

Total Daily Surface Ozone Concentration Exposure

Many mean exposure indices have been introduced over the years, some of these are called the Accumulated Ozone exposure above Threshold (AOT) and the Total Ozone Dose (TOD)[30, 158, 165]. These indices can be calculated by the integral expression

$$\text{AOT}x = \int \max(\text{O}_3 - x, x) dx \quad (3.18)$$

where the unit of x is ppbV. That means $\text{TOD} = \text{AOT}0^8$. AOT values are based on 24 hour time periods and are widely used in Europe[30, 165], especially the two AOT values: AOT40 and AOT60[30, 165]. AOT40 has been confirmed as a substantial threshold for ozone with respect to its effect on crops and forests. AOT60 is based on the guidelines from WHO as a health threshold. For AOT40 a critical threshold is set at 3000 ppbV×day over the entire growing season defined as May-July. Such a critical threshold is not defined for AOT60.

AOT values are critically dependent on the completeness of the data record. Missing data points can introduce large errors. Therefore, we have only calculated AOT values for the days with complete data sets. Furthermore, AOT40 measurements are very sensitive to the height above the surface of the station[167]. Thus, it is a prerequisite that AOT40 values from model simulations are calculated at the same height above the surface as the position of the measurement site. However, in DACFOS and the MOON model full vertical mixing of the ABL is assumed, a justification of this approximation is described in subsection 3.3.2 *Comparison 2, Daily Maximum Surface Ozone Concentration*. Therefore, this issue has been ignored here. The results for the five class representatives are shown in Tables 3.11-15.

In general we find that the MOON model's AOT0 values are in good agreement with the results obtained from the measurement data while DACFOS gives results that are far too low. Moreover, the agreement between model results and measurement data decreases with increasing x in AOT x , yet the MOON model still gives the best results. This substantiates the fact that the photochemical activity is higher for the measurements than the model results, and that the MOON model gives higher ozone concentrations than DACFOS.

⁸Note, TOD is usually not defined as an AOT, but we will do it in this chapter.

<i>Simulation Day, Date</i>													
11	12	13	14	15	16	17	18	19	20	21	22	23	24
Measurement Data, AOT0, AOT40, AOT60													
1538	1172	1306	1364	872	800	1080	1358	1349	888	1167	1307	1342	1157
605	227	356	422	82.5	37.5	206	408	419	84.0	287	372	383	213
260	1.50	54.0	88.5	0.00	0.00	6.00	111	94.5	0.00	81.0	108	76.5	19.5
DACFOS, AOT0, AOT40, AOT60													
915	752	808	822	796	805	887	945	835	833	947	1245	1069	1093
49.9	92.8	72.8	12.1	4.62	18.3	43.1	115	7.46	16.9	116	310	158	160
0.00	17.6	0.00	0.00	0.00	0.00	0.00	0.00	0.00	0.00	0.00	35.6	7.94	0.00
The MOON Model, AOT0, AOT40, AOT60													
1063	957	996	1303	1089	1052	1176	1138	1037	1068	1230	1413	1137	1248
127	154	154	360	165	127	222	204	110	148	285	453	193	288
8.58	70.0	22.5	92.4	2.45	0.00	45.2	29.2	0.00	0.00	34.5	139	14.0	31.3

Table 3.11: AOT values for the measurement data and model results for **Kosetice**. The first row is the AOT0 value in ppbV×day, the second row is the AOT40 value in ppbV×day and the third row is the AOT60 value in ppbV×day.

<i>Simulation Day, Date</i>													
11	12	13	14	15	16	17	18	19	20	21	22	23	24
Measurement Data, AOT0, AOT40, AOT60													
793	684	1100	623	525	554	563	759	882	835	704	545	818	464
84.3	96.6	292	0.00	0.00	22.8	90.3	137	231	103	31.8	0.00	109	0.00
0.00	0.00	158	0.00	0.00	0.00	0.00	2.40	36.0	5.10	0.00	0.00	0.00	0.00
DACFOS, AOT0, AOT40, AOT60													
444	189	692	625	376	291	483	450	624	585	419	186	371	612
0.00	0.00	34.5	0.00	0.00	0.00	13.8	10.7	54.7	0.00	0.00	0.00	0.00	0.00
0.00	0.00	0.00	0.00	0.00	0.00	0.00	0.00	0.00	0.00	0.00	0.00	0.00	0.00
The MOON Model, AOT0, AOT40, AOT60													
797	425	957	868	773	716	737	689	921	906	673	457	668	853
21.7	0.00	153	5.71	0.00	26.4	26.9	30.9	102	54.8	0.00	0.00	7.58	4.60
0.00	0.00	0.00	0.00	0.00	0.00	0.00	0.00	12.6	0.00	0.00	0.00	0.00	0.00

Table 3.12: AOT values for the measurement data and model results for **Jægersborg**. The first row is the AOT0 value in ppbV×day, the second row is the AOT40 value in ppbV×day and the third row is the AOT60 value in ppbV×day.

Comprehensive AOT calculations have been performed by Simpson and co-workers[30, 165]. Even though the model results presented here only are based on

<i>Simulation Day, Date</i>													
11	12	13	14	15	16	17	18	19	20	21	22	23	24
Measurement Data, AOT0, AOT40, AOT60													
1613	1397	1473	1136	918	804	1028	1425	1521	1286	1238	1483	1507	1422
653	437	513	185	41.7	3.15	109	465	561	326	294	523	547	462
173	54.2	78.6	0.00	0.00	0.00	0.00	62.7	102	35.7	29.6	55.6	147	97.1
DACFOS, AOT0, AOT40, AOT60													
1039	1075	816	795	940	984	1003	1109	1122	1024	1084	1071	912	1098
134	201	65	158	128	56.6	88.1	181	185	85.7	173	175	139	173
1.55	10.2	0.00	21.9	22.3	0.00	0.00	24.2	7.34	0.00	11.1	2.75	0.00	0.00
The MOON Model, AOT0, AOT40, AOT60													
1203	1283	1073	1245	1333	1240	1235	1309	1315	1319	1394	1289	1143	1310
264	354	173	378	373	280	277	352	355	359	434	350	275	351
69.9	102	0.00	160	137	27.6	59.5	83.8	88.7	59.2	137	77.3	45.7	59.5

Table 3.13: AOT values for the measurement data and model results for **Brotjackkriegel**. The first row is the AOT0 value in ppbV×day, the second row is the AOT40 value in ppbV×day and the third row is the AOT60 value in ppbV×day.

<i>Simulation Day, Date</i>													
11	12	13	14	15	16	17	18	19	20	21	22	23	24
Measurement Data, AOT0, AOT40, AOT60													
827	928	965	935	1084	1099	1152	1255	931	920	1100	1130	-	-
4.50	28.5	46.5	42.0	161	154	197	295	24.8	18.0	150	191	-	-
0.00	0.00	0.00	0.00	0.00	0.00	0.00	0.00	0.00	0.00	0.00	0.00	-	-
DACFOS, AOT0, AOT40, AOT60													
516	374	106	325	220	365	433	323	372	506	453	575	618	490
0.00	0.00	0.00	0.00	0.00	0.00	0.00	0.00	0.00	0.00	0.00	0.00	0.00	0.00
0.00	0.00	0.00	0.00	0.00	0.00	0.00	0.00	0.00	0.00	0.00	0.00	0.00	0.00
The MOON Model, AOT0, AOT40, AOT60													
686	664	429	630	594	808	887	711	773	738	710	828	984	733
0.00	0.00	0.00	0.00	5.63	20.6	40.2	11.2	4.57	0.00	0.00	55.4	102	8.94
0.00	0.00	0.00	0.00	0.00	0.00	0.00	0.00	0.00	0.00	0.00	0.00	0.00	0.00

Table 3.14: AOT values for the measurement data and model results for **Uto**. The first row is the AOT0 value in ppbV×day, the second row is the AOT40 value in ppbV×day and the third row is the AOT60 value in ppbV×day.

two week simulations, we find that they reproduce the general trends from the work

<i>Simulation Day, Date</i>													
11	12	13	14	15	16	17	18	19	20	21	22	23	24
Measurement Data, AOT0, AOT40, AOT60													
1005	1396	932	737	764	687	583	656	822	794	805	867	1001	801
145	439	79.6	0.00	0.00	0.00	0.00	5.9	53.1	61.7	81.0	78.2	150	0.00
0.00	147	0.00	0.00	0.00	0.00	0.00	0.00	0.00	0.00	0.00	0.00	0.00	0.00
DACFOS, AOT0, AOT40, AOT60													
571	710	682	500	503	402	343	271	399	507	779	243	232	572
19.1	32.5	0.00	0.00	0.00	0.00	0.00	0.00	0.00	19.7	61.6	0.00	0.00	0.00
0.00	0.00	0.00	0.00	0.00	0.00	0.00	0.00	0.00	0.00	0.00	0.00	0.00	0.00
The MOON Model, AOT0, AOT40, AOT60													
757	899	1007	814	848	792	737	519	694	793	1018	480	438	827
54.6	82.7	95.0	0.00	0.00	0.00	0.00	0.00	14.3	56.3	155	4.14	0.00	2.47
0.00	0.00	8.71	0.00	0.00	0.00	0.00	0.00	0.00	0.00	0.00	0.00	0.00	0.00

Table 3.15: AOT values for the measurement data and model results for **Ulborg**. The first row is the AOT0 value in $\text{ppbV} \times \text{day}$, the second row is the AOT40 value in $\text{ppbV} \times \text{day}$ and the third row is the AOT60 value in $\text{ppbV} \times \text{day}$.

by Simpson and co-workers. Low AOT values in northern and north western Europe and high values in southern and south western Europe: Kosetice, Deuselbach, Brotjacklriegel, Neuglobsow and Stara Lesna (see Table 3.16). For these locations, the highest values is obtained in southern Germany.

3.4 Conclusion

In this chapter we presented a new Lagrangian model (the MOON model). This model was based on the meteorology and physics from DACFOS and the “Eulerian” SMVGEAR solver developed by Jacobson[56]. The distinction between this new model and traditional Lagrangian transport-chemical models such as DACFOS is

- the solver used (Gear algorithm),
- the treatment of photolysis (modeled photolysis, not parameterized as in DACFOS), and
- the chemical scheme.

The tests and comparisons of the two models presented in this chapter together with the comparison of the EMEP MCH in contrast to the RACM MCH made in *Chapter 1* show that the first two items are of great importance in RAQMs. We found that oversimplified treatment of photolysis increased the ozone destruction in rural areas

Location	Average AOT x values for								
	Meas. Data			DACFOS			MOON		
	$x = 0$	$x = 40$	$x = 60$	$x = 0$	$x = 40$	$x = 60$	$x = 0$	$x = 40$	$x = 60$
Kosetice	1193	293.	64.3	911.	84.1	4.37	1136	214.	34.9
Ulborg	846.	78.1	10.5	480.	9.49	0.00	759.	33.2	0.622
Frederiksborg	827.	109.	23.6	491.	19.6	3.12	767.	52.8	6.41
Jægersborg	704.	85.6	14.4	453.	8.12	0.00	748.	31.0	0.90
Virolahti	610.	3.21	0.00	642.	2.99	0.00	849.	22.7	0.736
Uto	1027	109.	0.00	381.	0.00	0.00	705.	11.5	0.00
Westerland	990.	139.	23.7	465.	22.2	0.00	770.	61.9	11.2
Deuselbach	1294	399.	121.	835.	88.3	12.7	1078	187.	33.4
Brotjacklriegel	1303	366.	59.7	1005	139.	7.24	1264	327.	79.1
Neuglobsow	1125	306.	105.	826.	66.6	6.84	1038	158.	38.9
Zingst	920.	95.4	25.4	487.	8.08	0.00	796.	54.4	5.69
Meinerzhagen	1190	362.	119.	864.	90.3	6.07	1081	201.	30.9
Birkenes	709.	53.6	7.71	433.	0.00	0.00	719.	11.4	0.00
Osen	575.	33.4	5.79	513.	0.938	0.00	736.	7.05	0.00
Stara Lesna	1018	183.	19.7	771.	36.9	4.31	992.	101.	12.8
Rörvik	819.	84.9	6.05	424.	2.55	0.00	707.	16.0	0.00
Vavihill	969.	143.	30.4	503.	5.75	0.00	757.	30.5	1.51
Norra-Kvill	927.	103.	5.98	602.	8.42	0.00	810.	38.2	1.71
Strath Vaich	761.	98.1	25.8	539.	3.84	0.833	851.	20.4	0.925
Harwell	911.	191.	64.1	595.	52.8	17.9	806.	94.9	21.6

Table 3.16: Average of AOT x over the measured and simulated daily ozone concentrations. Days where at least one measurement data point is missing is not included in the average values. Units in the table are ppbV \times day.

(Figures 3.4 and 3.10), and that a QSSA solver together with this simple treatment of photolysis can create enormous errors in polluted areas⁹(Figure 3.12).

However, very often new solvers for RAQMs are evaluated for specific night- and daytime scenarios[48, 49] where photolysis is set to constant values during the entire simulation. The results presented in Figure 3.12 elucidate a very important result. Tests of a new chemical solver must be made together with the photolysis rates along 3-dimensional trajectories, where the CRS is simulated under relatively clean and polluted cases without chemical sources and sinks.

It has been widely recognized by scientists that the Gear algorithm is too comprehensive a solver for RAQMs, e.g. see Refs. [47, 48, 49]. The presentation of the computational speed of the MOON model compared to DACFOS shows that if a vector computer is available this is no longer the case (see Table 3.7). Considering the importance of the CRS in RAQMs and the misinterpretation a QSSA solver can

⁹Note the Urban case used in this context is less polluted than the most polluted scenarios used to evaluate the QSSA[47], EBI[48] and IEH[49] solvers.

introduce in RAQM simulations (Figure 3.12), the need of using a Gear algorithm in RAQMs is justified.

The general trends from the comparison of DACFOS and the MOON model to different measurement stations in Europe showed that the MOON model in general simulated higher surface ozone concentrations than DACFOS. This higher ozone concentration was in much better agreement with the measurement data. Most of the stations measurements of the daily TOD and the diurnal maximum ozone concentration closely resembles the results from the MOON model. Moreover, the diurnal maximum ozone peak in general appears in the afternoon for both the measurement data, DACFOS and the MOON model. The current problems with the MOON model (and also with DACFOS) is that it has a smaller diurnal cycle than the measurement data and that it can produce for some of the locations a high ozone concentration peak just after sunset, see for example Figure 3.15.

At present it is difficult to come up with the exact reason for these defects, but it is reasonable to believe that they do not come from the chemical mechanism. However, it is well-known that the emission of chemical compounds is poorly known. Furthermore, as described in the introduction to this chapter, warm temperatures can increase the evaporation of VOC emissions. In the MOON model a temperature dependence of VOC emissions is not incorporated. If this were done it could increase the diurnal cycle.

In conclusion, based on the comparison performed in this chapter between DACFOS, the MOON model and measurement data for a wide range of measurement stations in Europe, we can conclude that for these cases the MOON model simulates surface ozone concentrations far better than DACFOS. However, the model have only been tested for a two week period in August 1995. Additional validation for longer periods, for different years and for a more broad spectra of locations must be performed in order to confirm how well the MOON model performs compared to measurement data and DACFOS. We believe that due to the highly accurate solver and treatment of photolysis, this new Lagrangian model will be superior to DACFOS.

Chapter 4

Conclusion and Prospects

The main achievements of this thesis can be split in two:

- a highly vectorized Lagrangian transport-chemical model (the MOON model) using a Gear algorithm to solve the chemistry and modeled photolysis rates (not parameterized) has been developed, and
- a model to calculate rate constants for elementary gas-phase reactions with special application to atmospheric reactions has been developed.

Due to the enormous demand of theoretical as well as programming development, only primary tests of these models have been performed. Many improvements and tests still have to be made. The code for the MOON model is of 11772 lines (452 kbytes) and 8679 lines (250 kbytes) for the rate constant model.

4.1 The MOON Model

The development of the MOON model was initiated by making a comparison of the EMEP, RADM2 and RACM MCHs (*Chapter 1*) some of the most often used atmospheric gas-phase chemical mechanisms in air quality models. This work was done in order to chose the best mechanism among these three for the MOON model. The main results from this comparison were

- the EMEP MCH gives more ozone than the RACM MCH, and
- the RADM2 MCH gives less ozone than the RACM MCH.

Hence, based on this comparison it was not possible to conclude which of the mechanisms that describe tropospheric chemistry best. Since

- the RACM MCH is a revised version of the RADM2 MCH,
- the EMEP MCH is constrained to be used only in the ABL in a limited temperature interval, and

- the RACM MCH is the newest mechanism among the three i.e. includes the newest updated chemical reaction rates and chemical reaction scheme,

the RACM MCH was chosen as atmospheric gas-phase chemical mechanism for the MOON model, even through the EMEP MCH is more carbon conservative than the RACM MCH. Aside from these results, the comparison studies from *Chapter 1* also indicate that a single urban or rural scenario is not sufficient for comparing atmospheric chemical mechanisms. Simulations of an entire isopleth over a wide variety of $\text{NO}_{x,s}$ and VOC as done in *Chapter 1* give the best insight into the differences between atmospheric chemical mechanisms.

The main purposes of developing the MOON model as outlined in the *Introduction*, *Objectives* are accomplished very well. In *Chapter 3* the MOON model:

– from a numerical point of view,

- proved to be a more robust model (see Figure 3.12) than DACFOS,
- showed the use of the Gear algorithm and modeled photolysis, compared to fast solvers such as the QSSA and parameterized photolysis, is highly preferable (see Figure 3.4, 3.10 and 3.12), and
- ran with a computational speed of the same magnitude as that of DACFOS.

Therefore, the MOON model **can be** used as the surface ozone forecasting model at DMI.

– from a simulation result point of view,

- gave higher concentration levels of surface ozone than DACFOS,
- predicted the daily maximum ozone concentration reasonably well compared to measurement data (DACFOS gave values which were too low),
- predicted that the diurnal maximum ozone peak in general occurred in the afternoon as seen for the measurement data (this is also observed for DACFOS), and
- produced a daily TOD that closely resembled the measurement data (DACFOS gave values which were too low).

Therefore, the MOON model **ought to be** used as the surface ozone forecasting model at DMI.

Problems with the MOON model (and also with DACFOS) are that it has a lower diurnal cycle than the measurement data and sometimes the model gives a high ozone peak after sunset but before midnight compared with the measurement data. Thus, the MOON model gives at present too small AOT40 and AOT60 values (DACFOS gives even lower values).

It is a well-known fact that the emission of chemical compounds is poorly known and has a significant influence on the atmospheric chemical composition. This is a crucial problem in all air quality modeling. Nevertheless, the MOON model is a relatively simple transport-chemical model. Therefore many further developments and improvements of it can be made. Some of these are suggested below.

Scope for Further Investigations

Many uncertainties related to the atmospheric chemistry of ozone, NO₂ and SO₂ still remain e.g.

- chemistry of organic compounds: aromatic chemistry, isoprene and other biogenically emitted compounds,
- scavenging of nitrogen and sulfate, and
- formation ratios of aerosol precursors.

Thus, new atmospheric gas-phase kinetic data and improved atmospheric mechanisms must continuously be applied to the chemical scheme in the MOON model.

Clouds and aerosols can have a strong effect on radiation, on atmospheric radical concentrations and ozone precursors; they can therefore have a great impact on tropospheric ozone concentrations. In the present version of the MOON model the only cloud/aerosol parameter used is the total cloud cover fraction to adjust the photolysis.

Possible improvements of this part of the MOON model are:

- incorporating clouds in the MOON model using the cloud parameterization from HIRLAM,
- after the above task is accomplished it will be important to include their effect on photolysis reactions,
- developing an aqueous-phase chemical mechanism and implement it in the MOON model, and
- including aerosol chemistry in the MOON model.

Many aspects of aerosols and their chemistry (formation, size etc.) are poorly known and further research to incorporate aerosols and their chemistry into air quality models is required. The current guidelines from the EUROTRAC Chemical Mechanism Development (CMD) project can be used as the starting point.

Finally, since warm temperatures can increase the evaporation of VOC emissions, and surface roughness and landscape codes can be gained from DMI-HIRLAM it is possible to improve the treatment of

- VOC emissions, and

- dry depositions.

Many of these above items are relatively easy to implement because a chemical compiler is built into the MOON model, see for example *Appendix D*.

4.2 The New Quantum Statistical Model

The developed quantum statistical model is a very approximative method. For that reason the results from the model should not be used if experimental measurements are available. Nevertheless if an unknown rate constant for a chemical reaction needs to be calculated, tests of the model showed that it was superior to the traditionally used correlation methods. The new model could calculate rate constants within a factor of 10-25, while correlation methods can give errors between 10^2 to 10^4 . Furthermore, the quantum statistical model could predict the temperature dependence pretty well.

The main advantage of the model is that only a very limited number of input parameters are needed to calculate the rate constants for a reaction. These parameters can with good accuracy be calculated utilizing electronic structure calculations.

Hence, at present the quantum statistical model has only been tested on reactions without activation barriers. A natural next step will be to test it on chemical reactions with activation barriers.

Scope for Further Investigations

It is crucial for the success of the model if the theory can be expanded to reactions with activation energy barriers. Calculation of an activation energy, governed by the localization of molecular structures for reactants and transition states, for large organic molecules using standard electronic structure methods is very cumbersome.

However, we are in the process of making a model that enables a reasonable estimation of the activation energy using the information of molecular properties of reactants and products. The model uses the force constants of the equilibrium structures to estimate the energy necessary for climbing the potential barrier. It relates to previously published methods [168, 169] for calculating the activation barriers for electron and proton transfer reactions along with substitution reactions.

4.3 Concluding Remarks

The two new models presented in this dissertation show very promising results but further tests of both models are needed before we can determine their success conclusively: the quantum statistical method ought to be tested for a large variety of chemical reactions, and the MOON model ought to be tested for a larger variety of different geographic locations in Europe over longer periods of time.

However, even though the performance time is outstanding for the MOON model in its present form, many aspects of the MOON model can be improved further;

- until now all runs of the MOON model on the NEC SX-4 are based on a compilation of the code without optimization,
- the MFLOPS shown in Table 3.7 can be improved, and
- the code can be parallelized (NEC SX-4 has 16 processors) since the MOON model's trajectory-grouping concept is ideal for parallel computing.

This means with a little extra work, the MOON model's elapsed time can be improved tremendously. Therefore, we believe that it successfully can be adjusted to an Eulerian ozone forecasting model.

Appendix A

EMEP, RADM2 and RACM MCHs

In this appendix, three gas-phase chemical mechanisms are given: the EMEP[30], RADM2[31] and RACM MCHs[32]. The organic chemistry of the mechanisms shown in this appendix are written on an “as is” basis as given in Refs. [30, 31, 32]. In *Section 1.2.1* a more detailed description of the concept used to build up the mechanisms is given.

In Tables A.1 and A.2 the acronyms used in the three mechanisms for the organic lumping groups are shown. In Table A.3, A.5 and A.7 the different photolysis reactions for the mechanisms are shown. Finally, in Tables A.4, A.6 and A.8 the first-, second- and third-order reactions in the specific mechanisms are given.

Species	Definition	Carbon Number
OXYL	<i>o</i> -xylene	8
OXYO ₂	peroxy radical formed from <i>o</i> -xylene + HO	8
OXYO ₂ H	hydroperoxide from OXYO ₂	8
GLYOX	glyoxal (HCOCHO)	2
MGLYOX	methyl-glyoxal (CH ₃ COCHO)	3
MAL	CH ₃ COCH=CHCHO	5
MALO ₂	peroxy radical from MAL + HO	5
MALO ₂ H	hydroperoxide radical from MALO ₂	5
ISO	isoprene	5
ISRO ₂	peroxy radical from ISO + HO	5
ISRO ₂ H	hydroperoxy radical from ISRO ₂ + HO ₂	5
MACR	methacrolein	4
MACRO ₂	peroxy radical from MACR + HO	4
MACRO ₂ H	hydroperoxy radical from MACRO ₂ + HO ₂	4
PAN	peroxyacetyl nitrate (CH ₃ C(O)OONO ₂)	2
MPAN	peroxy methacryloyl nitrate (CH ₂ =C(CH ₃)C(O)OONO ₂)	4
MVK	methyl vinyl ketone	4
MVKO ₂	peroxy radical from methyl vinyl ketone	4
MVKO ₂ H	hydroperoxy radical from MVKO ₂ + HO ₂	4
ISNI	organic nitrate	5
ISNIR	alkyl peroxy radical from ISNI	5
ISNIRH	adduct from ISNIR + HO ₂	5
ISONO ₃	isoprene-NO ₃ adduct	5

continued on next page, EMEP MCH

<i>continued from previous page, EMEP MCH</i>		
Species	Definition	Carbon Number
ISONO ₃ H	adduct from ISONO ₃ + HO ₂	5
AOH1	O=CHC(OO·)(CH ₃)CH ₂ OH + O=CHC(OH)(CH ₃)CH ₂ OO·	4

Table A.1: Species list for some of the organic compounds in the EMEP MCH.

Species			Carbon Number
RADM2	RACM	Definition	Number
<i>Alkanes</i>			
CH ₄	CH ₄	methane	1.0
ETH	ETH	ethane	2.0
HC3	HC3	alkanes, alcohols, esters and alkynes with HO rate constant (298 K, 1 atm) less than $3.4 \times 10^{-12} \text{cm}^3 \text{s}^{-1}$	2.9
HC5	HC5	alkanes, alcohols, esters and alkynes with HO rate constant (298 K, 1 atm) between $3.4 \times 10^{-12} \text{cm}^3 \text{s}^{-1}$ and $6.8 \times 10^{-12} \text{cm}^3 \text{s}^{-1}$	4.8
HC8	HC8	alkanes, alcohols, esters and alkynes with HO rate constant (298 K, 1 atm) greater than $6.8 \times 10^{-12} \text{cm}^3 \text{s}^{-1}$	7.9
<i>Alkenes</i>			
OL2	ETE	ethene	2.0
OLT	OLT	terminal alkenes	3.8
OLI	OLI	internal alkenes	5.0
	DIEN	butadiene and other antropogenic dienes	4.0
<i>Stable Biogenic Alkenes</i>			
ISO	ISO	isoprene	5.0
	API	α -pinene and other cyclic terpenes with one double bond	10.0
	LIM	d-limonene and other cyclic diene-terpenes	10.0
<i>Aromatics</i>			
TOL	TOL	toluene and less reactive aromatics	7.1
XYL	XYL	xylene and more reactive aromatics	8.9
CSL	CSL	cresol and other hydroxy substituted aromatics	6.6
<i>Carbonyls</i>			
HCHO	HCHO	formaldehyde	1.0
ALD	ALD	acetaldehyde and higher aldehydes	2.4
KET	KET	ketones	3.9/3.5
GLY	GLY	glyoxal	2.0
MGLY	MGLY	methylglyoxal and other α -carbonyl aldehydes	3.0
DCB	DCB	unsaturated dicarbonyls	4.2
	MACR	methacrolein and other unsaturated monealdehydes	4.0
	UDD	unsaturated dihydroxy dicarbonyl	4.2
	HKET	hydroxy ketone	3.0
<i>Organic Nitrogen</i>			
ONIT	ONIT	organic nitrate	4.0
PAN	PAN	peroxyacetyl nitrate and higher saturated PANs	2.0
TPAN	TPAN	unsaturated PANs	4.0
<i>Organic Peroxides</i>			
OP1	OP1	methyl hydrogen peroxide	1.0
OP2	OP2	higher organic peroxides	2.0

continued on next page, RADM2 and RACM MCH

<i>continued from previous page, RADM2 and RACM MCH</i>			
Species			Carbon
RADM2	RACM	Definition	Number
PAA	PAA	peroxyacetic acid and higher analogs	2.0
<i>Organic Acids</i>			
ORA1	ORA1	formic acid	1.0
ORA2	ORA2	acetic acid and higher acids	2.0
<i>Peroxy Radicals From Alkanes</i>			
MO2	MO2	methyl peroxy radical	1.0
ETHP	ETHP	peroxy radical formed from ETH	2.0
HC3P	HC3P	peroxy radical formed from HC3	2.9
HC5P	HC5P	peroxy radical formed from HC5	4.8
HC8P	HC8P	peroxy radical formed from HC8	7.9
<i>Peroxy Radicals From Alkenes</i>			
OL2P	ETEP	peroxy radicals formed from OL2/ETE	2.0
OLTP	OLTP	peroxy radicals formed from OLT	3.8
OLIP	OLIP	peroxy radicals formed from OLI	4.8
<i>Peroxy Radicals From Biogenic Alkenes</i>			
	ISOP	peroxy radicals formed from ISO and DIEN	5.0
	APIP	peroxy radicals formed from API	10.0
	LIMP	peroxy radicals formed from LIM	10.0
<i>Radicals Produced From Aromatics</i>			
	PHO	phenoxy radical and similar radicals	6.6
	ADDT	aromatic-HO adduct from TOL	7.1
	ADDX	aromatic-HO adduct from XYL	8.9
	ADDC	aromatic-HO adduct from CSL	6.6
TOLP	TOLP	peroxy radicals formed from TOL	7.1
XYLP	XYLP	peroxy radicals formed from XYL	8.9
	CSLP	peroxy radicals formed from CSL	6.6
<i>Peroxy Radicals With Carbonyl Groups</i>			
ACO ₃	ACO ₃	acetyl peroxy and higher saturated acyl peroxy radicals	2.0
TCO ₃	TCO ₃	unsaturated acyl peroxy radicals	4.0
KETP	KETP	peroxy radicals formed from KET	3.9
<i>Other Peroxy Radicals</i>			
OLN	OLNN	NO ₃ -alkene adduct reaction to form carbonitrates + HO	3.0
	OLND	NO ₃ -alkene adduct reaction via decomposition	3.0
XNO ₂		accounts for additional organic nitrate formation affected by the lumped organic species	...
XO ₂	XO ₂	accounts for additional NO to NO ₂ conversions affected by the lumped organic species	...

Table A.2: Species list for the organic compounds in the RADM2 and RACM MCHs.

Reaction	A s ⁻¹	B	C
R1 O ₃ + hν → O(³ P) + O ₂	5.219×10 ⁻⁴	0.322	0.079
R2 O ₃ + hν → O(¹ D) + O ₂	8.978×10 ⁻⁵	1.436	0.936
R3 NO ₂ + hν → NO + O(³ P)	1.108×10 ⁻²	0.397	0.183
R4 NO ₃ + hν → NO + O ₂	2.669×10 ⁻²	0.185	0.103
R5 NO ₃ + hν → NO ₂ + O(³ P)	1.853×10 ⁻¹	0.189	0.112
R6 N ₂ O ₅ + hν → NO ₂ + NO ₃	3.324×10 ⁻⁵	0.000	0.566
R7 H ₂ O ₂ + hν → HO + HO	1.057×10 ⁻⁵	0.800	0.243
R8 HNO ₃ + hν → NO ₂ + HO	1.037×10 ⁻⁶	1.227	0.322
R9 CH ₃ O ₂ H + hν → CH ₃ O + HO	5.797×10 ⁻⁶	0.764	0.249
R10 HCHO + hν → HO ₂ + HO ₂ + CO	4.866×10 ⁻⁵	0.781	0.349
R11 HCHO + hν → CO + H ₂	6.790×10 ⁻⁵	0.565	0.275
R12 C ₂ H ₅ OOH + hν → C ₂ H ₅ O + HO	5.797×10 ⁻⁶	0.764	0.249
R13 CH ₃ CHO + hν → CH ₃ + HCO	8.443×10 ⁻⁶	1.177	0.437
R14 CH ₃ COO ₂ H + hν → CH ₃ O ₂ + CO ₂ + HO	5.797×10 ⁻⁶	0.764	0.249
R15 CH ₃ COC ₂ H ₅ + hν → CH ₃ COO ₂ + C ₂ H ₅ O ₂	6.591×10 ⁻⁶	1.070	0.399
R16 CH ₃ COCHO ₂ HCH ₃ + hν → CH ₃ CHO + CH ₃ COO ₂ + HO	5.797×10 ⁻⁶	0.764	0.249
R17 <i>sec</i> -C ₄ H ₉ O ₂ H + hν → HO + <i>sec</i> -C ₄ H ₉ O	5.797×10 ⁻⁶	0.764	0.249
R18 CH ₂ OOHCH ₂ OH + hν → HO ₂ + HO + 1.56 HCHO + 0.22 CH ₃ CHO	5.797×10 ⁻⁶	0.764	0.249
R19 CH ₃ CHOOHCH ₂ OH + hν → CH ₃ CHO + HCHO + HO ₂	5.797×10 ⁻⁶	0.764	0.249
R20 OXYO ₂ H + hν → HO + MGLYOX + MAL + HO ₂	5.797×10 ⁻⁶	0.764	0.249
R21 MALO ₂ H + hν → HO + HO ₂ + MGLYOX + GLYOX	5.797×10 ⁻⁶	0.764	0.249
R22 GLYOX + hν → 2.0 CO + 2.0 HO ₂	3.887×10 ⁻⁵	0.695	0.289
R23 GLYOX + hν → 0.13 HCHO + 0.87 H ₂ + 1.87 CO	1.030×10 ⁻⁵	0.222	0.154
R24 MGLYOX + hν → CH ₃ COO ₂ + CO + HO ₂	1.524×10 ⁻⁵	0.270	0.156

Table A.3: Photolysis reactions and rates for the EMEP MCH. The photolysis rates are calculated according to $J = A \cos(\theta)^B \exp(-C \sec(\theta))$. A, B and C are given in the table. θ is the solar zenith angle. J is in units of s⁻¹.

Reaction	Rate Constant
<i>Inorganic Chemistry</i>	
R25 O(³ P) + O ₂ → O ₃	5.7×10 ⁻³⁴ [M] (T/300) ^{-2.8}
R26 O(³ P) + NO → NO ₂	9.6×10 ⁻³² [M] (T/300) ^{-1.6}
R27 O(¹ D) → O(³ P)	2.0×10 ⁻¹¹ [M] exp(100/T)
R28 O(¹ D) → HO + HO	2.2×10 ⁻¹⁰ [H ₂ O]
R29 H + O ₂ → HO ₂	5.1×10 ⁻³² [M] (T/300) ^{-0.9}
R30 O ₃ + NO → NO ₂	1.8×10 ⁻¹² exp(-1370/T)
R31 O ₃ + NO ₂ → NO ₃	1.2×10 ⁻¹³ exp(-2450/T)
R32 O ₃ + HO → HO ₂	1.9×10 ⁻¹² exp(-1000/T)
R33 O ₃ + HO ₂ → HO	1.4×10 ⁻¹⁴ exp(-600/T)
R34 NO + NO ₃ → NO ₂ + NO ₂	1.8×10 ⁻¹¹ exp(110/T)
R35 NO + HO ₂ → NO ₂ + HO	3.7×10 ⁻¹² exp(240/T)
R36 NO ₂ + NO ₃ → NO + NO ₂	7.2×10 ⁻¹⁴ exp(-1414/T)
R37 NO ₂ + NO ₃ → N ₂ O ₅	1.4×10 ⁻¹²
R38 NO ₂ + HO → HNO ₃	1.4×10 ⁻¹¹
R39 NO ₃ + H ₂ O ₂ → HO ₂ + HNO ₃	4.1×10 ⁻¹⁶
R40 N ₂ O ₅ → NO ₂ + NO ₃	7.1×10 ⁺¹⁴ exp(-11080/T)

continued on next page, EMEP MCH

<i>continued from previous page, EMEP MCH</i>	
Reaction	Rate Constant
R41 HO + HO ₂ →	4.8 × 10 ⁻¹¹ exp(250/T)
R42 HO + H ₂ O ₂ → HO ₂	2.9 × 10 ⁻¹² exp(-160/T)
R43 HO + H ₂ → H	7.7 × 10 ⁻¹² exp(-2100/T)
R44 HO + HNO ₃ → NO ₃	1.0 × 10 ⁻¹⁴ exp(785/T)
R45 HO ₂ + HO ₂ → H ₂ O ₂	(1. + 1.4 × 10 ⁻²¹ [H ₂ O] exp(2200/T)) × 2.3 × 10 ⁻¹³ exp(600/T)
R46 HO ₂ + HO ₂ → H ₂ O ₂	(1. + 1.4 × 10 ⁻²¹ [H ₂ O] exp(2200/T)) × [M] 1.7 × 10 ⁻³³ exp(1000/T)
R47 HO + CO → H + CO ₂	2.4 × 10 ⁻¹³
<i>Sulphur Chemistry</i>	
R48 HO + SO ₂ → HSO ₃	1.35 × 10 ⁻¹²
R49 CH ₃ O ₂ + SO ₂ → SO ₃ + CH ₃ O	4.0 × 10 ⁻¹⁷
R50 HSO ₃ + O ₂ → HO ₂ + SO ₃	1.0 × 10 ⁻¹¹
R51 SO ₃ + H ₂ O → sulphate	9.1 × 10 ⁻¹³
<i>Methane Chemistry</i>	
R52 HO + CH ₄ → CH ₃	7.44 × 10 ⁻¹⁸ T ² exp(-1361/T)
R53 CH ₃ + O ₂ → CH ₃ O ₂	1.25 × 10 ⁻¹²
R54 CH ₃ O ₂ + NO → CH ₃ O + NO ₂	4.2 × 10 ⁻¹² exp(180/T)
R55 CH ₃ O ₂ + CH ₃ O ₂ → CH ₃ O + CH ₃ O	5.5 × 10 ⁻¹⁴ exp(365/T)
R56 CH ₃ O ₂ + CH ₃ O ₂ → CH ₃ OH + HCHO	5.5 × 10 ⁻¹⁴ exp(365/T)
R57 HO + CH ₃ OH → HO ₂ + HCHO	3.3 × 10 ⁻¹² exp(-380/T)
R58 HO ₂ + CH ₃ O ₂ → CH ₃ O ₂ H	3.8 × 10 ⁻¹³ exp(780/T)
R59 CH ₃ O + O ₂ → HCHO + HO ₂	1.1 × 10 ⁻¹³ exp(-1310/T)
R60 HO + HCHO → HCO	9.6 × 10 ⁻¹²
R61 HCO + O ₂ → CO + HO ₂	5.1 × 10 ⁻¹²
R62 CH ₃ O ₂ H + HO → HCHO + HO	1.0 × 10 ⁻¹² exp(190/T)
R63 CH ₃ O ₂ H + HO → CH ₃ O ₂	1.9 × 10 ⁻¹² exp(190/T)
R64 NO ₃ + HCHO → HNO ₃ + HCO	5.8 × 10 ⁻¹⁶
<i>Ethane Chemistry</i>	
R65 HO + C ₂ H ₆ → C ₂ H ₅ O ₂	7.8 × 10 ⁻¹² exp(-1020/T)
R66 C ₂ H ₅ O ₂ + NO → C ₂ H ₅ O + NO ₂	8.9 × 10 ⁻¹²
R67 C ₂ H ₅ O ₂ + HO ₂ → C ₂ H ₅ OOH	6.5 × 10 ⁻¹³ exp(650/T)
R68 C ₂ H ₅ OOH + HO → CH ₃ CHO + HO	5.8 × 10 ⁻¹² exp(190/T)
R69 C ₂ H ₅ OOH + HO → C ₂ H ₅ O ₂	1.9 × 10 ⁻¹² exp(190/T)
R70 C ₂ H ₅ O + O ₂ → HO ₂ + CH ₃ CHO	6.0 × 10 ⁻¹⁴ exp(-550/T)
R71 HO + CH ₃ CHO → CH ₃ COO ₂	5.6 × 10 ⁻¹² exp(310/T)
R72 CH ₃ COO ₂ + NO ₂ → PAN	1.0 × 10 ⁻¹¹
R73 PAN → CH ₃ COO ₂ + NO ₂	1.34 × 10 ¹⁶ exp(-13330/T)
R74 CH ₃ COO ₂ + NO → NO ₂ + CH ₃	2.0 × 10 ⁻¹¹
R75 CH ₃ O ₂ + CH ₃ COO ₂ → CH ₃ O + CH ₃	5.5 × 10 ⁻¹²
R76 CH ₃ O ₂ + CH ₃ COO ₂ → CH ₃ COOH + HCHO	5.5 × 10 ⁻¹²
R77 CH ₃ COO ₂ + CH ₃ COO ₂ → CH ₃ + CH ₃	2.8 × 10 ⁻¹² exp(530/T)
R78 CH ₃ COO ₂ + HO ₂ → CH ₃ COO ₂ H	1.3 × 10 ⁻¹³ exp(1040/T)
R79 CH ₃ COO ₂ H + HO → CH ₃ COO ₂	1.9 × 10 ⁻¹² exp(190/T)
R80 CH ₃ COO ₂ + HO ₂ → CH ₃ COOH + O ₃	3.0 × 10 ⁻¹³ exp(1040/T)
<i>Ethanol Chemistry</i>	
<i>continued on next page, EMEP MCH</i>	

<i>continued from previous page, EMEP MCH</i>		
	Reaction	Rate Constant
R81	$\text{OH} + \text{C}_2\text{H}_5\text{OH} \rightarrow \text{CH}_3\text{CHO} + \text{HO}_2$	3.2×10^{-12}
<i>n-Butane Chemistry</i>		
R82	$\text{HO} + n\text{-C}_4\text{H}_{10} \rightarrow \text{sec-C}_4\text{H}_9\text{O}_2$	$1.64 \times 10^{-11} \exp(-559/T)$
R83	$\text{NO} + \text{sec-C}_4\text{H}_9\text{O}_2 \rightarrow \text{NO}_2 + \text{sec-C}_4\text{H}_9\text{O}$	$4.2 \times 10^{-12} \exp(180/T)$
R84	$\text{sec-C}_4\text{H}_9\text{O} \rightarrow 0.65 \text{HO}_2 + 0.65 \text{CH}_3\text{COC}_2\text{H}_5$ $+ 0.35 \text{CH}_3\text{CHO} + 0.35 \text{C}_2\text{H}_5\text{O}_2$	7.8×10^4
R85	$\text{HO} + \text{CH}_3\text{COC}_2\text{H}_5 \rightarrow \text{CH}_3\text{COCHO}_2\text{CH}_3$	1.15×10^{-12}
R86	$\text{CH}_3\text{COCHO}_2\text{CH}_3 + \text{NO} \rightarrow \text{NO}_2 + \text{CH}_3\text{COO}_2$ $+ \text{CH}_3\text{CHO}$	$4.2 \times 10^{-12} \exp(180/T)$
R87	$\text{CH}_3\text{COCHO}_2\text{CH}_3 + \text{HO}_2 \rightarrow \text{CH}_3\text{COCHO}_2\text{HCH}_3$	1.0×10^{-11}
R88	$\text{CH}_3\text{COCHO}_2\text{HCH}_3 + \text{HO} \rightarrow \text{CH}_3\text{COCHO}_2\text{CH}_3$	4.8×10^{-12}
R89	$\text{sec-C}_4\text{H}_9\text{O}_2 + \text{HO}_2 \rightarrow \text{sec-C}_4\text{H}_9\text{O}_2\text{H}$	1.0×10^{-11}
R90	$\text{sec-C}_4\text{H}_9\text{O}_2\text{H} + \text{HO} \rightarrow \text{sec-C}_4\text{H}_9\text{O}_2$	$1.9 \times 10^{-12} \exp(190/T)$
R91	$\text{sec-C}_4\text{H}_9\text{O}_2\text{H} + \text{HO} \rightarrow \text{HO} + \text{CH}_3\text{COC}_2\text{H}_5$	$5.8 \times 10^{-12} \exp(190/T)$
<i>Ethene Chemistry</i>		
R92	$\text{C}_2\text{H}_4 + \text{HO} \rightarrow \text{CH}_2\text{O}_2\text{CH}_2\text{OH}$	$1.66 \times 10^{-12} \exp(474/T)$
R93	$\text{CH}_2\text{O}_2\text{CH}_2\text{OH} + \text{NO} \rightarrow \text{NO}_2 + \text{HCHO} + \text{HCHO}$ $+ \text{HO}_2$	$4.2 \times 10^{-12} \exp(180/T)$
R94	$\text{CH}_2\text{O}_2\text{CH}_2\text{OH} + \text{HO}_2 \rightarrow \text{CH}_2\text{OOHCH}_2\text{OH}$	1.0×10^{-11}
R95	$\text{CH}_2\text{OOHCH}_2\text{OH} + \text{HO} \rightarrow \text{CH}_3\text{CHO} + \text{HO}$	$5.8 \times 10^{-12} \exp(190/T)$
R96	$\text{CH}_2\text{OOHCH}_2\text{OH} + \text{HO} \rightarrow \text{CH}_2\text{O}_2\text{CH}_2\text{OH}$	$1.9 \times 10^{-12} \exp(190/T)$
R97	$\text{C}_2\text{H}_4 + \text{O}_3 \rightarrow \text{HCHO} + 0.44 \text{CO} + 0.12 \text{HO}_2$ $+ 0.4 \text{HCOOH} + 0.13 \text{H}_2$	$1.2 \times 10^{-14} \exp(-2630/T)$
<i>Propene Chemistry</i>		
R98	$\text{O}_3 + \text{C}_3\text{H}_6 \rightarrow 0.5 \text{HCHO} + 0.5 \text{CH}_3\text{CHO} + 0.07 \text{CH}_4$ $+ 0.4 \text{CO} + 0.28 \text{HO}_2 + 0.15 \text{HO}$ $+ 0.31 \text{CH}_3\text{O}_2 + 0.07 \text{H}_2$	$6.5 \times 10^{-15} \exp(-1880/T)$
R99	$\text{C}_3\text{H}_6 + \text{OH} \rightarrow \text{CH}_3\text{CHO}_2\text{CH}_2\text{OH}$	2.86×10^{-11}
R100	$\text{CH}_3\text{CHO}_2\text{CH}_2\text{OH} + \text{NO} \rightarrow \text{NO}_2 + \text{CH}_3\text{CHO}$ $+ \text{HCHO} + \text{HO}_2$	$4.2 \times 10^{-12} \exp(180/T)$
R101	$\text{CH}_3\text{CHO}_2\text{CH}_2\text{OH} + \text{HO}_2 \rightarrow \text{CH}_3\text{CHOOHCH}_2\text{OH}$	1.0×10^{-11}
R102	$\text{CH}_3\text{CHOOHCH}_2\text{OH} + \text{OH} \rightarrow \text{CH}_3\text{COC}_2\text{H}_5 + \text{OH}$	$5.8 \times 10^{-12} \exp(190/T)$
R103	$\text{CH}_3\text{CHOOHCH}_2\text{OH} + \text{HO} \rightarrow \text{CH}_3\text{CHO}_2\text{CH}_2\text{OH}$	$1.9 \times 10^{-12} \exp(190/T)$
<i>o-Xylene Chemistry</i>		
R104	$\text{OXYL} + \text{HO} \rightarrow \text{OXYO}_2$	1.37×10^{-11}
R105	$\text{OXYO}_2 + \text{NO} \rightarrow \text{NO}_2 + \text{MGLYOX} + \text{MAL} + \text{HO}_2$	$4.2 \times 10^{-12} \exp(180/T)$
R106	$\text{OXYO}_2 + \text{HO}_2 \rightarrow \text{OXYO}_2\text{H}$	1.0×10^{-11}
R107	$\text{OXYO}_2\text{H} + \text{HO} \rightarrow \text{OXYO}_2$	1.7×10^{-11}
R108	$\text{MAL} + \text{OH} \rightarrow \text{MALO}_2$	2.0×10^{-11}
R109	$\text{MALO}_2 + \text{NO} \rightarrow \text{NO}_2 + \text{HO}_2 + \text{MGLYOX} + \text{GLYOX}$	$4.2 \times 10^{-12} \exp(180/T)$
R110	$\text{MALO}_2 + \text{HO}_2 \rightarrow \text{MALO}_2\text{H}$	1.0×10^{-11}
R111	$\text{MALO}_2\text{H} + \text{HO} \rightarrow \text{MALO}_2$	2.4×10^{-11}
R112	$\text{HO} + \text{GLYOX} \rightarrow \text{HO}_2 + \text{CO} + \text{CO}$	1.1×10^{-11}
R113	$\text{HO} + \text{MGLYOX} \rightarrow \text{CH}_3\text{COO}_2 + \text{CO}$	1.70×10^{-11}
<i>Isoprene Chemistry</i>		
R114	$\text{ISO} + \text{O}_3 \rightarrow 0.67 \text{MACR} + 0.26 \text{MVK} + 0.3 \text{O}(^3\text{P})$	$12.3 \times 10^{-15} \exp(-2013/T)$
<i>continued on next page, EMEP MCH</i>		

<i>continued from previous page, EMEP MCH</i>		
Reaction		Rate Constant
	+ 0.55 HO + 0.07 C ₃ H ₆ + 0.8 HCHO + 0.06 HO ₂ + 0.05 CO	
R115	ISO + HO → ISRO ₂	2.54 × 10 ⁻¹¹ exp(410/T)
R116	ISRO ₂ + NO → 0.32 MACR + 0.42 MVK + 0.74 HCHO + 0.14 ISNI + 0.12 ISRO ₂ + 0.78 HO ₂ + 0.86 NO ₂	4.2 × 10 ⁻¹² exp(180/T)
R117	MVK + HO → MVKO ₂	4.13 × 10 ⁻¹² exp(452/T)
R118	MVKO ₂ + NO → 0.684 H ₃ CHO + 0.684 CH ₃ COO ₂ + 0.266 MGLYOX + 0.266 HCHO + 0.05 ISNI + 0.95 NO ₂ + 0.95 HO ₂	4.2 × 10 ⁻¹² exp(180/T)
R119	ISRO ₂ + HO ₂ → ISRO ₂ H	1.0 × 10 ⁻¹¹
R120	ISRO ₂ H + HO → HO + ISRO ₂	2.0 × 10 ⁻¹¹
R121	ISRO ₂ H + O ₃ → 0.7 HCHO	8.0 × 10 ⁻¹⁸
R122	MACR + HO → 0.5 AOH1 + 0.5 MACRO ₂	1.86 × 10 ⁻¹¹ exp(175/T)
R123	MACRO ₂ + NO ₂ → MPAN	1.0 × 10 ⁻¹¹
R124	MPAN → MACRO ₂ + NO ₂	1.34 × 10 ¹⁶ exp(-13330/T)
R125	MACRO ₂ + NO → CH ₂ CCH ₃ + NO ₂	2.0 × 10 ⁻¹¹
R126	CH ₂ CCH ₃ + NO → NO ₂ + CH ₃ COC ₂ H ₅ + HO ₂	4.2 × 10 ⁻¹² exp(180/T)
R127	MVK + O ₃ → 0.82 MGLYOX + 0.8 HCHO + 0.2 O(³ P) + 0.05 CO + 0.06 HO ₂ + 0.04 CH ₃ CHO + 0.08 HO	4.32 × 10 ⁻¹⁵ exp(-2016/T)
R128	ISNI + HO → ISNIR	3.35 × 10 ⁻¹¹
R129	ISNIR + NO → 0.05 HO ₂ + 2.0 NO ₂ + 0.95 CH ₃ CHO + 0.95 CH ₃ COC ₂ H ₅	4.2 × 10 ⁻¹² exp(180/T)
R130	ISO + NO ₃ → ISONO ₃	7.8 × 10 ⁻¹³
R131	ISONO ₃ + NO → 1.10 NO ₂ + 0.80 HO ₂ + 0.85 ISNI + 0.10 MACR + 0.15 HCHO + 0.05 MVK	4.2 × 10 ⁻¹² exp(180/T)
<i>Extra HO₂ Reactions</i>		
R132	MVKO ₂ + HO ₂ → MVKO ₂ H	1.0 × 10 ⁻¹¹
R133	MACRO ₂ + HO ₂ → MARO ₂ H	1.0 × 10 ⁻¹¹
R134	CH ₂ CCH ₃ + HO ₂ → CH ₂ CO ₂ HCH ₃	1.0 × 10 ⁻¹¹
R135	ISNIR + HO ₂ → ISNIRH	1.0 × 10 ⁻¹¹
R136	ISONO ₃ + HO ₂ → ISONO ₃ H	1.0 × 10 ⁻¹¹
<i>Extra Since EMEP MSC-W Note 2/93[82]</i>		
R137	CH ₂ CO ₂ HCH ₃ + HO → CH ₂ CCH ₃	3.2 × 10 ⁻¹¹
R138	ISONO ₃ H + HO → ISONO ₃	2.0 × 10 ⁻¹¹
R139	MVKO ₂ H + HO → MVKO ₂	2.2 × 10 ⁻¹¹
R140	ISNIRH + HO → ISNIR	3.7 × 10 ⁻¹¹
R141	MARO ₂ H + HO → MACRO ₂	3.7 × 10 ⁻¹¹

Table A.4: The EMEP MCH. Units for rate constants of first-order reactions are s⁻¹ and for second-order reactions cm³s⁻¹.

Reaction	Photolysis Frequency s ⁻¹	
R1	$\text{NO}_2 + h\nu \rightarrow \text{O}({}^3P) + \text{NO}$	7.72×10^{-3}
R2	$\text{O}_3 + h\nu \rightarrow \text{O}({}^1D) + \text{O}_2$	1.70×10^{-5}
R3	$\text{O}_3 + h\nu \rightarrow \text{O}({}^3P) + \text{O}_2$	4.22×10^{-4}
R4	$\text{HONO} + h\nu \rightarrow \text{HO} + \text{NO}$	1.39×10^{-3}
R5	$\text{HNO}_3 + h\nu \rightarrow \text{HO} + \text{NO}_2$	2.75×10^{-7}
R6	$\text{HNO}_4 + h\nu \rightarrow \text{HO}_2 + \text{NO}_2$	4.58×10^{-6}
R7	$\text{NO}_3 + h\nu \rightarrow \text{NO} + \text{O}_2$	2.02×10^{-2}
R8	$\text{NO}_3 + h\nu \rightarrow \text{NO}_2 + \text{O}({}^3P)$	1.64×10^{-1}
R9	$\text{H}_2\text{O}_2 + h\nu \rightarrow \text{HO} + \text{HO}$	5.67×10^{-6}
R10	$\text{HCHO} + h\nu \rightarrow \text{H}_2 + \text{CO}$	3.32×10^{-5}
R11	$\text{HCHO} + h\nu \rightarrow \text{HO}_2 + \text{HO}_2 + \text{CO}$	2.18×10^{-5}
R12	$\text{ALD} + h\nu \rightarrow \text{MO}_2 + \text{HO}_2 + \text{CO}$	3.55×10^{-6}
R13	$\text{OP1} + h\nu \rightarrow \text{HCHO} + \text{HO}_2 + \text{HO}$	5.57×10^{-6}
R14	$\text{OP2} + h\nu \rightarrow \text{ALD} + \text{HO}_2 + \text{HO}$	5.57×10^{-6}
R15	$\text{PAA} + h\nu \rightarrow \text{MO}_2 + \text{CO}_2 + \text{HO}$	1.59×10^{-6}
R16	$\text{KET} + h\nu \rightarrow \text{ACO}_3 + \text{ETHP}$	6.07×10^{-7}
R17	$\text{GLY} + h\nu \rightarrow 0.13 \text{ HCHO} + 1.87 \text{ CO}$	4.98×10^{-5}
R18	$\text{GLY} + h\nu \rightarrow 0.45 \text{ HCHO} + 1.55 \text{ CO} + 0.80 \text{ HO}_2$	5.17×10^{-5}
R19	$\text{MGLY} + h\nu \rightarrow \text{ACO}_3 + \text{HO}_2 + \text{CO}$	1.44×10^{-4}
R20	$\text{DCB} + h\nu \rightarrow 0.98 \text{ HO}_2 + 0.02 \text{ ACO}_3 + \text{TCO}_3$	4.30×10^{-4}
R21	$\text{ONIT} + h\nu \rightarrow 0.20 \text{ ALD} + 0.80 \text{ KET} + \text{HO}_2$	7.95×10^{-7}

Table A.5: Photolysis reactions and rates for the RADM2 MCH. The rates are given for solar zenith angle 40°, June 21, summer surface, 40° northern latitude.

Reaction	Rate Constant
<i>Inorganic Chemistry</i>	
R22	$\text{O}({}^3P) + \text{O}_2 \rightarrow \text{O}_3$ [M] $6.00 \times 10^{-34} (T/300)^{-2.3}$
R23	$\text{O}({}^3P) + \text{NO}_2 \rightarrow \text{NO} + \text{O}_2$ $6.50 \times 10^{-12} \exp(120/T)$
R24	$\text{O}({}^1D) + \text{N}_2 \rightarrow \text{O}({}^3P) + \text{N}_2$ $1.80 \times 10^{-11} \exp(110/T)$
R25	$\text{O}({}^1D) + \text{O}_2 \rightarrow \text{O}({}^3P) + \text{O}_2$ $3.20 \times 10^{-11} \exp(70/T)$
R26	$\text{O}({}^1D) + \text{H}_2\text{O} \rightarrow \text{HO} + \text{HO}$ 2.20×10^{-10}
R27	$\text{O}_3 + \text{NO} \rightarrow \text{NO}_2 + \text{O}_2$ $2.00 \times 10^{-12} \exp(-1400/T)$
R28	$\text{O}_3 + \text{HO} \rightarrow \text{HO}_2 + \text{O}_2$ $1.60 \times 10^{-12} \exp(-940/T)$
R29	$\text{O}_3 + \text{HO}_2 \rightarrow \text{HO} + 2 \text{ O}_2$ $1.10 \times 10^{-14} \exp(-500/T)$
R30	$\text{HO}_2 + \text{NO} \rightarrow \text{NO}_2 + \text{HO}$ $3.70 \times 10^{-12} \exp(240/T)$
R31	$\text{HO}_2 + \text{NO}_2 \rightarrow \text{HNO}_4$ $k_0(T) = 1.80 \times 10^{-31} (T/300)^{-3.2}$ $k_\infty = 4.70 \times 10^{-12} (T/300)^{-1.4}$ (see 1)
R32	$\text{HNO}_4 \rightarrow \text{HO}_2 + \text{NO}_2$ $k_{R31} \times 2.10 \times 10^{-27} \exp(-10900/T)$
R33	$\text{HO}_2 + \text{HO}_2 \rightarrow \text{H}_2\text{O}_2$ $2.2 \times 10^{-13} \exp(620/T)$ $+ 1.9 \times 10^{-33} [\text{M}] \exp(980/T)$
R34	$\text{HO}_2 + \text{HO}_2 + \text{H}_2\text{O} \rightarrow \text{H}_2\text{O}_2$ $3.08 \times 10^{-34} \exp(2820/T)$ $+ 2.66\text{E-}54 [\text{M}] \exp(3180/T)$
R35	$\text{H}_2\text{O}_2 + \text{HO} \rightarrow \text{HO}_2 + \text{H}_2\text{O}$ $3.30 \times 10^{-12} \exp(-200/T)$
R36	$\text{NO} + \text{HO} \rightarrow \text{HONO}$ $k_0(T) = 7.00 \times 10^{-31} (T/300)^{-2.6}$ $k_\infty = 1.50 \times 10^{-11} (T/300)^{-0.5}$ (see 1)
R37	$\text{NO} + \text{NO} + \text{O}_2 \rightarrow \text{NO}_2 + \text{NO}_2$ $3.30 \times 10^{-39} \exp(530/T)$
R38	$\text{O}_3 + \text{NO}_2 \rightarrow \text{NO}_3$ $1.40 \times 10^{-13} \exp(-2500/T)$

continued on next page, RADM2 MCH

continued from previous page, RADM2 MCH

Reaction	Rate Constant
R39 $\text{NO}_3 + \text{NO} \rightarrow \text{NO}_2 + \text{NO}_2$	$1.70 \times 10^{-11} \exp(150/T)$
R40 $\text{NO}_3 + \text{NO}_2 \rightarrow \text{NO} + \text{NO}_2 + \text{O}_2$	$2.50 \times 10^{-14} \exp(-1230/T)$
R41 $\text{NO}_3 + \text{HO}_2 \rightarrow \text{HNO}_3 + \text{O}_2$	2.50×10^{-12}
R42 $\text{NO}_3 + \text{NO}_2 \rightarrow \text{N}_2\text{O}_5$	$k_0(T) = 2.20 \times 10^{-30} (T/300)^{-4.3}$ $k_\infty = 1.50 \times 10^{-12} (T/300)^{-0.5}$ (see 1)
R43 $\text{N}_2\text{O}_5 \rightarrow \text{NO}_2 + \text{NO}_3$	$k_{R42} \times 1.10 \times 10^{-27} \exp(-11200/T)$
R44 "N ₂ O ₅ + H ₂ O → 2.0 HNO ₃ "	2.00×10^{-21}
R45 $\text{HO} + \text{NO}_2 \rightarrow \text{HNO}_3$	$k_0(T) = 2.60 \times 10^{-30} (T/300)^{-3.2}$ $k_\infty = 2.40 \times 10^{-11} (T/300)^{-1.3}$ (see 1)
R46 $\text{HO} + \text{HNO}_3 \rightarrow \text{NO}_3 + \text{H}_2\text{O}$	$k_0 = 7.2 \times 10^{-15} \exp(785/T)$ $k_2 = 4.1 \times 10^{-16} \exp(1440/T)$ $k_3 = 1.9 \times 10^{-33} \exp(725/T)$ [M] $k_{46} = k_0 + k_3/(1 + k_3/k_2)$
R47 $\text{HO} + \text{HNO}_4 \rightarrow \text{NO}_2 + \text{H}_2\text{O}$	$1.30 \times 10^{-12} \exp(380/T)$
R48 $\text{HO} + \text{HO}_2 \rightarrow \text{H}_2\text{O} + \text{O}_2$	$4.60 \times 10^{-11} \exp(230/T)$
R49 $\text{HO} + \text{SO}_2 \rightarrow \text{sulfuric acid} + \text{HO}_2$	$k_0(T) = 3.00 \times 10^{-31} (T/300)^{-3.3}$ $k_\infty = 1.50 \times 10^{-12}$ (see 1)
R50 $\text{CO} + \text{HO} \rightarrow \text{HO}_2 + \text{CO}_2$	$1.5 \times 10^{-13} (1 + 2.439 \times 10^{-20} [\text{M}])$
<i>HO + Organic Compounds</i>	
R51 $\text{CH}_4 + \text{HO} \rightarrow \text{MO}_2 + \text{H}_2\text{O}$	$T^2 6.95 \times 10^{-18} \exp(-1280/T)$
R52 $\text{ETH} + \text{HO} \rightarrow \text{ETHP} + \text{H}_2\text{O}$	$T^2 1.37 \times 10^{-17} \exp(-444/T)$
R53 $\text{HC3} + \text{HO} \rightarrow 0.83 \text{HC3P} + 0.17 \text{HO}_2 + .009 \text{HCHO}$ $+ .075 \text{ALD} + .025 \text{KET} + \text{H}_2\text{O}$	$1.59 \times 10^{-11} \exp(-540/T)$
R54 $\text{HC5} + \text{HO} \rightarrow \text{HC5P} + 0.25 \text{XO}_2 + \text{H}_2\text{O}$	$1.73 \times 10^{-11} \exp(-380/T)$
R55 $\text{HC8} + \text{HO} \rightarrow \text{HC8P} + 0.75 \text{XO}_2 + \text{H}_2\text{O}$	$3.64 \times 10^{-11} \exp(-380/T)$
R56 $\text{OL2} + \text{HO} \rightarrow \text{OL2P}$	$2.15 \times 10^{-12} \exp(411/T)$
R57 $\text{OLT} + \text{HO} \rightarrow \text{OLTTP}$	$5.32 \times 10^{-12} \exp(504/T)$
R58 $\text{OLI} + \text{HO} \rightarrow \text{OLIP}$	$1.07 \times 10^{-11} \exp(549/T)$
R59 $\text{TOL} + \text{HO} \rightarrow 0.75 \text{TOLP} + 0.25 \text{CSL} + 0.25 \text{HO}_2$	$2.10 \times 10^{-12} \exp(322/T)$
R60 $\text{XYL} + \text{HO} \rightarrow 0.83 \text{XYLP} + 0.17 \text{CSL} + 0.17 \text{HO}_2$	$1.89 \times 10^{-11} \exp(116/T)$
R61 $\text{CSL} + \text{HO} \rightarrow 0.1 \text{HO}_2 + 0.9 \text{XO}_2 + 0.9 \text{TCO}_3$	4.00×10^{-11}
R62 $\text{CSL} + \text{HO} \rightarrow \text{CSL}$	3.60×10^{-11}
R63 $\text{HCHO} + \text{HO} \rightarrow \text{HO}_2 + \text{CO} + \text{H}_2\text{O}$	9.00×10^{-12}
R64 $\text{ALD} + \text{HO} \rightarrow \text{ACO}_3 + \text{H}_2\text{O}$	$6.87 \times 10^{-12} \exp(256/T)$
R65 $\text{KET} + \text{HO} \rightarrow \text{KETP} + \text{H}_2\text{O}$	$1.20 \times 10^{-11} \exp(-745/T)$
R66 $\text{GLY} + \text{HO} \rightarrow \text{HO}_2 + 2.0 \text{CO} + \text{H}_2\text{O}$	1.15×10^{-11}
R67 $\text{MGLY} + \text{HO} \rightarrow \text{ACO}_3 + \text{CO} + \text{H}_2\text{O}$	1.70×10^{-11}
R68 $\text{DCB} + \text{HO} \rightarrow \text{TCO}_3 + \text{H}_2\text{O}$	2.80×10^{-11}
R69 $\text{OP1} + \text{HO} \rightarrow 0.5 \text{MO}_2 + 0.5 \text{HCHO} + 0.5 \text{HO}$	1.00×10^{-11}
R70 $\text{OP2} + \text{HO} \rightarrow 0.5 \text{HC3P} + 0.5 \text{ALD} + 0.5 \text{HO}$	1.00×10^{-11}
R71 $\text{PAA} + \text{HO} \rightarrow \text{ACO}_3 + \text{H}_2\text{O}$	1.00×10^{-11}
R72 $\text{PAN} + \text{HO} \rightarrow \text{HCHO} + \text{NO}_3 + \text{XO}_2$	$T^2 6.85 \times 10^{-18} \exp(-444/T)$
R73 $\text{ONIT} + \text{HO} \rightarrow \text{HC3P} + \text{NO}_2$	$1.55 \times 10^{-11} \exp(-540/T)$
R74 $\text{ISO} + \text{HO} \rightarrow \text{OLTTP}$	$2.55 \times 10^{-11} \exp(409/T)$
<i>Peroxyacynitrate Formation and Decomposition</i>	
R75 $\text{ACO}_3 + \text{NO}_2 \rightarrow \text{PAN}$	$2.80 \times 10^{-12} \exp(181.0/T)$

continued on next page, RADM2 MCH

<i>continued from previous page, RADM2 MCH</i>		
	Reaction	Rate Constant
R76	PAN → ACO ₃ + NO ₂	1.95 × 10 ¹⁶ exp(-13543.0/T)
R77	TCO ₃ + NO ₂ → TPAN	4.70 × 10 ⁻¹²
R78	TPAN → TCO ₃ + NO ₂	1.95 × 10 ¹⁶ exp(-13543./T)
<i>NO + Organic Peroxy Radicals</i>		
R79	MO ₂ + NO → HCHO + HO ₂ + NO ₂	4.20 × 10 ⁻¹² exp(180/T)
R80	HC3P + NO → 0.75 ALD + 0.25 KET + 0.09 HCHO + .036 ONIT + .964 NO ₂ + .964 HO ₂	4.20 × 10 ⁻¹² exp(180/T)
R81	HC5P + NO → 0.38 ALD + 0.69 KET + 0.08 ONIT + 0.92 NO ₂ + 0.92 HO ₂	4.20 × 10 ⁻¹² exp(180/T)
R82	HC8P + NO → 0.35 ALD + 1.06 KET + 0.04 HCHO + 0.24 ONIT + 0.76 NO ₂ + 0.76 HO ₂	4.20 × 10 ⁻¹² exp(180/T)
R83	OL2P + NO → 1.6 HCHO + HO ₂ + NO ₂ + 0.2 ALD	4.20 × 10 ⁻¹² exp(180/T)
R84	OLTP + NO → ALD + HCHO + HO ₂ + NO ₂	4.20 × 10 ⁻¹² exp(180/T)
R85	OLIP + NO → HO ₂ + 1.45 ALD + 0.28 HCHO + 0.10 KET + NO ₂	4.20 × 10 ⁻¹² exp(180/T)
R86	ACO ₃ + NO → MO ₂ + NO ₂	4.20 × 10 ⁻¹² exp(180/T)
R87	TCO ₃ + NO → NO ₂ + 0.92 HO ₂ + 0.89 GLY + 0.11 MGLY + 0.05 ACO ₃ + 0.95 CO + 2.0 XO ₂	4.20 × 10 ⁻¹² exp(180/T)
R88	TOLP + NO → NO ₂ + HO ₂ + 0.17 MGLY + 0.16 GLY + 0.70 DCB	4.20 × 10 ⁻¹² exp(180/T)
R89	XYLP + NO → NO ₂ + HO ₂ + .450 MGLY + .806 DCB	4.20 × 10 ⁻¹² exp(180/T)
R90	ETHP + NO → ALD + HO ₂ + NO ₂	4.20 × 10 ⁻¹² exp(180/T)
R91	KETP + NO → MGLY + NO ₂ + HO ₂	4.20 × 10 ⁻¹² exp(180/T)
R92	OLN + NO → HCHO + ALD + 2.0 NO ₂	4.20 × 10 ⁻¹² exp(180/T)
<i>NO₃ + Organic Compounds</i>		
R93	HCHO + NO ₃ → HO ₂ + HNO ₃ + CO	6.00 × 10 ⁻¹³ exp(-2058/T)
R94	ALD + NO ₃ → ACO ₃ + HNO ₃	1.40 × 10 ⁻¹² exp(-1900/T)
R95	GLY + NO ₃ → HNO ₃ + HO ₂ + 2.0 CO	6.00 × 10 ⁻¹³ exp(-2058/T)
R96	MGLY + NO ₃ → HNO ₃ + ACO ₃ + CO	1.40 × 10 ⁻¹² exp(-1900/T)
R97	DCB + NO ₃ → HNO ₃ + TCO ₃	1.40 × 10 ⁻¹² exp(-1900/T)
R98	CSL + NO ₃ → HNO ₃ + XNO ₂ + 0.5 CSL	2.20 × 10 ⁻¹¹
R99	OL2 + NO ₃ → OLN	2.00 × 10 ⁻¹² exp(-2923/T)
R100	OLT + NO ₃ → OLN	1.00 × 10 ⁻¹¹ exp(-1895/T)
R101	OLI + NO ₃ → OLN	3.23 × 10 ⁻¹¹ exp(-975/T)
R102	ISO + NO ₃ → OLN	5.81 × 10 ⁻¹³
<i>O₃ + Organic Compounds</i>		
R103	OL2 + O ₃ → HCHO + 0.42 CO + 0.4 ORA1 + 0.12 HO ₂	1.20 × 10 ⁻¹⁴ exp(-2633/T)
R104	OLT + O ₃ → 0.53 HCHO + 0.50 ALD + 0.33 CO + 0.20 ORA1 + 0.20 ORA2 + 0.23 HO ₂ + 0.22 MO2 + 0.10 HO + 0.06 CH ₄	1.32 × 10 ⁻¹⁴ exp(-2105/T)
R105	OLI + O ₃ → 0.18 HCHO + 0.72 ALD + 0.10 KET + 0.23 CO + 0.06 ORA1 + 0.29 ORA2	7.29 × 10 ⁻¹⁵ exp(-1136/T)

continued on next page, RADM2 MCH

continued from previous page, RADM2 MCH

Reaction	Rate Constant
R106	$1.23 \times 10^{-14} \exp(-2013/T)$

HO₂ + Organic Peroxy Radicals

R107	$7.70 \times 10^{-14} \exp(1300/T)$
R108	$7.70 \times 10^{-14} \exp(1300/T)$
R109	$7.70 \times 10^{-14} \exp(1300/T)$
R110	$7.70 \times 10^{-14} \exp(1300/T)$
R111	$7.70 \times 10^{-14} \exp(1300/T)$
R112	$7.70 \times 10^{-14} \exp(1300/T)$
R113	$7.70 \times 10^{-14} \exp(1300/T)$
R114	$7.70 \times 10^{-14} \exp(1300/T)$
R115	$7.70 \times 10^{-14} \exp(1300/T)$
R116	$7.70 \times 10^{-14} \exp(1300/T)$
R117	$7.70 \times 10^{-14} \exp(1300/T)$
R118	$7.70 \times 10^{-14} \exp(1300/T)$
R119	$7.70 \times 10^{-14} \exp(1300/T)$
R120	$7.70 \times 10^{-14} \exp(1300/T)$

Methyl Peroxy Radical + Organic Peroxy Radical

R121	$1.90 \times 10^{-13} \exp(220/T)$
R122	$1.40 \times 10^{-13} \exp(220/T)$
R123	$4.20 \times 10^{-14} \exp(220/T)$
R124	$3.40 \times 10^{-14} \exp(220/T)$
R125	$2.90 \times 10^{-14} \exp(220/T)$
R126	$1.40 \times 10^{-13} \exp(220/T)$
R127	$1.40 \times 10^{-13} \exp(220/T)$
R128	$1.70 \times 10^{-14} \exp(220/T)$
R129	$1.70 \times 10^{-14} \exp(220/T)$
R130	$9.60 \times 10^{-13} \exp(220/T)$
R131	$1.70 \times 10^{-14} \exp(220/T)$
R132	$1.70 \times 10^{-14} \exp(220/T)$
R133	$9.60 \times 10^{-13} \exp(220/T)$
R134	$1.70 \times 10^{-14} \exp(220/T)$

Acetyl Radical + Organic Peroxy Radicals

R135	$3.40 \times 10^{-13} \exp(220/T)$
------	------------------------------------

continued on next page, RADM2 MCH

<i>continued from previous page, RADM2 MCH</i>		
Reaction		Rate Constant
R136	HC3P + ACO ₃ → 0.77 ALD + .26 KET + 0.5 HO ₂ + 0.5 MO ₂ + 0.5 ORA2	1.00 × 10 ⁻¹³ exp(220/T)
R137	HC5P + ACO ₃ → 0.41 ALD + 0.75 KET + 0.5 HO ₂ + 0.5 MO ₂ + 0.5 ORA2	8.40 × 10 ⁻¹⁴ exp(220/T)
R138	HC8P + ACO ₃ → 0.46 ALD + 1.39 KET + 0.5 HO ₂ + 0.5 MO ₂ + 0.5 ORA2	7.20 × 10 ⁻¹⁴ exp(220/T)
R139	OL2P + ACO ₃ → 0.8 HCHO + 0.6 ALD + 0.5 HO ₂ + 0.5 MO ₂ + 0.5 ORA2	3.40 × 10 ⁻¹³ exp(220/T)
R140	OLTP + ACO ₃ → ALD + 0.5 HCHO + 0.5 HO ₂ + 0.5 MO ₂ + 0.5 ORA2	3.40 × 10 ⁻¹³ exp(220/T)
R141	OLIP + ACO ₃ → .725 ALD + 0.55 KET + 0.14 HCHO + 0.50 HO ₂ + 0.50 MO ₂ + 0.50 ORA2	4.20 × 10 ⁻¹⁴ exp(220/T)
R142	KETP + ACO ₃ → MGLY + 0.5 HO ₂ + 0.5 MO ₂ + 0.5 ORA2	4.20 × 10 ⁻¹⁴ exp(220/T)
R143	ACO ₃ + ACO ₃ → 2.0 MO ₂	1.19 × 10 ⁻¹² exp(220/T)
R144	ACO ₃ + TOLP → MO ₂ + .17 MGLY + .16 GLY + .70 DCB + HO ₂	4.20 × 10 ⁻¹⁴ exp(220/T)
R145	ACO ₃ + XYLP → MO ₂ + .45 MGLY + .806 DCB + HO ₂	4.20 × 10 ⁻¹⁴ exp(220/T)
R146	ACO ₃ + TCO ₃ → MO ₂ + 0.92 HO ₂ + .890 GLY + .11 MGLY + .05 ACO ₃ + .950 CO + 2.0 XO ₂	1.19 × 10 ⁻¹² exp(220/T)
R147	ACO ₃ + OLN → HCHO + ALD + 0.5 ORA2 + NO ₂ + 0.5 MO ₂ + NO ₂	4.20 × 10 ⁻¹⁴ exp(220/T)
<i>NO₃-Alkene-Peroxyradical + NO₃-Alkene-Peroxyradical Reactions</i>		
R148	OLN + OLN → 2.0 HCHO + 2.0 ALD + 2.0 NO ₂	3.60 × 10 ⁻¹⁶ exp(220/T)
<i>Operator Reactions</i>		
R149	XO ₂ + HO ₂ → OP2	7.70 × 10 ⁻¹⁴ exp(1300/T)
R150	XO ₂ + MO ₂ → HCHO + HO2	1.70 × 10 ⁻¹⁴ exp(220/T)
R151	XO ₂ + ACO ₃ → MO ₂	4.20 × 10 ⁻¹⁴ exp(220/T)
R152	XO ₂ + XO ₂ →	3.60 × 10 ⁻¹⁶ exp(220/T)
R153	XO ₂ + NO → NO ₂	4.20 × 10 ⁻¹² exp(180/T)
R154	XNO ₂ + NO ₂ → ONIT	4.20 × 10 ⁻¹² exp(180/T)
R155	XNO ₂ + HO ₂ → OP2	7.70 × 10 ⁻¹⁴ exp(1300/T)
R156	XNO ₂ + MO ₂ → HCHO + HO2	1.70 × 10 ⁻¹⁴ exp(220/T)
R157	XNO ₂ + ACO ₃ → MO ₂	4.20 × 10 ⁻¹⁴ exp(220/T)
R158	XNO ₂ + XNO ₂ →	3.60 × 10 ⁻¹⁶ exp(220/T)

$$1: k = (k_0[M]/(1 + k_0[M]/k_\infty)) \times 0.6^f$$

$$f = (1 + (\log_{10}(k_0[M]/k_\infty))^2)^{-1}$$

Table A.6: The RADM2 MCH. Units for rate constants of first-order reactions are s⁻¹, for second-order reactions cm³s⁻¹ and third-order reactions cm⁶s⁻¹. The reaction of N₂O₅ with H₂O (R44) is omitted in all simulations involving the RADM2 MCH, because it now is realized that it is a heterogeneous reaction.

	Reaction	Photolysis Frequency s ⁻¹
R1	$\text{NO}_2 + h\nu \rightarrow \text{O}({}^3P) + \text{NO}$	7.50×10^{-3}
R2	$\text{O}_3 + h\nu \rightarrow \text{O}({}^1D) + \text{O}_2$	1.62×10^{-5}
R3	$\text{O}_3 + h\nu \rightarrow \text{O}({}^3P) + \text{O}_2$	4.17×10^{-4}
R4	$\text{HONO} + h\nu \rightarrow \text{HO} + \text{NO}$	1.63×10^{-3}
R5	$\text{HNO}_3 + h\nu \rightarrow \text{HO} + \text{NO}_2$	4.50×10^{-7}
R6	$\text{HNO}_4 + h\nu \rightarrow 0.65 \text{HO}_2 + 0.65 \text{NO}_2 + 0.35 \text{HO} + 0.35 \text{NO}_3$	3.17×10^{-6}
R7	$\text{NO}_3 + h\nu \rightarrow \text{NO} + \text{O}_2$	2.33×10^{-2}
R8	$\text{NO}_3 + h\nu \rightarrow \text{NO}_2 + \text{O}({}^3P)$	1.87×10^{-1}
R9	$\text{H}_2\text{O}_2 + h\nu \rightarrow \text{HO} + \text{HO}$	6.00×10^{-6}
R10	$\text{HCHO} + h\nu \rightarrow \text{H}_2 + \text{CO}$	3.50×10^{-5}
R11	$\text{HCHO} + h\nu \rightarrow \text{HO}_2 + \text{HO}_2 + \text{CO}$	2.17×10^{-5}
R12	$\text{ALD} + h\nu \rightarrow \text{MO}_2 + \text{HO}_2 + \text{CO}$	3.67×10^{-6}
R13	$\text{OP1} + h\nu \rightarrow \text{HCHO} + \text{HO}_2 + \text{HO}$	4.17×10^{-6}
R14	$\text{OP2} + h\nu \rightarrow \text{ALD} + \text{HO}_2 + \text{HO}$	4.17×10^{-6}
R15	$\text{PAA} + h\nu \rightarrow \text{MO}_2 + \text{HO}$	1.57×10^{-6}
R16	$\text{KET} + h\nu \rightarrow \text{ACO}_3 + \text{ETHP}$	6.67×10^{-7}
R17	$\text{GLY} + h\nu \rightarrow 0.13 \text{HCHO} + 1.87 \text{CO} + 0.87 \text{H}_2$	5.83×10^{-5}
R18	$\text{GLY} + h\nu \rightarrow 0.45 \text{HCHO} + 1.55 \text{CO} + 0.80 \text{HO}_2 + 0.15 \text{H}_2$	2.00×10^{-5}
R19	$\text{MGLY} + h\nu \rightarrow \text{ACO}_3 + \text{HO}_2 + \text{CO}$	9.33×10^{-5}
R20	$\text{DCB} + h\nu \rightarrow \text{TCO}_3 + \text{HO}_2$	4.33×10^{-4}
R21	$\text{ONIT} + h\nu \rightarrow 0.20 \text{ALD} + 0.80 \text{KET} + \text{HO}_2 + \text{NO}_2$	2.17×10^{-6}
R22	$\text{MACR} + h\nu \rightarrow \text{HCHO} + \text{ACO}_3 + \text{CO} + \text{HO}_2$	1.33×10^{-6}
R23	$\text{HKET} + h\nu \rightarrow \text{ACO}_3 + \text{HCHO} + \text{HO}_2$	6.67×10^{-7}

Table A.7: Photolysis reactions and rates for the RACM MCH. The rates are given for solar zenith angle 40°, June 21, summer surface, 40° northern latitude.

Reaction	Rate Constant
<i>Inorganic Chemistry</i>	
R24 $O(^3P) + O_2 \rightarrow O_3$	[M] $6.00 \times 10^{-34} (T/300)^{-2.3}$
R25 $O(^3P) + O_3 \rightarrow 2.0 O_2$	$8.00 \times 10^{-12} \exp(-2060/T)$
R26 $O(^1D) + N_2 \rightarrow O(^3P) + N_2$	$1.80 \times 10^{-11} \exp(110/T)$
R27 $O(^1D) + O_2 \rightarrow O(^3P) + O_2$	$3.20 \times 10^{-11} \exp(-70/T)$
R28 $O(^1D) + H_2O \rightarrow HO + HO$	2.20×10^{-10}
R29 $O_3 + HO \rightarrow HO_2 + O_2$	$1.60 \times 10^{-12} \exp(-940/T)$
R30 $O_3 + HO_2 \rightarrow HO + 2.0 O_2$	$1.10 \times 10^{-14} \exp(-500/T)$
R31 $HO + HO_2 \rightarrow H_2O + O_2$	$4.80 \times 10^{-11} \exp(250/T)$
R32 $H_2O_2 + HO \rightarrow HO_2 + H_2O$	$2.90 \times 10^{-12} \exp(-160/T)$
R33 $HO_2 + HO_2 \rightarrow H_2O_2 + O_2$	$2.3 \times 10^{-13} \exp(600/T)$ $+ 1.7 \times 10^{-33} [M] \exp(1000/T)$
R34 $HO_2 + HO_2 + H_2O \rightarrow H_2O_2 + H_2O + O_2$	$3.22 \times 10^{-34} \exp(2800/T)$ $+ 2.38 \times 10^{-54} [M] \exp(3200/T)$
R35 $O(^3P) + NO \rightarrow NO_2$	$k_0 = 9.00 \times 10^{-32} (T/300)^{-1.5}$ $k_\infty = 3.00 \times 10^{-11}$ (see 1)
R36 $O(^3P) + NO_2 \rightarrow NO + O_2$	$6.50 \times 10^{-12} \exp(120/T)$
R37 $O(^3P) + NO_2 \rightarrow NO_3$	$k_0 = 9.00 \times 10^{-32} (T/300)^{-2.0}$ $k_\infty = 2.20 \times 10^{-11}$ (see 1)
R38 $HO + NO \rightarrow HONO$	$k_0 = 7.00 \times 10^{-31} (T/300)^{-2.6}$ $k_\infty = 1.50 \times 10^{-11} (T/300)^{-0.5}$ (see 1)
R39 $HO + NO_2 \rightarrow HNO_3$	$k_0 = 2.60 \times 10^{-30} (T/300)^{-3.2}$ $k_\infty = 2.40 \times 10^{-11} (T/300)^{-1.3}$ (see 1)
R40 $HO + NO_3 \rightarrow NO_2 + HO_2$	2.20×10^{-11}
R41 $HO_2 + NO \rightarrow NO_2 + HO$	$3.70 \times 10^{-12} \exp(250/T)$
R42 $HO_2 + NO_2 \rightarrow HNO_4$	$k_0 = 1.80 \times 10^{-31} (T/300)^{-3.2}$ $k_\infty = 4.70 \times 10^{-12} (T/300)^{-1.4}$ (see 1)
R43 $HNO_4 \rightarrow HO_2 + NO_2$	$k_{R42} 2.10 \times 10^{-27} \exp(-10900/T)$
R44 $HO_2 + NO_3 \rightarrow 0.3 HNO_3 + 0.7 NO_2 + 0.7 HO$	3.50×10^{-12}
R45 $HO + HONO \rightarrow H_2O + NO_2$	$1.80 \times 10^{-11} \exp(-390/T)$
R46 $HO + HNO_3 \rightarrow NO_3 + H_2O$	$k_0 = 7.2 \times 10^{-15} \exp(785/T)$ $k_2 = 4.1 \times 10^{-16} \exp(1440/T)$ $k_3 = 1.9 \times 10^{-33} \exp(725/T) [M]$ $k_{R46} = k_0 + k_3/(1 + k_3/k_2)$
R47 $HO + HNO_4 \rightarrow NO_2 + H_2O + O_2$	$1.30 \times 10^{-12} \exp(380/T)$
R48 $O_3 + NO \rightarrow NO_2 + O_2$	$2.00 \times 10^{-12} \exp(-1400/T)$
R49 $O_3 + NO_2 \rightarrow NO_3 + O_2$	$1.20 \times 10^{-13} \exp(-2450/T)$
R50 $NO + NO + O_2 \rightarrow NO_2 + NO_2$	$3.30 \times 10^{-39} \exp(530/T)$
R51 $NO_3 + NO \rightarrow NO_2 + NO_2$	$1.50 \times 10^{-11} \exp(170/T)$
R52 $NO_3 + NO_2 \rightarrow NO + NO_2 + O_2$	$4.50 \times 10^{-14} \exp(-1260/T)$
R53 $NO_3 + NO_2 \rightarrow N_2O_5$	$k_0 = 2.20 \times 10^{-30} (T/300)^{-3.9}$ $k_\infty = 1.50 \times 10^{-12} (T/300)^{-0.7}$ (see 1)
R54 $N_2O_5 \rightarrow NO_2 + NO_3$	$k_{R53} = 2.70 \times 10^{-27} \exp(-11000/T)$
R55 $NO_3 + NO_3 \rightarrow NO_2 + NO_2 + O_2$	$8.50 \times 10^{-13} \exp(-2450/T)$
R56 $HO + H_2 \rightarrow H_2O + HO_2$	$5.50 \times 10^{-12} \exp(-2000/T)$
R57 $HO + SO_2 \rightarrow \text{sulfuric acid} + HO_2$	$k_0 = 3.00 \times 10^{-31} (T/300)^{-3.3}$ $k_\infty = 1.50 \times 10^{-12}$ (see 1)

continued on next page, RACM MCH

continued from previous page, RACM MCH

Reaction	Rate Constant
R58 CO + HO → HO ₂ + CO ₂	$1.5 \times 10^{-13} (1 + 2.439 \times 10^{-20} [M])$
<i>O(³P) + Organic Compounds</i>	
R59 ISO + O(³ P) → 0.86 OLT + 0.05 HCHO + 0.02 HO + 0.01 CO + 0.13 DCB + 0.28 HO ₂ + 0.15 XO ₂	6.00×10^{-11}
R60 MACR + O(³ P) → ALD	$1.59 \times 10^{-11} \exp(13/T)$
<i>HO + Organic Compounds</i>	
R61 CH ₄ + HO → MO ₂ + H ₂ O	$T^2 7.44 \times 10^{-18} \exp(-1361/T)$
R62 ETH + HO → ETHP + H ₂ O	$T^2 1.51 \times 10^{-17} \exp(-492/T)$
R63 HC3 + HO → .583 HC3P + .381 HO ₂ + .335 ALD + .036 ORA1 + .036 CO + .036 GLY + .036 HO + .010 HCHO + H ₂ O	$5.26 \times 10^{-12} \exp(-260/T)$
R64 HC5 + HO → .750 HC5P + .250 KET + .250 HO ₂ + H ₂ O	$8.02 \times 10^{-12} \exp(-155/T)$
R65 HC8 + HO → .951 HC8P + .025 ALD + .024 HKET + .049 HO ₂ + H ₂ O	$1.64 \times 10^{-11} \exp(-125/T)$
R66 ETE + HO → ETEP	$1.96 \times 10^{-12} \exp(438/T)$
R67 OLT + HO → OLTP	$5.72 \times 10^{-12} \exp(500/T)$
R68 OLI + HO → OLIP	$1.33 \times 10^{-11} \exp(500/T)$
R69 DIEN + HO → ISOP	$1.48 \times 10^{-11} \exp(448/T)$
R70 ISO + HO → ISOP	$2.54 \times 10^{-11} \exp(410/T)$
R71 API + HO → APIP	$1.21 \times 10^{-11} \exp(444/T)$
R72 LIM + HO → LIMP	1.71×10^{-10}
R73 TOL + HO → 0.90 ADDT + 0.10 XO ₂ + 0.10 HO ₂	$1.81 \times 10^{-12} \exp(355/T)$
R74 XYL + HO → 0.90 ADDX + 0.10 XO ₂ + 0.10 HO ₂	$7.30 \times 10^{-12} \exp(355/T)$
R75 CSL + HO → 0.85 ADDC + 0.10 PHO + 0.05 HO ₂ + 0.05 XO ₂	6.00×10^{-11}
R76 HCHO + HO → HO ₂ + CO + H ₂ O	1.00×10^{-11}
R77 ALD + HO → ACO ₃ + H ₂ O	$5.55 \times 10^{-12} \exp(331/T)$
R78 KET + HO → KETP + H ₂ O	$T^2 5.68 \times 10^{-18} \exp(92/T)$
R79 HKET + HO → HO ₂ + MGLY + H ₂ O	3.00×10^{-12}
R80 GLY + HO → HO ₂ + 2.0 CO + H ₂ O	1.14×10^{-11}
R81 MGLY + HO → ACO ₃ + CO + H ₂ O	1.72×10^{-11}
R82 MACR + HO → 0.51 TCO ₃ + 0.41 HKET + 0.08 MGLY + 0.41 CO + 0.08 HCHO + 0.49 HO ₂ + 0.49 XO ₂	$1.86 \times 10^{-11} \exp(175/T)$
R83 HO + DCB → 0.50 TCO ₃ + 0.50 HO ₂ + 0.50 XO ₂ + 0.35 UDD + 0.15 GLY + 0.15 MGLY	$2.80 \times 10^{-11} \exp(175/T)$
R84 HO + UDD → 0.88 ALD + 0.12 KET + HO ₂	2.70×10^{-10}
R85 OP1 + HO → .65 MO ₂ + .35 HCHO + 0.35 HO	$2.93 \times 10^{-12} \exp(190/T)$
R86 OP2 + HO → 0.44 HC3P + 0.08 ALD + 0.49 HO + 0.07 XO ₂ + 0.41 KET	$3.40 \times 10^{-12} \exp(190/T)$
R87 PAA + HO → 0.65 ACO ₃ + 0.35 HO ₂ + 0.35 HCHO + 0.35 XO ₂	$2.93 \times 10^{-12} \exp(190/T)$
R88 PAN + HO → HCHO + NO ₃ + XO ₂ + H ₂ O	4.00×10^{-14}
R89 TPAN + HO → 0.60 HKET + 0.60 NO ₃ + 0.40 PAN	$3.25 \times 10^{-13} \exp(500/T)$

continued on next page, RACM MCH

continued from previous page, RACM MCH

Reaction	Rate Constant
R90 ONIT + HO → HC3P + NO ₂ + H ₂ O + 0.40 HCHO + 0.40 HO ₂ + XO ₂	5.31 × 10 ⁻¹² exp(-260/T)
<i>NO₃ + Organic Compounds</i>	
R91 HCHO + NO ₃ → HO ₂ + HNO ₃ + CO	3.40 × 10 ⁻¹³ exp(-1900/T)
R92 ALD + NO ₃ → ACO ₃ + HNO ₃	1.40 × 10 ⁻¹² exp(-1900/T)
R93 GLY + NO ₃ → HNO ₃ + HO ₂ + 2.0 CO	2.90 × 10 ⁻¹² exp(-1900/T)
R94 MGLY + NO ₃ → HNO ₃ + ACO ₃ + CO	1.40 × 10 ⁻¹² exp(-1900/T)
R95 MACR + NO ₃ → 0.20 TCO ₃ + 0.20 HNO ₃ + 0.80 OLNN + 0.80 CO	8.27 × 10 ⁻¹⁵ exp(-150/T)
R96 DCB + NO ₃ → 0.50 TCO ₃ + 0.50 HO ₂ + 0.50 XO ₂ + 0.25 GLY + 0.25 ALD + 0.50 NO ₂ + 0.03 KET + 0.25 MGLY + 0.50 HNO ₃	2.87 × 10 ⁻¹³ exp(-1000/T)
R97 CSL + NO ₃ → HNO ₃ + PHO	2.20 × 10 ⁻¹¹
R98 ETE + NO ₃ → 0.80 OLNN + 0.20 OLND	T ² 4.88 × 10 ⁻¹⁸ exp(-2282/T)
R99 OLT + NO ₃ → 0.43 OLNN + 0.57 OLND	1.79 × 10 ⁻¹³ exp(-450/T)
R100 OLI + NO ₃ → 0.11 OLNN + 0.89 OLND	8.64 × 10 ⁻¹³ exp(450/T)
R101 DIEN + NO ₃ → 0.90 OLNN + 0.10 OLND + 0.90 MACR	1.00 × 10 ⁻¹³
R102 ISO + NO ₃ → 0.90 OLNN + 0.10 OLND + 0.90 MACR	4.00 × 10 ⁻¹² exp(-446/T)
R103 API + NO ₃ → 0.10 OLNN + 0.90 OLND	1.19 × 10 ⁻¹² exp(490/T)
R104 LIM + NO ₃ → 0.13 OLNN + 0.87 OLND	1.22 × 10 ⁻¹¹
R105 TPAN + NO ₃ → 0.60 ONIT + 0.60 NO ₃ + 0.40 PAN + 0.40 HCHO + 0.40 NO ₂ + XO ₂	2.20 × 10 ⁻¹⁴ exp(-500/T)
<i>O₃ + Organic Compounds</i>	
R106 ETE + O ₃ → HCHO + 0.43 CO + 0.37 ORA1 + 0.26 HO ₂ + 0.13 H ₂ + 0.12 HO	9.14 × 10 ⁻¹⁵ exp(-2580/T)
R107 OLT + O ₃ → 0.64 HCHO + 0.44 ALD + 0.37 CO + 0.14 ORA1 + 0.10 ORA2 + 0.25 HO ₂ + 0.40 HO + 0.03 KET + 0.03 KETP + 0.06 CH ₄ + 0.05 H ₂ + 0.03 ETH + .006 H ₂ O ₂ + 0.19 MO ₂ + 0.10 ETHP	4.33 × 10 ⁻¹⁵ exp(-1800/T)
R108 OLI + O ₃ → 0.02 HCHO + 0.99 ALD + 0.16 KET + 0.30 CO + .011 H ₂ O ₂ + 0.14 ORA2 + 0.07 CH ₄ + 0.22 HO ₂ + 0.63 HO + 0.23 MO ₂ + 0.12 KETP + 0.06 ETH + 0.18 ETHP	4.40 × 10 ⁻¹⁵ exp(-845/T)
R109 DIEN + O ₃ → 0.90 HCHO + 0.39 MACR + 0.36 CO + 0.15 ORA1 + 0.09 O(³ P) + 0.30 HO ₂ + 0.35 OLT + 0.28 HO + 0.05 H ₂ + 0.15 ACO ₃ + 0.03 MO ₂ + 0.02 KETP + 0.13 XO ₂ + .001 H ₂ O ₂	1.34 × 10 ⁻¹⁴ exp(-2283/T)
R110 ISO + O ₃ → 0.90 HCHO + 0.39 MACR + 0.36 CO + 0.15 ORA1 + 0.09 O(³ P) + 0.30 HO ₂ + 0.35 OLT + 0.28 HO + 0.05 H ₂ + 0.15 ACO ₃ + 0.03 MO ₂ + 0.02 KETP + 0.13 XO ₂ + .001 H ₂ O ₂	7.86 × 10 ⁻¹⁵ exp(-1913/T)
R111 API + O ₃ → 0.65 ALD + 0.53 KET + 0.14 CO	1.01 × 10 ⁻¹⁵ exp(-732/T)

continued on next page, RACM MCH

continued from previous page, RACM MCH

Reaction	Rate Constant
R112 LIM + O ₃ → 0.20 ETHP + 0.42 KETP + 0.85 HO + 0.10 HO ₂ + 0.02 H ₂ O ₂ + 0.04 HCHO + 0.46 OLT + 0.14 CO	2.00 × 10 ⁻¹⁶
R113 MACR + O ₃ → 0.16 ETHP + 0.42 KETP + 0.85 HO + 0.10 HO ₂ + 0.02 H ₂ O ₂ + 0.79 MACR + 0.01 ORA1 + 0.07 ORA2 + 0.40 HCHO + 0.60 MGLY + 0.13 ORA2	1.36 × 10 ⁻¹⁵ exp(-2112/T)
R114 DCB + O ₃ → 0.54 CO + 0.08 H ₂ + 0.22 ORA1 + 0.29 HO ₂ + 0.07 HO + 0.13 OP2 + 0.13 ACO ₃	2.00 × 10 ⁻¹⁸
R115 TPAN + O ₃ → 0.21 HO + 0.29 HO ₂ + 0.66 CO + 0.50 GLY + 0.62 MGLY + 0.28 ACO ₃ + 0.16 ALD + 0.11 PAA + 0.11 ORA1 + 0.21 ORA2 + 0.70 HCHO + 0.30 PAN + 0.70 NO ₂ + 0.13 CO + 0.04 H ₂ + 0.11 ORA1 + 0.08 HO ₂ + .036 HO + 0.70 ACO ₃	2.46 × 10 ⁻¹⁵ exp(-1700/T)
<i>Reactions of Intermediates Produced by Aromatic Oxidation</i>	
R116 PHO + NO ₂ → 0.10 CSL + ONIT	2.00 × 10 ⁻¹¹
R117 PHO + HO ₂ → CSL	1.00 × 10 ⁻¹¹
R118 ADDT + NO ₂ → CSL + HONO	3.60 × 10 ⁻¹¹
R119 ADDT + O ₂ → 0.98 TOLP + 0.02 CSL + 0.02 HO ₂	1.66 × 10 ⁻¹⁷ exp(1044/T)
R120 ADDT + O ₃ → CSL + HO	5.00 × 10 ⁻¹¹
R121 ADDX + NO ₂ → CSL + HONO	3.60 × 10 ⁻¹¹
R122 ADDX + O ₂ → 0.98 XYLP + 0.02 CSL + 0.02 HO ₂	1.66 × 10 ⁻¹⁷ exp(1044/T)
R123 ADDX + O ₃ → CSL + HO	1.00 × 10 ⁻¹¹
R124 ADDC + NO ₂ → CSL + HONO	3.60 × 10 ⁻¹¹
R125 ADDC + O ₂ → 0.98 CSLP + 0.02 CSL + 0.02 HO ₂	1.66 × 10 ⁻¹⁷ exp(1044/T)
R126 ADDC + O ₃ → CSL + HO	5.00 × 10 ⁻¹¹
<i>Peroxyacynitrate Formation and Decomposition</i>	
R127 ACO ₃ + NO ₂ → PAN	k ₀ = 9.70 × 10 ⁻²⁹ (T/300) ^{-5.6} k _∞ = 9.30 × 10 ⁻¹² (T/300) ^{-1.5} (see 1)
R128 PAN → ACO ₃ + NO ₂	k _{R127} 8.60 × 10 ⁻²⁹ exp(-13954/T)
R129 TCO ₃ + NO ₂ → TPAN	k ₀ = 9.70 × 10 ⁻²⁹ (T/300) ^{-5.6} k _∞ = 9.30 × 10 ⁻¹² (T/300) ^{-1.5} (see 1)
R130 TPAN → TCO ₃ + NO ₂	k _{R129} 8.60 × 10 ⁻²⁹ exp(-13954/T)
<i>NO + Organic Peroxy Radicals</i>	
R131 MO ₂ + NO → HCHO + HO ₂ + NO ₂	4.20 × 10 ⁻¹² exp(180/T)
R132 ETHP + NO → ALD + HO ₂ + NO ₂	8.70 × 10 ⁻¹²
R133 HC3P + NO → .047 HCHO + .233 ALD + .623 KET + .063 GLY + .742 HO ₂ + .150 MO ₂ + .048 ETHP + .048 XO ₂ + .059 ONIT + .941 NO ₂	4.00 × 10 ⁻¹²
R134 HC5P + NO → .021 HCHO + .211 ALD + .722 KET + .599 HO ₂ + .031 MO ₂ + .245 ETHP + .334 XO ₂ + .124 ONIT + .876 NO ₂	4.00 × 10 ⁻¹²

continued on next page, RACM MCH

<i>continued from previous page, RACM MCH</i>		
Reaction	Rate Constant	
R135 HC8P + NO → .150 ALD + .642 KET + .133 ETHP + .261 ONIT + .739 NO ₂ + .606 HO ₂ + .416 XO ₂	4.00 × 10 ⁻¹²	
R136 ETEP + NO → 1.6 HCHO + HO ₂ + NO ₂ + 0.2 ALD	9.00 × 10 ⁻¹²	
R137 OLTP + NO → 0.94 ALD + HCHO + HO ₂ + NO ₂ + 0.06 KET	4.00 × 10 ⁻¹²	
R138 OLIP + NO → HO ₂ + 1.71 ALD + 0.29 KET + NO ₂	4.00 × 10 ⁻¹²	
R139 ISOP + NO → .446 MACR + .354 OLT + .847 HO ₂ + .847 NO ₂ + .153 ONIT + .606 HCHO	4.00 × 10 ⁻¹²	
R140 APIP + NO → 0.80 HO ₂ + 0.80 ALD + 0.80 NO ₂ + 0.80 KET + 0.20 ONIT	4.00 × 10 ⁻¹²	
R141 LIMP + NO → 0.65 HO ₂ + 0.40 MACR + 0.25 OLI + 0.25 HCHO + 0.65 NO ₂ + 0.35 ONIT	4.00 × 10 ⁻¹²	
R142 TOLP + NO → 0.95 NO ₂ + 0.95 HO ₂ + 1.20 GLY + 0.50 DCB + 0.05 ONIT + 0.65 MGLY	4.00 × 10 ⁻¹²	
R143 XYLP + NO → 0.95 NO ₂ + 0.95 HO ₂ + 0.35 GLY + 0.95 DCB + 0.05 ONIT + 0.60 MGLY	4.00 × 10 ⁻¹²	
R144 CSLP + NO → GLY + MGLY + NO ₂ + HO ₂	4.00 × 10 ⁻¹²	
R145 ACO ₃ + NO → MO ₂ + NO ₂	2.00 × 10 ⁻¹¹	
R146 TCO ₃ + NO → NO ₂ + ACO ₃ + HCHO	2.00 × 10 ⁻¹¹	
R147 KETP + NO → 0.54 MGLY + 0.46 ALD + 0.23 ACO ₃ + 0.77 HO ₂ + 0.16 XO ₂ + NO ₂	4.00 × 10 ⁻¹²	
R148 OLNN + NO → ONIT + NO ₂ + HO ₂	4.00 × 10 ⁻¹²	
R149 OLND + NO → .287 HCHO + 1.24 ALD + .464 KET + 2.00 NO ₂	4.00 × 10 ⁻¹²	
<i>HO₂ + Organic Peroxy Radicals</i>		
R150 MO ₂ + HO ₂ → OP1	3.80 × 10 ⁻¹³	exp(800/T)
R151 ETHP + HO ₂ → OP2	7.50 × 10 ⁻¹³	exp(700/T)
R152 HC3P + HO ₂ → OP2	1.66 × 10 ⁻¹³	exp(1300/T)
R153 HC5P + HO ₂ → OP2	1.66 × 10 ⁻¹³	exp(1300/T)
R154 HC8P + HO ₂ → OP2	1.66 × 10 ⁻¹³	exp(1300/T)
R155 ETEP + HO ₂ → OP2	1.90 × 10 ⁻¹³	exp(1300/T)
R156 OLTP + HO ₂ → OP2	1.66 × 10 ⁻¹³	exp(1300/T)
R157 OLIP + HO ₂ → OP2	1.66 × 10 ⁻¹³	exp(1300/T)
R158 ISOP + HO ₂ → OP2	1.28 × 10 ⁻¹³	exp(1300/T)
R159 APIP + HO ₂ → OP2	1.50 × 10 ⁻¹¹	
R160 LIMP + HO ₂ → OP2	1.50 × 10 ⁻¹¹	
R161 TOLP + HO ₂ → OP2	3.75 × 10 ⁻¹³	exp(980/T)
R162 XYLP + HO ₂ → OP2	3.75 × 10 ⁻¹³	exp(980/T)
R163 CSLP + HO ₂ → OP2	3.75 × 10 ⁻¹³	exp(980/T)
R164 ACO ₃ + HO ₂ → PAA	1.15 × 10 ⁻¹²	exp(550/T)
R165 ACO ₃ + HO ₂ → ORA2 + O ₃	3.86 × 10 ⁻¹⁶	exp(2640/T)
R166 TCO ₃ + HO ₂ → OP2	1.15 × 10 ⁻¹²	exp(550/T)
<i>continued on next page, RACM MCH</i>		

continued from previous page, RACM MCH

Reaction	Rate Constant
R167 TCO ₃ + HO ₂ → ORA2 + O ₃	3.86 × 10 ⁻¹⁶ exp(2640/T)
R168 KETP + HO ₂ → OP2	1.15 × 10 ⁻¹³ exp(1300/T)
R169 OLNN + HO ₂ → ONIT	1.66 × 10 ⁻¹³ exp(1300/T)
R170 OLND + HO ₂ → ONIT	1.66 × 10 ⁻¹³ exp(1300/T)
<i>Methyl Peroxy Radical + Organic Peroxy Radicals</i>	
R171 MO ₂ + MO ₂ → 1.33 HCHO + 0.66 HO ₂	9.10 × 10 ⁻¹⁴ exp(416/T)
R172 ETHP + MO ₂ → 0.75 HCHO + HO ₂ + 0.75 ALD	1.18 × 10 ⁻¹³ exp(158/T)
R173 HC3P + MO ₂ → .810 HCHO + .992 HO ₂ + .580 ALD + .018 KET + .007 MO ₂ + .005 MGLY + .085 XO ₂ + .119 GLY	9.46 × 10 ⁻¹⁴ exp(431/T)
R174 HC5P + MO ₂ → .829 HCHO + .946 HO ₂ + .523 ALD + .240 KET + .014 ETHP + .245 XO ₂ + .049 MO ₂	1.00 × 10 ⁻¹³ exp(467/T)
R175 HC8P + MO ₂ → .753 HCHO + .993 HO ₂ + .411 ALD + .419 KET + .322 XO ₂ + .013 ETHP	4.34 × 10 ⁻¹⁴ exp(633/T)
R176 ETEP + MO ₂ → 1.55 HCHO + HO ₂ + 0.35 ALD	1.71 × 10 ⁻¹³ exp(708/T)
R177 OLTP + MO ₂ → 1.25 HCHO + HO ₂ + .669 ALD + .081 KET	1.46 × 10 ⁻¹³ exp(708/T)
R178 OLIP + MO ₂ → .755 HCHO + HO ₂ + .932 ALD + .313 KET	9.18 × 10 ⁻¹⁴ exp(708/T)
R179 ISOP + MO ₂ → .550 MACR + .370 OLT + HO ₂ + .080 OLI + 1.09 HCHO	1.36 × 10 ⁻¹³ exp(708/T)
R180 APIP + MO ₂ → 2.00 HO ₂ + ALD + HCHO + KET	3.56 × 10 ⁻¹⁴ exp(708/T)
R181 LIMP + MO ₂ → 2.00 HO ₂ + 0.60 MACR + 0.40 OLI + 1.40 HCHO	3.56 × 10 ⁻¹⁴ exp(708/T)
R182 TOLP + MO ₂ → HCHO + HO ₂ + 0.65 GLY + DCB + 0.35 MGLY	3.56 × 10 ⁻¹⁴ exp(708/T)
R183 XYLP + MO ₂ → HCHO + HO ₂ + 0.37 GLY + DCB + 0.63 MGLY	3.56 × 10 ⁻¹⁴ exp(708/T)
R184 CSLP + MO ₂ → GLY + MGLY + 2.00 HO ₂ + HCHO	3.56 × 10 ⁻¹⁴ exp(708/T)
R185 ACO ₃ + MO ₂ → HCHO + HO ₂ + MO ₂	3.21 × 10 ⁻¹¹ exp(-440/T)
R186 ACO ₃ + MO ₂ → HCHO + ORA2	2.68 × 10 ⁻¹⁶ exp(2510/T)
R187 TCO ₃ + MO ₂ → ACO ₃ + 2.00 HCHO + HO ₂	3.21 × 10 ⁻¹¹ exp(-440/T)
R188 TCO ₃ + MO ₂ → HCHO + ORA2	2.68 × 10 ⁻¹⁶ exp(2510/T)
R189 KETP + MO ₂ → 0.40 MGLY + 0.30 ALD + 0.30 HKET + 0.88 HO ₂ + 0.08 XO ₂ + 0.12 ACO ₃ + 0.75 HCHO	6.91 × 10 ⁻¹³ exp(508/T)
R190 OLNN + MO ₂ → 0.75 HCHO + HO ₂ + ONIT	1.60 × 10 ⁻¹³ exp(708/T)
R191 OLND + MO ₂ → .960 HCHO + .500 HO ₂ + .640 ALD + .149 KET + .500 NO ₂ + .500 ONIT	9.68 × 10 ⁻¹⁴ exp(708/T)
<i>Acetyl Radical + Organic Peroxy Radicals</i>	
R192 ETHP + ACO ₃ → ALD + .500 HO ₂ + 0.5 MO ₂ + 0.5 ORA2	1.03 × 10 ⁻¹² exp(211/T)
R193 HC3P + ACO ₃ → .724 ALD + .127 KET + .488 HO ₂	6.90 × 10 ⁻¹³ exp(460/T)

continued on next page, RACM MCH

<i>continued from previous page, RACM MCH</i>		
Reaction		Rate Constant
R194	$\text{HC5P} + \text{ACO}_3 \rightarrow$ $+ .508 \text{ MO}_2 + .499 \text{ ORA2} + .091 \text{ HCHO}$ $+ .006 \text{ ETHP} + .071 \text{ XO}_2 + .004 \text{ MGLY}$ $+ .100 \text{ GLY}$ $\rightarrow .677 \text{ ALD} + .330 \text{ KET} + .438 \text{ HO}_2$	$5.59 \times 10^{-13} \exp(522/T)$
R195	$\text{HC8P} + \text{ACO}_3 \rightarrow$ $+ .554 \text{ MO}_2 + .495 \text{ ORA2} + .076 \text{ HCHO}$ $+ .018 \text{ ETHP} + .237 \text{ XO}_2$ $\rightarrow .497 \text{ ALD} + .581 \text{ KET} + .489 \text{ HO}_2$ $+ .507 \text{ MO}_2 + .495 \text{ ORA2} + .015 \text{ ETHP}$ $+ .318 \text{ XO}_2$	$2.47 \times 10^{-13} \exp(683/T)$
R196	$\text{ETEP} + \text{ACO}_3 \rightarrow$ $0.8 \text{ HCHO} + 0.6 \text{ ALD} + 0.5 \text{ HO}_2$ $+ 0.5 \text{ MO}_2 + 0.5 \text{ ORA2}$	$9.48 \times 10^{-13} \exp(765/T)$
R197	$\text{OLTP} + \text{ACO}_3 \rightarrow$ $.859 \text{ ALD} + .501 \text{ HCHO} + .501 \text{ HO}_2$ $+ .501 \text{ MO}_2 + .499 \text{ ORA2} + .141 \text{ KET}$	$8.11 \times 10^{-13} \exp(765/T)$
R198	$\text{OLIP} + \text{ACO}_3 \rightarrow$ $.941 \text{ ALD} + .510 \text{ HO}_2 + .510 \text{ MO}_2$ $+ .569 \text{ KET} + .490 \text{ ORA2}$	$5.09 \times 10^{-13} \exp(765/T)$
R199	$\text{ISOP} + \text{ACO}_3 \rightarrow$ $.771 \text{ MACR} + .229 \text{ OLT} + .506 \text{ HO}_2$ $+ .494 \text{ ORA2} + .340 \text{ HCHO} + .506 \text{ MO}_2$	$7.60 \times 10^{-13} \exp(765/T)$
R200	$\text{APIP} + \text{ACO}_3 \rightarrow \text{HO}_2 + \text{ALD} + \text{MO}_2 + \text{KET}$	$7.40 \times 10^{-13} \exp(765/T)$
R201	$\text{LIMP} + \text{ACO}_3 \rightarrow$ $\text{HO}_2 + 0.60 \text{ MACR} + 0.40 \text{ OLI}$ $+ 0.40 \text{ HCHO} + \text{MO}_2$	$7.40 \times 10^{-13} \exp(765/T)$
R202	$\text{TOLP} + \text{ACO}_3 \rightarrow$ $\text{MO}_2 + \text{HO}_2 + \text{DCB}$ $+ 0.65 \text{ GLY} + 0.35 \text{ MGLY}$	$7.40 \times 10^{-13} \exp(765/T)$
R203	$\text{XYLP} + \text{ACO}_3 \rightarrow$ $\text{MO}_2 + \text{HO}_2 + \text{DCB}$ $+ 0.37 \text{ GLY} + 0.63 \text{ MGLY}$	$7.40 \times 10^{-13} \exp(765/T)$
R204	$\text{CSLP} + \text{ACO}_3 \rightarrow$ $\text{GLY} + \text{MGLY} + \text{HO}_2$ $+ \text{MO}_2$	$7.40 \times 10^{-13} \exp(765/T)$
R205	$\text{ACO}_3 + \text{ACO}_3 \rightarrow 2.0 \text{ MO}_2$	$2.80 \times 10^{-12} \exp(530/T)$
R206	$\text{TCO}_3 + \text{ACO}_3 \rightarrow \text{MO}_2 + \text{ACO}_3 + \text{HCHO}$	$2.80 \times 10^{-12} \exp(530/T)$
R207	$\text{KETP} + \text{ACO}_3 \rightarrow$ $0.54 \text{ MGLY} + 0.35 \text{ ALD} + 0.11 \text{ KET}$ $+ 0.12 \text{ ACO}_3 + 0.38 \text{ HO}_2 + 0.08 \text{ XO}_2$ $+ 0.50 \text{ MO}_2 + 0.50 \text{ ORA2}$	$7.51 \times 10^{-13} \exp(565/T)$
R208	$\text{OLNN} + \text{ACO}_3 \rightarrow$ $\text{ONIT} + 0.50 \text{ MO}_2 + 0.50 \text{ ORA2}$ $+ 0.50 \text{ HO}_2$	$8.85 \times 10^{-13} \exp(765/T)$
R209	$\text{OLND} + \text{ACO}_3 \rightarrow$ $.207 \text{ HCHO} + .650 \text{ ALD} + .167 \text{ KET}$ $+ .516 \text{ MO}_2 + .484 \text{ ORA2} + .484 \text{ ONIT}$ $+ .516 \text{ NO}_2$	$5.37 \times 10^{-13} \exp(765/T)$
<i>NO₃-Alkene-Peroxyradical + NO₃-Alkene-Peroxyradical Reactions</i>		
R210	$\text{OLNN} + \text{OLNN} \rightarrow 2.00 \text{ ONIT} + \text{HO}_2$	$7.00 \times 10^{-14} \exp(1000/T)$
R211	$\text{OLNN} + \text{OLND} \rightarrow$ $.202 \text{ HCHO} + .640 \text{ ALD} + .149 \text{ KET}$ $+ .500 \text{ HO}_2 + .500 \text{ NO}_2 + 1.50 \text{ ONIT}$	$4.25 \times 10^{-14} \exp(1000/T)$
R212	$\text{OLND} + \text{OLND} \rightarrow$ $.504 \text{ HCHO} + 1.21 \text{ ALD} + .285 \text{ KET}$ $+ \text{ONIT} + \text{NO}_2$	$2.96 \times 10^{-14} \exp(1000/T)$
<i>NO₃ + Organic Peroxy Radicals</i>		
R213	$\text{MO}_2 + \text{NO}_3 \rightarrow \text{HCHO} + \text{HO}_2 + \text{NO}_2$	1.20×10^{-12}
R214	$\text{ETHP} + \text{NO}_3 \rightarrow \text{ALD} + \text{HO}_2 + \text{NO}_2$	1.20×10^{-12}
R215	$\text{HC3P} + \text{NO}_3 \rightarrow .048 \text{ HCHO} + .243 \text{ ALD} + .670 \text{ KET}$	1.20×10^{-12}
<i>continued on next page, RACM MCH</i>		

<i>continued from previous page, RACM MCH</i>		
Reaction		Rate Constant
R216	HC5P + NO ₃ → .063 GLY + .792 HO ₂ + .155 MO ₂ + .053 ETHP + .051 XO ₂ + NO ₂ .021 HCHO + .239 ALD + .828 KET + .699 HO ₂ + .040 MO ₂ + .262 ETHP + .391 XO ₂ + NO ₂	1.20 × 10 ⁻¹²
R217	HC8P + NO ₃ → .187 ALD + .880 KET + .155 ETHP + NO ₂ + .845 HO ₂ + .587 XO ₂	1.20 × 10 ⁻¹²
R218	ETEP + NO ₃ → 1.6 HCHO + HO ₂ + NO ₂ + 0.2 ALD	1.20 × 10 ⁻¹²
R219	OLTP + NO ₃ → 0.94 ALD + HCHO + HO ₂ + NO ₂ + 0.06 KET	1.20 × 10 ⁻¹²
R220	OLIP + NO ₃ → HO ₂ + 1.71 ALD + 0.29 KET + NO ₂	1.20 × 10 ⁻¹²
R221	ISOP + NO ₃ → .600 MACR + .400 OLT + HO ₂ + NO ₂ + .686 HCHO	1.20 × 10 ⁻¹²
R222	APIP + NO ₃ → HO ₂ + ALD + NO ₂ + KET	1.20 × 10 ⁻¹²
R223	LIMP + NO ₃ → HO ₂ + 0.60 MACR + 0.40 OLI + 0.40 HCHO + NO ₂	1.20 × 10 ⁻¹²
R224	TOLP + NO ₃ → NO ₂ + HO ₂ + 0.50 DCB + 1.30 GLY + 0.70 MGLY	1.20 × 10 ⁻¹²
R225	XYLP + NO ₃ → NO ₂ + HO ₂ + DCB + 0.74 GLY + 1.26 MGLY	1.20 × 10 ⁻¹²
R226	CSLP + NO ₃ → GLY + MGLY + NO ₂ + HO ₂	1.20 × 10 ⁻¹²
R227	ACO3 + NO ₃ → MO ₂ + NO ₂	4.00 × 10 ⁻¹²
R228	TCO3 + NO ₃ → NO ₂ + ACO ₃ + HCHO	4.00 × 10 ⁻¹²
R229	KETP + NO ₃ → 0.54 MGLY + 0.46 ALD + 0.23 ACO ₃ + 0.77 HO ₂ + 0.16 XO ₂ + NO ₂	1.20 × 10 ⁻¹²
R230	OLNN + NO ₃ → ONIT + NO ₂ + HO ₂	1.20 × 10 ⁻¹²
R231	OLND + NO ₃ → .280 HCHO + 1.24 ALD + .469 KET + 2.00 NO ₂	1.20 × 10 ⁻¹²
<i>Operator Reactions</i>		
R232	XO ₂ + HO ₂ → OP2	1.66 × 10 ⁻¹³ exp(1300/T)
R233	XO ₂ + MO ₂ → HCHO + HO ₂	5.99 × 10 ⁻¹⁵ exp(1510/T)
R234	XO ₂ + ACO ₃ → MO ₂	3.40 × 10 ⁻¹⁴ exp(1560/T)
R235	XO ₂ + XO ₂ →	7.13 × 10 ⁻¹⁷ exp(2950/T)
R236	XO ₂ + NO → NO ₂	4.00 × 10 ⁻¹²
R237	XO ₂ + NO ₃ → NO ₂	1.20 × 10 ⁻¹²

$$1: k = (k_0[M]/(1 + k_0[M]/k_\infty)) \times 0.6^f$$

$$f = (1 + (\log_{10}(k_0[M]/k_\infty))^2)^{-1}$$

Table A.8: The RACM MCH. Units for rate constants of first-order reactions are s⁻¹, for second-order reactions cm³s⁻¹ and third-order reactions cm⁶s⁻¹.

Appendix B

Implementation of VOC Emissions

VOC have an important role in atmospheric chemical processes, it is therefore important to handle these in a proper way in atmospheric chemical mechanisms. This is not a simple task, the associated problems can be summarized as follows:

- hundreds of different types of VOC are emitted into the atmosphere, but knowledge of VOC emission rates and how they react with other species in the atmosphere is very limited,
- since the EMEP, RADM2 and RACM MCHs are lumped mechanisms, it is not possible to implement the compounds actually emitted one by one. They must be implemented in their specific classified lumping group. These groups are classified according to their chemical reactivity characteristics. Afterwards, the magnitude of the emission coming from the different lumping groups must be calculated, and
- VOC effects on the chemical processes vary greatly. When VOC are implemented in the chemical schemes, these differences must therefore be represented in a reasonable manner.

Therefore, only a limited number of VOC have been considered in model simulations presented up to now.

The purpose of this appendix is to explain how VOC emissions are implemented in the EMEP, RADM2 and RACM MCHs. Middleton et al.[170] and Stockwell et al.[31, 32] have given detailed descriptions of how this is done for the RADM2 and RACM MCHs. In contrast, the methodology applied for the EMEP MCH has not been described in any reports or review papers yet. Therefore, the method for the EMEP MCH is based upon recommendations by Simpson[30]. Instead of just giving a summary of the papers by Middleton et al.[170] and Stockwell et al.[31, 32], we will explain how VOC emissions are implemented using the example list of VOC species given in Table B.1. The VOC emissions in Table B.1 represent the case for the continental European boundary layer based upon the paper by Derwent and Jenkin[21]. The table is taken from Ref. [38].

Note, the VOC emission inventory presented in Table B.1 (and Table B.4) is used in the majority of the simulations presented in the thesis.

B.1 Methods

EMEP MCH

In the EMEP MCH each species represents a range of organic compounds of similar chemical structure and reactivity. For example lumping group $n\text{-C}_4\text{H}_{10}$ (n -butane) represents n -butane and all higher alkanes from the emission inventory given in Table B.1. In Table B.2 (column three) it is seen how the different VOC from the emission inventory given in Table B.1 are grouped.

The next step in implementing VOC emissions into the mechanisms is to determine to which extent the different VOC must be considered, i.e. which aggregation factor. For this Simpson[30] used mass weighting. For example, consider lumping group CH_3CHO (the acetaldehyde group). The VOC in the emission inventory given in Table B.1 that go into this lumping group are

- acetaldehyde,
- proprionaldehyde,
- butyraldehyde,
- i -butyraldehyde, and
- valeraldehyde.

These molecules have the weights 44u, 58u, 72u, 72u and 86u, respectively. Therefore, these five compounds' emissions are implemented in the EMEP MCH through lumping group CH_3CHO as follows

$$\begin{aligned} \{\text{CH}_3\text{CHO}\} &= \{\text{acetaldehyde}\} + 58/44 \times \{\text{proprionaldehyde}\} & \text{(B.1)} \\ &+ 72/44 \times \{\text{butyraldehyde}\} + 72/44 \times \{i\text{-butyraldehyde}\} \\ &+ 86/44 \times \{\text{valeraldehyde}\} \end{aligned}$$

In this contents $\{x\}$ means emission of x as given in Table B.1 column two. The result of using this procedure and the emission inventory given in Table B.1 are given in Table B.4.

RADM2 and RACM MCH

Implementation of VOC emissions into the RADM2 and RACM MCHs is described simultaneously, because as stated in *Section 1.2.1*, the RACM MCH is the successor of the RADM2 MCH, therefore the same lumping methodology is used for both mechanisms.

The VOC from the atmosphere are implemented in the RACM and RADM2 MCHs on the basis of three constraints[31, 170]:

- magnitudes of emission rates,
- similarities in functional groups, and
- compounds' reactivity to HO.

The emission rates used in the development of the RACM and RADM2 MCHs are taken from the NAPAP inventory for anthropogenic emissions of VOC in the contiguous portion of U.S. (see appendix A in Ref. [170]). The method is completely general, therefore in principle other emission inventories can be used to adapt the aggregation factors.

In order to implement the VOC emissions from the atmosphere into the RACM and RADM2 MCHs, these chemical compounds are grouped into 32 emission categories, see appendix A in Ref. [170]. Furthermore, these 32 categories are aggregated into 15 RACM and RADM2 species, see table 3 in Ref. [32] and table 2 in Ref. [170].

In the RACM and RADM2 MCHs the emissions are counted by first looking up which category the different VOC, e.g. the species written in Table B.1, belong to. A list of over 550 VOC emissions are given in appendix A in Ref. [170]). For these different categories the aggregation factor can be found in table 3 in Ref. [32] for the RACM MCH and table 2 in Ref. [170] for the RADM2 MCH. As an example let us look at lumping group HC3. From appendix A in Ref. [170] we find that the only species from Table B.1 that belong to HC3 are:

- propane,
- *n*-butane,
- *i*-butane,
- 2,2-dimethylbutane,
- acetylene,
- methanol,
- ethanol,
- methyl-acetate,
- ethyl-acetate,
- *i*-propyl-acetate, and
- tetrachloroethylene.

From table 3 in Ref. [32] and table 2 in Ref. [170] we get the following aggregation factors for the two mechanisms

- $(0.57 \wedge 0.519)$,

- $(1.11 \wedge 0.964)$,
- $(1.11 \wedge 0.964)$,
- $(1.11 \wedge 0.964)$,
- $(0.41 \wedge 0.343)$,
- $(0.49 \wedge 0.404)$,
- $(1.37 \wedge 1.215)$,
- $(0.49 \wedge 0.404)$,
- $(0.49 \wedge 0.404)$,
- $(1.37 \wedge 1.215)$, and
- $(0.44 \wedge 0.078)$.

This means the total amount of ALD emission into the RACM MCH will be

$$\begin{aligned}
 \{\text{ALD}\} &= 0.57 \times \{\text{propane}\} + 1.11 \times \{n\text{-butane}\} & (\text{B.2}) \\
 &+ 1.11 \times \{i\text{-butane}\} + 1.11 \times \{2,2\text{-dimethylbutane}\} \\
 &+ 0.41 \times \{\text{acetylene}\} + 0.49 \times \{\text{methanol}\} \\
 &+ 1.37 \times \{\text{ethanol}\} + 0.49 \times \{\text{methyl-acetate}\} \\
 &+ 0.49 \times \{\text{ethyl-acetate}\} + 1.37 \times \{i\text{-propyl-acetate}\} \\
 &+ 0.44 \times \{\text{tetrachloroethylene}\}
 \end{aligned}$$

and the RADM2 MCH will be

$$\begin{aligned}
 \{\text{ALD}\} &= 0.519 \times \{\text{propane}\} + 0.964 \times \{n\text{-butane}\} & (\text{B.3}) \\
 &+ 0.964 \times \{i\text{-butane}\} + 0.964 \times \{2,2\text{-dimethylbutane}\} \\
 &+ 0.343 \times \{\text{acetylene}\} + 0.404 \times \{\text{methanol}\} \\
 &+ 1.215 \times \{\text{ethanol}\} + 0.404 \times \{\text{methyl-acetate}\} \\
 &+ 0.404 \times \{\text{ethyl-acetate}\} + 1.215 \times \{i\text{-propyl-acetate}\} \\
 &+ 0.078 \times \{\text{tetrachloroethylene}\}
 \end{aligned}$$

For all the VOC presented in Table B.1, we have copied the lumping group they belong to and their aggregation factor from table 3 in Ref. [32] and table 2 in Ref. [170] and written this in Table B.3. The results for all the different organic RACM and RADM2 lumping groups using the emission inventory given by Table B.1 are written in Table B.4

B.2 Comment

The results using the VOC emissions given in Table B.1 and the distribution keys described in this appendix to implement emissions into the EMEP, RADM2 and RACM MCHs are given in Table B.4. Table B.4 shows that the EMEP MCH add 18.78% more carbon to the mechanism than the VOC emissions given in Table B.1, while the RADM2 and RACM MCHs lose 8.367% and 0.331%, respectively. Hence, great improvement in the carbon conservation has appeared from the RADM2 MCH to the RACM MCH. It is claimed that the EMEP MCH is carbon conservative[38]. For the EMEP MCH, if VOC emissions instead were implemented according to the VOC carbon number then it would be carbon conservative.

A more detailed description of the three mechanisms' carbon conservation is given in *Section 1.2.2.1*.

Species		Emission
methane	CH ₄	0.0
ethane	C ₂ H ₆	{VOC} × 0.0340956
propane	C ₃ H ₈	{VOC} × 0.00554352
<i>n</i> -butane	<i>n</i> -C ₄ H ₁₀	{VOC} × 0.0800388
<i>i</i> -butane	<i>i</i> -C ₄ H ₁₀	{VOC} × 0.0434109
<i>n</i> -pentane	<i>n</i> -C ₅ H ₁₂	{VOC} × 0.0240418
<i>i</i> -pentane	<i>i</i> -C ₅ H ₁₂	{VOC} × 0.0371555
<i>n</i> -hexane	<i>n</i> -C ₆ H ₁₄	{VOC} × 0.0137236
2-methylpentane	CH ₃ C ₅ H ₁₁	{VOC} × 0.0155535
3-methylpentane	CH ₃ C ₅ H ₁₁	{VOC} × 0.0109789
2,2-dimethylbutane	CH ₃ CH ₃ C ₄ H ₈	{VOC} × 0.00155535
2,3-dimethylbutane	CH ₃ CH ₃ C ₄ H ₈	{VOC} × 0.00494051
<i>n</i> -heptane	<i>n</i> -C ₇ H ₁₆	{VOC} × 0.00621589
2-methylhexane	CH ₃ C ₆ H ₁₃	{VOC} × 0.00519302
3-methylhexane	CH ₃ C ₆ H ₁₃	{VOC} × 0.00448488
<i>n</i> -octane	<i>n</i> -C ₈ H ₁₈	{VOC} × 0.00400313
methylheptanes	CH ₃ C ₇ H ₁₅	{VOC} × 0.0138039
<i>n</i> -nonane	<i>n</i> -C ₉ H ₂₀	{VOC} × 0.00737645
methyloctanes	CH ₃ C ₈ H ₁₇	{VOC} × 0.00301205
<i>n</i> -decane	<i>n</i> -C ₁₀ H ₂₂	{VOC} × 0.005541
methylnonanes	CH ₃ C ₉ H ₁₉	{VOC} × 0.00354624
<i>n</i> -undecane	<i>n</i> -C ₁₁ H ₂₄	{VOC} × 0.00706122
<i>n</i> -dodecane	<i>n</i> -C ₁₂ H ₂₆	{VOC} × 0.00647971
ethylene	C ₂ H ₄	{VOC} × 0.0646318
propylene	C ₃ H ₆	{VOC} × 0.0155491
but-1-ene	C ₄ H ₈	{VOC} × 0.0073062
but-2-ene	C ₄ H ₈	{VOC} × 0.0134884
pent-2-ene	C ₅ H ₁₀	{VOC} × 0.00809302
pent-1-ene	C ₅ H ₁₀	{VOC} × 0.00314729
2-methylbut-1-ene	CH ₃ C ₄ H ₇	{VOC} × 0.00179845
3-methylbut-1-ene	CH ₃ C ₄ H ₇	{VOC} × 0.00213566
2-methylbut-2-ene	CH ₃ C ₄ H ₇	{VOC} × 0.00393411
butylene	C ₄ H ₆	{VOC} × 0.00210756
acetylene	C ₂ H ₂	{VOC} × 0.0393411
benzene	C ₆ H ₆	{VOC} × 0.0171487
toluene	CH ₃ C ₆ H ₅	{VOC} × 0.0624326
<i>o</i> -xylene	<i>o</i> -C ₆ H ₄ (CH ₃)CH ₃	{VOC} × 0.0126188
<i>m</i> -xylene	<i>m</i> -C ₆ H ₄ (CH ₃)CH ₃	{VOC} × 0.0163303
<i>p</i> -xylene	<i>p</i> -C ₆ H ₄ (CH ₃)CH ₃	{VOC} × 0.0163303
ethylbenzene	C ₂ H ₅ C ₆ H ₅	{VOC} × 0.010392
<i>n</i> -propylbenzene	<i>n</i> -C ₃ H ₇ C ₆ H ₅	{VOC} × 0.00216376
<i>i</i> -propylbenzene	<i>i</i> -C ₃ H ₇ C ₆ H ₅	{VOC} × 0.00111466
1,2,3-trimethylbenzene	(CH ₃) ₃ C ₆ H ₃	{VOC} × 0.00255717
1,2,4-trimethylbenzene	(CH ₃) ₃ C ₆ H ₃	{VOC} × 0.00983527
1,3,5-trimethylbenzene	(CH ₃) ₃ C ₆ H ₃	{VOC} × 0.00367183
<i>o</i> -ethyltoluene	<i>o</i> -CH ₃ C ₆ H ₄ C ₂ H ₅	{VOC} × 0.00334399
<i>m</i> -ethyltoluene	<i>m</i> -CH ₃ C ₆ H ₄ C ₂ H ₅	{VOC} × 0.00467639
<i>continued on next page</i>		

<i>continued from previous page</i>		
Species		Emission
<i>p</i> -ethyltoluene	<i>p</i> -CH ₃ C ₆ H ₄ C ₂ H ₅	{VOC} × 0.00413081
formaldehyd	HCHO	{VOC} × 0.0196705
acetaldehyle	CH ₃ CHO	{VOC} × 0.00178823
propionaldehyde	C ₂ H ₅ CHO	{VOC} × 0.00149225
butyraldehyde	<i>n</i> -C ₃ H ₇ CHO	{VOC} × 0.00079775
<i>i</i> -butyraldehyde	(CH ₃) ₂ CHCHO	{VOC} × 0.000710325
valeraldehyde	<i>n</i> -C ₄ H ₉ CHO	{VOC} × 0.0000365964
benzaldehyde	C ₆ H ₅ CHO	{VOC} × 0.000296914
acetone	CH ₃ COCH ₃	{VOC} × 0.023062
methyl-ethyl-ketone	CH ₃ COC ₂ H ₅	{VOC} × 0.0316914
methyl-isobuty-ketone	CH ₃ COC ₄ H ₉	{VOC} × 0.00778954
methanol	CH ₃ OH	{VOC} × 0.0209
ethanol	C ₂ H ₅ OH	{VOC} × 0.174469
methyl-acetate	CH ₃ CO ₂ CH ₃	{VOC} × 0.00170124
ethyl-acetate	C ₂ H ₅ CO ₂ CH ₃	{VOC} × 0.00554352
<i>i</i> -propyl-acetate	<i>i</i> -C ₃ H ₇ CH ₃ CO ₂	{VOC} × 0.0021599
<i>n</i> -butyl-acetate	<i>n</i> -C ₄ H ₉ CH ₃ CO ₂	{VOC} × 0.00244186
<i>i</i> -butyl-acetate	<i>i</i> -C ₄ H ₉ CH ₃ CO ₂	{VOC} × 0.00305233
methane-chloride	CH ₃ Cl ₂	{VOC} × 0.0112403
methyl-chloroform	CH ₃ CCl ₃	{VOC} × 0.00943007
tetrachloroethylene	C ₂ Cl ₄	{VOC} × 0.00671677
VOC		{VOC} × 0.991025
VOC of carbon		{VOC} C × 4.23223

Table B.1: Representation of VOC emission for the continental European boundary layer[38]. {VOC} is the emissions of VOC.

	Species		Lumping Group	Aggregation Factor
0	methane	CH ₄	CH ₄	1
1	ethane	C ₂ H ₆	C ₂ H ₆	1
2	propane	C ₃ H ₈	<i>n</i> -C ₄ H ₁₀	44/58
3	<i>n</i> -butane	<i>n</i> -C ₄ H ₁₀	<i>n</i> -C ₄ H ₁₀	1
4	<i>i</i> -butane	<i>i</i> -C ₄ H ₁₀	<i>n</i> -C ₄ H ₁₀	1
5	<i>n</i> -pentane	<i>n</i> -C ₅ H ₁₂	<i>n</i> -C ₄ H ₁₀	72/58
6	<i>i</i> -pentane	<i>i</i> -C ₅ H ₁₂	<i>n</i> -C ₄ H ₁₀	72/58
7	<i>n</i> -hexane	<i>n</i> -C ₆ H ₁₄	<i>n</i> -C ₄ H ₁₀	86/58
8	2-methylpentane	CH ₃ C ₅ H ₁₁	<i>n</i> -C ₄ H ₁₀	86/58
9	3-methylpentane	CH ₃ C ₅ H ₁₁	<i>n</i> -C ₄ H ₁₀	86/58
10	2,2-dimethylbutane	CH ₃ CH ₃ C ₄ H ₈	<i>n</i> -C ₄ H ₁₀	86/58
11	2,3-dimethylbutane	CH ₃ CH ₃ C ₄ H ₈	<i>n</i> -C ₄ H ₁₀	86/58
12	<i>n</i> -heptane	<i>n</i> -C ₇ H ₁₆	<i>n</i> -C ₄ H ₁₀	100/58
13	2-methylhexane	CH ₃ C ₆ H ₁₃	<i>n</i> -C ₄ H ₁₀	100/58
14	3-methylhexane	CH ₃ C ₆ H ₁₃	<i>n</i> -C ₄ H ₁₀	100/58
15	<i>n</i> -octane	<i>n</i> -C ₈ H ₁₈	<i>n</i> -C ₄ H ₁₀	114/58
16	methylheptanes	CH ₃ C ₇ H ₁₅	<i>n</i> -C ₄ H ₁₀	114/58
17	<i>n</i> -nonane	<i>n</i> -C ₉ H ₂₀	<i>n</i> -C ₄ H ₁₀	128/58
18	methyloctanes	CH ₃ C ₈ H ₁₇	<i>n</i> -C ₄ H ₁₀	128/58
19	<i>n</i> -decane	<i>n</i> -C ₁₀ H ₂₂	<i>n</i> -C ₄ H ₁₀	142/58
20	methylnonanes	CH ₃ C ₉ H ₁₉	<i>n</i> -C ₄ H ₁₀	142/58
21	<i>n</i> -undecane	<i>n</i> -C ₁₁ H ₂₄	<i>n</i> -C ₄ H ₁₀	156/58
22	<i>n</i> -dodecane	<i>n</i> -C ₁₂ H ₂₆	<i>n</i> -C ₄ H ₁₀	170/58
23	ethylene	C ₂ H ₄	C ₂ H ₄	1
24	propylene	C ₃ H ₆	C ₃ H ₆	1
25	but-1-ene	C ₄ H ₈	C ₃ H ₆	56/42
26	but-2-ene	C ₄ H ₈	C ₃ H ₆	56/42
27	pent-2-ene	C ₅ H ₁₀	C ₃ H ₆	70/42
28	pent-1-ene	C ₅ H ₁₀	C ₃ H ₆	70/42
29	2-methylbut-1-ene	CH ₃ C ₄ H ₇	C ₃ H ₆	70/42
30	3-methylbut-1-ene	CH ₃ C ₄ H ₇	C ₃ H ₆	70/42
31	2-methylbut-2-ene	CH ₃ C ₄ H ₇	C ₃ H ₆	70/42
32	butylene	C ₄ H ₈	C ₃ H ₆	56/42
33	acetylene	C ₂ H ₂	C ₂ H ₆	26/30
34	benzene	C ₆ H ₆	<i>o</i> -xylene	78/106
35	toluene	CH ₃ C ₆ H ₅	<i>o</i> -xylene	92/106
36	<i>o</i> -xylene	<i>o</i> -C ₆ H ₄ (CH ₃)CH ₃	<i>o</i> -xylene	1
37	<i>m</i> -xylene	<i>m</i> -C ₆ H ₄ (CH ₃)CH ₃	<i>o</i> -xylene	1
38	<i>p</i> -xylene	<i>p</i> -C ₆ H ₄ (CH ₃)CH ₃	<i>o</i> -xylene	1
39	ethylbenzene	C ₂ H ₅ C ₆ H ₅	<i>o</i> -xylene	1
40	<i>n</i> -propylbenzene	<i>n</i> -C ₃ H ₇ C ₆ H ₅	<i>o</i> -xylene	120/106
41	<i>i</i> -propylbenzene	<i>i</i> -C ₃ H ₇ C ₆ H ₅	<i>o</i> -xylene	120/106
42	1,2,3-trimethylbenzene	(CH ₃) ₃ C ₆ H ₃	<i>o</i> -xylene	120/106
43	1,2,4-trimethylbenzene	(CH ₃) ₃ C ₆ H ₃	<i>o</i> -xylene	120/106
44	1,3,5-trimethylbenzene	(CH ₃) ₃ C ₆ H ₃	<i>o</i> -xylene	120/106
45	<i>o</i> -ethyltoluene	<i>o</i> -CH ₃ C ₆ H ₄ C ₂ H ₅	<i>o</i> -xylene	120/106

continued on next page

<i>continued from previous page</i>				
	Species		Lumping Group	Aggregation Factor
46	<i>m</i> -ethyltoluene	$m\text{-CH}_3\text{C}_6\text{H}_4\text{C}_2\text{H}_5$	<i>o</i> -xylene	120/106
47	<i>p</i> -ethyltoluene	$p\text{-CH}_3\text{C}_6\text{H}_4\text{C}_2\text{H}_5$	<i>o</i> -xylene	120/106
48	formaldehyd	HCHO	HCHO	1
49	acetaldehyle	CH ₃ CHO	CH ₃ CHO	1
50	propionaldehyde	C ₂ H ₅ CHO	CH ₃ CHO	58/44
51	butyraldehyde	$n\text{-C}_3\text{H}_7\text{CHO}$	CH ₃ CHO	72/44
52	<i>i</i> -butyraldehyde	(CH ₃) ₂ CHCHO	CH ₃ CHO	72/44
53	valeraldehyde	$n\text{-C}_4\text{H}_9\text{CHO}$	CH ₃ CHO	86/44
54	benzaldehyde	C ₆ H ₅ CHO	<i>o</i> -xylene	1
55	acetone	CH ₃ COCH ₃	C ₂ H ₆	58/30
56	methyl-ethyl-ketone	CH ₃ COC ₂ H ₅	CH ₃ COC ₂ H ₅	1
57	methyl-isobutyl-ketone	CH ₃ COC ₄ H ₉	CH ₃ COC ₂ H ₅	2.93
58	methanol	CH ₃ OH	CH ₃ OH	1
59	ethanol	C ₂ H ₅ OH	C ₂ H ₅ OH	1
60	methyl-acetate	CH ₃ CO ₂ CH ₃	C ₂ H ₅ OH	74/46
61	ethyl-acetate	C ₂ H ₅ CO ₂ CH ₃	C ₂ H ₆	88/30
62	<i>i</i> -propyl-acetate	$i\text{-C}_3\text{H}_7\text{CH}_3\text{CO}_2$	C ₂ H ₆	102/30
63	<i>n</i> -butyl-acetate	$n\text{-C}_4\text{H}_9\text{CH}_3\text{CO}_2$	C ₂ H ₆	116/30
64	<i>i</i> -butyl-acetate	$i\text{-C}_4\text{H}_9\text{CH}_3\text{CO}_2$	C ₂ H ₆	116/30
65	methane-chloride	CH ₃ Cl	unreactive	
66	methyl-chloroform	CH ₃ CCl ₃	$n\text{-C}_4\text{H}_{10}$	2.69
67	tetrachloroethylene	C ₂ Cl ₄	C ₂ H ₆	1.00

Table B.2: Distribution of the VOC given in Table B.1 in their specific EMEP lumping groups and the size of the aggregation factor[30].

	Species		Category	Lumping Group	Aggregation Factor	
					RADM2	RACM
0	methane	CH ₄	1	CH ₄	1.000	1.00
1	ethane	C ₂ H ₆	2	ETH	1.000	1.00
2	propane	C ₃ H ₈	3	HC3	0.519	0.57
3	<i>n</i> -butane	<i>n</i> -C ₄ H ₁₀	4	HC3	0.964	1.11
4	<i>i</i> -butane	<i>i</i> -C ₄ H ₁₀	4	HC3	0.964	1.11
5	<i>n</i> -pentane	<i>n</i> -C ₅ H ₁₂	5	HC5	0.956	0.97
6	<i>i</i> -pentane	<i>i</i> -C ₅ H ₁₂	5	HC5	0.956	0.97
7	<i>n</i> -hexane	<i>n</i> -C ₆ H ₁₄	5	HC5	0.956	0.97
8	2-methylpentane	CH ₃ C ₅ H ₁₁	5	HC5	0.956	0.97
9	3-methylpentane	CH ₃ C ₅ H ₁₁	5	HC5	0.956	0.97
10	2,2-dimethylbutane	CH ₃ CH ₃ C ₄ H ₈	4	HC3	0.964	1.11
11	2,3-dimethylbutane	CH ₃ CH ₃ C ₄ H ₈	5	HC5	0.956	0.97
12	<i>n</i> -heptane	<i>n</i> -C ₇ H ₁₆	6	HC8	0.945	0.94
13	2-methylhexane	CH ₃ C ₆ H ₁₃	6	HC8	0.945	0.94
14	3-methylhexane	CH ₃ C ₆ H ₁₃	6	HC8	0.945	0.94
15	<i>n</i> -octane	<i>n</i> -C ₈ H ₁₈	6	HC8	0.945	0.94
16	methylheptanes	CH ₃ C ₇ H ₁₅	6	HC8	0.945	0.94
17	<i>n</i> -nonane	<i>n</i> -C ₉ H ₂₀	6	HC8	0.945	0.94
18	methyloctanes	CH ₃ C ₈ H ₁₇	6	HC8	0.945	0.94
19	<i>n</i> -decane	<i>n</i> -C ₁₀ H ₂₂	6	HC8	0.945	0.94
20	methylnonanes	CH ₃ C ₉ H ₁₉	6	HC8	0.945	0.94
21	<i>n</i> -undecane	<i>n</i> -C ₁₁ H ₂₄	6	HC8	0.945	0.94
22	<i>n</i> -dodecane	<i>n</i> -C ₁₂ H ₂₆	7	HC8	1.141	1.14
23	ethylene	C ₂ H ₄	9	ETE/OL2	1.000	1.00
24	propylene	C ₃ H ₆	10	OLT	1.000	1.00
25	but-1-ene	C ₄ H ₈	11	OLT	1.000	1.00
26	but-2-ene	C ₄ H ₈	12	OLI	1.000	1.00
27	pent-2-ene	C ₅ H ₁₀	12	OLI	1.000	1.00
28	pent-1-ene	C ₅ H ₁₀	11	OLT	1.000	1.00
29	2-methylbut-1-ene	CH ₃ C ₄ H ₇	11	OLT	1.000	1.00
30	3-methylbut-1-ene	CH ₃ C ₄ H ₇	11	OLT	1.000	1.00
31	2-methylbut-2-ene	CH ₃ C ₄ H ₇	12	OLI	1.000	1.00
32	butylene	C ₄ H ₈	13	OLT	0.500	0.50
			13	OLI	0.500	0.50
33	acetylene	C ₂ H ₂	24	HC3	0.343	0.41
34	benzene	C ₆ H ₆	14	TOL	0.293	0.29
35	toluene	CH ₃ C ₆ H ₅	15	TOL	1.000	1.00
36	<i>o</i> -xylene	<i>o</i> -C ₆ H ₄ (CH ₃)CH ₃	16	XYL	1.000	1.00
37	<i>m</i> -xylene	<i>m</i> -C ₆ H ₄ (CH ₃)CH ₃	16	XYL	1.000	1.00
38	<i>p</i> -xylene	<i>p</i> -C ₆ H ₄ (CH ₃)CH ₃	16	XYL	1.000	1.00
39	ethylbenzene	C ₂ H ₅ C ₆ H ₅	15	TOL	1.000	1.00
40	<i>n</i> -propylbenzene	<i>n</i> -C ₃ H ₇ C ₆ H ₅	15	TOL	1.000	1.00
41	<i>i</i> -propylbenzene	<i>i</i> -C ₃ H ₇ C ₆ H ₅	15	TOL	1.000	1.00
42	1,2,3-trimethylbenzene	(CH ₃) ₃ C ₆ H ₃	16	XYL	1.000	1.00
43	1,2,4-trimethylbenzene	(CH ₃) ₃ C ₆ H ₃	16	XYL	1.000	1.00
44	1,3,5-trimethylbenzene	(CH ₃) ₃ C ₆ H ₃	16	XYL	1.000	1.00

continued on next page

<i>continued from previous page</i>						
	Species		Category	Lumping Group	Aggregation Factor	
					RADM2	RACM
45	<i>o</i> -ethyltoluene	<i>o</i> -CH ₃ C ₆ H ₄ C ₂ H ₅	16	XYL	1.000	1.00
46	<i>m</i> -ethyltoluene	<i>m</i> -CH ₃ C ₆ H ₄ C ₂ H ₅	16	XYL	1.000	1.00
47	<i>p</i> -ethyltoluene	<i>p</i> -CH ₃ C ₆ H ₄ C ₂ H ₅	16	XYL	1.000	1.00
48	formaldehyd	HCHO	19	HCHO	1.000	1.00
49	acetaldehyle	CH ₃ CHO	20	ALD	1.000	1.00
50	propionaldehyde	C ₂ H ₅ CHO	20	ALD	1.000	1.00
51	butyraldehyde	<i>n</i> -C ₃ H ₇ CHO	20	ALD	1.000	1.00
52	<i>i</i> -butyraldehyde	(CH ₃) ₂ CHCHO	20	ALD	1.000	1.00
53	valeraldehyde	<i>n</i> -C ₄ H ₉ CHO	20	ALD	1.000	1.00
54	benzaldehyde	C ₆ H ₅ CHO	20	ALD	1.000	1.00
55	acetone	CH ₃ COCH ₃	21	KET	0.253	0.33
56	methyl-ethyl-ketone	CH ₃ COC ₂ H ₅	22	KET	1.000	1.61
57	methyl-isobutyl-ketone	CH ₃ COC ₄ H ₉	22	KET	1.000	1.61
58	methanol	CH ₃ OH	27	HC3	0.404	0.49
59	ethanol	C ₂ H ₅ OH	28	HC3	1.215	1.37
60	methyl-acetate	CH ₃ CO ₂ CH ₃	27	HC3	0.404	0.49
61	ethyl-acetate	C ₂ H ₅ CO ₂ CH ₃	27	HC3	0.404	0.49
62	<i>i</i> -propyl-acetate	<i>i</i> -C ₃ H ₇ CH ₃ CO ₂	28	HC3	1.215	1.37
63	<i>n</i> -butyl-acetate	<i>n</i> -C ₄ H ₉ CH ₃ CO ₂	29	HC5	1.075	1.07
64	<i>i</i> -butyl-acetate	<i>i</i> -C ₄ H ₉ CH ₃ CO ₂	29	HC5	1.075	1.07
65	methane-chloride	CH ₃ Cl	26	non reactive		
66	methyl-chloroform	CH ₃ CCl ₃	26	non reactive		
67	tetrachloroethylene	C ₂ Cl ₄	25	HC3	0.078	0.44

Table B.3: Distribution of the VOC given in Table B.1 in their specific RACM and RADM2 lumping groups and the size of the aggregation factor[31, 32, 170].

EMEP MCH	
Lumping Group	Emission
C ₂ H ₆	{VOC} × 0.164343
<i>n</i> -C ₄ H ₁₀	{VOC} × 0.443875
C ₂ H ₄	{VOC} × 0.0646318
C ₃ H ₆	{VOC} × 0.0779329
<i>o</i> -xylene	{VOC} × 0.158427
HCHO	{VOC} × 0.0196705
CH ₃ CHO	{VOC} × 0.00629458
CH ₃ COC ₂ H ₅	{VOC} × 0.0545148
CH ₃ OH	{VOC} × 0.0209999
C ₂ H ₅ OH	{VOC} × 0.177206
VOC	{VOC} × 1.18780
VOC of carbon	{VOC} × 4.36030
RADM2 MCH	
Lumping Group	Emission
ALD	{VOC} × 0.00512207
OL2	{VOC} × 0.0646318
ETH	{VOC} × 0.0340956
HC3	{VOC} × 0.363374
HC5	{VOC} × 0.107619
HC8	{VOC} × 0.0643180
HCHO	{VOC} × 0.0196705
KET	{VOC} × 0.0453156
OLI	{VOC} × 0.0265693
OLT	{VOC} × 0.0309905
TOL	{VOC} × 0.0811276
XYL	{VOC} × 0.0734949
VOC	{VOC} × 0.916329
VOC of carbon	{VOC} × 3.96002
RACM MCH	
Lumping Group	Emission
ALD	{VOC} × 0.00512207
ETE	{VOC} × 0.0646318
ETH	{VOC} × 0.0340956
HC3	{VOC} × 0.416773
HC5	{VOC} × 0.109081
HC8	{VOC} × 0.0640104
HCHO	{VOC} × 0.0196705
KET	{VOC} × 0.0711748
OLI	{VOC} × 0.0265693
OLT	{VOC} × 0.0309905
TOL	{VOC} × 0.0810761
XYL	{VOC} × 0.0734949
<i>continued on next page</i>	

<i>continued from previous page</i>	
VOC	$\{\text{VOC}\} \times 0.996690$
VOC of carbon	$\{\text{VOC}\} \times 4.19680$

Table B.4: VOC emissions into the EMEP, RADM2 and RACM MCHs for the continental European boundary layer given in Ref. [38]. $\{\text{VOC}\}$ is the emissions of VOC.

Appendix C

Numerical Solution of Complex Chemical MCHs

Theoretical models of for example atmospheric chemistry-transport, combustion and hydrocarbon cracking systems involve complex CRSs. Often the operator splitting method approach is used in order to solve numerically the CRS independently from the other degrees of freedom in such models. A complex CRS typically includes elementary reactions and the time (t) dependence of the chemical species concentration (\bar{y}). These schemes can be described by ODEs:

$$\frac{d\bar{y}}{dt} = \bar{f}(\bar{y}, t, \bar{k}) \quad (\text{C.1})$$

where \bar{f} contains the rate constants (\bar{k}) and may be non-linear in \bar{y} . For the CRSs mentioned above the problem of solving Eq. (C.1) arises from the different sizes of the rate constants (stiffness of the ODE) in \bar{f} , therefore standard explicit methods such as the Runge–Kutta method cannot be used directly without either some kind of lumping of the species to remove the stiffness of the CRS or numerous short time steps which must be used in order to maintain stability.

The most successful algorithm for directly numerically solving stiff ODEs without any kind of lumping is the Gear algorithm[51, 56]. It employs a hybrid explicit/implicit predictor-corrector method in which an explicit equation is used to predict $\bar{y}(t + \Delta t)$, which then is corrected using an implicit method. Hindmarsh[54] and Brown et al.[55] have developed Gear algorithms using the sparse-matrix technique¹ with the benefit of economizing the algebra. These solvers are called Livermore Solver for Ordinary Differential Equations (LSODE) and Variable Coefficient Ordinary Differential Equation Solver (VODE) respectively, and can be downloaded from the World Wide Web[54, 55]. Although these solvers have been improved with sparse-matrix technique, the disadvantage of using a Gear algorithm is that such high- and variable-order techniques can be very time consuming compared to the explicit methods such as QSSA. Especially if the concentrations of the species are disturbed under the numerical integration by for example time varying emission,

¹The sparse-matrix technique will be explained in *Section C.2*.

depositions and/or transport. In these cases the solver has to “start over again” in each time step, and the initial time step is always the time consuming step for a Gear algorithm. On the other hand if such a disturbance does not occur, the Gear solver is very efficient and arbitrarily large time steps can be performed.

Due to the long computational time related to using the solvers developed by Hindmarsh[54] and Brown et al.[55], fast solvers have been developed and are presently used to solve CRS in air quality models. Some examples are the QSSA[47], IEH[49], and EBI solvers[48]. Even though the QSSA solver is the least accurate of the fast solvers, it has been one of the most widely used methods.

Two solvers will be described in this appendix:

- the QSSA solver (*Section C.1*) since this solver has been used to solve the chemistry in DACFOS[13], and
- the chemical solver in the MOON model that is based on the recently developed SMVGEAR algorithm[56].

C.1 The QSSA Solver

Consider the following rewrite of Eq. (C.1)

$$\frac{d\bar{y}}{dt} = \bar{P}(\bar{y}, t, \bar{k}) - \bar{L}(\bar{y}, t, \bar{k}) \bar{y}(t) \quad (\text{C.2})$$

where $\bar{P}(\bar{y}, t, \bar{k})$ and $\bar{L}(\bar{y}, t, \bar{k}) \bar{y}(t)$ represents the production and loss terms, respectively. The QSSA solver is an explicit method that uses quasi-steady-state approximations to reduce the ODE, Eq. (C.2). This means, $d\bar{y}/dt \approx 0$ or

$$y_i(t + \Delta t) \approx P_i(t)/L_i(t) \quad (\text{C.3})$$

for the i th compound[47], where Δt is the time step. The quasi-steady-state approximation is applied when the characteristic time (or photochemical lifetime) of the compound $\tau_i = 1/L_i < \Delta t/10$. This means the photochemical lifetime is much lower than the time step. When this condition is not obeyed, the differential equation is solved as follows[47]:

- first, when $\tau_i \gg \Delta t$ (in DACFOS[13] when $\tau_i > 100\Delta t$) the Taylor equation to first order of Eq. (C.2) is used as the solution. This gives

$$y_i(t + \Delta t) = y_i(t) + (P_i(t) - L_i(t) y_i(t)) \Delta t \quad (\text{C.4})$$

This formula is well applied when the concentration of the i th compound is slow, because then it can be considered to be linear in $[t; t + \Delta t]$.

- Second, when $\tau \in [\Delta t/10; 100\Delta t]$ it is assumed that \bar{P} and \bar{L} are constant over the time step (Δt). This makes it possible to solve Eq. (C.2) analytically, and the result becomes

$$y_i(t + \Delta t) = P_i(t)/L_i(t) + (y_i(t) - P_i(t)/L_i(t)) \exp(-L_i(t)\Delta t) \quad (\text{C.5})$$

However, in order to increase the accuracy[47] for compounds in “instant” equilibrium with other species, five iterations are performed in each time step[13]. This procedure is especially important for compounds having cyclic character such as H, HO and HO₂.

Special Treatment of Compounds in the QSSA Solver

Some species in the QSSA solver used by DACFOS have been treated in a special manner, that is O(¹D), O(³P), HO, O₃, NO, NO₂, NO₃, N₂O₅ and ISONO₃ (the acronym ISONO₃ is described in Table A.1). The first three species are radicals i.e. their concentrations are always low. Hence, they are assumed to be in a steady-state and their concentrations are calculated according to Eq. (C.3).

For reducing the chemical mass imbalance and to avoid too small time steps, the following lumping groups were introduced into DACFOS’s QSSA solver[13, 47]:

$$[\text{O}_3\text{NO}] = [\text{O}_3] - [\text{NO}] \quad (\text{C.6})$$

$$[\text{NO}_y] = [\text{NO}] + [\text{NO}_2] + [\text{PAN}] + [\text{NO}_3] + 2 \times [\text{N}_2\text{O}_5] + [\text{MPAN}] \quad (\text{C.7})$$

$$[\text{NO}_z] = [\text{NO}_3] + [\text{N}_2\text{O}_5] \quad (\text{C.8})$$

the acronyms for PAN and MPAN are described in Table A.1. The lumping species defined in Eqs. (C.6–C.8) are calculated using Eq. (C.4), Eqs. (C.4–C.5) and Eqs. (C.3–C.5), respectively. Based on these calculations, the concentration of O₃, NO and NO₂ are estimated as follows:

- If $[\text{O}_3] \geq [\text{NO}]$:

$[\text{NO}]$ is calculated according to Eq. (C.5) and $[\text{O}_3]$ as follows

$$[\text{O}_3]_{(t+\Delta t)} = [\text{O}_3\text{NO}]_{(t+\Delta t)} + [\text{NO}]_{(t+\Delta t)} \quad (\text{C.9})$$

- and if $[\text{O}_3] < [\text{NO}]$:

$[\text{O}_3]$ is calculated according to Eq. (C.5) and $[\text{NO}]$ as follows

$$[\text{NO}]_{(t+\Delta t)} = [\text{O}_3]_{(t+\Delta t)} - [\text{O}_3\text{NO}]_{(t+\Delta t)} \quad (\text{C.10})$$

$[\text{NO}_2]$ is calculated according to

$$\begin{aligned} [\text{NO}_2]_{t+\Delta t} = & [\text{NO}_y]_{t+\Delta t} - ([\text{NO}]_{t+\Delta t} + [\text{PAN}]_{t+\Delta t} \\ & + [\text{MAPAN}]_{t+\Delta t} + [\text{NO}_3]_t + 2 \times [\text{N}_2\text{O}_5]_t) \end{aligned} \quad (\text{C.11})$$

The next step is to calculate the concentration of NO₃ and N₂O₅. Consider first the EMEP reactions R6, R37 and R40. These are the reactions for formation and decomposition of N₂O₅. It is assumed that $[\text{NO}_3]$ and $[\text{N}_2\text{O}_5]$ are in a steady-state for these three reactions. This means $d[\text{NO}_3]/dt \approx 0$, and we get

$$[\text{NO}_3] = [\text{N}_2\text{O}_5] \frac{k_{R40} + k_{R6}}{k_{R37}[\text{NO}_2]} \quad (\text{C.12})$$

and from $d[\text{N}_2\text{O}_5]/dt \approx 0$ we get

$$[\text{NO}_z] = [\text{NO}_2][\text{NO}_3] \frac{k_{R37}}{k_{40} + k_{R6}} + \frac{[\text{N}_2\text{O}_5](k_{R40} - k_{R6})}{k_{37}[\text{NO}_2]} \quad (\text{C.13})$$

Using the last two equations, we can write

$$[\text{N}_2\text{O}_5] = [\text{NO}_z] \frac{k_{R37}[\text{NO}_2]}{k_{R37}[\text{NO}_2] + k_{R6} + k_{R40}} \quad (\text{C.14})$$

Because the concentration of lumping variable NO_z is known we can calculate $[\text{N}_2\text{O}_5]$ from Eq. (C.14) and $[\text{NO}_3]$ from Eq.(C.8).

Finally, an analytic solution for $[\text{ISONO}_3]$ is obtained by setting the solution of $[\text{NO}_z]$ into the differential equation for $[\text{ISONO}_3]$. This methodology is used because on occasion the build up of the concentration of ISONO_3 based upon $[\text{NO}_3]$ would be much too fast, meaning that NO_y molecules are generated. This assumption gives us the following coupled ODE

$$\frac{d[\text{ISONO}_3]}{dt} = P_{\text{ISONO}_3}^{R122}[\text{NO}_z] + P_{\text{ISONO}_3}^{R130} - L_{\text{ISONO}_3}[\text{ISONO}_3] \quad (\text{C.15})$$

$$\frac{d[\text{NO}_z]}{dt} = P_{\text{NO}_z} - L_{\text{NO}_z}[\text{NO}_z] \quad (\text{C.16})$$

This ODE can be solved exact, and the solution become

$$\begin{aligned} [\text{ISONO}_3] &= P_{\text{ISONO}_3}^{R122} ([\text{NO}_z^{t_{beg}}] - P_{\text{NO}_z}/L_{\text{NO}_z}) \\ &\times (\exp(-L_{\text{NO}_z}\Delta t) - \exp(-L_{\text{ISONO}_3}\Delta t)) \\ &\times (L_{\text{ISONO}_3} - L_{\text{NO}_z})^{-1} \\ &+ \frac{P_{\text{ISONO}_3}^{R122}P_{\text{NO}_z} + P_{\text{ISONO}_3}^{R130}L_{\text{NO}_z}}{L_{\text{ISONO}_3}L_{\text{NO}_z}} \\ &\times (1 - \exp(-L_{\text{ISONO}_3}\Delta t)) + [\text{ISONO}_3^{t_{beg}}] \\ &\times \exp(-L_{\text{ISONO}_3}\Delta t) \end{aligned} \quad (\text{C.17})$$

A further description of the utility of the QSSA solver is given in *Section 3.3.1*, and *Introduction, Solvers (QSSA and Gear)*. There we compare the QSSA solver with a Gear algorithm.

C.2 The Chemical Solver in the MOON Model

The computationally expensive part of the MOON model is solving the ODE of the CRS. According to the reasons described in the introduction to this appendix and in the introduction of the thesis, we have decided to use a Gear algorithm to solve the ODE. Because of this decision, several special computational techniques must be used in order to improve the speed of traditional Gear algorithms[54, 55]. For this purpose we have taken the SMVGEAR algorithm from Jacobson[56] and on the outside of this solver the trajectories have been built up. The following techniques are used to increase the computational speed of this Gear algorithm[56]:

1. the code gathers the trajectories into groups for vectorization,
2. a sparse-matrix technique is used to estimate the corrector vector for the Gear algorithm,
3. the trajectory groups are sorted according to stiffness,
4. the chemical reactions are sorted by the number of reactant and product terms,
5. the transport-chemical model can solve different chemical mechanisms in different areas of the atmosphere: the stratosphere, the free troposphere and inside the ALB, and
6. sparse-matrices for night and day gas-phase chemistry and night and day heterogeneous chemistry, in all the three areas of the atmosphere mentioned under point 5, are used.

In the following subsections we will describe the techniques and theories for items 1-3. Items 5-6 will not be described further, as the advantage of using these approaches is logical, because it reduces the chemistry to the largest extent in the simulations.

Gear Algorithm

The Gear algorithm is a hybrid explicit/implicit predictor-corrector method. The Gear algorithm is self-starting, in contrast to other predictor-corrector methods, where one first must use another method to generate the first points. The Gear algorithm is based on the backward differential formula[55, 54]

$$\bar{y}(t_n) = \sum_{i=1}^{q_n} \alpha_i \bar{y}(t_{n-i}) + \Delta t \beta \bar{f}(\bar{y}(t_n), t_n, \bar{k}) \quad (\text{C.18})$$

with

$$\bar{y}(t = 0) = \bar{y}_0 \quad (\text{C.19})$$

where the first term on the right side of Eq. (C.18) is the predictor based on the earlier time steps $t_{n-1}, t_{n-2}, \dots, t_0$, and the second term is the implicit corrector which depends on the concentrations of the compounds at t_n . $\Delta t = t_n - t_{n-1}$ is the time step. q_n is the order of approximation, which means the number of concentrations from the earlier time steps included in the calculation at time t_n . From a predetermined accuracy, the Gear algorithm estimates Δt and the order of the approximation itself. α_i and $\beta > 0$ are coefficients that depend on the current order. From that we can write Eq. (C.18) in a more compressed form

$$\bar{y}(t_n) = C + \Delta t \beta \bar{f}(\bar{y}_n, t_n, \bar{k}) \quad (\text{C.20})$$

or

$$\bar{F}(y) = \bar{y} - C - \Delta t \beta \bar{f}(\bar{y}) \quad (\text{C.21})$$

where \underline{J}_F is the Jacobian for \bar{F} :

$$\underline{J}_F = \underline{I} - \Delta t \beta \underline{J} \quad (\text{C.22})$$

\underline{I} is the identity matrix and \underline{J} is the Jacobian for \bar{f} . Applying Newton's method on \bar{F} , we get

$$\bar{y}_{m+1} = \bar{y}_m - (\underline{I} - \Delta t \beta \underline{J}_m)^{-1} (\bar{y}_m - \bar{C} - \Delta t \beta \bar{f}(\bar{y}_m)) \quad (\text{C.23})$$

If we define the predictor matrix \underline{P} as

$$\underline{P}_m = \underline{I} - \Delta t \beta \underline{J}_m \quad (\text{C.24})$$

Eq. (C.23) becomes

$$\bar{y}_{n(m+1)} = \bar{y}_{n(m)} - \underline{P}_m^{-1} \left(\bar{y}_{n(m)} - \sum_{i=1}^{q_n} \alpha_i \bar{y}_{n-1} - \Delta t \beta \bar{f}(\bar{y}_{n(m)}) \right) \quad (\text{C.25})$$

How to evaluate $\bar{\alpha}$ and β is given by Gear[51].

In the Gear algorithm the code iteratively solves the equation system

$$\underline{P} \bar{x} = \bar{b} \quad (\text{C.26})$$

The \bar{b} -vector comes from solving Eq. (C.1), \bar{b} is a vector that is changed continuously during the generation of the time step with the corrected \bar{y} values. \bar{y} and its derivatives are corrected by the corrector \bar{x} . Therefore, in the Gear algorithm vector \bar{x} must be solved from equation system Eq. (C.26).

The Gear algorithm is a self-starting adaptive algorithm. Convergence in the algorithm is ensured by a local and global error test. The local test is performed after each iteration in a time step, and a global error test are made after all the iterations of the time step have been completed. The error tests are Normalized-Root-Mean-Square (*NRMS*) errors. The local error test is

$$NRMS_{t,n} = \sqrt{\frac{1}{N} \sum_{i=1}^N \left(\frac{\Delta y_{i,t,n}}{R_{tol} y_{i,t,1} + A_{tol,t}} \right)^2} \quad (\text{C.27})$$

where $y_{i,t,n}$ is the concentration of the i th species at time step t for the n th iteration. $\Delta y_{i,t,n}$ is the change of concentration, and N is the total number of species. R_{tol} and $A_{tol,t}$ are the relative and absolute error tolerances, respectively. The Global error test is

$$NRMS_t = \sqrt{\frac{1}{N} \sum_{i=1}^N \left(\frac{\sum_n \Delta y_{i,t,n}}{R_{tol} y_{i,t,1} + A_{tol,t}} \right)^2} \quad (\text{C.28})$$

In the SMVGEAR/MOON model, the error tests are performed as follows:

- if $NRMS_{t,n}$ is decreasing with increasing n , then sufficient converging of the solution has occurred and it proceeds to the global error test.

- Otherwise, iterations of the time step continue until $NRMSt_{t,n}$ passes the local error test.

Afterwards, the global error test is performed. The global error test is achieved when $NRMSt_t$ comes below a parameter that depends on the order of the approximation and the number of species with a production and/or loss term. If the global error test fails, the derivatives are reset to the value from before the last time step then three successive steps are performed:

1. reestimate a time step at the same or one order lower and retry the step,
2. if the previous attempt fails, then the step is retried with a smaller time step, and
3. if this also fails, the order of the Gear algorithm is reset to 1 and the algorithm starts over.

If all of these attempts fail, the program stops.

Contrary to the other Gear algorithms[55, 54] this algorithm uses variable absolute error tolerances. The reason for this is a constant absolute error tolerance can build up errors of the species concentrations if too many concentrations of these are lower than the absolute tolerances. Tests of previous generations of the SMVGEAR solver[56] have shown that the only cases where the solver breaks down are when too many concentrations come below the absolute error tolerance. To avoid this problem a lower absolute error tolerance than required for the majority of the time steps has been used. Therefore, a variable absolute error tolerance will also increase the speed of the algorithm.

Hence, instead of choosing a constant absolute error tolerance we first choose ranges of absolute error tolerances. For urban chemistry $A_{tol,t} \in [10^3; 10^7]$ molecules/cm³, while for free tropospheric and stratospheric chemistry $A_{tol,t} \in [10^5; 10^7]$ molecules/cm³. Hence, larger values can create too large errors in the concentrations, and lower values do not increase the accuracy significantly, only the computer time. On the basis of these maxima ($F_{tol,max}$) and minima ($F_{tol,min}$) an algorithm for the selection of $A_{tol,t}$ is built. First, six fixed tolerances $F_{tol,i}$, $i \in \{1, 2, 3, 4, 5, 6\}$, are calculated according to

$$F_{tol,i} = 10 \log F_{tol,min} + (\log F_{tol,max} - \log F_{tol,min}) (6 - i)/5 \quad (C.29)$$

These six F values are used first to count the number of species having a given concentration relative to $F_{tol,i}$ as follows:

$$\begin{aligned} N_1 &= N_1 + 1 & \text{if } & y_{i,t,n} > F_{tol,1} \\ N_2 &= N_2 + 1 & \text{if } & F_{tol,2} > y_{i,t,n} \geq F_{tol,1} \\ N_3 &= N_3 + 1 & \text{if } & F_{tol,3} > y_{i,t,n} \geq F_{tol,2} \\ N_4 &= N_4 + 1 & \text{if } & F_{tol,4} > y_{i,t,n} \geq F_{tol,3} \\ N_5 &= N_5 + 1 & \text{if } & F_{tol,5} > y_{i,t,n} \geq F_{tol,4} \end{aligned} \quad (C.30)$$

and then to set up the final total error tolerance:

$$A_{tol,t} = \begin{cases} F_{tot,1} & \text{if } N_1 > f N \\ F_{tot,2} & \text{if } N_1 + N_2 > f N \geq N_1 \\ F_{tot,3} & \text{if } N_1 + N_2 + N_3 > f N \geq N_1 + N_2 \\ F_{tot,4} & \text{if } N_1 + N_2 + N_3 + N_4 > f N \geq N_1 + N_2 + N_3 \\ F_{tot,5} & \text{if } N_1 + N_2 + N_3 + N_4 + N_5 > f N \geq N_1 + N_2 + N_3 + N_4 \\ F_{tot,6} & \text{if } f N \geq N_1 + N_2 + N_3 + N_4 + N_5 \end{cases} \quad (\text{C.31})$$

where f is a fraction of the number of species N . In the solver f is chosen as 0.40. This way of grouping the species together before $A_{tol,t}$ is chosen is a much faster procedure than first sorting the species after concentration and then setting the tolerance of the 40th percentile species.

The above procedure could be applied every time step, but the counting procedure can be relatively time consuming, therefore the method is only carried out every third Gear time step. Hence, this restriction will not damage the advantage of the variable $A_{tol,t}$ method.

The Sparse Matrix

For the EMEP MCH $\underline{P} \in \mathbf{R}^{79 \times 79}$ while for the RACM MCH $\underline{P} \in \mathbf{R}^{77 \times 77}$. During the running time of the MOON model, \bar{x} in Eq. (C.26) must be calculated many times. However, the \underline{P} -matrix is a sparse matrix, which means \underline{P} contains relatively few non-zero elements. Taking advantage of the knowledge of where the zeros of the sparse matrix are placed, special techniques can be used in order to increase the computational speed of the program.

For the MOON model the \bar{y} -vector is rearranged so the species with fewest production and loss terms appear first and the species with most last. This means that when the \underline{P} -matrix is made, it will contain fewest non-zero elements in row one and most in the last row. Furthermore, to solve Eq. (C.26) \underline{P} is $\underline{L}\underline{U}$ -decomposed. The advantage of this technique is that \bar{x} can be found by forward and backward substitution in \underline{L} and \underline{U} , respectively. Since Eq. (C.26) has to be solved many times during the program run, the solver determines in advance all zero multiplications in the code.

The chemical solver runs different chemistry in different regions of the atmosphere, day and night chemistry, and gas-phase and heterogeneous chemistry, and different sparse matrices of these different cases are set up. All of these sparse matrices are set up in the beginning of the MOON model before any dynamic or numerical chemical solution of the problem has taken place, in order to decrease the computational effort of the solver.

Vectorization of the Code

When many trajectories with an attached chemical box are to be run, a vectorization of the code can be done in two ways – either vectorization around species

or vectorization around trajectories. Jacobson[56] have investigated which type of vectorization the computational speed for the Gear solver would benefit most from. He found that vectorization around trajectories is much faster compared with vectorization around species, even though it is much simpler to vectorize around species than trajectories. However, tests of Jacobson[56] show that the maximum speed of the solver is achieved when trajectory cells of around 512 are used.

There are a couple of reasons why vectorization around cells is more efficient than around species. One reason is that the code needs to perform many decompositions/back substitutions. All the codes that have been developed for that purpose use varying length inner loops. Therefore, if the code is to run many trajectories it will be highly efficient if it is possible to vectorize the code over trajectories.

Reordering of Trajectory Groups

Due to different geographical and daily influences on the chemistry, the different trajectory groups will have different stiffnesses. In the MOON model the trajectory group stiffness is calculated as

$$S_{t,k} = \frac{1}{M} \sum_{i=1}^M \left(\frac{dy_{i,k,t}/dt}{y_{i,k,t} + A_{i,k,t}} \right)^2 \quad (\text{C.32})$$

where M is the order of the matrix of partial derivatives, $y_{i,k,t}$ the species concentrations, $A_{i,k,t}$ the absolute error tolerance, i the species indices, n the time and k the trajectory group number. After this is done the trajectory groups are reordered with the group with the smallest $S_{t,k}$ -value first and the largest $S_{t,k}$ -value last using an $N \log_2 N$ heap sorting routine.

Comment

Application	Improved Speed Factor
Sparse-matrix technique	≈ 2
Vectorization	≈ 120
Reordering of grid cells	≥ 2
Variable absolute tolerance	2-3
Total	960 - 1440

Table C.1: How the different new numerical techniques described in *Appendix C* have improved the speed of the Gear algorithm when the code for an urban case is run at a CRAY Y-MP[56].

In this thesis we will not describe to which extent the computer speed is improved using the Gear algorithm presented here compared with traditional Gear algorithms, because it is neither the subject for this appendix nor the thesis. However this is described in detail by Jacobson[56] and his results are illustrated briefly in Table C.1.

The only test of the computational speed of the new Gear algorithm has been a comparison between DACFOS on a Silicon Graphics 180 MHz IP32 processor and the MOON model on a NEC SX-4 and a Silicon Graphics 180 MHz IP32 processor, see *Section 3.3.2*.

Appendix D

How to run the MOON Model

The MOON model's program package can be used to simulate different atmospheric chemistry cases. Some of these cases can be summarized as follows, it is possible to:

- turn on and off the transport and the chemistry independently from each other,
- solve different kinds of chemistry in the different sections of the atmosphere, and
- the model can handle gas-phase and surface reactions.

Furthermore, the MOON model has been programmed in standard F77 which makes it easy to compile and run on almost every computer that has a Fortran compiler. Therefore, in the *makefile* compiler options that can be used for several different types of computers are described.

The MOON model's program package has a large variety of options, many parameters of the model must be set in order to run the model as wanted. This section give a detailed description of these parameters and the different types of input files the program needs to run it.

Makefile

Determine the type of machine you wish to run the program package on and compile the program, after selecting or adding the machine-dependent compiling commands in the *makefile* included in the package.

The *makefile* contains compiler options for CRAY, SUN, SGI, NEC and PC's with LINUX. For CRAY and NEC, the compiler is set for single-precision (13 digit accuracy) while for the other computers the compiler is set for double precision (14 digit accuracy). To run the program package on the different computers the only necessary changes are the compiling commands in the *makefile*.

If you want to use the program on another computer, you may have to change the compiling commands, but **you must** make sure that you run the model with at **least 12 digits of accuracy**, since it is required by the matrix decomposition described in *Section D.2, The Sparse Matrix* and the photolysis program.

The Chemistry Module

The chemical box can be setup to run different types of chemical reactions (gas-phase and surface reactions) and different kinds of chemistry in different sections of the atmosphere (urban, free troposphere and stratosphere). The chemical reactions are setup in *globchem.dat*, and the options for the type of chemistry to solve are IFURBAN, IFTROP and IFSTRAT, see Table D.1. These parameters are set up in *mglob.dat*. To run the model as a zero dimensional box without any kind of

IFURBAN	IFTROP	IFSTRAT	Type of chemistry solved
0	0	0	Do not solve chemistry
1	0	0	Solve U everywhere
0	1	0	Solve T everywhere
0	0	1	Solve S everywhere
1	1	1	Solve U below PLOURB, T between PLOURB and S above PLOTROP
0	2	2	Solve T/S chemistry everywhere
2	2	2	Solve U/T/S chemistry everywhere

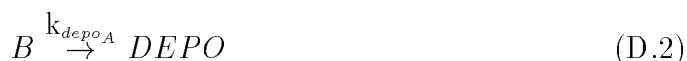
Table D.1: Parameters to define in order to solve different kind of chemistry in different regions of the atmosphere. U = Urban, T = free Tropospheric, S = Stratospheric. The parameters PLOURB and PLOTROP are explained in *Section D.3*.

transport, set IFBOX to 1 in *mglob.dat*, and select the necessary meteorological parameters in *m0dbox.dat*.

Aside from reading in the chemical mechanism, it is also possible to add emissions and depositions into the MOON model by the *globchem.dat* data file on a reaction basis, for example, for emissions of compound *A*



and depositions of compound *B*



Emissions and depositions are included in the photolysis part of the program.

Since depositions are a loss of a compound they must be included in the first and partial derivative equations. The emission of a compound into the chemical box is constant for a given time step, therefore emission rates must only be included in the first derivative, not in the Jacobian. Given the way in which the chemical compiler (*readchem.f*) sets up the partial derivative and the Jacobian for the chemical mechanism, it is not possible to handle the emission exactly, but almost exactly using some manipulation. From Eq. (D.1) we have

$$\begin{aligned} \frac{d[EMIS]}{dt} &= -k_{emis_A}[EMIS] \\ \frac{d[A]}{dt} &= k_{emis_A}[EMIS] \end{aligned} \quad (D.3)$$

For this small system we get the Jacobian

$$\underline{J} = \begin{pmatrix} -k_{emis_A} & 0 \\ k_{emis_A} & 0 \end{pmatrix} \quad (\text{D.4})$$

From Eqs. (D.3-D.4) we see that if k_{emis_A} is very small and $[EMIS]$ is so large that $k_{emis_A} \times [EMIS]$ corresponds to the emission of A into the box, then the error introduced into the box will be insignificant.

Photorates

This package also includes a photolysis program *photo_2d.f*. The *photo_2d.f* program simulates diurnal height and latitudinally varying solar radiation. This program calculates a three dimensional grid of photolysis parameters for each reaction. The three dimensions are local hour angle, altitude and latitude at a specific longitude. Linear interpolation is then used to calculate the photorates at a given trajectory point, see *Section 3.1.2* for further description.

The Transport Module

The transport in the model is described by trajectories. To run the program as a multi-trajectory chemistry box model, the format of the trajectories must be (the format can be considered as instant pictures for each trajectory point toward the receptor point):

Line 1: date and time of program run

year / month / day / hour / minute.
ex. 98 02 17 14 53

Line 2: start time of trajectory and time step

Not Used / number of arrival times / time step between the arrival times /
year / month / day / hour / minute.
ex. 60 5 60 98 02 18 20 00

Line 3: not used.

ex. F 240 98 02 19 00 00

Line 4: current trajectory time

year / month / day / hour / minute / Not Used / Not Used.
ex. 98 02 18 21 00 -150 15

Line 5: trajectories and heights

number of receptor points / number of arrival heights in a given receptor points
/ Not Used
ex. 3 4 T

Line 1: number of existing trajectories in heights-1 / number of existing trajectories at an arrival time-1 / height point number at a receptor point
 ex. 3 3 1

Loop over receptor points and for each receptor point over the arrival heights:

Line 1: trajectory starting point
 longitude / latitude
 ex. 12.53000 55.76000

Finally, loop over arrival times:

Line 1: T

Line 2: meteorological information along the trajectories, i.e., longitude along the trajectory, latitude along the trajectory, height above sea level, u component of the wind, v component of the wind, temperature, relative humidity, surface temperature, ABL height, precipitation, total cloud cover in percent and pressure in 1 hPa = 100 Pa = 1 mbar

Running the Code

The program is initially set up to run a simulation over 9900 trajectories. If the memory requirements for this simulation are too large for your computer, go into *comode.h* and change “I_RECP”, “I_HEIG” and “I_ARRI” to smaller numbers. Then, go into *mglob.dat* and change “N_RECP”, “N_HEIG” and “N_ARRI” to smaller numbers (note $N_RECP \leq I_RECP$, $N_HEIG \leq I_HEIG$ and $N_ARRI \leq I_ARRI$). Then recompile the code. If the memory now fits in your computer, just type “*smogout > xxl*” and the code will run a simulation according to the length of the trajectories, using full urban, tropospheric, and stratospheric chemistry.

If you want to run with a larger number of trajectories, you can do that by changing the default “I_RECP”, “I_HEIG” and “I_ARRI” values given in *comode.h*, and changing “N_RECP”, “N_HEIG” and “N_ARRI” to the same values in *mglob.dat*. If the memory requirement then becomes too high, you must reduce the number of chemical equations and/or species solved. These can be turned off in *globchem.dat*, then reduce “IGAS” and/or “NMTRATE” in *comode.h*.

You can change the type of chemistry by changing “IFURBAN”, “IFTROP” and “IFSTRAT”, as defined in Table D.1 above.

The model can be run in box mode, creating an accurate solution to compare results with. By setting “ITESTGEAR” = 2 in *mglob.dat*, you automatically create a box model (you do not need to change “N_RECP”, “N_HEIG” and “N_ARRI”), in which the error tolerances are tightened significantly. You can change this in *reader.f*. Solutions for comparison will be written to *compare.dat*. You can specify whether you want to test the urban, free-tropospheric or stratospheric chemistry set by changing “IFURBAN”, “IFTROP” and “IFSTRAT” as described in Table D.1. To test the accuracy of any error tolerance, set “ITESTGEAR = 1” in *mglob.dat*,

specify the relative and absolute tolerances you want to test in *mglob.dat* (ERMAX., YLOW., YHI). The code will run the model in box mode and compare the solutions to those in file *compare.dat*. Note, you must create a *compare.dat* file with “ITESTGEAR” = 2 before comparing results with “ITESTGEAR” = 1.

The code can be sped up by varying absolute error tolerances. This code re-determines the absolute error tolerance every Gear time step. The range of absolute tolerances is set in *mglob.dat*. The current setting will give fast solutions with some small loss of accuracy (less than 1% over all species). For more accurate solutions, decrease “YHIU”, “YHIR”, and/or “YHIS”, which are the upper bounds of the error tolerances. The lower bounds (“YLOWU”, “YLOWR”, and “YLOWS”) can also be decreased, but these will have less effect on improving accuracy.

Finally, to change the chemical species and equations, enter *globchem.dat*, and add or remove species and add or remove equations. If your format is incorrect, the program will inform you on execution. The file *globchem.dat* and the subroutine *readchem.f* explain the types of chemical equations currently allowed.

When compiling on a different computer, you may encounter compiler errors not recognized as errors on CRAY, SUN, SGI, NEC and PC's with LINUX. In such cases, modify the code as needed.

D.1 Subroutines

The program package consists of a large number of subroutines in this section these subroutine are described briefly.

main.f: in the main program, the MOON model sets up parameter readed from the instant pictures of the trajectories and makes linear interpolation between these instant pictures if necessary. Moreover, the main program calls the following subroutines: *back_corr.f*, *back_para.f*, *const_zenith.f*, *depositions.f*, *depositions_ini.f*, *emission.f*, *emission_ini.f*, *gas_prnt.f*, *ini_conc.f*, *out_ini_conc.f*, *out_print.f*, *photo_grid.f*, *photorates.f*, *photorates_ini.f*, *physproc.f*, *read_chem.f*, *read_traj.f*, *readchem.f*, *reader.f*, *test_res.f* and *timepara.f*.

back_corr.f: corrects the background concentrations according to the geographic position of the trajectory.

Called in *main.f* in the time loop.

back_para.f: sets up background concentration parameters. Uses parameters from *globchem.dat* and *mixratio.dat*.

Called in *main.f* before the time loop.

backsub.f: performs back-substitution for the Gear algorithm.

Called by *smvgear.f*.

calcrate.f: calculates kinetic reaction, photorates, emissions, dry depositions and wet depositions rates.

Called by *physproc.f*.

const_zenith.f: calculates zenith angle constants.

Called in *main.f* in the time loop.

decomp.f: performs L-U decomposition of the sparse matrices.

Called by *smvgear.f*.

deposition.f: recalculation of dry and wet depositions, in cm/s and 1/s.

Called in *main.f* in the time loop.

deposition_ini.f: initial setup of dry and wet depositions, in cm/s and 1/s.

Called in *main.f* before the time loop.

emission.f: recalculation of emission, in $\text{cm}^{-2} \text{ s}$.

Called in *main.f* in the time loop.

emission_ini.f: initial setup of emission, in $\text{cm}^{-2} \text{ s}$. Reads the emission files to produce totals of SO_2 , NO_x and anthropogenic VOC for each grid point. Opens the files *tab.so2*, *tab.nox* and *tab.voc*.

Called in *main.f* before the time loop.

gas_prnt.f: identify gases for printing.

Called in *main.f* before the time loop.

ini_conc.f: initialize gas concentrations in the model, in cm^{-3} .

Called in *main.f* before the time loop.

jsparse.f: set up sparse-matrix and other arrays for the Gear algorithm. It sets arrays for gas-phase, aqueous-phase and any other types of chemistry. It also sets arrays for both day and night chemistry of each type. Furthermore, set up arrays for gas- and aqueous-phase chemistry include arrays for calculating first derivatives, partial derivatives, matrix decomposition, and matrix back-substitution. First, *jsparse.f* re-orders the ODEs to maximize the number of zeros in the matrix of partial derivatives. It later sets arrays to eliminate all calculations involving a zero.

Called by *readchem.f*.

ksparse.f: set up sparse-matrix and other arrays. It also sets arrays for gas-phase, aqueous-phase or any other type of chemistry. It sets arrays for both day and

night chemistry of each type. Furthermore, sets up arrays for decomposition/back-substitution of sparse matrices by removing all calculations involving a zero. Finally, sets arrays to take advantage of sparse matrices.

Called by *jsparse.f*.

local_hour_angle.f: from a given latitude, longitude, day of year and time of day this subroutine calculates the local hour angle.

Called by *const_zenith.f*.

local_hour_angle_ini.f: from a given latitude, longitude, day of year and time of day this subroutine calculates the initial local hour angle.

Called by *timepara.f*.

out_ini_conc.f: prints out initial concentration information.

Called in *main.f* before the time loop.

out_print.f: prints out concentrations for individual gases.

Called in *main.f* before the time loop and in the time loop.

pderiv.f: puts the partial derivatives of each ODE into the matrix \underline{P}_m (Eq. C.24).

Called by *smvgear.f*.

photo_grid.f: input of the three dimensional grid of photolysis parameters. Note, the input of the parameters must come in the same order as in the chemical reaction scheme *globchem.dat*. The three dimensions are latitude, altitude and local hour angle. The photolysis parameters are calculated by the program *photo_2d.f*, and the parameters from this program are written in *photorate.dat*. Unit of the photolysis parameters are in min^{-1} .

Called in *main.f* before the time loop.

photorates.f: estimates the photorates at the given trajectory points using linear interpolation of the grid points read by *photo_grid.f*. Units of the photolysis in the program must be in s^{-1} .

Called in *main.f* in the time loop.

photorates_ini.f: estimates the photorates at the given initial trajectory points using linear interpolation of the grid points read by *photo_grid.f*. Units of the photolysis in the program must be in s^{-1} .

Called in *main.f* before the time loop.

physproc.f: this subroutine calls *calcrate.f* and *smvgear.f*. Solves gas-phase chemical equations. The routine divides the trajectories into trajectory groups, and the code vectorizes around the number of trajectory groups in each block.

Called in *main.f* in the time loop.

read_traj.f: reads the meteorological parameter from the trajectories.

Called in *main.f* before the time loop and in the time loop.

readchem.f: set up routine for gas-phase chemistry. Reads species names, chemical reactions and photoprocesses from an input data set. It then places all necessary information into arrays and prints out the input information.

Called in *main.f* before the time loop.

reader.f: opens all data files and reads data from *mglob.dat*.

Called in *main.f* before the time loop.

smvgear.f: a Gear-type integrator that solves first-order ODEs with initial value boundary conditions. This solver differs from an original Gear code in that it uses sparse-matrix and vectorization techniques to improve speed. Much of the speed up in this program is due to sparse-matrix techniques and vectorization.

This version includes re-ordering of trajectory groups prior to each time-interval. The purpose of the reordering is to group the trajectory groups with stiff equations together and those with non-stiff equations together. This re-ordering can save significant computer time (e.g. speed the code by a factor of two or more), depending on the variation in stiffness throughout the trajectory-domain. When the stiffness is the same throughout the grid-domain (e.g. if all concentrations and rates are the same), then re-ordering is unnecessary and will not speed solutions.

This version includes a variable absolute error tolerance. The absolute tolerance is recalculated every Gear time step.

This version contains different sets of chemistry for different regions of the atmosphere. Thus, urban, free tropospheric and stratospheric chemistry can be solved during the same model run.

Called by *physproc.f*.

subfun.f: evaluates the first derivative of each ODE.

Called by *smvgear.f*.

test_res.f: reads data for testing results from chemistry.

Called in *main.f* before the time loop.

timepara.f: sets up time parameters for running the model, i.e. total number of seconds in a model run, total number of time-intervals for gas chemistry during the total length of the run and time-intervals for calling subroutine *out_print.f*.

Called in *main.f* before the time loop.

update.f: updates the time dependent parameters: photorates, emissions, dry depositions and wet depositions for each time step. Photorates and depositions are included in first and partial derivative equations while emissions are included in first derivative equations only. Since emission rates are constant for a given time step and location (although they change with each time step and location) they are put into the first derivative term of *subfun.f* only (not into partial derivative terms).

Called by *smvgear.f*.

Figure D.1 shows how the different subroutines are called in the MOON model.

D.2 Input (*.dat) Output (*.out) and Other Non- fortran Files

comode.h: dimensions arrays, serves as a common block.

makefile: links subroutines and compiles program.

gasconc.out: output file for gas concentration results. Carried out in *out_print.f*.

compare.dat: accurate results written in *compare.dat* when ITESTGEAR = 2, and accurate results read from *compare.dat* when ITESTGEAR = 1.

globchem.dat: input file for the chemistry mechanism, dry depositions, wet depositions and emissions. Read from *readchem.f*.

mglob.dat: input file of the parameters to initialize the MOON model. Read from *reader.f*.

mixratio.dat: input file of background concentrations. The background concentrations depends on the month of the year and the latitude, see Table 3.1. Read from *back_para.f*.

phorate.dat: three dimensional grid of photolysis parameters. The three dimensions are latitude, altitude and local hour angle. Read from *photo_grid.f*.

tab.nox: emission grid of NO_x. Read from *emission_ini.f*.

tab.so2: emission grid of SO₂. Read from *emission_ini.f*.

tab.voc: emission grid of VOC. Read from *emission_ini.f*.

forest.dat: emission grid of isoprene from forest. Read from *emission_ini.f*.

m0dbox.dat: file with meteorological data for 0-dimensional chemical box model simulations.

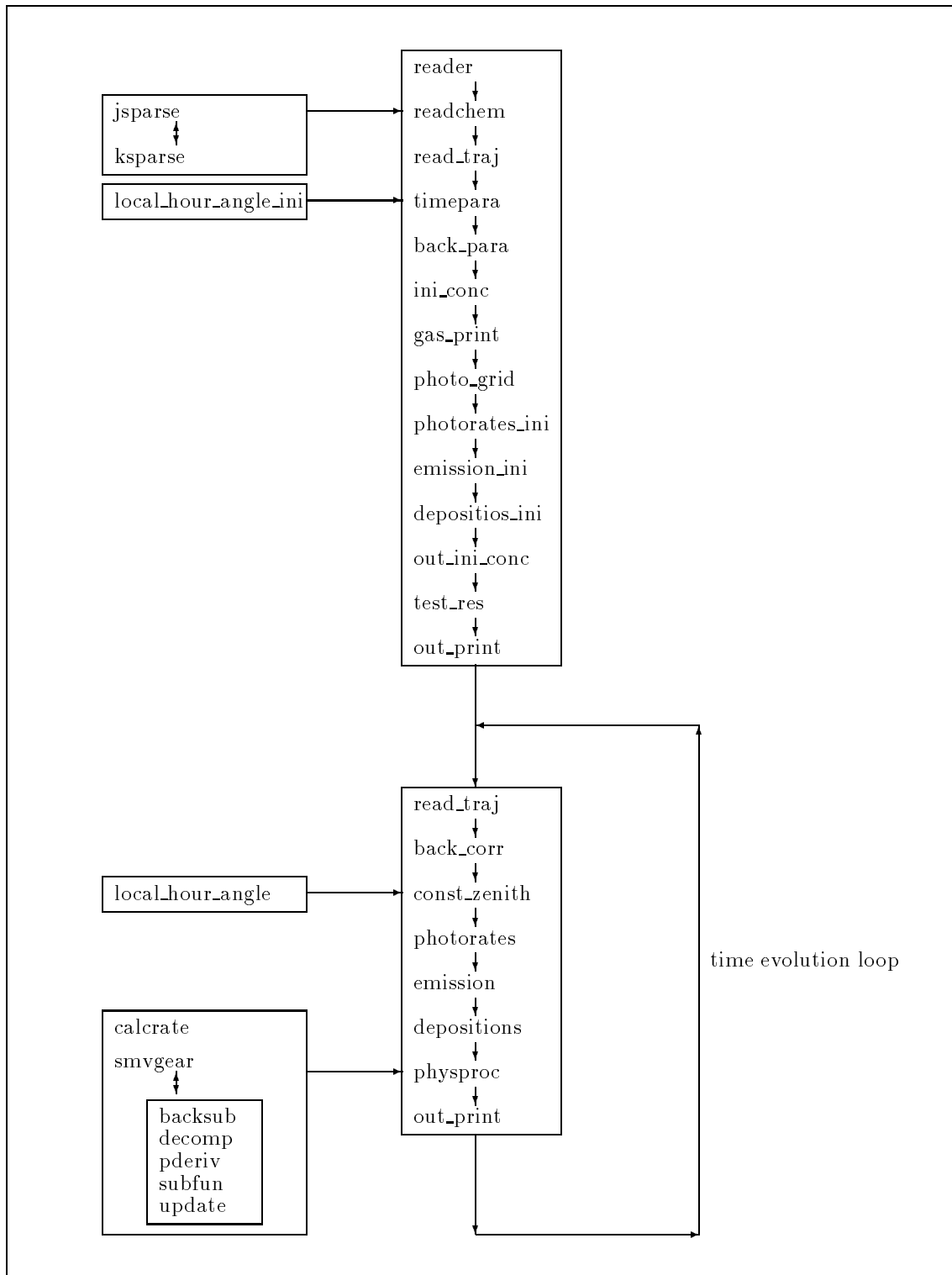


Figure D.1: Flow diagram of the subroutines in the MOON model.

D.3 List of Non-Array Parameters

In this section the non-array parameters that are important to know in order to set up and run the MOON model are given.

- APGASA-H: character names of gases whose concentration you want to print out during the simulation. (*mglob.dat*, *gasconc.f*).
- CHEMINTV: time interval (sec) for chemical processes. (*mglob.dat*).
- DTOUT: time step (sec) for calls to subroutine *out_print.f*, that means print out of species concentrations defined by APGASA-H. (*mglob.dat*).
- ERRMAXR: relative error tolerance for tropospheric chemistry. (*mglob.dat*).
- ERRMAXS: relative error tolerance for stratospheric chemistry. (*mglob.dat*).
- ERRMAXU: relative error tolerance for urban chemistry. (*mglob.dat*).
- FINHOUR: number of hours (whole number) of the model run. (*mglob.dat*).
- FINMIN: number of minutes (whole number) of the model run. (*mglob.dat*).
- FINSEC: number of seconds (whole number) of the model run. (*mglob.dat*).
- FRACDEC: fractional cut in the model time step. (*mglob.dat*).
- HMAXDAYR: maximum time step (sec) for day tropospheric chemistry. (*mglob.dat*).
- HMAXDAYS: maximum time step (sec) for day stratospheric chemistry. (*mglob.dat*).
- HMAXDAYU: maximum time step (sec) for day urban chemistry. (*mglob.dat*).
- HMAXNIT: maximum time step (sec) for night chemistry in all the atmospheric altitudes. (*mglob.dat*).
- LARRI: number of arrival times.
- LFOR: array dimension for forest data.
- LHEIG: number of heights.
- LRECP: number of receptor points.
- IBACK_LAT: array dimension for background concentrations.
- ICOORD = 1: rectangular coordinate system. = 2: Non-global spherical coordinates. = 3: Global spherical coordinates. (*mglob.dat*, *setmodel.f*).
- ICS: number of equation sets for the Gear algorithm: 3 gaschem + 1 aqchem + 1 growth.
- ICP: number of chemistry sets $\times 2 + 1$ (for growth) for the Gear algorithm.
- IDAY: starting day of month (1,2,..31) of the model run. (*mglob.dat*).

- IDAYPNTS_PH: array dimension for photolysis rates (photolysis rate points for one day).
- IFBOX = 1: sets up box model to solve urban/tropospheric/stratospheric chemistry together using default photorates. (*mglob.dat*).
- IFPRAT = 1: use default photorates from *phorate.dat* and = 0 use default photorates from *globchem.dat*. In the last case the formula Eq. (1.91) is used.
- IFPR1 = 1: call *out_print.f* to print initial information and = 0 for no print. (*mglob.dat*).
- IFREORD = 1: reorder trajectory groups according to stiffness. (*mglob.dat*).
- IFSOLVE = 1: solve chemical equations with the model, = 0 do not solve any chemical equations. (*mglob.dat*).
- IFSTRAT = 1: solve stratospheric chemistry, and = 0 do not. (*mglob.dat*).
- IFTROP = 1: solve free tropospheric chemistry, and = 0 do not. (*mglob.dat*).
- IFURBAN = 1: solve urban chemistry, and = 0 do not. (*mglob.dat*).
- IGAS: maximum number of gases, active + inactive.
- IHOUR: starting hour (0,1,2,..23) of model run. (*mglob.dat*).
- ILAT_PH: array dimension for photolysis rates (number of latitudes).
- ILAYER_PH: array dimension for photolysis rates (number of layers).
- ILONG_PH: array dimension for photolysis rates (number of longitudes).
- IMIN: starting minute (0,1,2,..59) of the model run. (*mglob.dat*)
- IMONTH: starting month (1,2,..12) of the model run. (*mglob.dat*)
- IPHOT: maximum number of photolysis rates.
- ITESTGEAR = 1: compare box model results from the model to results in file *compare.dat*, if = 2 create *compare.dat* to compare box model results against, if = 0 do not compare results or create a file. (*mglob.dat*).
- IYEAR: starting year of model run. (*mglob.dat*).
- KBLOOP: maximum number of trajectories in a vectorized block.
- KULoop: intended number of trajectories in a trajectory group. (*mglob.dat*).
- MAXDAYS: maximum number of days for the model to run.

- MAXGL: maximum number of gains/losses for given array.
- MORDER: maximum order for Gear parameters for dimension purposes.
- MXARRAY: maximum length of matrix put in one-dimensional array.
- MXBLOCK: maximum number of trajectory groups.
- MXCOF: maximum number of rate coefficient terms.
- MXCOUNT2-4: arrays sizes used to minimize matrix space.
- MXHOLD: maximum number of time steps for storing comparison data.
- MXRP: maximum number of reactants \times maximum number of products.
- N_ARRI: maximum number of arrival times.
- N_HEIG: maximum number of heights.
- N_RECP: maximum number of receptor points.
- NMDEAD: maximum number of dead species.
- NMRPROD: maximum number of species in a reaction.
- NMRATE: maximum number of rate constants.
- NMTRATE: maximum number of kinetic + photolysis reactions.
- NPHOTDRYDEP: number of dry deposition rates.
- NPHOTEMI: number of emission rates.
- NPHOTWETDEP: number of wet deposition rates.
- NREAC_PH: number of photolysis rates.
- NVERT = 1. (*mglob.dat*).
- PLOTROP: pressure (mbar) above which stratospheric chemistry is solved. (*mglob.dat*).
- PLOURB: pressure (mbar) below which urban chemistry is solved. (*mglob.dat*).
- YLOWR: lower bound of absolute error tolerance for tropospheric chemistry. (cm^{-3}).
(*mglob.dat*).
- YLOWS: lower bound of absolute error tolerance for stratospheric chemistry (cm^{-3}).
(*mglob.dat*).
- YLOWU: lower bound of absolute error tolerance for urban chemistry (cm^{-3}).
(*mglob.dat*).

YHIR: upper bound of absolute error tolerance for tropospheric chemistry (cm^{-3}).
(*mglob.dat*).

YHIS: upper bound of absolute error tolerance for stratospheric chemistry (cm^{-3}).
(*mglob.dat*).

YHIU: upper bound of absolute error tolerance for urban chemistry (cm^{-3}). (*mglob.dat*).

Appendix E

Isopleths and Scatter Plots

In this appendix isopleths and scatter plots of HO, HO₂, RO₂, NO and NO₂ are presented. These figures are based on the 81 box model simulations with varied initial concentrations without any emissions as described in Tables 1.1 and 1.2. The figures in this appendix are discussed in *Section 1.2.2*.

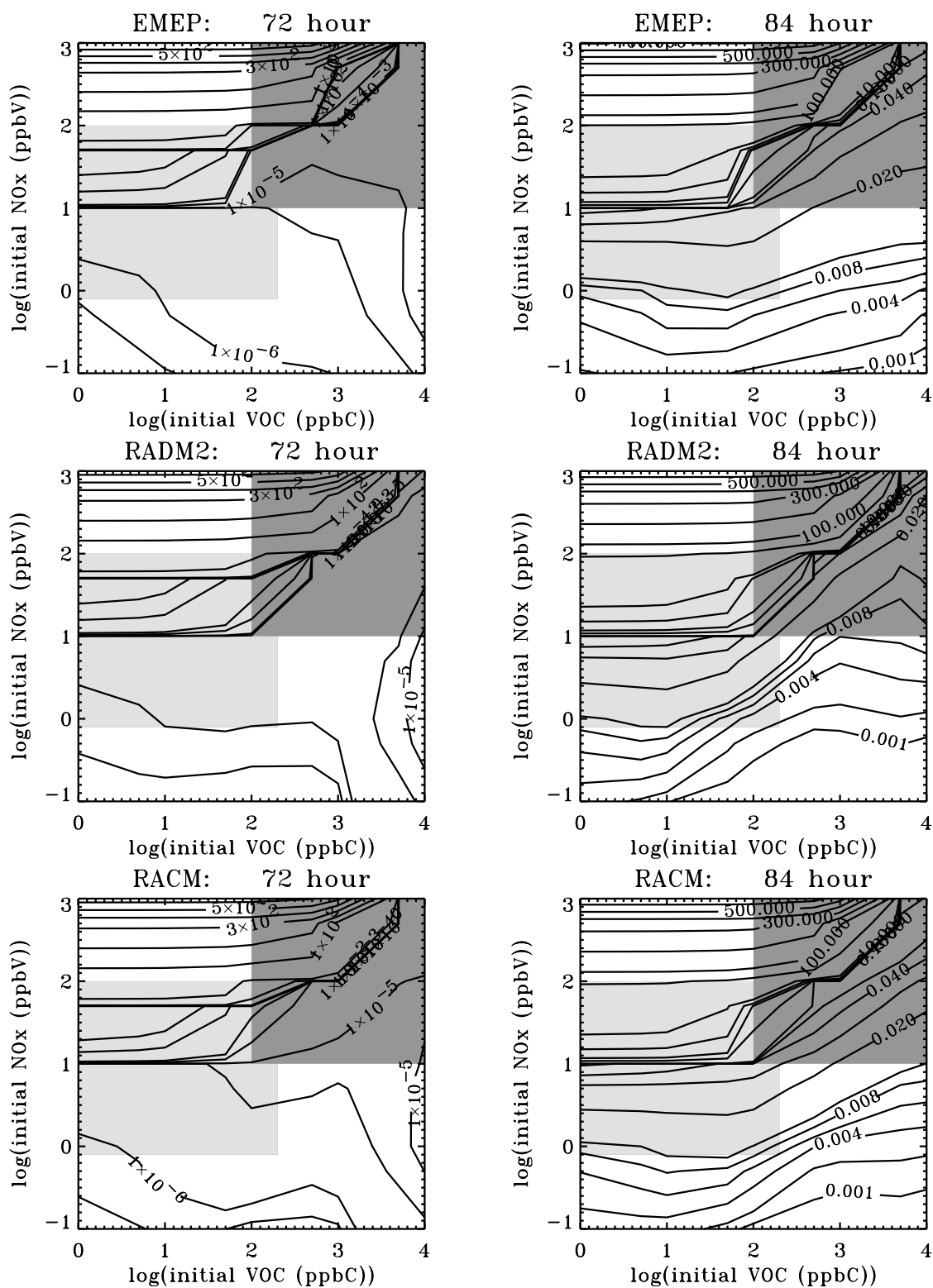


Figure E.1: Isopleths of the NO concentration (in ppbV) obtained from the EMEP, RADM2 and RACM MCHs after hour 72 (nighttime) and 84 (daytime). The plots are based on 81 zero-dimensional box model simulations as described in Tables 1.1 and 1.2. Contour levels are $1e-7$, $5e-7$, $1e-6$, $5e-6$, $1e-5$, $5e-5$, $1e-4$, $5e-4$, $1e-3$, $5e-3$, $1e-2$, $1e-1$, 1 , 10 , 100 , 200 , 300 , 400 , 500 , 600 and 700 for hour 72 plots, and $1e-3$, $2e-3$, $4e-3$, $6e-3$, $8e-3$, $1e-2$, $2e-2$, $3e-2$, $4e-2$, $5e-2$, $1e-1$, 1 , 2 , 5 , 10 , 50 , 100 , 200 , 300 , 400 , 500 , 600 and 700 for hour 84 plots. VOC represents anthropogenic non-methane VOC. For a definition of the light and dark gray areas, see the figure caption for Figure 1.4.

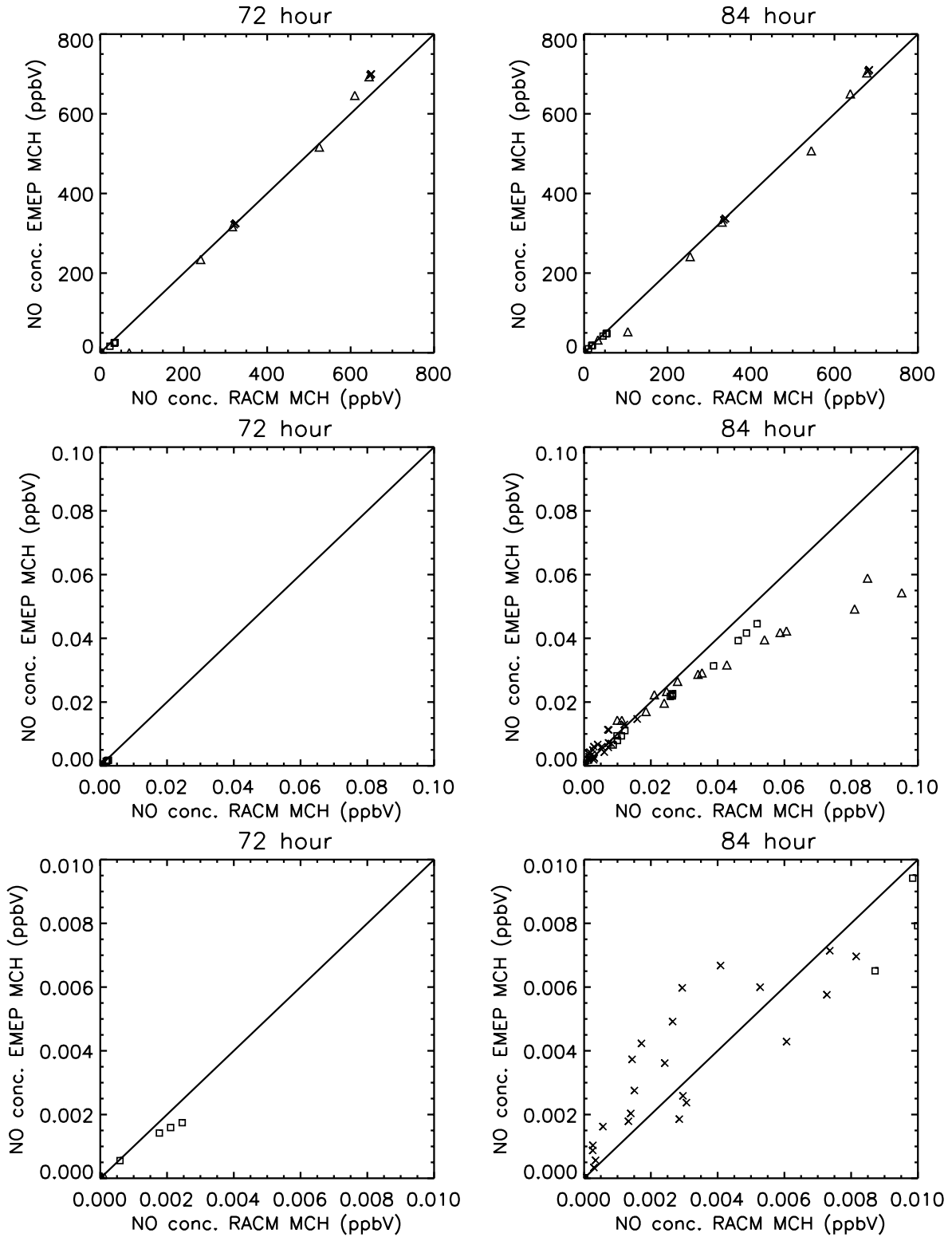


Figure E.2: Scatter plots for the NO concentration between the RACM and EMEP MCHs for the 81 zero-dimensional box model simulations as described in Tables 1.1 and 1.2 after hour 72 (nighttime) and 84 (daytime). \square : rural, \triangle : urban and \times : neither rural nor urban. The definition of urban and rural is according to the light and dark gray areas described in the caption for Figure 1.4. Note that the lower plots are zoom-ins of the upper plots.

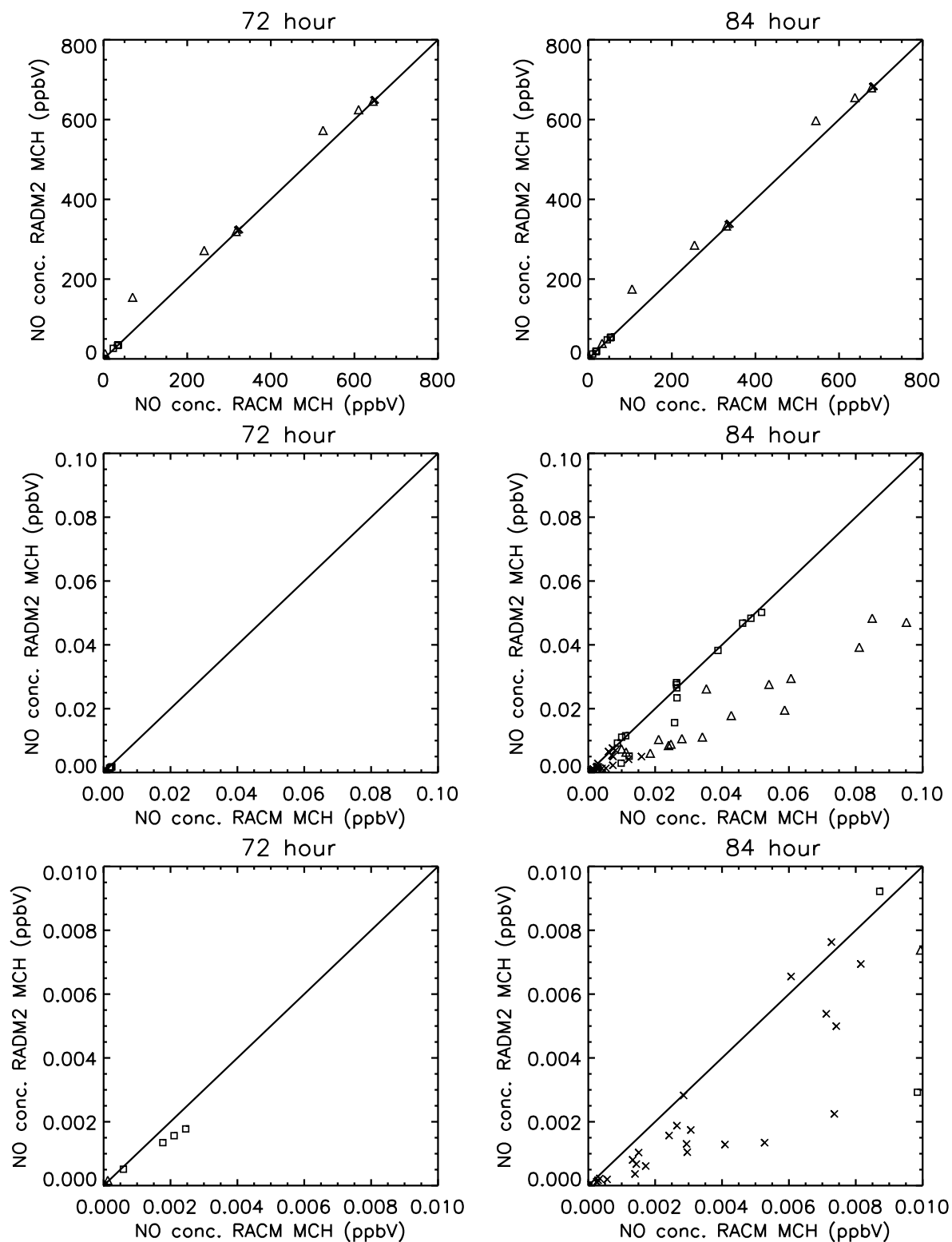


Figure E.3: Scatter plots for the NO concentration between the RACM and RADM2 MCHs for the 81 zero-dimensional box model simulations as described in Tables 1.1 and 1.2 after hour 72 (nighttime) and 84 (daytime). \square : rural, \triangle : urban and \times : neither rural nor urban. The definition of urban and rural is according to the light and dark gray areas described in the caption for Figure 1.4. Note that the lower plots are zoom-ins of the upper plots.

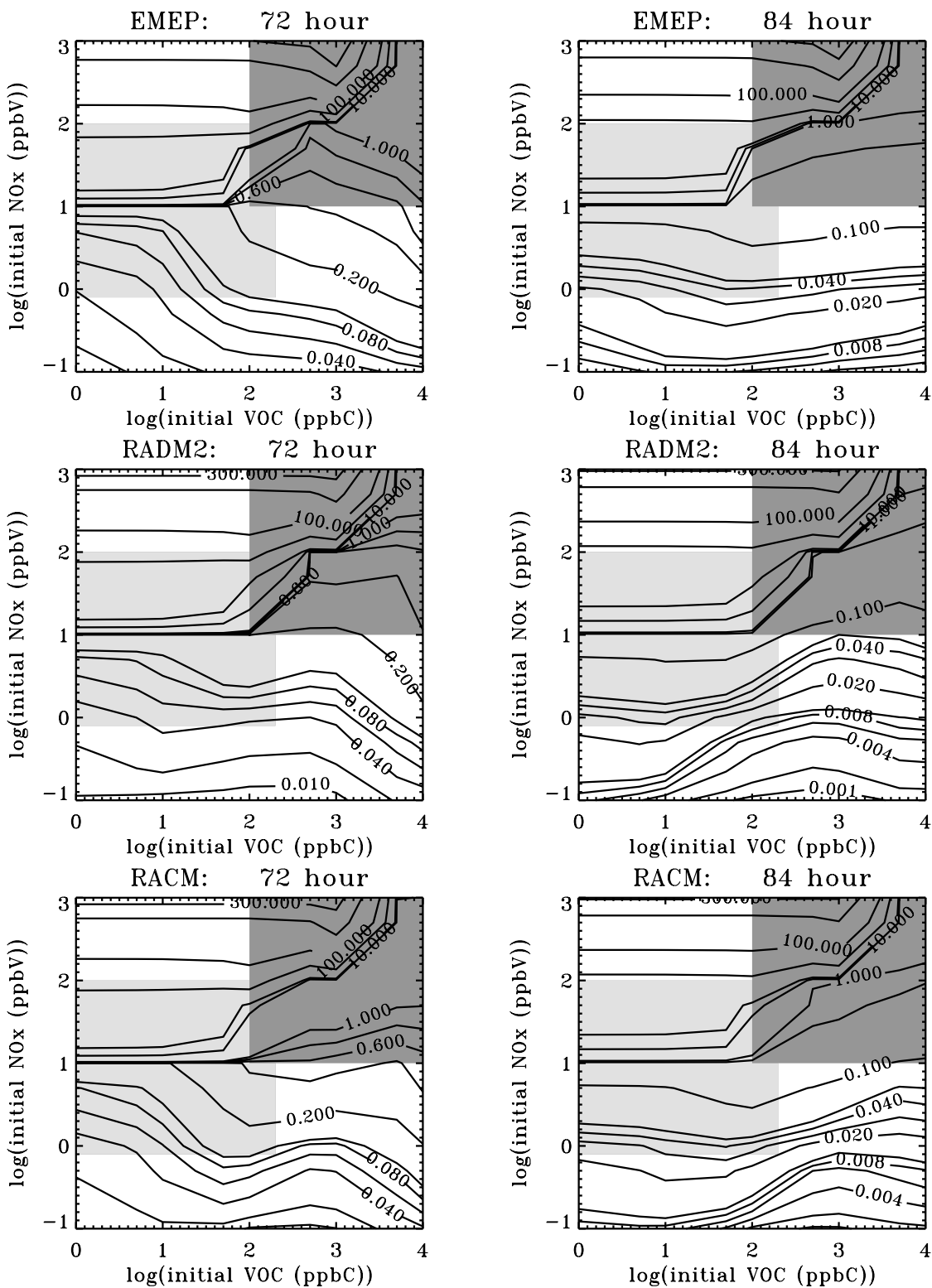


Figure E.4: Isopleths of the NO₂ concentration (in ppbV) obtained from the EMEP, RADM2 and RACM MCHs after hour 72 (nighttime) and 84 (daytime). The plots are based on 81 zero-dimensional box model simulations as described in Tables 1.1 and 1.2. Contour levels are 1e-2, 2e-2, 4e-2, 6e-2, 8e-2, 1e-1, 2e-1, 4e-1, 6e-1, 8e-1, 1, 5, 10, 50, 100, 200 and 300 for hour 72 plots, and 1e-3, 2e-3, 4e-3, 6e-3, 8e-3, 1e-2, 2e-2, 3e-2, 4e-2, 5e-2, 1e-1, 5e-1, 1, 5, 10, 50, 100, 200 and 300 for hour 84 plots. VOC represents anthropogenic non-methane VOC. For a definition of the light and dark gray areas, see the figure caption to Figure 1.4.

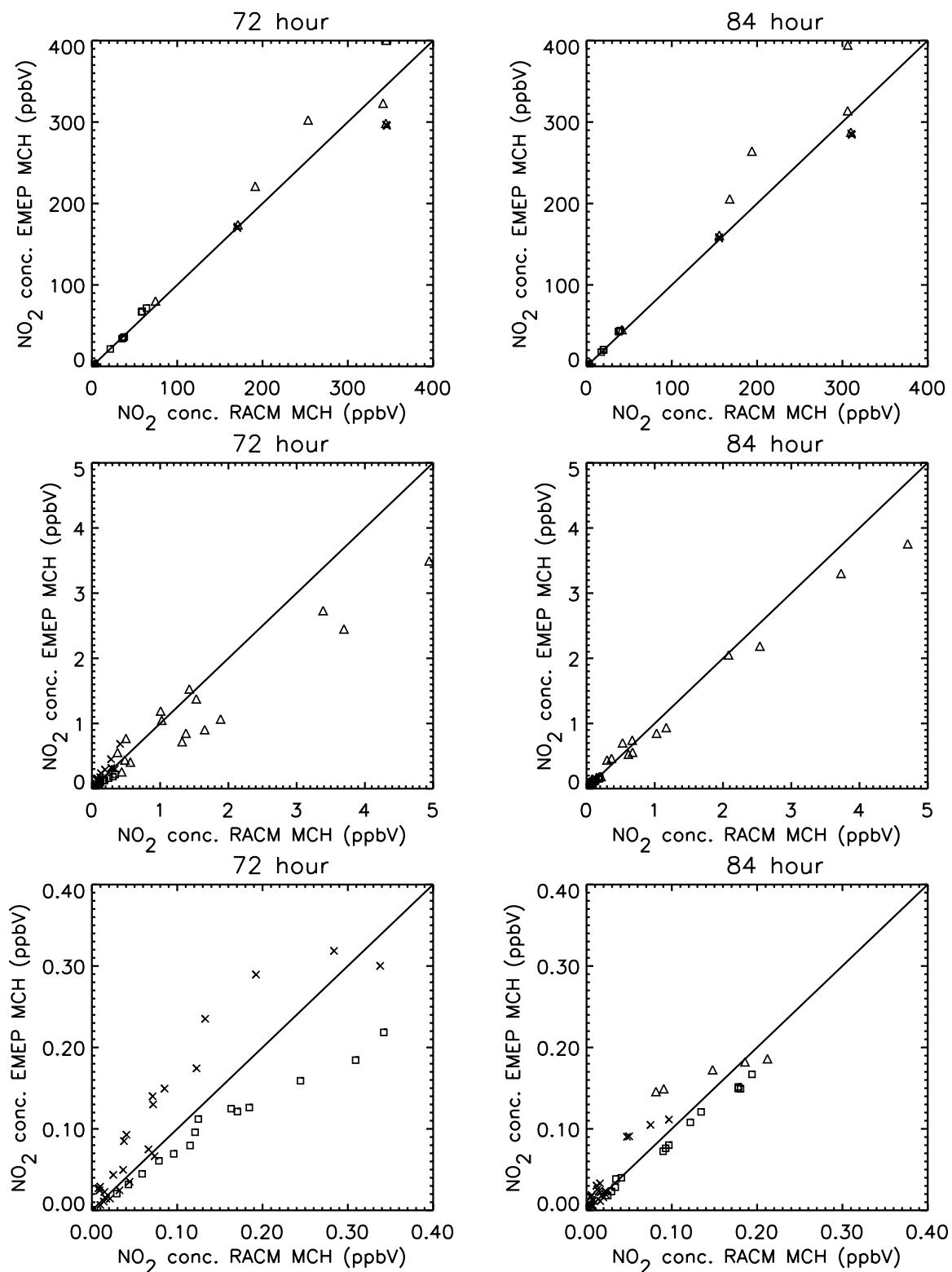


Figure E.5: Scatter plots for the NO₂ concentration between the RACM and EMEP MCHs for the 81 zero-dimensional box model simulations as described in Tables 1.1 and 1.2 after hour 72 (nighttime) and 84 (daytime). □: rural, △: urban and ×: neither rural nor urban. The definition of urban and rural is according to the light and dark gray areas described in the caption for Figure 1.4. Note that the lower plots are zoom-ins of the upper plots.

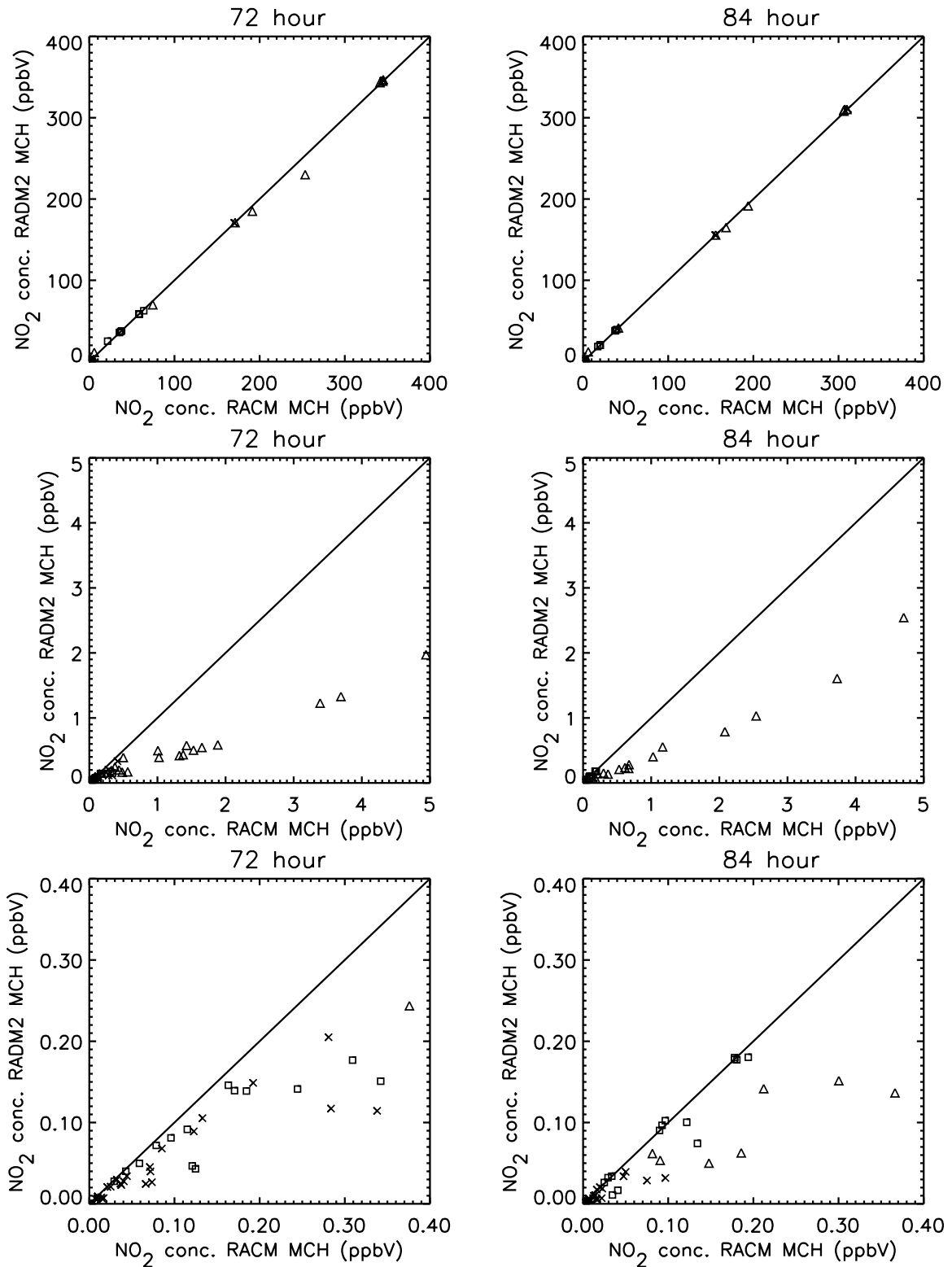


Figure E.6: Scatter plots for the NO₂ concentration between the RACM and RADM2 MCHs for the 81 zero-dimensional box model simulations as described in Tables 1.1 and 1.2 after hour 72 (nighttime) and 84 (daytime). □: rural, △: urban and ×: neither rural nor urban. The definition of urban and rural is according to the light and dark gray areas described in the caption for Figure 1.4. Note that the lower plots are zoom-ins of the upper plots.

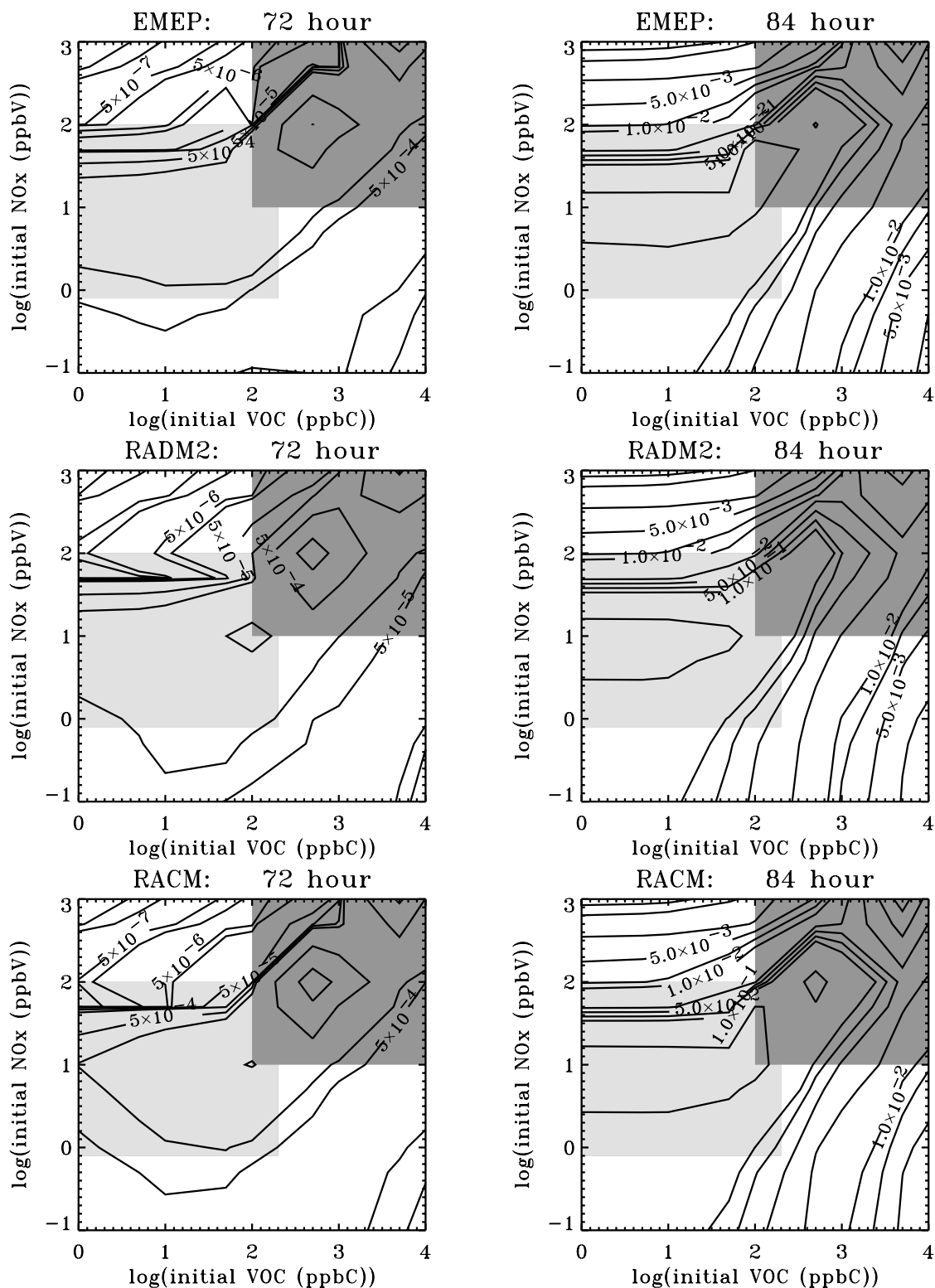


Figure E.7: Isopleths of the HO concentration (in pptV) obtained from the EMEP, RADM2 and RACM MCHs after hour 72 (nighttime) and 84 (daytime). The plots are based on 81 zero-dimensional box model simulations as described in Tables 1.1 and 1.2. Contour levels are $5e-8$, $1e-7$, $5e-7$, $1e-6$, $5e-6$, $1e-5$, $5e-5$, $1e-4$, $5e-4$, $1e-3$, $5e-3$ and $1e-2$ for hour 72 plots, and $7.5e-4$, $1.e-3$, $2.5e-3$, $5.e-3$, $7.5e-3$ and $1.e-2$ for hour 84 plots. VOC represents anthropogenic non-methane VOC. For a definition of the light and dark gray areas, see the figure caption for Figure 1.4.

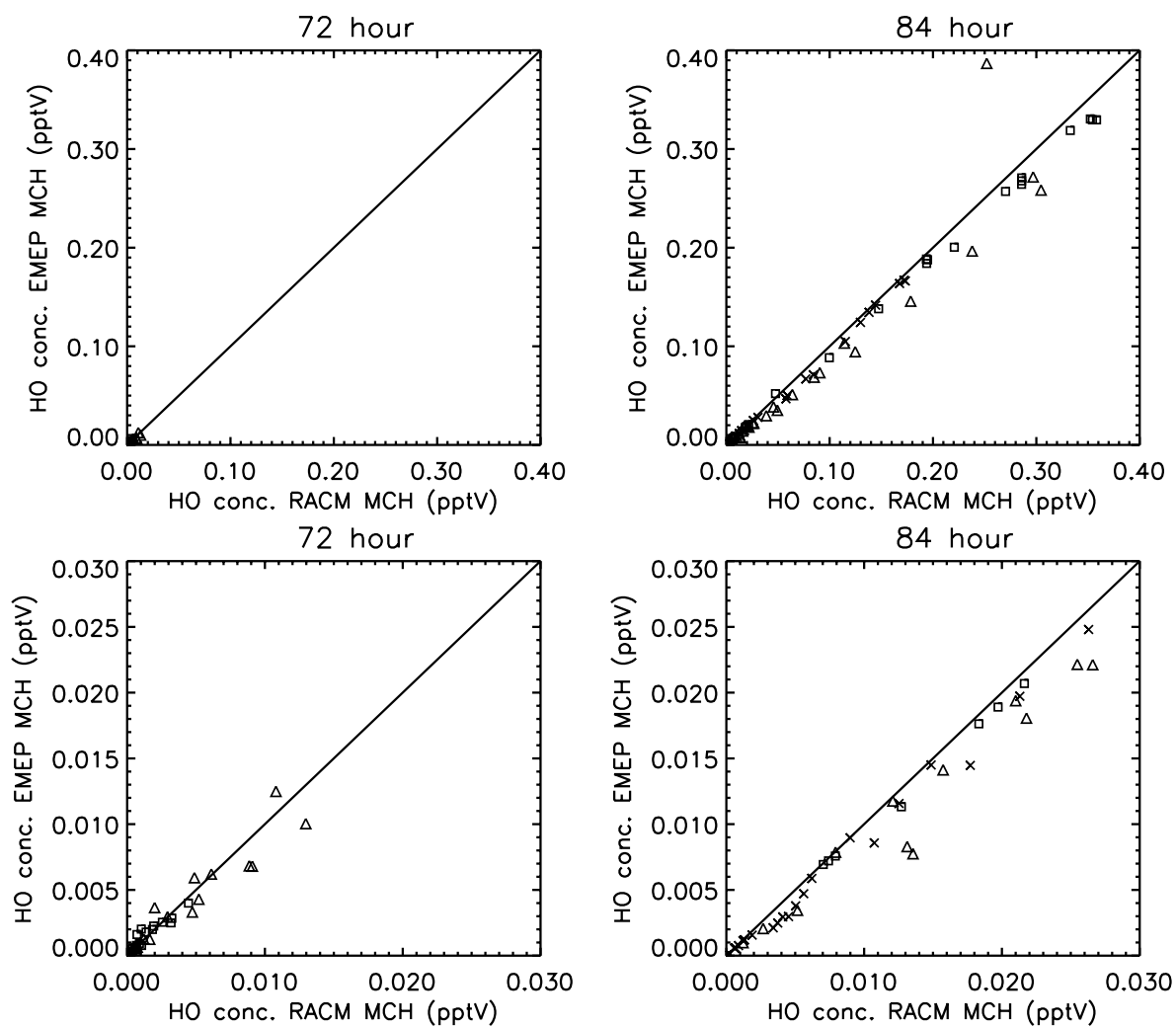


Figure E.8: Scatter plots for the HO concentration between the RACM and EMEP MCHs for the 81 zero-dimensional box model simulations as described in Tables 1.1 and 1.2 after hour 72 (nighttime) and 84 (daytime). □: rural, △: urban and ×: neither rural nor urban. The definition of urban and rural is according to the light and dark gray areas described in the caption for Figure 1.4. Note that the lower plots are zoom-ins of the upper plots.

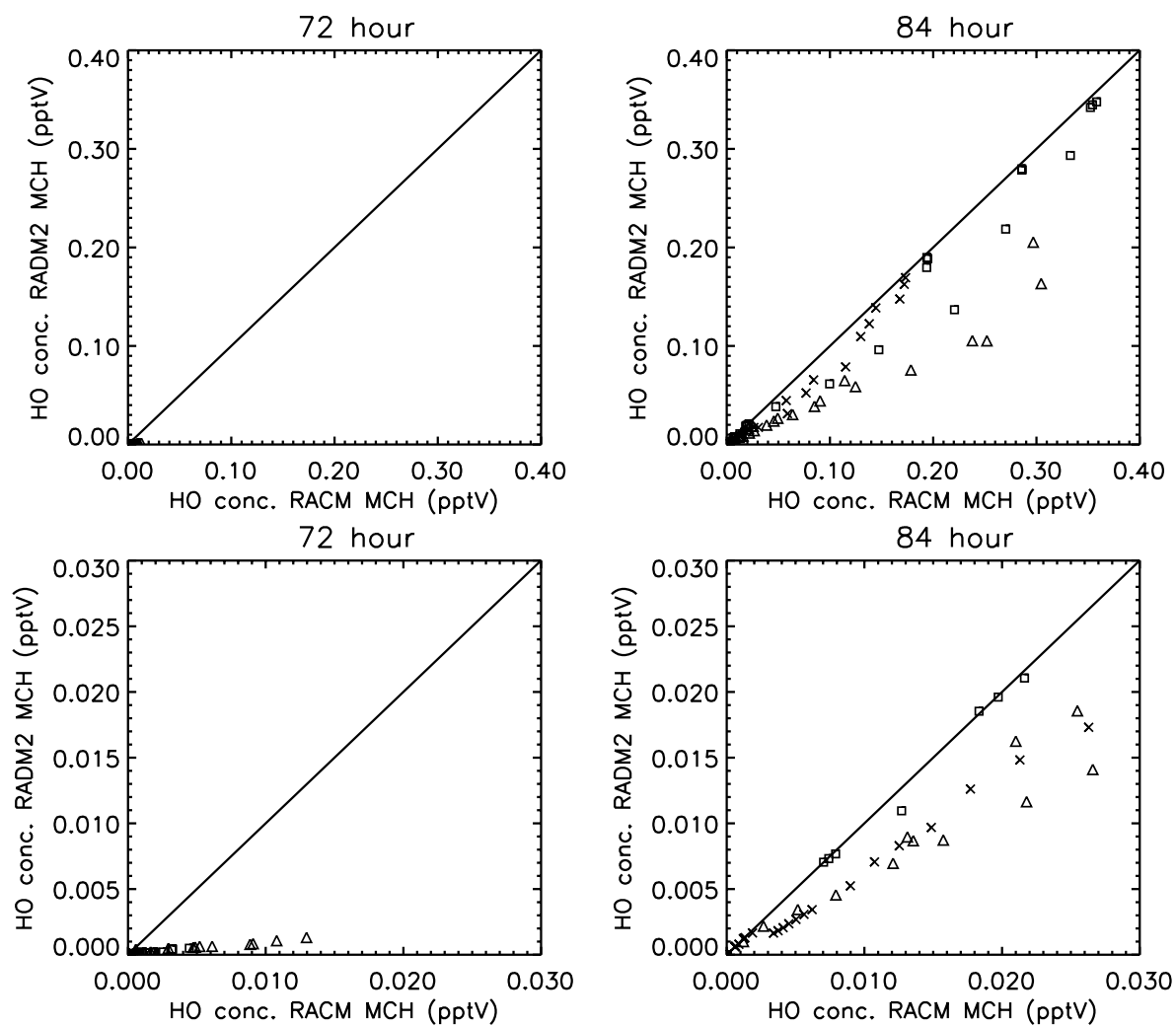


Figure E.9: Scatter plots for the HO concentration between the RACM and RADM2 MCHs for the 81 zero-dimensional box model simulations as described in Tables 1.1 and 1.2 after hour 72 (nighttime) and 84 (daytime). \square : rural, \triangle : urban and \times : neither rural nor urban. The definition of urban and rural is according to the light and dark gray areas described in the caption for Figure 1.4. Note that the lower plots are zoom-ins of the upper plots.

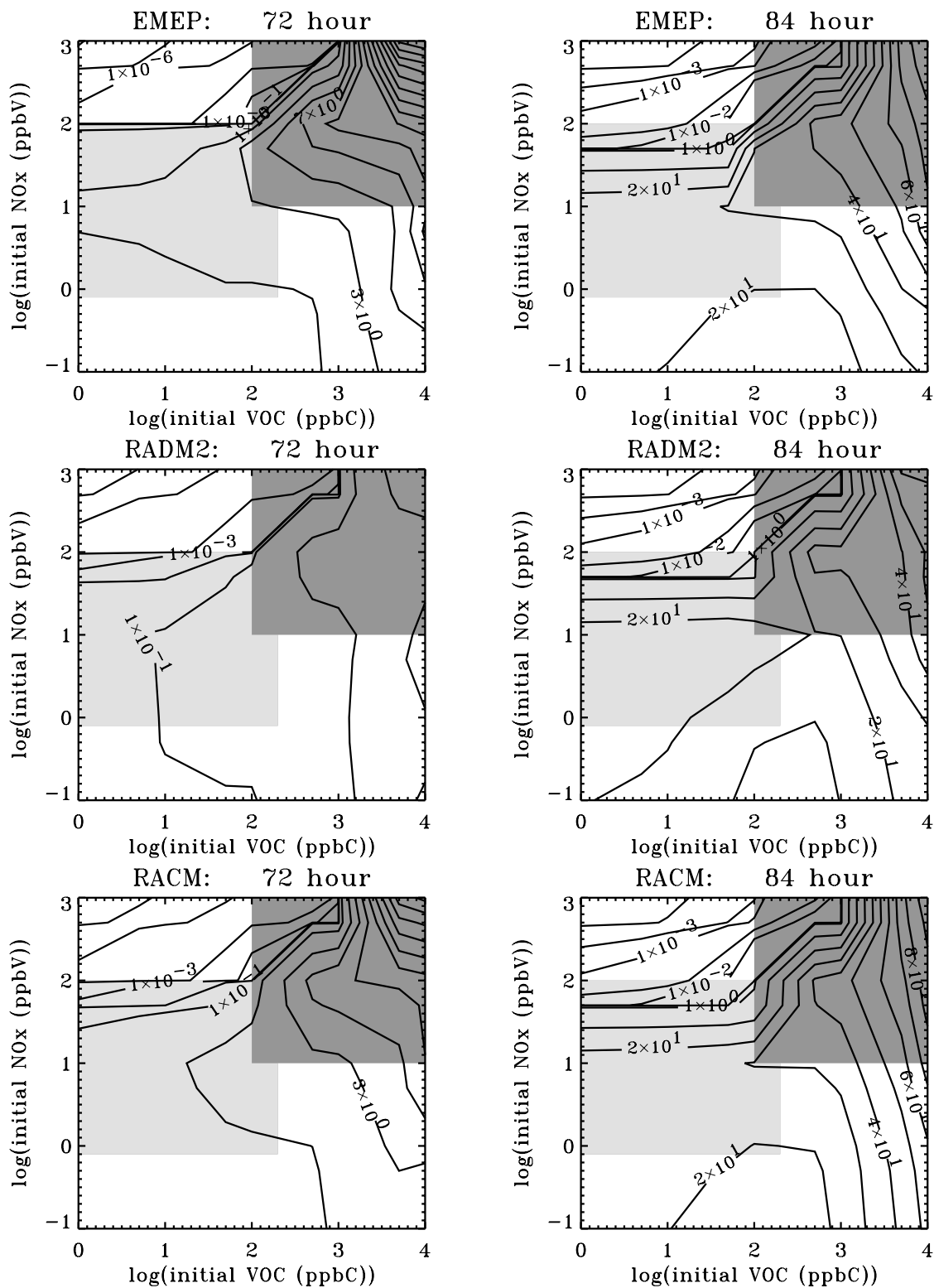


Figure E.10: Isopleths of the HO₂ concentration (in pptV) obtained from the EMEP, RADM2 and RACM MCHs after hour 72 (nighttime) and 84 (daytime). The plots are based on 81 zero-dimensional box model simulations as described in Tables 1.1 and 1.2. Contour levels are 1e-8, 1e-7, 1e-6, 1e-4, 1e-3, 1e-2, 1e-1, 1, 3, 5, 7, 9, 11, 13, 15, 17, 19, 21, 23, 25, 27 and 29 for hour 72 plots, and 1e-4, 5e-4, 1e-3, 5e-3, 1e-2, 1e-1, 1, 10, 20, 30, 40, 50, 60, 70, 80 and 90 for hour 84 plots. VOC represents anthropogenic non-methane VOC. For a definition of the light and dark gray areas, see the figure caption for Figure 1.4.

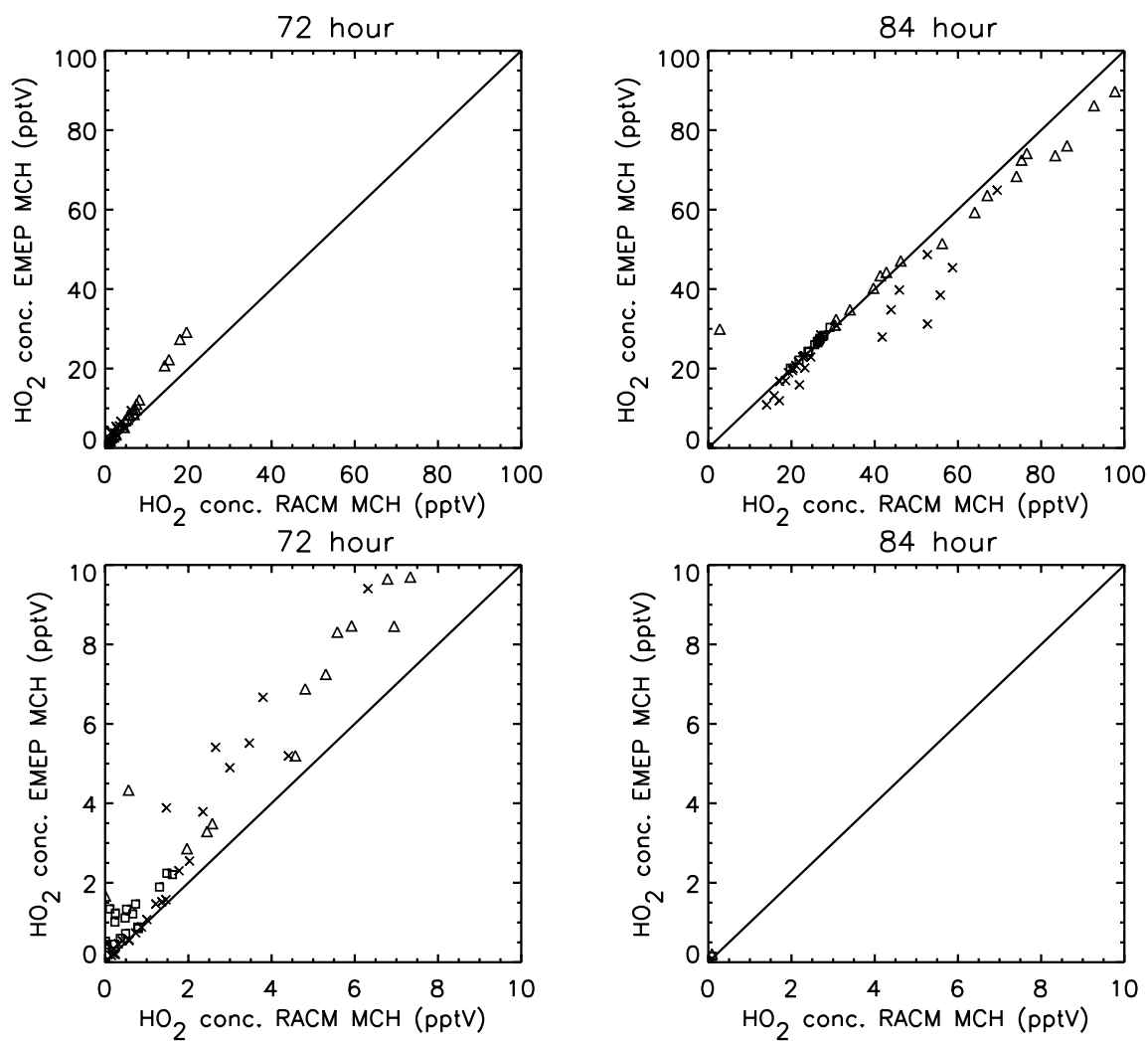


Figure E.11: Scatter plots for the HO₂ concentration between the RACM and EMEP MCHs for the 81 zero-dimensional box model simulations as described in Tables 1.1 and 1.2 after hour 72 (nighttime) and 84 (daytime). □: rural, △: urban and ×: neither rural nor urban. The definition of urban and rural is according to the light and dark gray areas described in the caption for Figure 1.4. Note that the lower plots are zoom-ins of the upper plots.

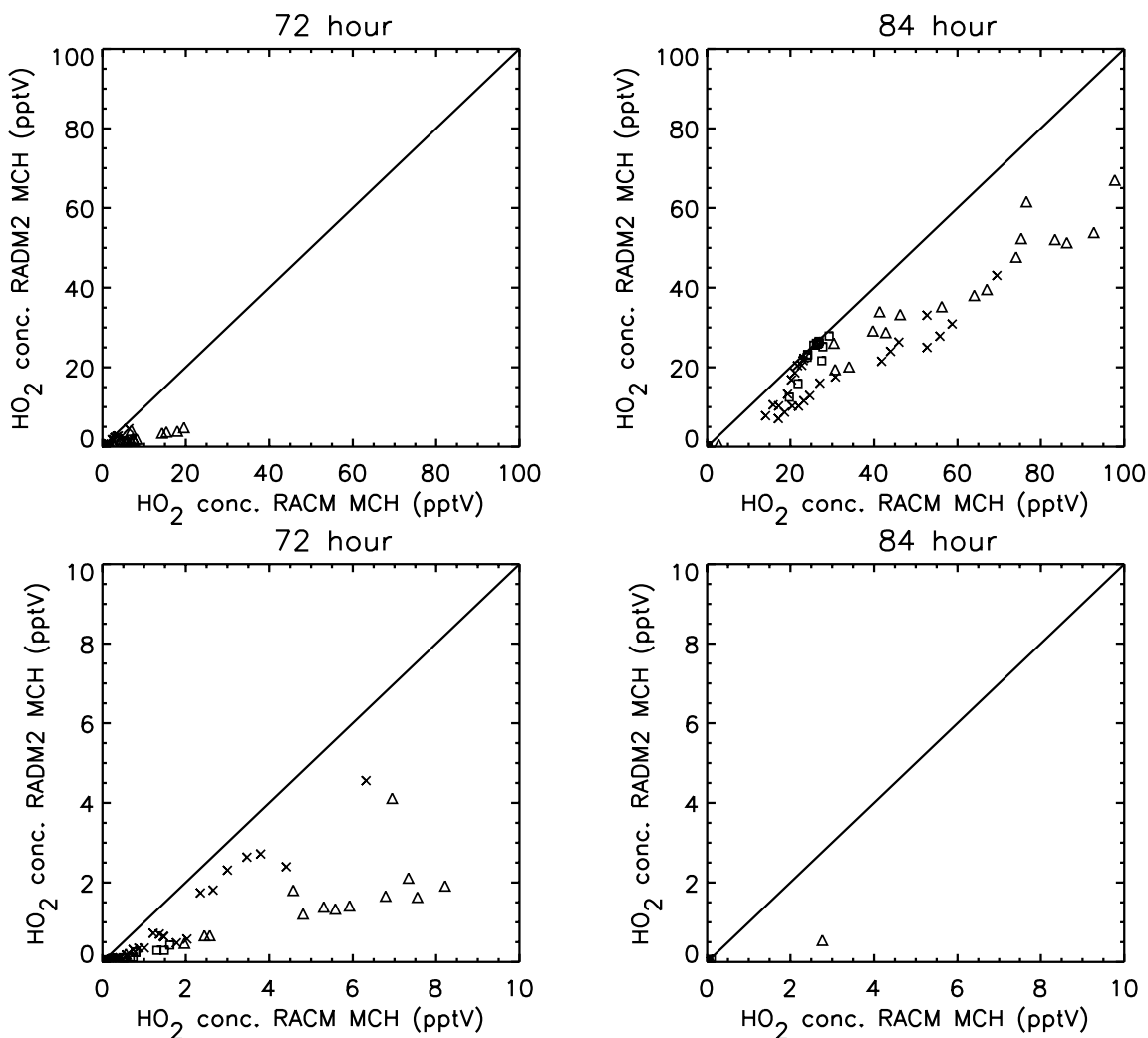


Figure E.12: Scatter plots for the HO₂ concentration between the RACM and RADM2 MCHs for the 81 zero-dimensional box model simulations as described in Tables 1.1 and 1.2 after hour 72 (nighttime) and 84 (daytime). □: rural, △: urban and ×: neither rural nor urban. The definition of urban and rural is according to the light and dark gray areas described in the caption for Figure 1.4. Note that the lower plots are zoom-ins of the upper plots.

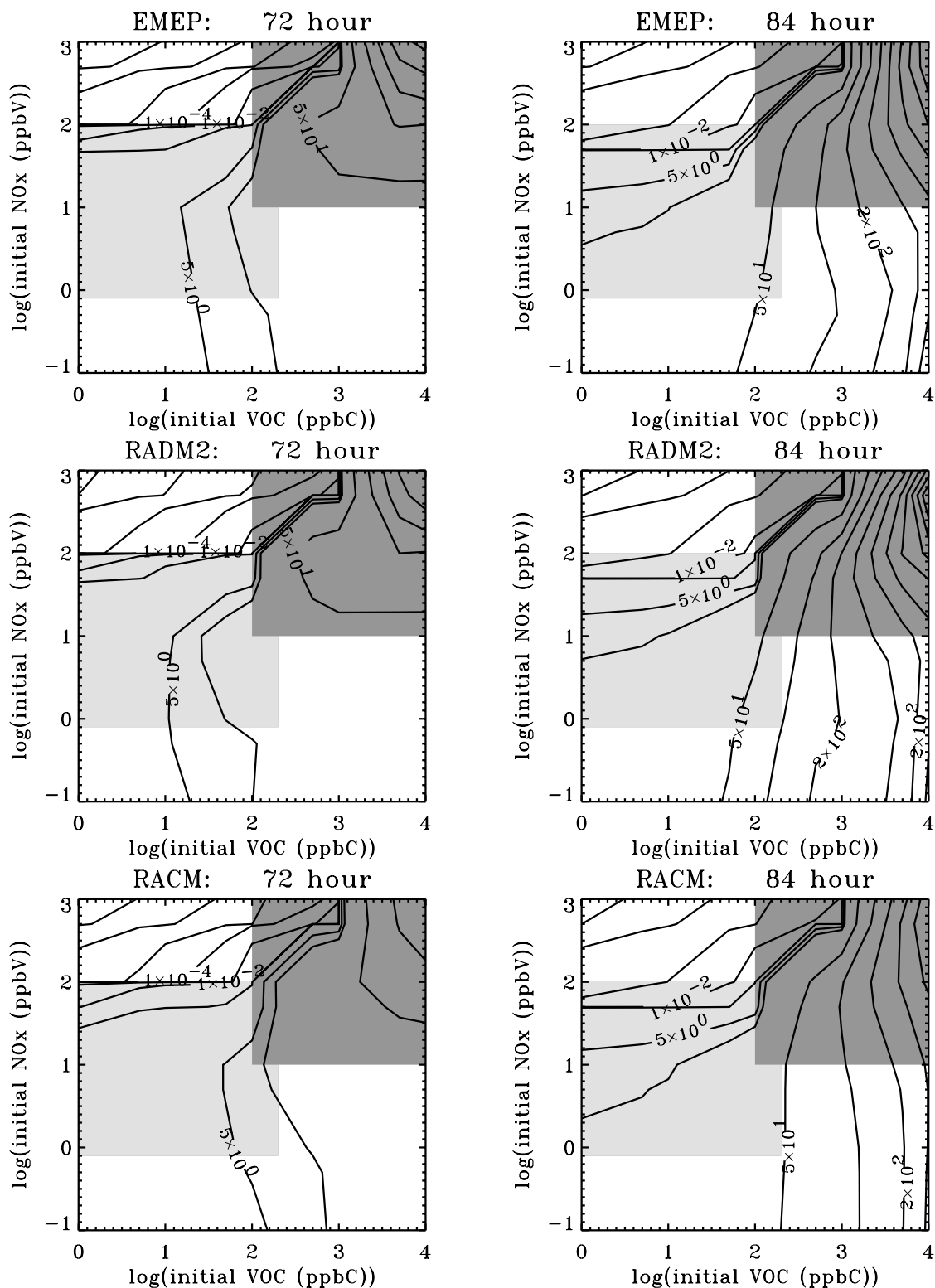


Figure E.13: Isopleths of the RO₂ concentration (in pptV) obtained from the EMEP, RADM2 and RACM MCHs after hour 72 (nighttime) and 84 (daytime). The plots are based on 81 zero-dimensional box model simulations as described in Tables 1.1 and 1.2. Contour levels are $1e-8$, $1e-7$, $1e-6$, $1e-5$, $1e-4$, $1e-3$, $1e-2$, $1e-1$, 5, 10, 50, 100, 150, 200, 250, 300, 350, 400, 450 and 500. VOC represents anthropogenic non-methane VOC. For a definition of the light and dark gray areas, see the figure caption for Figure 1.4.

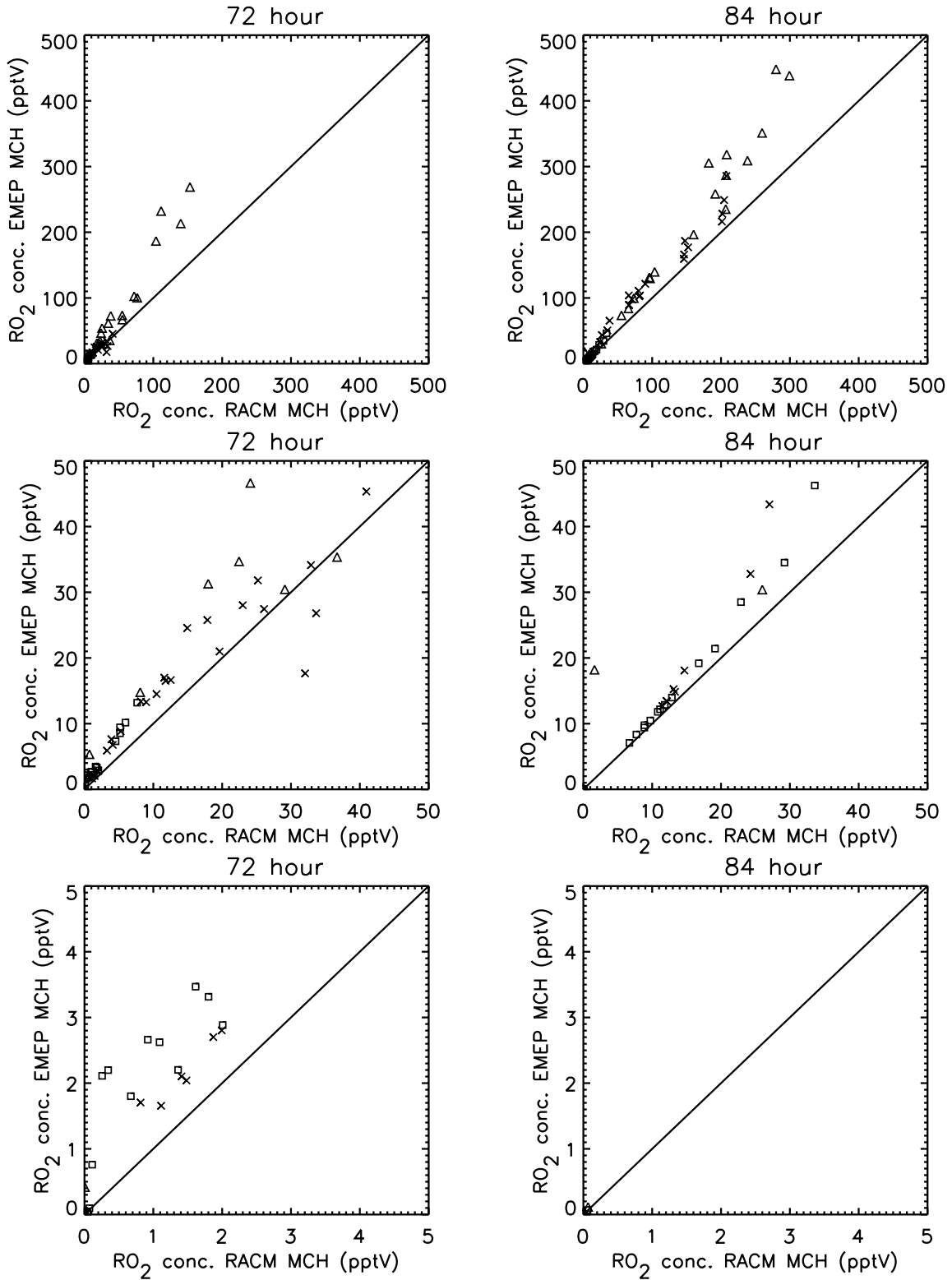


Figure E.14: Scatter plots for the RO₂ concentration between the RACM and EMEP MCHs for the 81 zero-dimensional box model simulations as described in Tables 1.1 and 1.2 after hour 72 (nighttime) and 84 (daytime). □: rural, △: urban and ×: neither rural nor urban. The definition of urban and rural is according to the light and dark gray areas described in the caption for Figure 1.4. Note that the lower plots are zoom-ins of the upper plots.

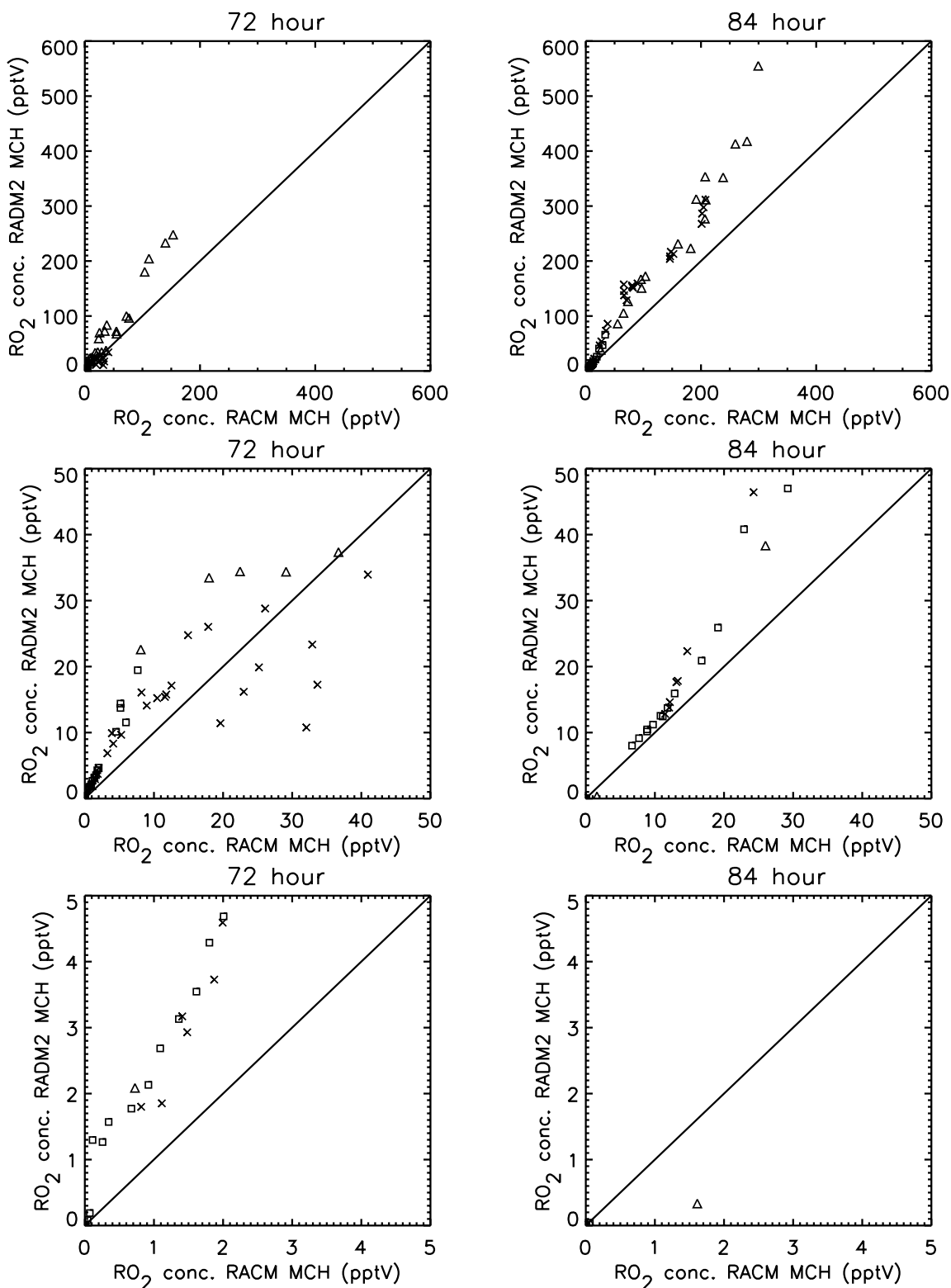


Figure E.15: Scatter plots for the RO_2 concentration between the RACM and RADM2 MCHs for the 81 zero-dimensional box model simulations as described in Tables 1.1 and 1.2 after hour 72 (nighttime) and 84 (daytime). \square : rural, \triangle : urban and \times : neither rural nor urban. The definition of urban and rural is according to the light and dark gray areas described in the caption for Figure 1.4. Note that the lower plots are zoom-ins of the upper plots.

Appendix F

3-Dimensional Simulations

In this appendix time series of measured data and calculated surface ozone concentrations at 25 different locations in Europe for the period August 11 to August 25 1995 are shown.

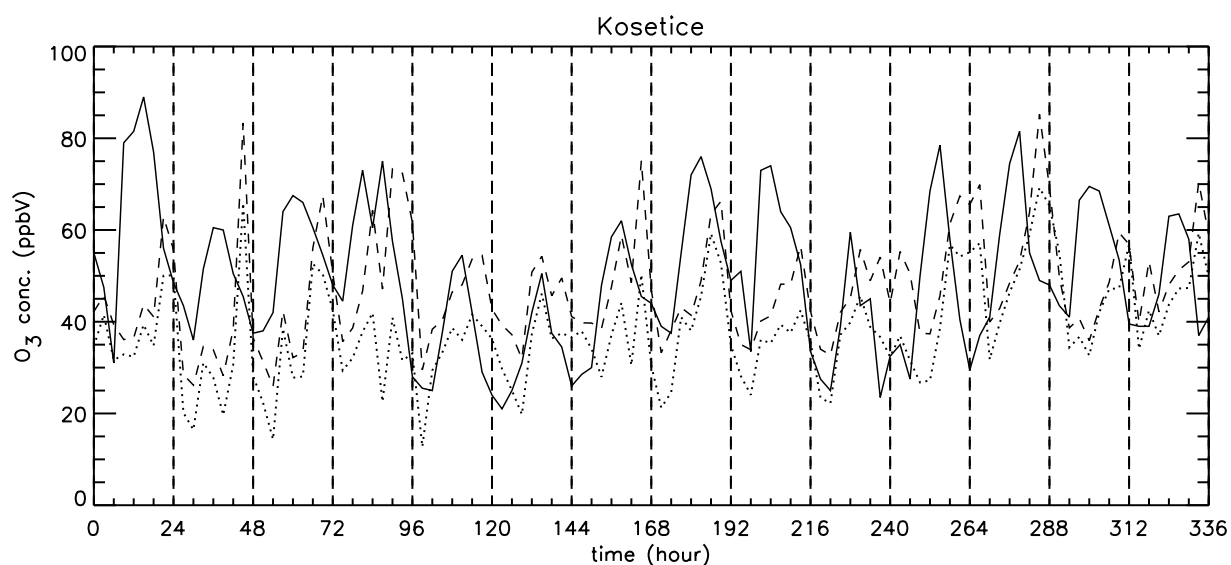


Figure F.1: Model and observed ozone concentrations for the period August 11 to August 24 1995. Measured data is the solid line, DACFOS's results the dotted line, and the MOON model the dashed line.

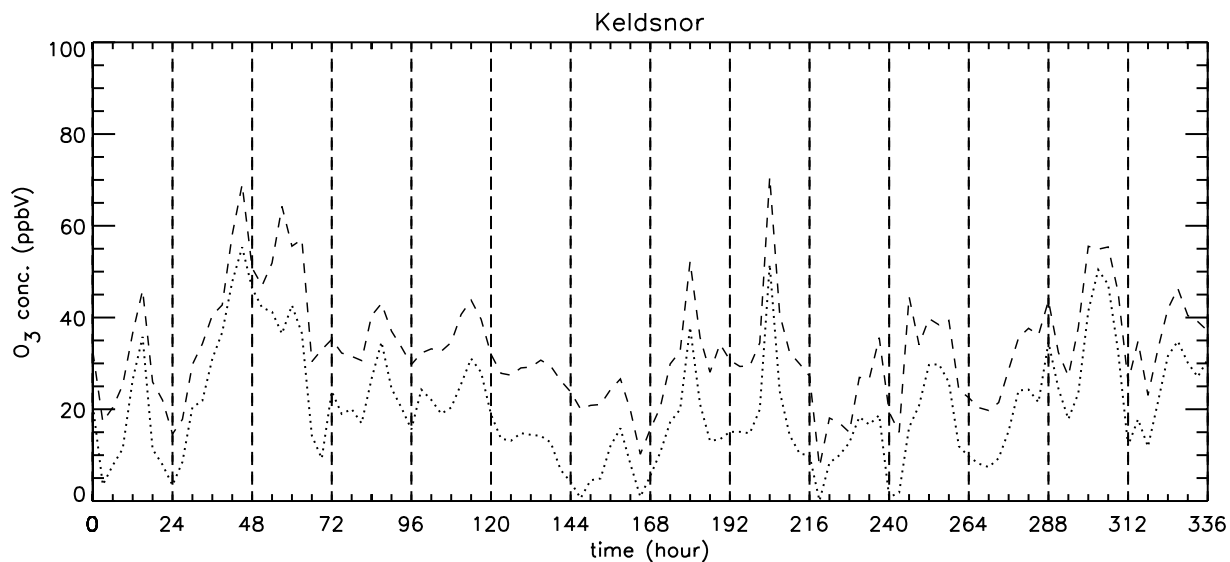


Figure F.2: Model ozone concentrations for the period August 11 to August 24 1995. DACFOS's results is the dotted line, and the MOON model the dashed line.

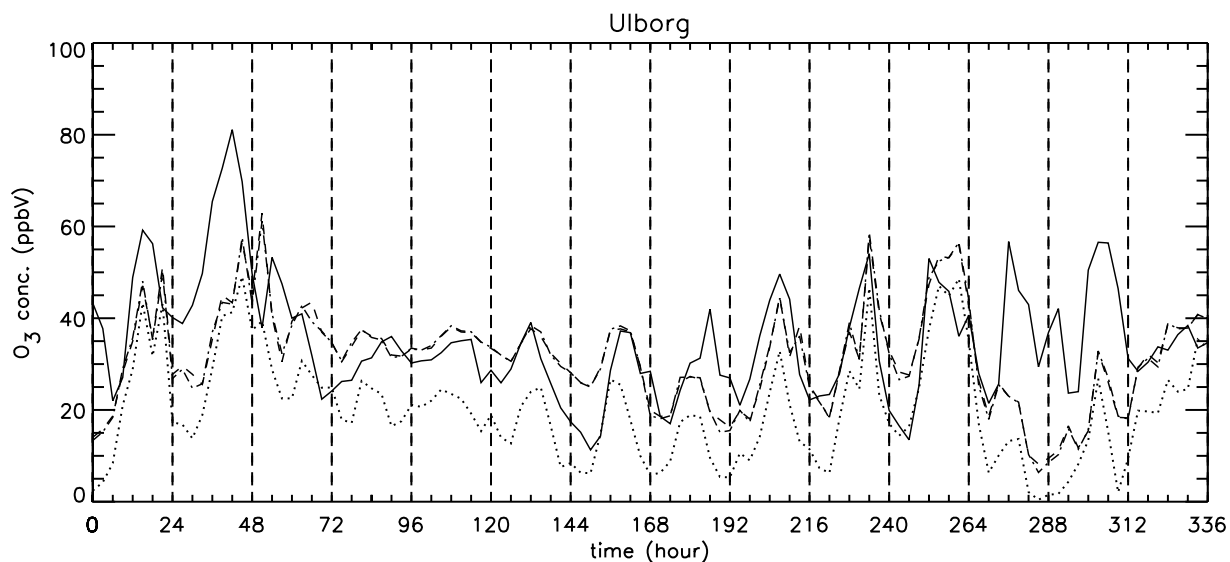


Figure F.3: Model and observed ozone concentrations for the period August 11 to August 24 1995. Measured data is the solid line, DACFOS's results the dotted line, and the MOON model the dashed line.

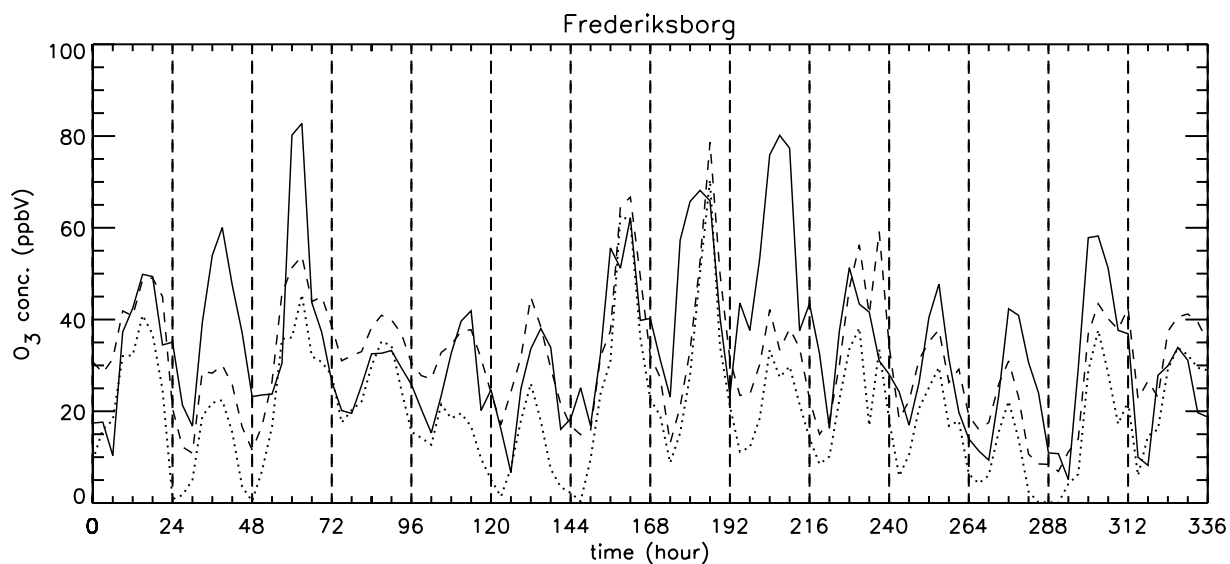


Figure F.4: Model and observed ozone concentrations for the period August 11 to August 24 1995. Measured data is the solid line, DACFOS's results the dotted line, and the MOON model the dashed line.

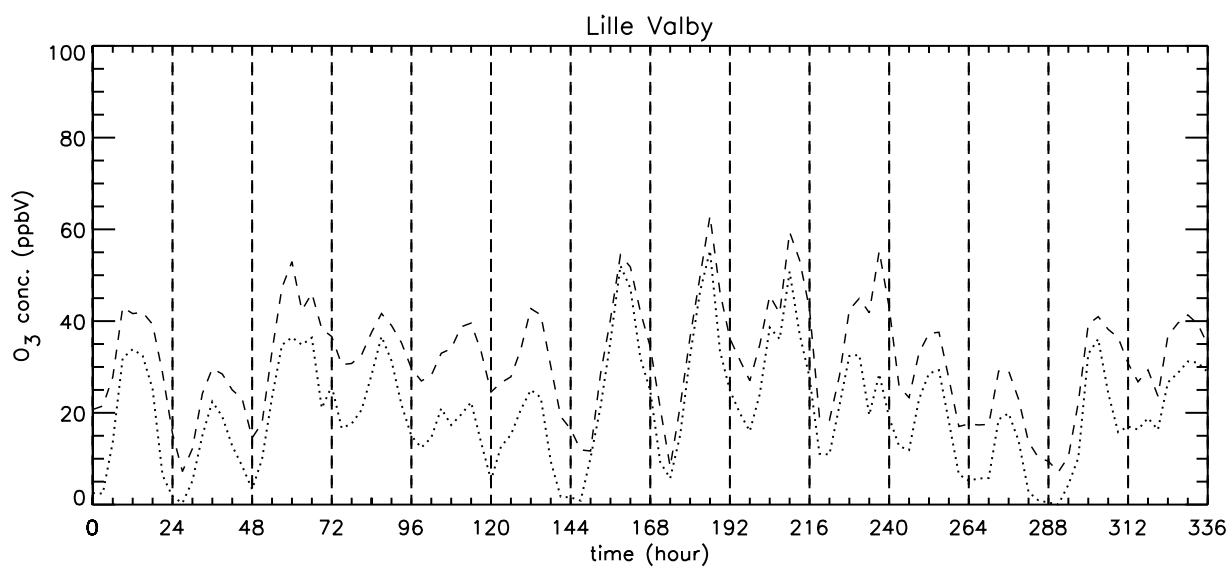


Figure F.5: Model ozone concentrations for the period August 11 to August 24 1995. DACFOS's results is the dotted line, and the MOON model the dashed line.

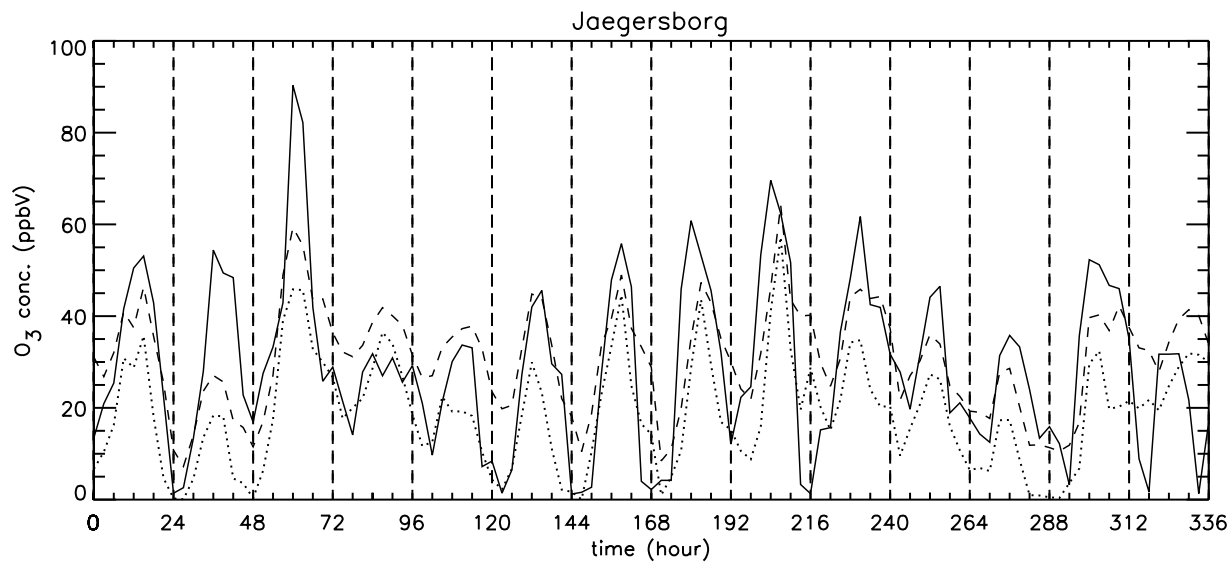


Figure F.6: Model and observed ozone concentrations for the period August 11 to August 24 1995. Measured data is the solid line, DACFOS's results the dotted line, and the MOON model the dashed line.

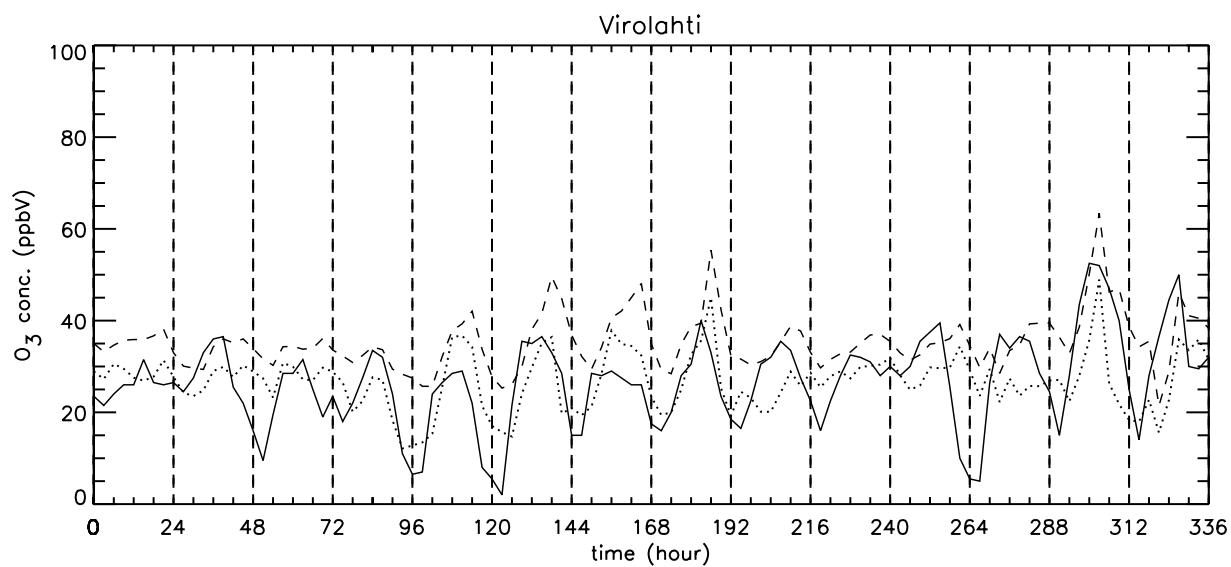


Figure F.7: Model and observed ozone concentrations for the period August 11 to August 24 1995. Measured data is the solid line, DACFOS's results the dotted line, and the MOON model the dashed line.

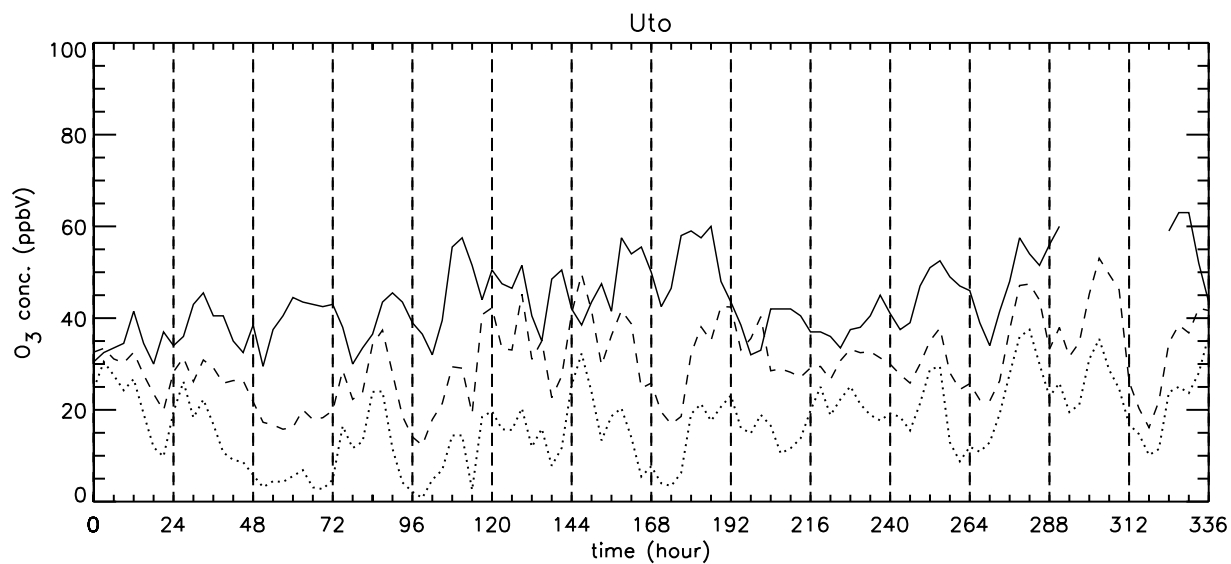


Figure F.8: Model and observed ozone concentrations for the period August 11 to August 24 1995. Measured data is the solid line, DACFOS's results the dotted line, and the MOON model the dashed line.

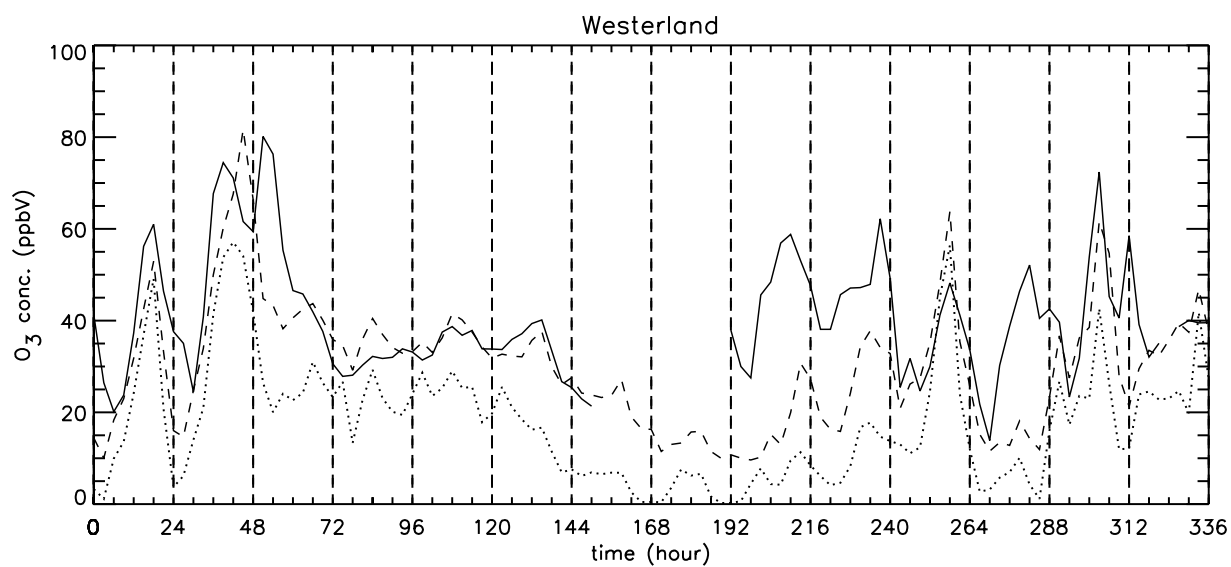


Figure F.9: Model and observed ozone concentrations for the period August 11 to August 24 1995. Measured data is the solid line, DACFOS's results the dotted line, and the MOON model the dashed line.

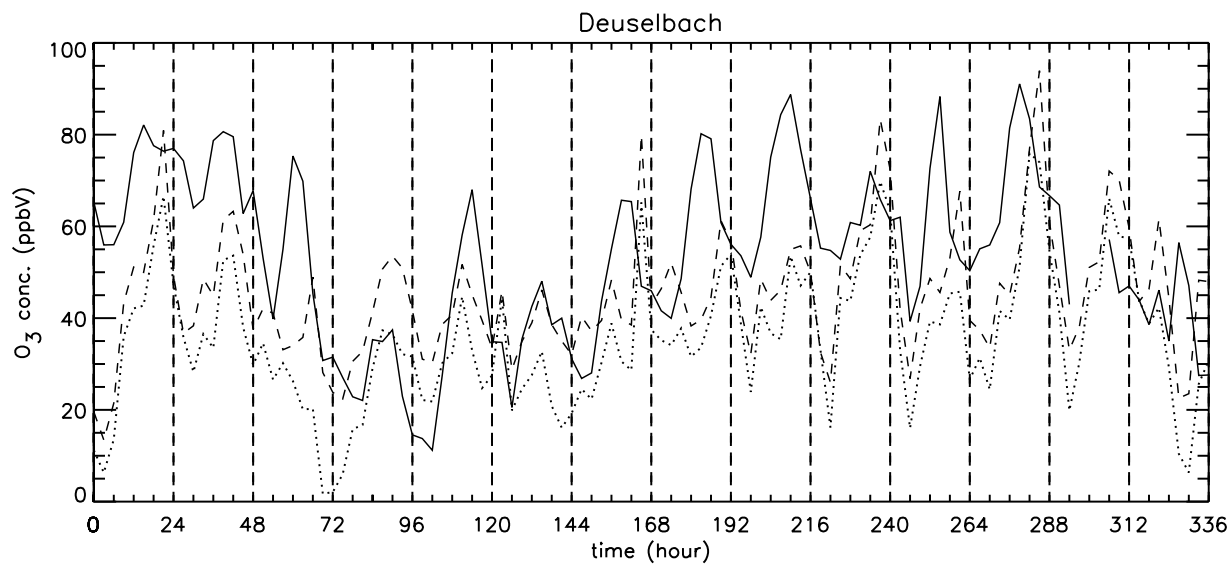


Figure F.10: Model and observed ozone concentrations for the period August 11 to August 24 1995. Measured data is the solid line, DACFOS's results the dotted line, and the MOON model the dashed line.

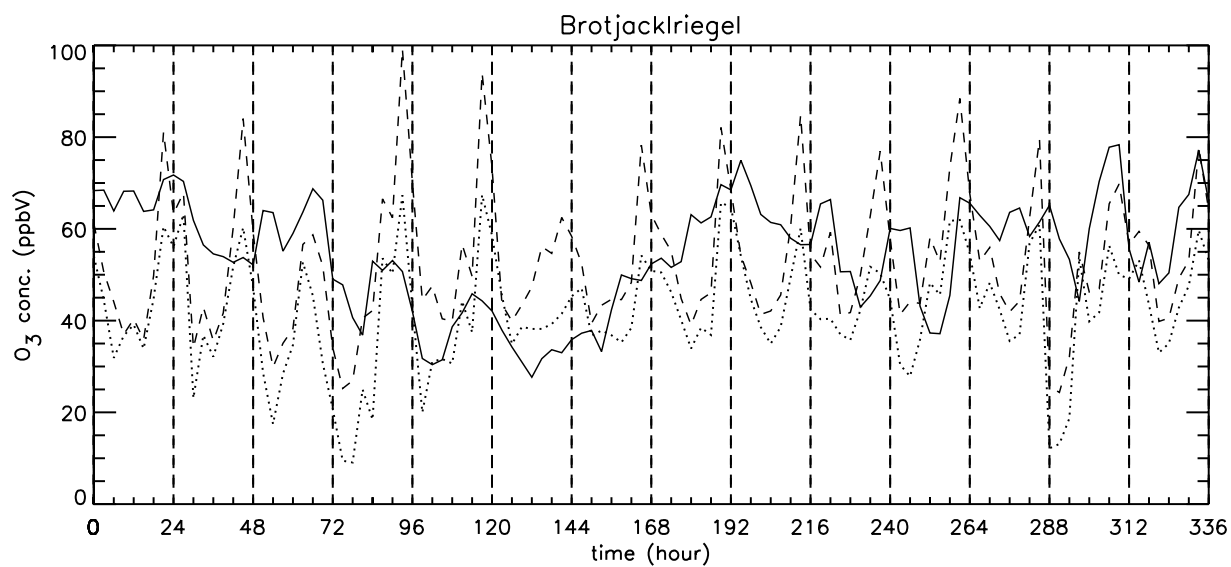


Figure F.11: Model and observed ozone concentrations for the period August 11 to August 24 1995. Measured data is the solid line, DACFOS's results the dotted line, and the MOON model the dashed line.

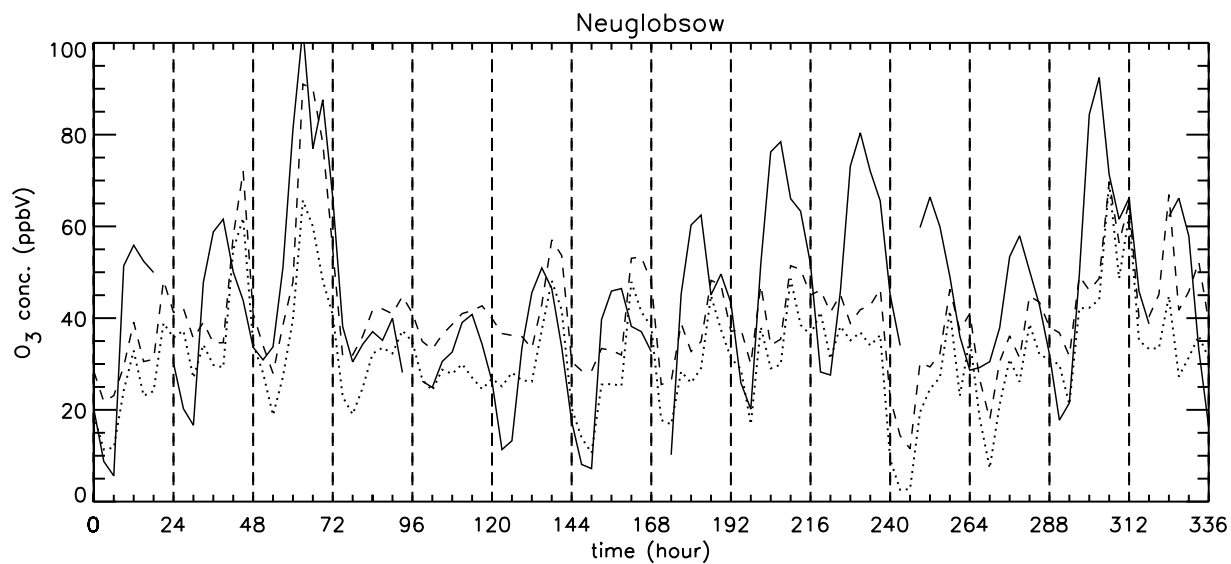


Figure F.12: Model and observed ozone concentrations for the period August 11 to August 24 1995. Measured data is the solid line, DACFOS's results the dotted line, and the MOON model the dashed line.

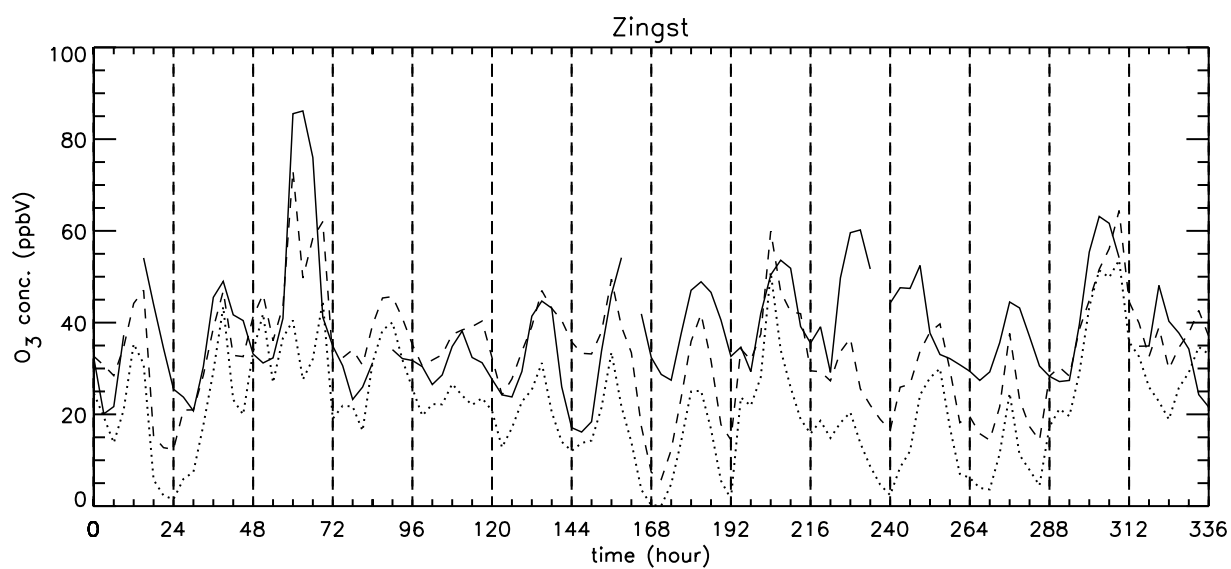


Figure F.13: Model and observed ozone concentrations for the period August 11 to August 24 1995. Measured data is the solid line, DACFOS's results the dotted line, and the MOON model the dashed line.

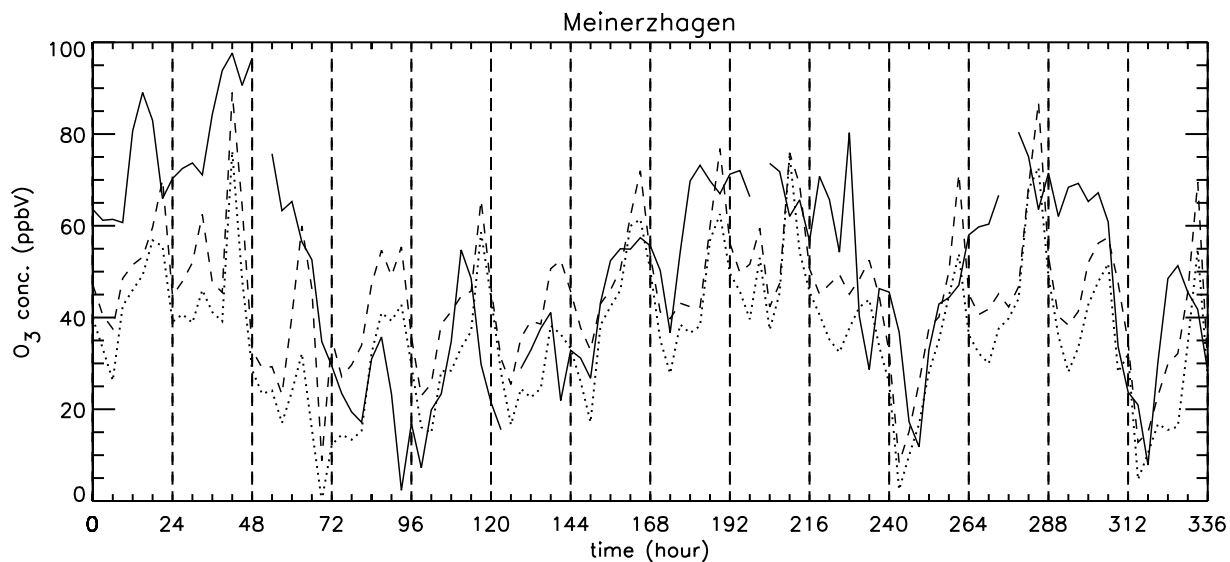


Figure F.14: Model and observed ozone concentrations for the period August 11 to August 24 1995. Measured data is the solid line, DACFOS's results the dotted line, and the MOON model the dashed line.

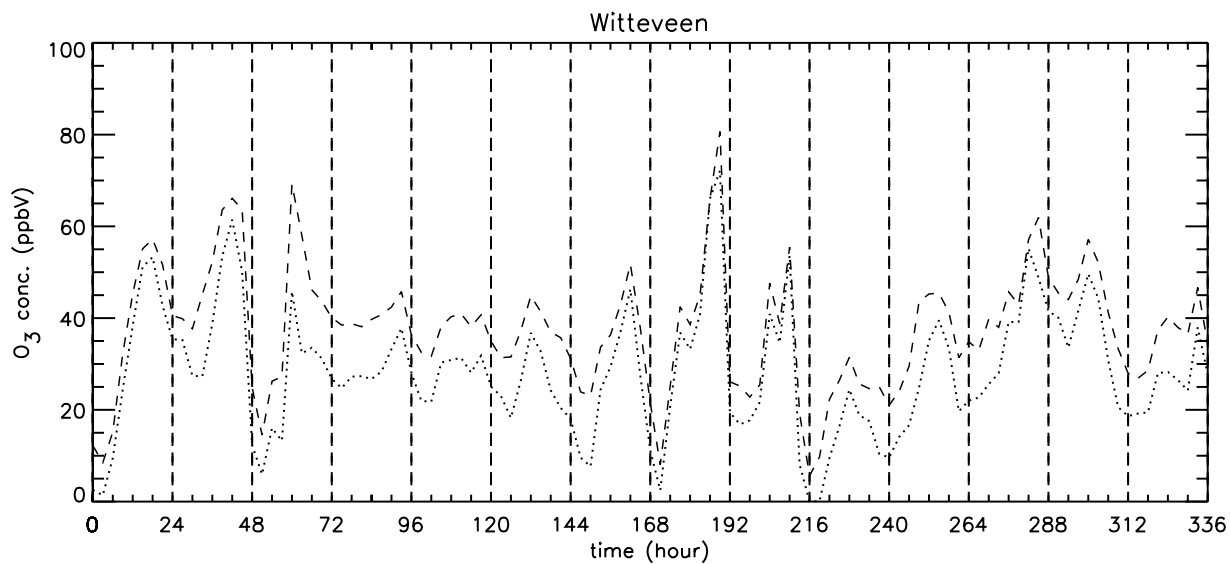


Figure F.15: Model ozone concentrations for the period August 11 to August 24 1995. DACFOS's results is the dotted line, and the MOON model the dashed line.

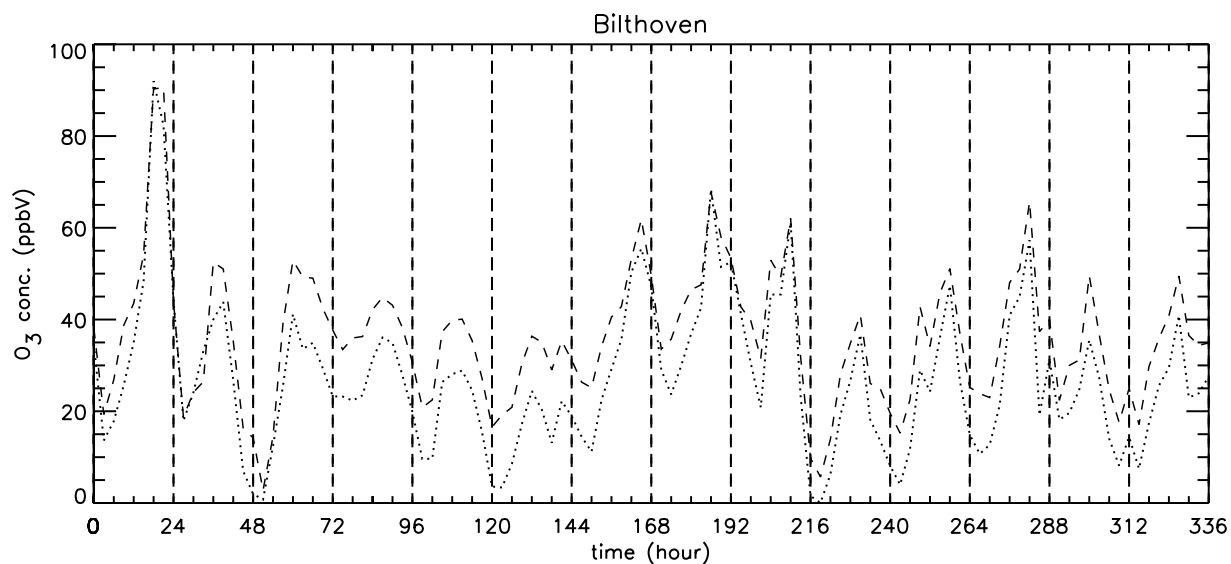


Figure F.16: Model ozone concentrations for the period August 11 to August 24 1995. DACFOS's results is the dotted line, and the MOON model the dashed line.

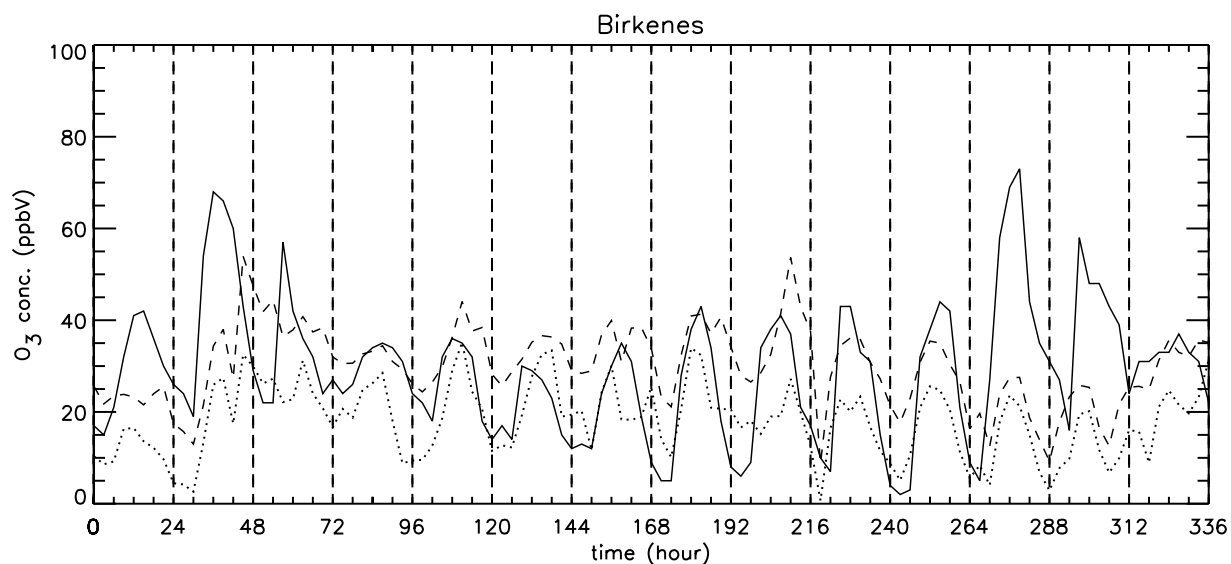


Figure F.17: Model and observed ozone concentrations for the period August 11 to August 24 1995. Measured data is the solid line, DACFOS's results the dotted line, and the MOON model the dashed line.

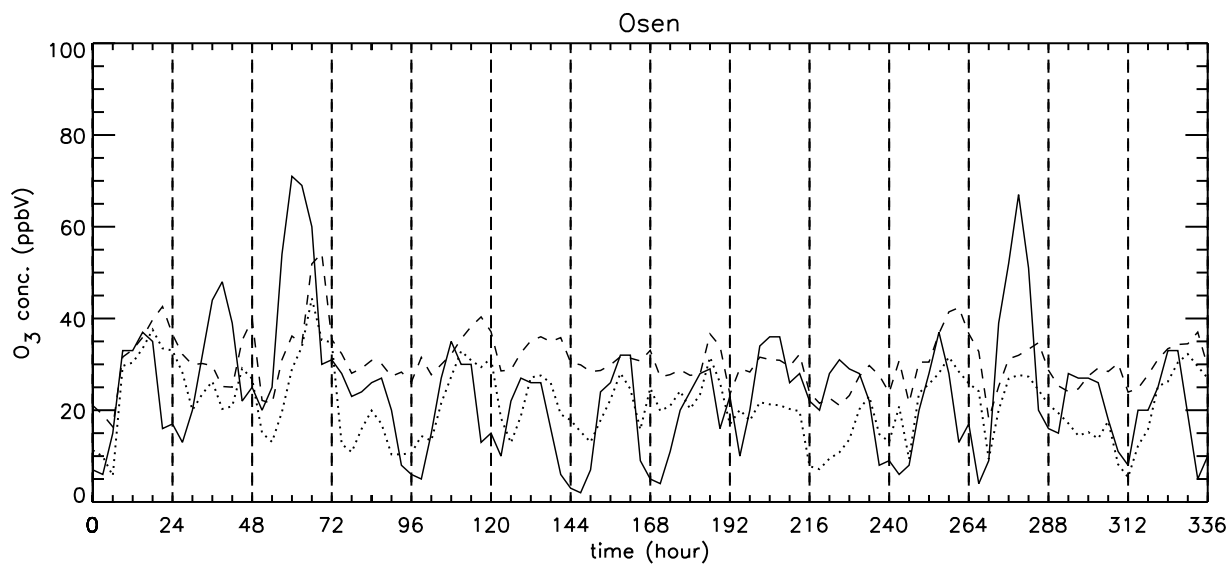


Figure F.18: Model and observed ozone concentrations for the period August 11 to August 24 1995. Measured data is the solid line, DACFOS's results the dotted line, and the MOON model the dashed line.

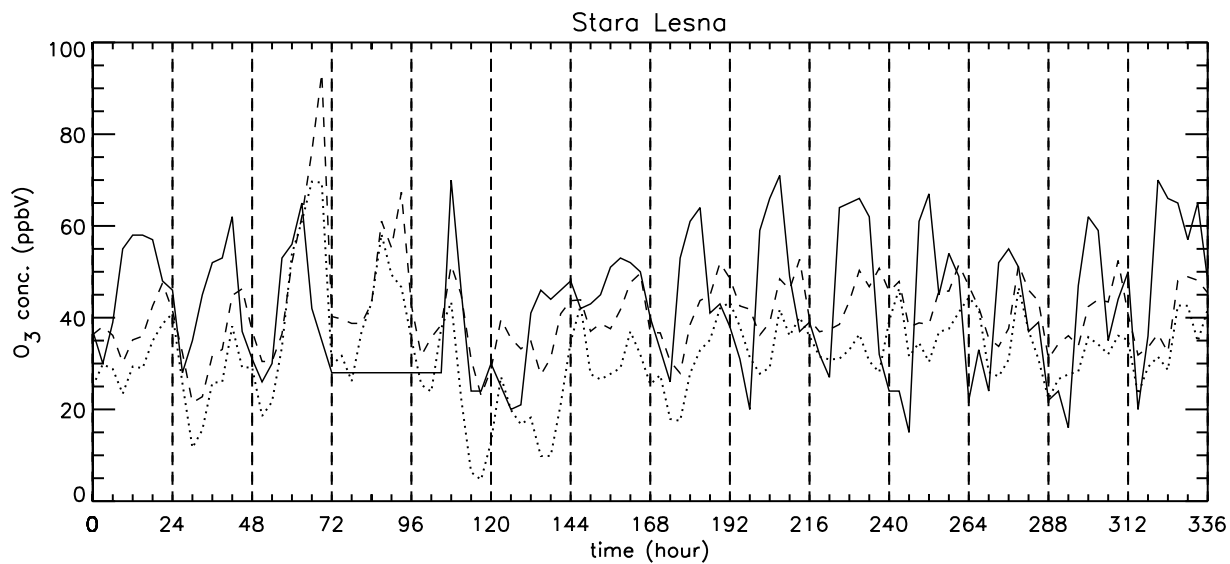


Figure F.19: Model and observed ozone concentrations for the period August 11 to August 24 1995. Measured data is the solid line, DACFOS's results the dotted line, and the MOON model the dashed line.

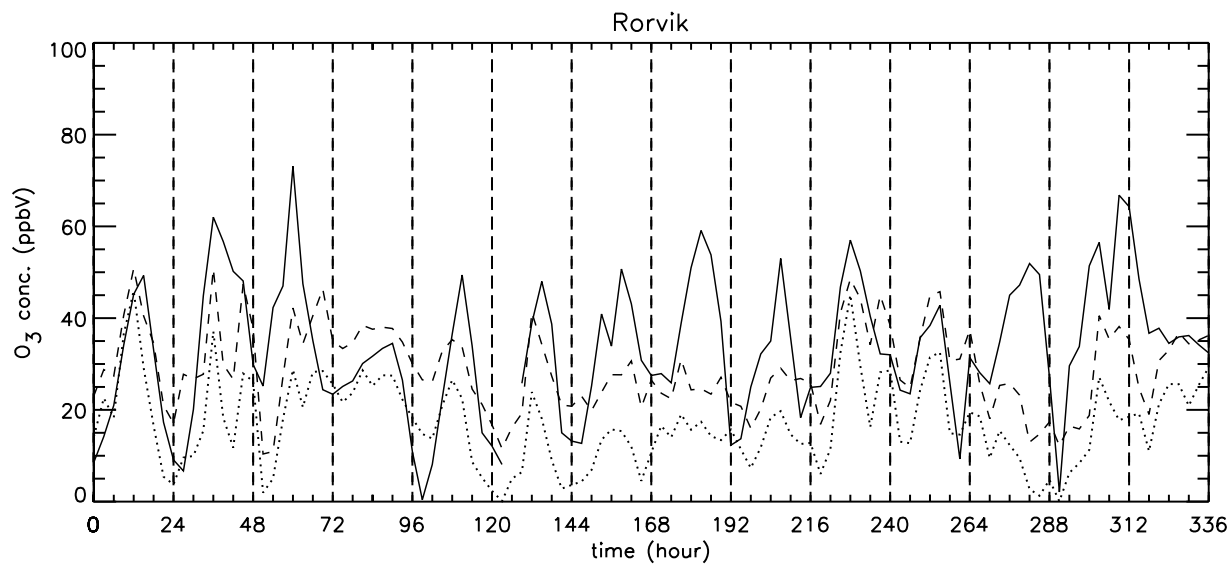


Figure F.20: Model and observed ozone concentrations for the period August 11 to August 24 1995. Measured data is the solid line, DACFOS's results the dotted line, and the MOON model the dashed line.

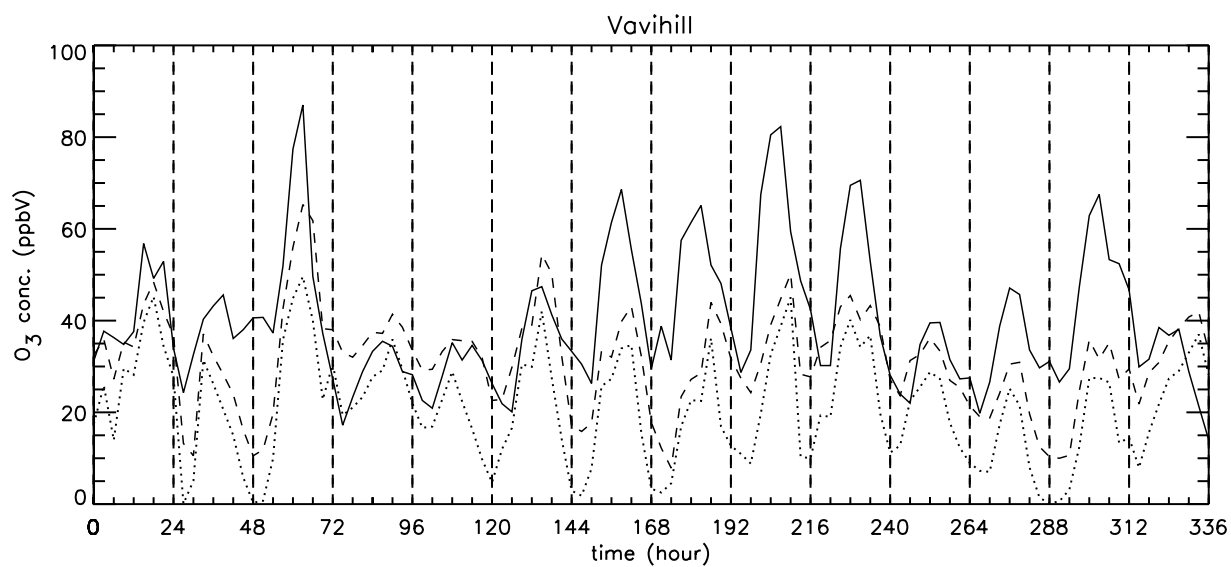


Figure F.21: Model and observed ozone concentrations for the period August 11 to August 24 1995. Measured data is the solid line, DACFOS's results the dotted line, and the MOON model the dashed line.

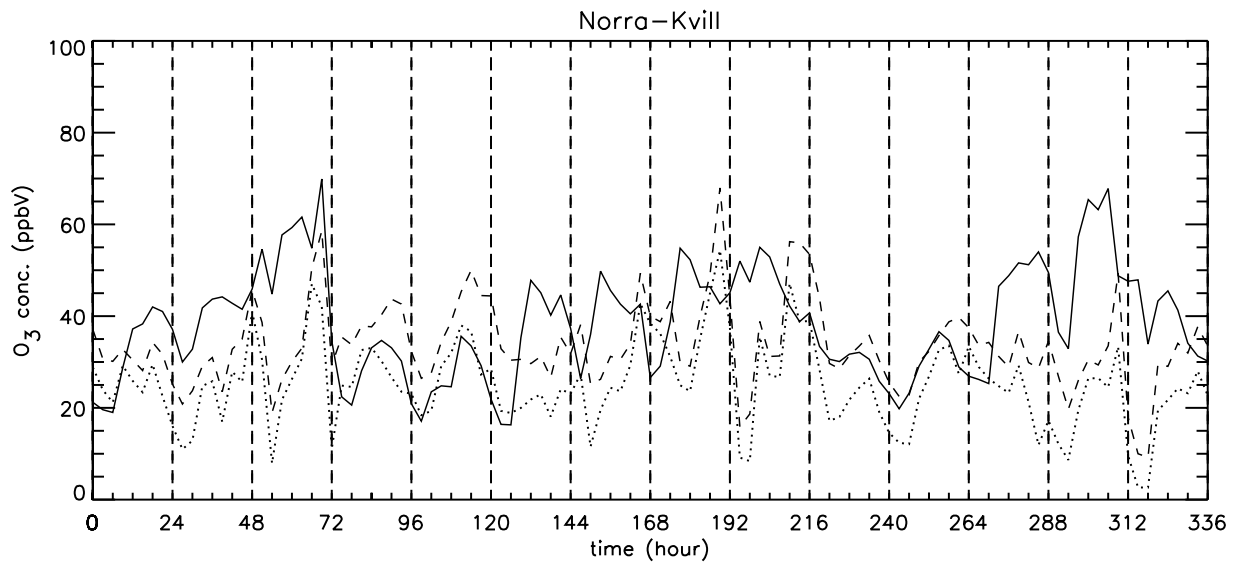


Figure F.22: Model and observed ozone concentrations for the period August 11 to August 24 1995. Measured data is the solid line, DACFOS's results the dotted line, and the MOON model the dashed line.

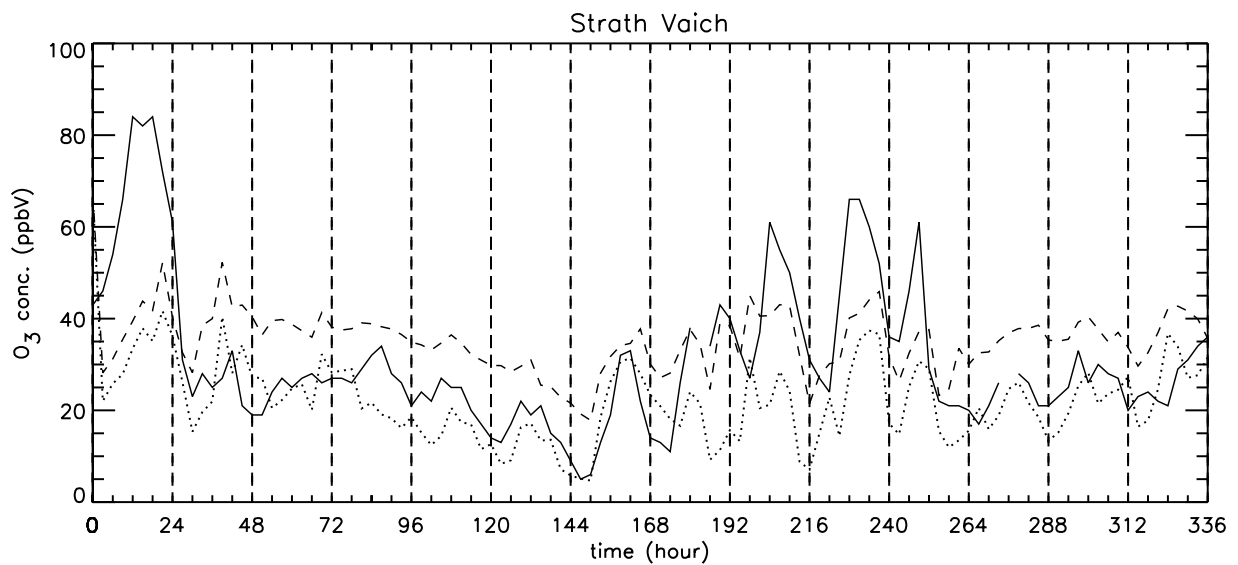


Figure F.23: Model and observed ozone concentrations for the period August 11 to August 24 1995. Measured data is the solid line, DACFOS's results the dotted line, and the MOON model the dashed line.

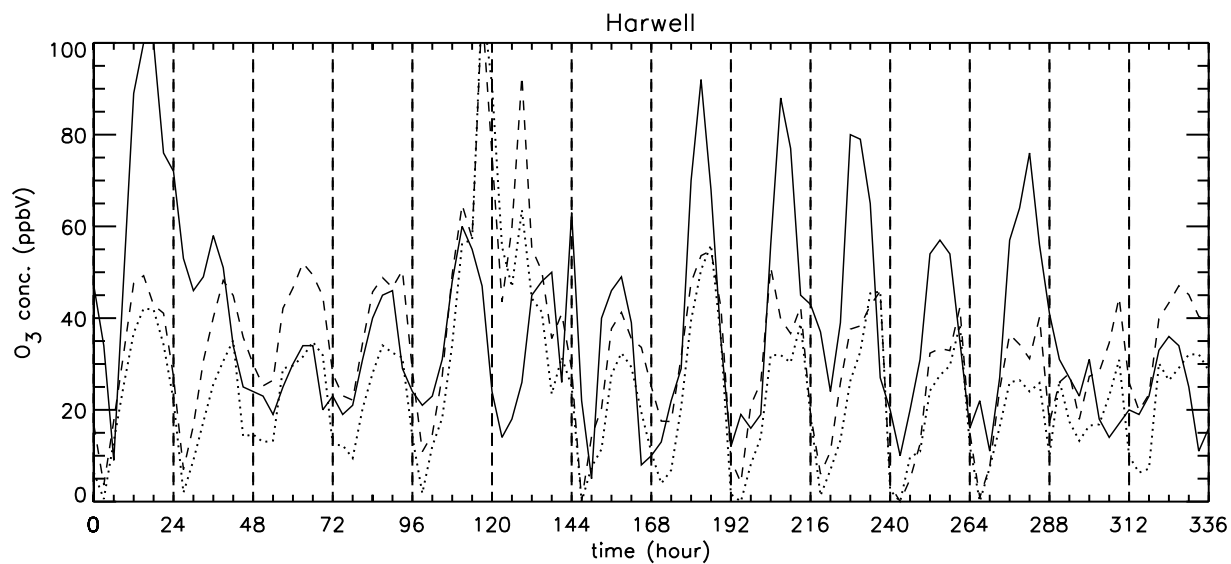


Figure F.24: Model and observed ozone concentrations for the period August 11 to August 24 1995. Measured data is the solid line, DACFOS's results the dotted line, and the MOON model the dashed line.

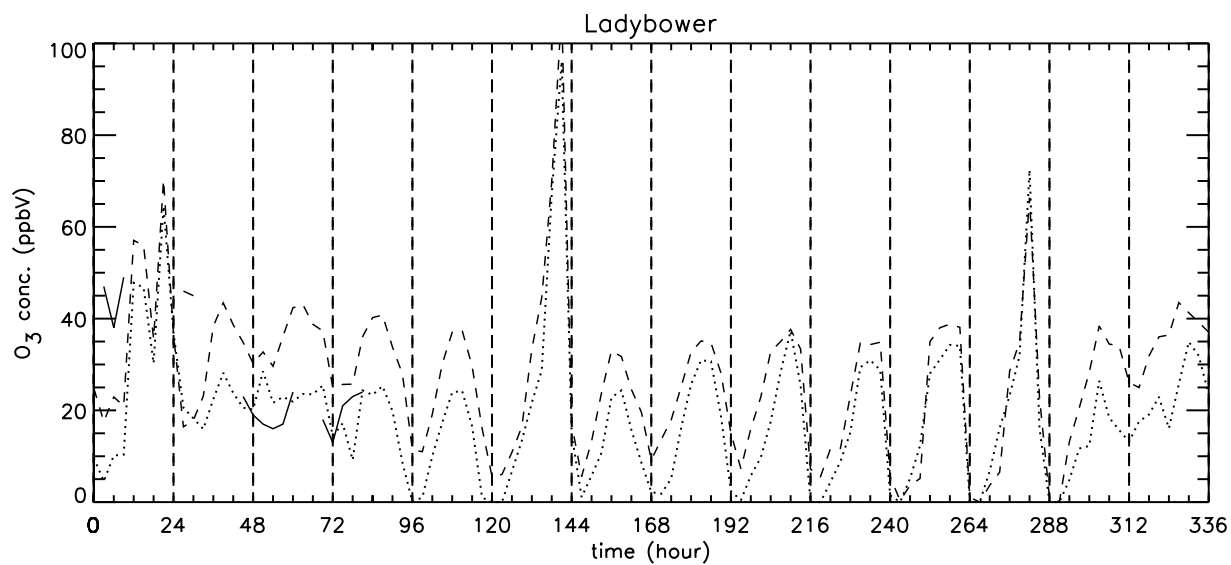


Figure F.25: Model and observed ozone concentrations for the period August 11 to August 24 1995. Measured data is the solid line, DACFOS's results the dotted line, and the MOON model the dashed line.

Appendix G

Titles and Abstracts of Articles

G.1 Tropospheric Chemistry

(Paper 1)

Comparison of the EMEP, RADM2 and RACM mechanisms

by

A. Gross and W.R. Stockwell

Submitted to Atm. Env.

abstract

A comparison of the EMEP, RADM2 and RACM mechanisms has been conducted. The comparison of the mechanisms has been made based on 3×81 simulations without emissions and 3×150 simulations with emissions of Volatile Organic Compounds (VOC), NO, NO₂, SO₂ and CO. These simulations cover rural to polluted scenarios.

The mechanisms were compared primarily on how they predict ozone concentrations and on their carbon conservation. The three mechanisms give very similar results for clean conditions but for polluted conditions the differences are more pronounced. In general the EMEP mechanism yields the most ozone and RADM2 yields the least. Despite expectations that the EMEP mechanism should be carbon conservative this was not a property of any of the mechanisms. The RACM mechanism was determined to be more carbon conservative than the RADM2 mechanism.

Key word index: Photochemical mechanisms; ozone; isopleths; carbon conservatism.

G.2 Theoretical Treatment of Elementary Chemical Reactions

(Paper 2)

Isotope effects on the Rate Constants for the Processes $O_2 + O \rightarrow O + O_2$ and $O_2 + O + Ar \rightarrow O_3 + Ar$ On a Modified Ground-State Potential Energy Surface for Ozone

by

A. Gross and G.D. Billing

Chem. Phys. **1997**, *217*, 1-18.

abstract

Rate constants for the formation of ozone $O_2(X, {}^3\Sigma_g^-) + O({}^3P) + Ar \rightarrow O_3(\tilde{X}, {}^1A_1) + Ar$ and the exchange reaction $O_2(X, {}^3\Sigma_g^-) + O({}^3P) \rightarrow O({}^3P) + O_2(X, {}^3\Sigma_g^-)$ have been calculated at 300 K for various isotopic oxygen atoms on a modified model potential energy surface (PES). The dynamics for both of the processes has been simulated using quasiclassical trajectories and importance sampling methods. Due to experience from previously performed calculations on the systems, we have modified the ground state PES for ozone obtained by Yamashita et al. (YMQ). To describe the Ar-(O₃) potential we used a pairwise additive potential for the Ar-O interaction from Ar-glyoxal.

(Paper 3)

A Phase-Space Method for Arbitrary Bi-Molecular
Gas-Phase Reactions: Theoretical Description

by

A. Gross, K.V. Mikkelsen and W.R. Stockwell

Submitted to J. Phys. Chem.

abstract

A theoretical model for the calculation of rate constants for arbitrary bi-molecular gas-phase reactions is developed. The method is based on the phase-space statistical method developed by Light and co-workers [1]-[6]. In the present paper this method is extended to arbitrary molecular systems. The new method requires knowledge of the molecular properties in the reaction and products channels of the chemical system. The properties are the vibrational frequencies, the moments of inertia and the potential energies for the interacting species in their ground state equilibrium configuration. Furthermore, we have to calculate either the energy barrier or the long-range potential for the chemical system (if the reaction channel does not have an energy barrier).

The usefulness of the method is that it can be applied to all bi-molecular reactions, ter-molecular reactions and even reactions of higher orders. Therefore, it can be applied to cases where rate constants of complex chemical reactions are required but reliable laboratory measurements or other means to estimate rate parameters are not yet possible. The only required information is knowledge of the identity of the species in the reactant and products channels. Even if spectroscopic data is not available for the reactants and products, it is possible to use electronic structure theory to calculate the required data.

(Paper 4)

A Phase-Space Method for Arbitrary Bi-Molecular
Gas-Phase Reactions: Application to the $\text{CH}_3\text{CHO} + \text{HO}$
and $\text{CH}_3\text{OOH} + \text{HO}$ reactions

by

A. Gross, K.V. Mikkelsen and W.R. Stockwell

Submitted to J. Phys. Chem.

abstract

A new method based upon phase-space methods presented in Ref. [1] has been tested on reaction $\text{CH}_3\text{CHO} + \text{HO} \rightarrow \text{CH}_3\text{CO} + \text{H}_2\text{O}$ and $\text{HO} + \text{CH}_3\text{OOH} \rightarrow$ products. The method has been used to calculate cross sections, and rate constants in the temperature range 200 K to 550 K. The method requires knowledge of the system's reaction and product channels for the interacting species, the vibrational frequencies, the moments of inertia and the potential energy in their ground state equilibrium configuration. Furthermore, the long-rang potential between the reactant and product species are required. Due to the lack of experimentally determined spectroscopic data and potential energies for the reactants and products, these values have been calculated using electronic structure theory. We have used many-body Second order Møller Plesset perturbation theory (MP2) for the treatment of electron correlation in the molecules together with two different Gaussian Type Orbital (GTO) basis sets 6-31G and 6-31G*. The calculated rates are compared with the experimental data estimated by Refs. [2]-[14].

On the basis of our limited tests the method appears to yield rate constants that within a factor of 10-25 at 300 K of the true value which is much more accurate than currently used empirical estimation methods.

G.3 Air Quality Modeling

(Paper 5)

Presentation and Validation of a Multi-Trajectory Vectorized Gear Model

by

A. Gross, J.H. Sørensen and W.R. Stockwell

In Preparation

abstract

A new Lagrangian transport-chemical model is discussed and verified against measurement from 25 sites in Europe for the period August 11 to August 24, 1995. The model is based on meteorological data from DMI-HIRLAM, the chemical, physical, and meteorological parameterization from the Lagrangian EMEP model, the Regional Atmospheric Chemistry Mechanism and calculated photolysis from a program developed by S. Madronich, NCAR. To solve the stiff chemical rate equations, a sparse-matrix, vectorized Gear algorithm (SMVGEAR) is used. The results are compared with measurement data and a QSSA based Lagrangian model using the EMEP mechanism. The main results are that the vectorized Gear based model improves the simulation results compared to the QSSA based model, and the vectorized Gear based model's performance time is sufficiently low that it can be used as an ozone forecasting model.

References

- [1] J. Staehelin, J. Thudium, R. Buehler, A. Volz-Thomas and W. Graber. *Atm. Env.* **1994**, *28*, 75.
- [2] J.H. Seinfeld. “*Atmospheric Chemistry and Physics of Air Pollution*”. *John Wiley & Sons, New York, U.S.* **1986**.
J.H. Seinfeld and S. N. Pandis. “*Atmospheric Chemistry and Physics. From Air Pollution to Climate Change*”. *John Wiley & Sons, New York, U.S.* **1997**.
- [3] EEC. “*Directive 92/72/EEC of September 21 on Ozone Air Pollution*”. *J. Europ. Commun.* **1992**, *L297/1*.
- [4] Web address – www.aqmd.gov/smog/o3trend.html.
- [5] I.S.A. Isaksen, Ø. Hov and E. Hesstvedt. *Environ. Sci. Technol.* **1978**, *12*, 1279.
- [6] J.F. Müller and G. Brasseur. *J. Geophys. Res.* **1995**, *100*, 16445.
- [7] R.G. Derwent, A.J. Apling, M.R. Ashmore, D.J. Ball, P.A. Clark, A.T. Cocks, R.A. Cox, D. Fowler, M. Gay, R.M. Harrison, G.J. Jenkins, P.J.A. Kay, D.P.H. Laxen, A. Martin. D. McKenna, S.A. Penkett, M.L. Williams and P.J. Woods. “*Ozone in the United Kingdom*”. *Report of the United Kingdom Photochemical Oxidants Review Group*.
- [8] Web address – www.ivl.se/Proj/Ostad/clover_s.htm.
- [9] Web address – www.ivl.se/Proj/Ostad/spruce_s.htm.
- [10] Web address – www.ivl.se/Proj/Ostad/wheat.htm.
Web address – www.ivl.se/Proj/Ostad/wheat_s.htm.
- [11] D. Fowler, G.J. Dollard, M.R. Ashmore, R.A. Cox, P.A. Clark, R.G. Derwent, R.M. Harrison, C.N. Hewitt, Ø. Hov, J.G. Irwin, D.P.H. Laxen, R.L. Maynard, S.A. Penkett, K.J. Weston, M.L. Williams and P.J. Woods. “*Ozone in the United Kingdom 1993*”. *Third Report of the United Kingdom Photochemical Oxidants Review Group*.
- [12] H. Svensmark. *DMI, Technical Report 95-5*. **1995**.
- [13] M.H. Jensen, A. Rasmussen, H. Svensmark and J.H. Sørensen, *DMI, Technical Report 96-3*. **1996**.
- [14] Web address – www.dmi.dk/vejrozon/smog.html.
- [15] J.H. Sørensen. *DMI, Technical Report 93-5*. **1993**.

- [16] D. Simpson. *Atm. Env.* **1992**, *26A*, 1609.
- [17] D. Simpson. *Atm. Env.* **1993**, *27A*, 921.
- [18] D. Simpson. *J. Geophys. Res.* **1995**, *100*, 22891.
- [19] J.R. Stedman and M.L. Williams. *Atm. Env.* **1992**, *26A*, 1271.
- [20] A.M. Hough and R.G. Derwent. *Atm. Env.* **1987**, *21*, 2015.
- [21] R.G. Derwent and M.E. Jenkin. *Atm. Env.* **1991**, *25A*, 1661.
- [22] O. Hertel, J. Christensen and Ø. Hov. *Atm. Env.* **1994**, *28*, 2431.
- [23] O. Hertel, J. Christensen, E.H. Runge, W.A.H. Asman, R. Berkowicz, M.F. Hovmand and Ø. Hov. *Atm. Env.* **1995**, *29*, 1267.
- [24] W.R. Stockwell. *Atm. Env.* **1986**, *20*, 1615.
- [25] M.E. Jenkin, S.M. Saunders and M.J. Pilling. *Atm. Env.* **1997**, *31*, 81.
Web address – www.chem.leeds.ac.uk:80/Atmospheric/MCM/mcmproj.html.
- [26] R.G. Derwent, M.E. Jenkin, S.M. Saunders and M.J. Pilling. *Atm. Env.* **1998**, *32*, 2429.
- [27] W.G. Mallard, F. Westley, J.T. Herron, R.F. Hampson and D.H. Fizzell. “*NIST Chemical Kinetics Database: Version 6.0*”. *Natl. Inst. of Stand. and Technol., Gaithersburg, Md.* **1994**.
- [28] R. Atkinson, D.L. Baulch, R.A. Cox, R.F. Hampson, J.A. Kerr M.J. Rossi and J. Troe. *J. Phys. Chem. Ref. Data.* **1997**, *26*, 521.
- [29] W.B. DeMore, S.P. Sander, D.M. Golden, R.F. Hampson, M.J. Kurylo, C.J. Howard, A.R. Ravishankara, C.E. Kolb and M.J. Molina. “*NASA Panel for Data Evaluation, Chemical Kinetics and Photochemical Data for Use in Stratospheric Modeling, Evaluation Number 12*”. *JPL Publication 97-4.* **1997**.
- [30] D. Simpson, K. Olendrzyński, A. Semb, E. Støren and S. Unger. *EMEP MSC-W Report 3/97.* **1997**.
D. Simpson, Norwegian Meteorological Institute, Norway. *Private communication*.
- [31] W.R. Stockwell, P. Middleton, J.S. Chang and X. Tang. *J. Geophys. Res.* **1990**, *95*, 16343.
- [32] W.R. Stockwell, F. Kirchner, M. Kuhn and S. Seefeld. *J. Geophys. Res.* **1997**, *102*, 25847.
- [33] F.W. Lurmann, A.C. Lloyd and R. Atkinson. *J. Geophys. Res.* **1986**, *91*, 10905.
- [34] M.W. Gery, G.Z. Whitten, J.P. Killus and M.C. Dodge. *J. Geophys. Res.* **1989**, *94*, 12925.
- [35] J.S. Chang, R.A. Brost, I.S.A. Isaksen, S. Madronich, P. Middleton, W.R. Stockwell and C.J. Walcek. *J. Geophys. Res.* **1987**, *92* 14681.

- J.S. Chang, F.S. Binkowski, N.L. Seaman, J.N. McHenry, P.J. Samson, W.R. Stockwell, C.J. Walcek, S. Madronich, P.B. Middleton, J.E. Pleim and H.H. Lansford. *"The Regional Acid Deposition Model and Engineering Model. State-of-Science/Technology"*. Report. National Acid Precipitation Assessment Program. Washington DC. **1989**.
- [36] G. Grell, W.R. Stockwell, T. Schoenemayer, J. Michalakes, R. Forkel and S. Emeis. *"A Coupled MM5/Chemistry Model"*. NCAR Workshop. **July 1997**.
- [37] Y. Andersson-Sköld and D. Simpson. *EMEP MSC-W Note 1/97*. **1997**.
- [38] D. Poppe, Y. Andersson-Sköld, A. Baart, P.J.H. Builtjes, M. Das, F. Fiedler, Ø. Hov, F. Kirchner, M. Kuhn, P.A. Makar, J.B. Milford, M.G.M. Roemer, R. Ruhnke, D. Simpson, W.R. Stockwell, A. Strand, B. Vogel and H. Vogel. *"Gas-Phase Reactions In Atmospheric Chemistry and Transport Models: A Model Intercomparison"*. EUROTRAC-report. **February 1996**.
- M. Kuhn, P.J.H. Builtjes, D. Poppe, D. Simpson, W.R. Stockwell, Y. Andersson-Sköld, A. Baart, M. Das, F. Fiedler, Ø. Hov, F. Kirchner, P.A. Makar, J.B. Milford, M.G.M. Roemer, R. Ruhnke, A. Strand, B. Vogel and H. Vogel. *Atm. Env.* **1998**, *32*, 693.
- [39] H. Hass, A. Ebel, H. Feldmann, H.J. Jakobs and M. Memmesheimer. *Atm. Env.* **1993**, *27A*, 867.
- [40] B. Vogel, F. Fiedler and H. Vogel. *J. Geophys. Res.* **1995**, *100*, 22907.
- [41] H. Hass, P.J.H. Builtjes, D. Simpson, R. Stern, H.J. Jakobs, M. Memmesheimer, G. Piekorz, M. Roemer, P. Esser and E. Reimer. *"Comparison of Photo-oxidant Dispersion Model Results"*. EUROTRAC-report. **February 1996**.
- [42] W.P. Carter. *Atm. Env.* **1990**, *24A*, 481.
- [43] G. Li and H. Rabitz. *Chem. Eng. Sci.* **1989**, *44*, 1413.
G. Li and H. Rabitz. *Chem. Eng. Sci.* **1990**, *45*, 977.
G. Li and H. Rabitz. *Chem. Eng. Sci.* **1991**, *46*, 95.
G. Li and H. Rabitz. *Chem. Eng. Sci.* **1991**, *46*, 583.
G. Li and H. Rabitz. *Chem. Eng. Sci.* **1991**, *46*, 2041.
G. Li and H. Rabitz. *Chem. Eng. Sci.* **1993**, *48*, 1903.
G. Li and H. Rabitz. *Chem. Eng. Sci.* **1994**, *49*, 343.
G. Li, A.S. Tomlin, H. Rabitz and J. Tóth. *J. Chem. Phys.* **1993**, *99*, 3562.
G. Li, A.S. Tomlin, H. Rabitz and J. Tóth. *J. Chem. Phys.* **1994**, *101*, 1172.
A.S. Tomlin, G. Li, H. Rabitz and J. Tóth. *J. Chem. Phys.* **1994**, *101*, 1188.
G. Li and H. Rabitz. *J. Chem. Phys.* **1995**, *102*, 7006.
- [44] D.L. Chapmann and L.K. Underhill. *J. Chem. Soc. Trans.* **1913**, *103*, 496.
- [45] M.Z. Bodenstein. *Z. Phys. Chem.* **1913**, *85*, 329.
- [46] N.N. Semenov. *J. Chem. Phys.* **1939**, *17*, 683.
- [47] E. Hesstvedt, Ø. Hov and I.S.A. Isaksen. *Int. J. Chem. Kinet.* **1978**, *10*, 971.

- [48] O. Hertel, R. Berkowicz, J. Christensen and Ø. Hov. *Atm. Env.* **1993**, 27A, 2591.
- [49] D.P. Chock, S.L. Winkler and P. Sun. *Environ. Sci. Technol.* **1994**, 28, 1882.
- [50] T. Turányi, A.S. Tomlin and M.J. Pilling. *J. Phys. Chem.* **1993**, 97, 163.
- [51] D.M. Hirst. “*A Computational Approach to Chemistry*”, 1st ed. Blackwell Scientific Publications. **1991**.
- [52] W.R. Stockwell. *SBOX (0-dimension gas-phase boxmodel using the Gear algorithm)*. Desert Research Institute, U.S. Private communication.
- [53] A. Gross and W.R. Stockwell. “*Comparison of the EMEP, RADM2 and RACM mechanisms*”. Submitted to *Atm. Env.* (**Paper 1**).
- [54] A.C. Hindmarsh. “*ODEPACK: A systematized collection of ODE solvers*. Ed. R.S. Stepleman, *IMACS Trans. on Scientific Computation, Vol. 1*”. Scientific Computing, North Holland, Amsterdam. **1983**.
Web address – netlib.bell-labs.com/netlib/odepack/index.html.
- [55] P.N. Brown, G.D. Bryne and A.C. Hindmarsh. *SIAM J. Sci. Stat. Comput.* **1989**, 10, 1038.
Web address – www.nea.tr/abs/html/ests0426.html.
- [56] M.Z. Jacobson and R.P. Turco. *Atm. Env.* **1994**, 28, 273.
M.Z. Jacobson. *Atm. Env.* **1995**, 29, 2541.
M.Z. Jacobson. *Atm. Env.* **1998**, 32, 791.
M.Z. Jacobson, Department of Civil Engineering, Stanford University, Stanford, California, U.S. Private communication.
- [57] A. Gross, J.H. Sørensen and W.R. Stockwell. “*Presentation and Validation of a Multi-Trajectory Vectorized Gear Model*”. In Preparation. (**Paper 5**).
- [58] A. Gross. “*A contribution to the Understanding of Ozone’s Chemistry*”. Master Thesis. **1995**.
- [59] A. Gross and G.D. Billing. *Chem. Phys.* **1997**, 217, 1. (**Paper 2**).
- [60] A. Gross and G.D. Billing. *Chem. Phys.* **1993**, 173, 393.
- [61] A. Gross and G.D. Billing. *Chem. Phys.* **1994**, 187, 329.
- [62] A. Gross, K.V. Mikkelsen and W.R. Stockwell. “*A Phase Space Method for Arbitrary Bi-Molecular Gas-Phase Reactions: Theoretical Description*”. Submitted to *J. Phys. Chem.* (**Paper 3**).
- [63] A. Gross, K.V. Mikkelsen and W.R. Stockwell. “*A Phase Space Method for Arbitrary Bi-Molecular Gas-Phase Reactions: Application to the CH₃CHO + HO and CH₃OOH + HO reactions*”. Submitted to *J. Chem. Phys.* (**Paper 4**).
- [64] **Gaussian 94, Revision B.3**, M.J. Frisch, G.W. Trucks, H.B. Schlegel, P.M.W. Gill, B.G. Johnson, M.A. Robb, J.R. Cheeseman, T. Keith, G.A.

- Petersson, J.A. Montgomery, K. Raghavachari, M.A. Al-Laham, V.G. Zakrzewski, J.V. Ortiz, J.B. Foresman, C.Y. Peng, P.Y. Ayala, W. Chen, M.W. Wong, J.L. Andres, E.S. Replogle, R. Gomperts, R.L. Martin, D.J. Fox, J.S. Binkley, D.J. Defrees, J. Baker, J.P. Stewart, M. Head-Gordon, C. Gonzalez, and J.A. Pople. *Gaussian, Inc., Pittsburgh PA. 1995.*
- [65] P.J. Crutzen. *Faraday Discussions. "Atmospheric Chemistry: Measurements Mechanisms and Models"*. **1995**, 100, 1.
- [66] J.J. Houghton, L.G. Meira Filho, B.A. Callander, N. Harris, A. Kattenberg and K. Maskell (Editors). *"Climate Change 1995 – The Science of Climate Change"*. Cambridge Univ. Press., Chambridge. **1995**.
- [67] T.E. Graedel and P.J. Crutzen. *"Atmospheric Change, An Earth System Perspective"*. W.H. Freeman and Company, New York, US. **1993**.
- [68] M. Bassett and J.H. Seinfeld. *Atm. Env.* **1983**, 88, 6611.
M. Bassett and J.H. Seinfeld. *Atm. Env.* **1986**, 91, 1089.
D.J. Jacob. *J. Geophys. Res.* **1986**, 91, 9807.
- [69] J.C. Farman, B.G. Gardiner og J.D. Shanklin. *Nature.* **1985**, 315, 207.
- [70] R. Atkinson. *J. Phys. Chem. Ref. Data, Monograph No. 2.* **1994**.
- [71] R. Atkinson. *J. Phys. Chem. Ref. Data, Monograph No. 1.* **1989**.
- [72] R. Atkinson. *Atm. Env.* **1990**, 24A, 1.
- [73] H. Güsten. *"Formation, Transport and Control of Photochemical Smog"* in *The Handbook of Environmental Chemistry. Volume 4 Part A, Air Pollution*, O. Hutzinger (editor). Springer-Verlag. **1985**.
- [74] B.J. Finlayson-Pitts and J.N. Pitts Jr. *"Atmospheric Chemistry: Fundamentals and Experimental Techniques"*. John Wiley & Sons, New York, U.S. **1986**.
- [75] P.D. Lightfoot, R. Lesclaux and B. Veyret. *J. Phys. Chem.* **1990**, 94, 700.
P.D. Lightfoot, B. Veyret and R. Lesclaux. *J. Phys. Chem.* **1990**, 94, 708.
- [76] F. Kirchner and W.R. Stockwell. *J. Geophys. Res.* **1996**, 101, 21007.
- [77] R. Atkinson. *J. Phys. Chem. Ref. Data.* **1991**, 20, 459.
- [78] W.R. Stockwell and J.G. Calvert. *J. Geophys. Res.* **1983**, 88, 6673.
R. Atkinson, C.N. Plum, W.P.L. Carter, A.M. Winer and J.N. Pitts, Jr. *J. Phys. Chem.* **1984**, 88, 1210.
C.A. Cantrell, W.R. Stockwell, L.G. Anderson, K.L. Busarow, D. Perner, A. Schmeltekopf, J.G. Calvert and H.S. Johnson. *J. Phys. Chem.* **1985**, 89, 139.
- [79] W.R. Stockwell and J.G. Calvert. *Atm. Env.* **1983**, 17, 2231.
- [80] A. Eliassen, Ø. Hov, I.S.A. Isaksen, J. Saltbones and F. Stordal. *J. Appl. Met.* **1982**, 21, 1645.
- [81] Ø. Hov, F. Stordal and A. Eliassen. *Norwegian Institute for Air Research Report NILU TR 5/85.* **1985**.

- [82] D. Simpson, Y. Andersson-Sköld and M.E. Jenkin. *EMEP MSC-W Note 2/93*. **1993**.
- [83] R. Atkinson, D.L. Baulch, R.A. Cox, R.F. Hampson, J.A. Kerr and J. Troe. *J. Phys. Chem. Ref. Data*. **1992**, *21*, 1125.
- [84] S.E. Paulson and J.H. Seinfeld. *J. Geophys. Res.* **1992**, *97*, 20703.
- [85] K. Barrett and E. Berge (editors). *EMEP MSC-W Report 1/96*. **1996**.
- [86] R.G. Derwent, M.E. Jenkin and S.M. Saunders. *Atm. Env.* **1996**, *30*, 189.
- [87] J.A. Leone and J.H. Seinfeld. *Atm. Env.* **1985**, *19*, 437.
- [88] J.A. Kerr and J.G. Calvert. "Chemical Transformation Modules for Eulerian Acid Deposition Models, Vol. 1, The Gas Phase Chemistry". Report EPA/600/3-85/015, U.S. Environ. Prot. Agency, Washington, D.C. **1985**.
- [89] W.B. DeMore, S.P. Sander, D.M. Golden, R.F. Hampson, M.J. Kurylo, C.J. Howard, A.R. Ravishankara, C.E. Kolb and M.J. Molina. "NASA Panel for Data Evaluation, Chemical Kinetics and Photochemical Data for Use in Stratospheric Modeling, Evaluation Number 11". JPL Publication. **1994**.
- [90] W.P.L. Carter, D. Luo, I.L. Malkina and D. Fitz. "The University of California, Riverside Environmental Chamber Data Base for Evaluating Oxidant Mechanisms. Indoor Chamber Experiments Through 1993". **1995**, 1–2.
FTP site – <ftp://cert.ucr.edu/pub/carter>.
- [91] W.R. Stockwell, J.B. Milford, G.J. McRae, P. Middleton and J.S. Chang. *Atm. Env.* **1988**, *22*, 2481.
- [92] T.E. Graedel. "The Photochemistry of Atmospheres: Earth, the Other Planets, and Comets. J.S. Levine (editor)". Academic Press, Inc. **1985**.
- [93] A.M. Dunker, S. Kumar and P.H. Berzins. *Atm. Env.* **1984**, *18*, 311.
- [94] T.B. Shafer and J.H. Seinfeld. *Atm. Env.* **1986**, *20*, 487.
- [95] A.M. Hough. *J. Geophys. Res.* **1988**, *93*, 3789.
- [96] M.C. Dodge. *J. Geophys. Res.* **1989**, *94*, 5121.
- [97] R.G. Derwent. *Atm. Env.* **1990**, *24A*, 2615.
- [98] R.G. Derwent. *Atm. Env.* **1993**, *27A*, 277.
- [99] H.E. Jeffries and S. Tonnesen. *Atm. Env.* **1994**, *28*, 2991.
- [100] J. Olson, M. Prather, T. Berntsen, G. Carmichael, R. Chatfield, P. Connell, R. Derwent, L. Horowitz, S. Jin, M. Kanakidou, R. Kotamarthi, M. Kuhn, K. Law, J. Penner, L. Perliski, S. Sillman, F. Stordal, A. Thomson and O. Wild. *J. Geophys. Res.* **1997**, *102*, 5979.
- [101] E. Berge (editor). *EMEP MSC-W Report 1/97*. **1997**.
- [102] X. Lin, M. Trainer and S.C. Liu. *J. Geophys. Res.* **1988**, *93*, 15879.
- [103] S. Sillman. *Atm. Env.* **1999**, *33*, 1823.

- [104] P. Warneck. "Chemistry of the Natural Atmosphere". Academic Press, San Diego. **1988**.
- [105] S. Madronich and J.G. Calvert. *J. Geophys. Res.* **1990**, *95*, 5697.
- [106] R.P. Wayne, I. Barnes, P. Biggs, J.P. Burrows, C.E. Canosa-Mas, J. Hjorth, G. Le Bras, G.K. Moortgat, D. Perner, G. Poulet, G. Restelli and H. Sidebottom. *Atm. Env.* **1991**, *25A*, 1.
- [107] J.C. Light. *J. Chem. Phys.*, **1964**, *40*, 3221.
P. Pechukas and J.C. Light. *J. Chem. Phys.* **1965**, *42*, 3281.
J.C. Light and J. Lin. *J. Chem. Phys.* **1965**, *43*, 3209.
P. Pechukas, J.C. Light and C. Rankin. *J. Chem. Phys.* **1966**, *44*, 794.
J. Lin and J.C. Light. *J. Chem. Phys.* **1966**, *45*, 2545.
J.C. Light. *Disc. Faraday Soc.* **1967**, *44*, 14.
- [108] G.D. Billing and K.V. Mikkelsen. "Advanced Molecular Dynamics and Chemical Kinetics". John Wiley & Sons, New York, U.S. **1997**.
- [109] M.G. Sheppard and R.B. Walker. *J. Chem. Phys.* **1983**, *78*, 7191.
- [110] K. Yamashita and K. Morokuma, F. Le Quéré and C. Leforestier. *Chem. Phys. Lett.* **1992**, *191*, 515.
- [111] A. J. Stace and J. N. Murrell. *J. Chem. Soc. Faraday II.* **1978**, *74*, 2182.
- [112] A. J. C. Varandas and J. N. Murrell. *Chem. Phys. Lett.* **1982**, *88*, 1.
- [113] A. J. C. Varandas and A. A. C. C. Pais. *Mol. Phys.* **1988**, *65*, 843.
- [114] M. Chajia and M. Jacon. *J. Chem. Phys.* **1994**, *101*, 271.
- [115] M. Chajia and M. Jacon. *Chem. Phys.* **1995**, *195*, 195.
- [116] W. Brennen and H. Niki. *J. Chem. Phys.* **1965**, *42*, 3725.
- [117] J. T. Herron and F. S. Klein. *J. Chem. Phys.* **1964**, *40*, 2731.
- [118] S. Jaffe and F. S. Klein. *Trans. Faraday Soc.* **1966**, *62*, 3135.
- [119] H. Hippler and J. Troe. *Ber. Bunsenges. Phys. Chem.* **1971**, *75*, 27.
- [120] M. Quack and J. Troe. *Ber. Bunsenges. Phys. Chem.* **1977**, *81*, 160.
- [121] M. Quack and J. Troe. *Ber. Bunsenges. Phys. Chem.* **1977**, *81*, 329.
- [122] A. E. Croce De Cobos and J. Troe. *Int. J. Chem. Kinet.* **1984**, *16*, 1519.
- [123] S. M. Anderson, F. S. Klein and F. Kaufman. *J. Chem. Phys.* **1985**, *83*, 1648.
- [124] H. Hippler, R. Rahn and J. Troe. *J. Chem. Phys.* **1990**, *93*, 6560.
- [125] A. J. C. Varandas, A. A. C. C. Pais, J. M. C. Marques and W. Wang. *Chem. Phys. Lett.* **1996**, *249*, 264.
- [126] F. Jensen. "Introduction to Computational Chemistry". John Wiley & Sons, New York, U.S. **1998**.

- [127] G. Herzberg. *“Molecular Spectra and Molecular Structure – I. Spectra of Diatomic Molecules”*. Second edition, D. van Nostrand Company, Inc., Princeton, New Jersey, U.S. **1959**.
- [128] G. Herzberg. *“Molecular Spectra and Molecular Structure – III. Electronic Spectra and Electronic Structure of Polyatomic Molecules.”* Second edition, 1966, D. van Nostrand Company, Inc., Princeton, New Jersey, U.S. **1966**.
- [129] R.D. Levine and R.B. Bernstein, *“Molecular Reaction Dynamics and Chemical Reactivity”*. Oxford University Press. **1987**.
- [130] R.A. Alberty. *“Physical Chemistry”*. 7th edition, John Wiley & Sons, York, U.S. **1987**.
- [131] J.N. Israelachvili. *“Intermolecular and Surface Forces”*, Academic Press. **1985**.
- [132] S.R. Polo. *Can. J. Phys.* **1957**, *35*, 880.
- [133] R.E. Roberts, R.B. Bernstein and C.F. Curtiss. *J. Chem. Phys.* **1969**, *50*, 5163.
- [134] E.D. Morris, D.H. Stedman and H. Niki. *J. Am. Chem. Soc.* **1971**, *93*, 3570.
- [135] R.A. Cox, R.G. Derwent, P.M. Holt and J.A. Kerr. *J. Chem. Soc. Faraday Trans.* **1976**, *72*, 2061.
- [136] H. Niki, P.D. Maker, C.M. Savage and L.P. Breitenbach. *J. Phys. Chem.* **1978**, *82*, 132.
- [137] R. Atkinson and J.N. Pitts Jr. *J. Chem. Phys.* **1978**, *68*, 3581.
- [138] J.A. Kerr and D.W. Sheppard. *Environ. Sci. Technol.* **1981**, *15*, 960.
- [139] G.J. Audley, D.L. Baulch, I.M. Campbell. *J. Chem. Soc. Faraday Trans.* **1981**, *77*, 2541.
- [140] D.H. Semmes, A.R. Ravishankara, A.A. Cump-Perkins and P.H. Wine. *Int. J. Chem. Kinet.* **1985**, *17*, 303.
- [141] J.V. Michael, D.G. Keil and R.B. Klemm. *J. Chem. Phys.* **1985**, *83*, 1630.
- [142] S. Dóbbé, L.A. Khachatryan and T. Bérces. *Ber. Bunsenges. Phys. Chem.* **1989**, *93*, 847.
- [143] C. Balestra-Garcia, G. LeBras and H. Mac Leod. *J. Phys. Chem.* **1992**, *96*, 3312.
- [144] D.J. Scollard, J.J. Treacy, H.W. Sidebottom, C. Balestra-Garcia, G. Laverdet, G. LeBras, H. Mac Leod and S. Téton. *J. Phys. Chem.* **1993**, *97*, 4683.
- [145] B. D’Anna and C.J. Nielsen. *J. Chem. Soc. Faraday Trans.* **1997**, *29*, 1234.
- [146] C.J. Nielsen, Oslo University, Norway. *Private communication*.
- [147] SPARTAN. Version 4.1. Wavefunction Inc., Irvine, California, U.S.

- [148] H. Niki, P.D. Maker, C.M. Savage and L.P Breitenbach. *J. Phys. Chem.* **1983**, *87*, 2190.
- [149] G.L. Vaghjiani and A.R. Ravishankara. *J. Phys. Chem.* *1989*, **93**, 1948.
- [150] W. Junkermann and W.R. Stockwell. "On the Budget of Photooxidants in the Marine Boundary Layer of the Tropical South Atlantic". Submitted to *J. Geophys. Res.*
- [151] C.E. Klots. *Zeitschrift für Naturforschung.* **1972**, *27a*, 553.
- [152] C.E. Klots. *J. Phys. Chem.* **1971**, *75*, 1526.
- [153] E.E. Nikitin. *Theor. and Exp. Chem.* **1965**, *1*, 90.
- [154] S.J. Klippenstein and R.A. Marcus. *J. Chem. Phys.* **1989**, *91*, 2280.
- [155] W.J. Chesnavich and M.T. Bowers. *J. Chem. Phys.* **1977**, *66*, 2306.
- [156] W.J. Chesnavich and M.T. Bowers. *J. Am. Chem. Soc.* **1976**, *26*, 8301.
- [157] J.E. Jonsen, D. Simpson, L. Tarasson, S. Unger, J. Altenstedt, A.-G. Hjellbrekke, T. Berntsen and J. Sundet. *EMEP/MSC-W Report 1/98.* **1998**.
- [158] W.R. Stockwell, G. Kramm, H.-E. Scheel, V.A. Mohnen and W. Seiler. "Forest Decline and Ozone: a Comparison of Controlled Chamber and Field Experiments, Chapter 1: Ozone Formation, Destruction and Exposure in Europe and the United States. H. Sandermann Jr., A.R. Wellburn and R.L. Heath (Editors). *Ecological Studies, Series Editor: O.L. Lange, Würzburg*". Springer Verlag. **1996**.
- [159] J.H. Sørensen. *Atm. Env.* **1998**, *32*, 4195.
- [160] J.G. Watson, D.W. DuBois, R. DeMandel, A. Kaduwela, K. Magliano, C. McDale, P.K. Mueller, A. Ranzieri, P.M. Roth and S. Tanrikulu, "Aerometric Monitoring Program Plan for the California Regional PM_{2.5}/PM₁₀ Air Quality Study". *DRI Document No. 9801.1D5.* 1998.
- [161] S. Madronich. *J. Geophys. Res.* **1987**, *92*, 9740.
- [162] B.H. Sass, DMI, FM, Denmark. *Private communication.*
- [163] K.L. Demerjian, K.L. Schere and J.T. Petersen. "Advances in Environmental Science and Technology. (editors: J.N. Pitts and R.L. Metcalf)". *John Wiley & Sons, New York, U.S.* **1980**, *10*.
- [164] D.P. Chock, Ford Research Laboratory, Ford Motor Company, Dearborn, U.S. *Private communication.*
- [165] D. Simpson and A. Eliassen. *EMEP/MSC-W Note 5/97.* **1997**.
- [166] P. Thejll, DMI, FS, Denmark. *Private communication.*
- [167] P.J.H. Builtjes. "Model validation of AOT40". *Proceedings 2nd GLOREAM Workshop, Madrid.* **1998**.
- [168] S.S. Shaik, H.B. Schlegel and S. Wolfe. "Theoretical Aspects of Physical Organic Chemistry". *John Wiley & Sons, New York, U.S.* **1991**.

- [169] K.V. Mikkelsen, S.U. Pedersen, H. Lund and P. Swanstrøm. *J. Phys. Chem.* **1991**, *95*, 8892.
- [170] P. Middleton, W.R. Stockwell and W.P.L. Carter. *Atm. Env.* **1990**, *24A*, 1107.

DANISH METEOROLOGICAL INSTITUTE

Scientific Reports

Scientific reports from the Danish Meteorological Institute cover a variety of geophysical fields, i.e. meteorology (including climatology), oceanography, subjects on air and sea pollution, geomagnetism, solar-terrestrial physics, and physics of the middle and upper atmosphere.

Reports in the series within the last five years:

No. 95-1

Peter Stauning and T.J. Rosenberg:
High-Latitude, day-time absorption spike events
1. morphology and occurrence statistics
Not published

No. 95-2

Niels Larsen: Modelling of changes in stratospheric ozone and other trace gases due to the emission changes : CEC Environment Program Contract No. EV5V-CT92-0079. Contribution to the final report

No. 95-3

Niels Larsen, Bjørn Knudsen, Paul Eriksen, Ib Steen Mikkelsen, Signe Bech Andersen and Torben Stockflet Jørgensen: Investigations of ozone, aerosols, and clouds in the arctic stratosphere : CEC Environment Program Contract No. EV5V-CT92-0074. Contribution to the final report

No. 95-4

Per Høeg and Stig Syndergaard: Study of the derivation of atmospheric properties using radio-occultation technique

No. 95-5

Xiao-Ding Yu, **Xiang-Yu Huang** and **Leif Laurssen** and Erik Rasmussen: Application of the HIRLAM system in China: heavy rain forecast experiments in Yangtze River Region

No. 95-6

Bent Hansen Sass: A numerical forecasting system for the prediction of slippery roads

No. 95-7

Per Høeg: Proceeding of URSI International Conference, Working Group AFG1 Copenhagen, June 1995. Atmospheric research and applications using observations based on the GPS/GLONASS System
Not published

No. 95-8

Julie D. Pietrzak: A comparison of advection schemes for ocean modelling

No. 96-1

Poul Frich (co-ordinator), H. Alexandersson, J. Ashcroft, B. Dahlström, G.R. Demarée, A. Drebs, A.F.V. van Engelen, E.J. Førland, I. Hanssen-Bauer, R. Heino, T. Jónsson, K. Jonasson, L. Keegan, P.Ø. Nordli, **T. Schmith, P. Steffensen, H. Tuomenvirta, O.E. Tveito**: North Atlantic Climatological Dataset (NACD Version 1) - Final report

No. 96-2

Georg Kjærgaard Andreasen: Daily response of high-latitude current systems to solar wind variations: application of robust multiple regression. Methods on Godhavn magnetometer data

No. 96-3

Jacob Woge Nielsen, Karsten Bolding Kristensen, Lonny Hansen: Extreme sea level highs: a statistical tide gauge data study

No. 96-4

Jens Hesselbjerg Christensen, Ole Bøssing Christensen, Philippe Lopez, Erik van Meijgaard, Michael Botzet: The HIRLAM4 Regional Atmospheric Climate Model

No. 96-5

Xiang-Yu Huang: Horizontal diffusion and filtering in a mesoscale numerical weather prediction model

No. 96-6

Henrik Svensmark and Eigil Friis-Christensen: Variation of cosmic ray flux and global cloud coverage - a missing link in solar-climate relationships

No. 96-7

Jens Havskov Sørensen and Christian Ødum Jensen: A computer system for the management of epidemiological data and prediction of risk and economic consequences during outbreaks of foot-and-mouth disease. CEC AIR Programme. Contract No. AIR3 - CT92-0652

No. 96-8

Jens Havskov Sørensen: Quasi-automatic of input for LINCOM and RIMPUFF, and output conversion. CEC AIR Programme. Contract No. AIR3 - CT92-0652

No. 96-9

Rashpal S. Gill and Hans H. Valeur:
Evaluation of the radarsat imagery for the operational mapping of sea ice around Greenland

No. 96-10

Jens Hesselbjerg Christensen, Bennert Machenhauer, Richard G. Jones, Christoph Schär, Paolo Michele Ruti, Manuel Castro and Guido Visconti:
Validation of present-day regional climate simulations over Europe: LAM simulations with observed boundary conditions

No. 96-11

Niels Larsen, Bjørn Knudsen, Paul Eriksen, Ib Steen Mikkelsen, Signe Bech Andersen and Torben Stockflet Jørgensen: European Stratospheric Monitoring Stations in the Arctic: An European contribution to the Network for Detection of Stratospheric Change (NDSC): CEC Environment Programme Contract EV5V-CT93-0333: DMI contribution to the final report

No. 96-12

Niels Larsen: Effects of heterogeneous chemistry on the composition of the stratosphere: CEC Environment Programme Contract EV5V-CT93-0349: DMI contribution to the final report

No. 97-1

E. Friis Christensen og C. Skøtt: Contributions from the International Science Team. The Ørsted Mission - a pre-launch compendium

No. 97-2

Alix Rasmussen, Sissi Kiilsholm, Jens Havskov Sørensen, Ib Steen Mikkelsen: Analysis of tropospheric ozone measurements in Greenland: Contract No. EV5V-CT93-0318 (DG 12 DTEE): DMI's contribution to CEC Final Report Arctic Tropospheric Ozone Chemistry ARCTOC

No. 97-3

Peter Thejll: A search for effects of external events on terrestrial atmospheric pressure: cosmic rays

No. 97-4

Peter Thejll: A search for effects of external events on terrestrial atmospheric pressure: sector boundary crossings

No. 97-5

Knud Lassen: Twentieth century retreat of sea-ice in the Greenland Sea

No. 98-1

Niels Woetman Nielsen, Bjarne Amstrup, Jess U. Jørgensen:
HIRLAM 2.5 parallel tests at DMI: sensitivity to type of schemes for turbulence, moist processes and advection

No. 98-2

Per Høeg, Georg Bergeton Larsen, Hans-Henrik Benzou, Stig Syndergaard, Mette Dahl Mortensen: The GPSOS project
Algorithm functional design and analysis of ionosphere, stratosphere and troposphere observations

No. 98-3

Mette Dahl Mortensen, Per Høeg:
Satellite atmosphere profiling retrieval in a nonlinear troposphere
Previously entitled: Limitations induced by Multipath

No. 98-4

Mette Dahl Mortensen, Per Høeg:
Resolution properties in atmospheric profiling with GPS

No. 98-5

R.S. Gill and M. K. Rosengren
Evaluation of the Radarsat imagery for the operational mapping of sea ice around Greenland in 1997

No. 98-6

R.S. Gill, H.H. Valeur, P. Nielsen and K.Q. Hansen: Using ERS SAR images in the operational mapping of sea ice in the Greenland waters: final report for ESA-ESRIN's: pilot projekt no. PP2.PP2.DK2 and 2nd announcement of opportunity for the exploitation of ERS data projekt No. AO2..DK 102
Not published

No. 98-7

Per Høeg et al.: GPS Atmosphere profiling methods and error assessments

No. 98-8

H. Svensmark, N. Woetmann Nielsen and A.M. Sempreviva: Large scale soft and hard turbulent states of the atmosphere

No. 98-9

Philippe Lopez, Eigil Kaas and Annette Guldborg: The full particle-in-cell advection scheme in spherical geometry

No. 98-10

H. Svensmark: Influence of cosmic rays on earth's climate

No. 98-11

Peter Thejll and Henrik Svensmark: Notes on the method of normalized multivariate regression

No. 98-12

K. Lassen: Extent of sea ice in the Greenland Sea 1877-1997: an extension of DMI Scientific Report 97-5

No. 98-13

Niels Larsen, Alberto Adriani and Guido DiDonfrancesco: Microphysical analysis of polar stratospheric clouds observed by lidar at McMurdo, Antarctica

No.98-14

Mette Dahl Mortensen: The back-propagation method for inversion of radio occultation data

No. 98-15

Xiang-Yu Huang: Variational analysis using spatial filters

No. 99-1

Henrik Feddersen: Project on prediction of climate variations on seasonal to interannual time-scales (PROVOST) EU contract ENVA4-CT95-0109: DMI contribution to the final report: Statistical analysis and post-processing of uncoupled PROVOST simulations

No. 99-2

Wilhelm May: A time-slice experiment with the ECHAM4 A-GCM at high resolution: the experimental design and the assessment of climate change as compared to a greenhouse gas experiment with ECHAM4/OPYC at low resolution

No. 99-3

Niels Larsen et al.: European stratospheric monitoring stations in the Arctic II: CEC Environment and Climate Programme Contract ENV4-CT95-0136. DMI Contributions to the project

No. 99-4

Alexander Baklanov: Parameterisation of the deposition processes and radioactive decay: a review and some preliminary results with the DERMA model

No. 99-5

Mette Dahl Mortensen: Non-linear high resolution inversion of radio occultation data

No. 99-6

Stig Syndergaard: Retrieval analysis and methodologies in atmospheric limb sounding using the GNSS radio occultation technique

No. 99-7

Jun She, Jacob Woge Nielsen: Operational wave forecasts over the Baltic and North Sea

No. 99-8

Henrik Feddersen: Monthly temperature forecasts for Denmark - statistical or dynamical?

No. 99-9

P. Thejll, K. Lassen: Solar forcing of the Northern hemisphere air temperature: new data (In Press)

No. 99-10

Torben Stockflet Jørgensen, Aksel Walløe Hansen: Comment on "Variation of cosmic ray flux and global coverage - a missing link in solar-climate relationships" by Henrik Svensmark and Eigil Friis-Christensen

No. 99-11

Mette Dahl Meincke: Inversion methods for atmospheric profiling with GPS occultations

No. 99-12

Benzon, Hans-Henrik; Olsen, Laust: Simulations of current density measurements with a Faraday Current Meter and a magnetometer

No. 00-01

Høeg, P.; Leppelmeier, G: Ace. Atmosphere Climate Experiment. Proposers of the mission

No. 00-02

Høeg, P.: Face-it. Field-aligned current experiment in the ionosphere and thermosphere

No. 00-03

Allan Gross: Surface ozone and tropospheric chemistry with applications to regional air quality modeling. PhD thesis